STATIC AND DYNAMIC ANALYSES OF MOUNTAIN BIKES AND THEIR RIDERS

Chia-Chin Wu

A Thesis Submitted for the Degree of Doctor of Philosophy in Engineering

Department of Mechanical Engineering
University of Glasgow
November 2012

Abstract

Mountain biking is a globally popular sport, in which the rider uses a mountain bike to ride on off-road terrain. A mountain bike has either a front suspension system only or a full-suspension system to decrease the external vibration resulting from the terrain irregularities and to increase riding comfort. Despite the added comfort of full-suspension of mountain bikes, there are some disadvantages because the chain-suspension interaction and bobbing effect absorb some of the rider's pedalling power and lead to the reduction of pedalling efficiency.

In this study, a technique for evaluating the pedalling efficiency of a bike rider in seated cycling by using engineering mechanics is developed. This method is also found to be useful for determining the correct crank angle for the beginning of the downstroke and that of the upstroke during each pedalling cycle. Next, five mathematical models of rider-bike systems are developed in Simulink and SimMechanics, including one hard-tail (HT) bike, and four full-suspension (FS) bikes [single pivot, four-bar-linkage horst link, four-bar-linkage faux bar, and virtual pivot point (VPP)]. In each of the five rider-bike systems, a PID controller is applied on the rider's elbow to prevent his upper body from falling down due to gravity. A pedalling controller is also developed in Simulink, which is based on the previous theory for evaluating the rider's pedalling efficiency written in Matlab. Another PID controller is used for the pedalling control by sensing the real-time moving speed and applying a suitable pedalling force to achieve a desired speed.

The dynamic responses for each of the five rider-bike systems moving on a flat road surface (without bumps) and rough terrain (with bumps) are investigated. The values determined include the pedalling force, pedalling torque and power, forward velocity, contact forces of front and rear wheels, compressions of front suspension (front fork) and rear suspension (rear shock absorber), sprocket distance, chain tension force, and vertical accelerations of handlebar and seats. The numerical results reveal that, while moving on flat road surface, the pedalling efficiency of hard-tail bike is highest, and the bobbing effect of the VPP bike is most serious. However, while moving on rough

terrain, the riding conditions for each of the four full-suspension bikes are more stable than the hard-tail bike.

Keywords: Mountain bike, full-suspension system, bumps, bobbing effect, pedalling efficiency, pedalling cycle, vertical accelerations, PID controller, SimMechanics.

Acknowledgements

First of all, I will give my sincere appreciations to Dr. Donald Ballance and Dr. Arthur Whittaker for their supervisions and advices during the progress of my Ph. D. thesis. Next, I will give my deep gratitude to Prof. Atanas Popov, Prof. Margaret Lucas, and Dr. Henrik Gollee for their suggestions on my research. Furthermore, the instructions and recommendations of my former teachers, Prof. Cho-Chung Liang and Prof. Tso-Liang Tend, are highly appreciated.

I will thank one of my best friends, Dr. Tsung-Han Hsieh, for his encouragements and helps in the period before I got my Ph. D. I will also say "many thanks" to some of my friends for the discussions and sharing the academic experiences during my Ph. D. study, including Dong Wang, Juan Fang, Dr. S.M. Wong, Paul Turko, Dr. Patrick Harkness, Dr. Andrew Mathieson, ... etc. Finally, I will appreciate my parents for providing the tuition and living expenses in the past years. I will thank my wife for her encouragements and supports in the past months when I am in the hard time.

Table of Contents

List of Figures

List of Tables

Nomenclature

C_1 ……..A constant $[=(x_c^2+y_c^2+L_3^2-L_{12}^2)/(2L_3)]$

C_3 ……A constant $(=x_c+L_1)$

C_4 ……A constant $(=y_c+L_1)$

C_5 …… A parameter $(=y_c-L_3\sin\theta_3)$

C_5' ……A parameter $(=y_c-L_1\cos\theta_1)$

C_5'' ……A parameter $(=y_c+L_1\sin\theta_1')$

C_6 ……...A parameter $(=-y_c+L_3\sin\theta_3)$

C_6' ……A parameter $(=y_c+L_1\cos\theta_1')$

c ……..Damping coefficient

c_{equi} …… Equivalent damping coefficient of the dynamic system

D_3 ……...A constant $[=(C_3^2+y_c^2+L_3^2-L_2^2)/(2L_3)]$

D_4 ……A constant $[=(x_c^2+C_4^2+L_3^2-L_2^2)/(2L_3)]$

D_5 ……..A parameter $(=-x_c+L_3\cos\theta_3)$

D_5' ……A parameter $(=-x_c-L_1\sin\theta_1)$

D_5'' ……A parameter $(=x_c+L_1\cos\theta_1')$

D_6 ……A parameter $(=x_c-L_3\cos\theta_3)$

D_6' ……...A parameter $(=-x_c+L_1\sin\theta_1')$

d ……Distance between front and rear axles (wheel base)

E_2 ……A constant$[=\{x_c^2+y_c^2+L_3^2-(L_2-L_1)^2\}/(2L_3)]$

E_5 ……A parameter $[=(C_5^2+D_5^2+L_1^2-L_2^2)/(2L_1)]$

E_5' ……..A parameter $[=(C_5'^2+D_5'^2+L_3^2-L_2^2)/(2L_3)]$

E_5'' ……A parameter $[=(C_5''^2+D_5''^2+L_3^2-L_2^2)/(2L_3)]$

E_6 ……A parameter $[=(C_6^2+D_6^2+L_1^2-L_2^2)/(2L_1)]$

E_6' ……..A parameter $[=(C_6'^2+D_6'^2+L_3^2-L_2^2)/(2L_3)]$

FS bike……Full-suspension bike

$F_2(t)$ ……..Pedalling force applied by Rod2 (shank) at time *t*

$F_t(t)$ ……Pedalling-force component normal to crank (and *tangential* to the path of crank pin)

$F_{contact}$ …….....Contact force between wheels and ground

$F_{c,f}$ ……Contact force between front wheel and ground

$F_{c,r}$ ……...Contact force between rear wheel and ground

F_f ……Chain (tensile) force tangential to front sprocket

F_r ……..….Chain (tensile) force tangential to rear sprocket

$F_x(t)$ …….Reactive force at rear wheel in *x*-direction

$F_y(t)$ ……Downward pedalling force applied on the pedal at time *t*

f_e ……Cyclic exciting frequency of pedalling forces ($=\omega_e/2\pi$)

g …….Gravitational acceleration

HT bike……...Hard tail bike

h_b ……Height of bump or hollow

I …….Inertial tensor (or matrix for mass moment of inertia I_{ij} with $i, j = x, y, z$)

I_{ij} ……...Mass moment of inertia about i and j axes (with $i, j = x, y, z$)

$I_{\text{hollow circular cylinder}}$ ……..Matrix for mass moment of inertia of hollow circular cylinder

$I_{\text{muscular part}}$ ……..Matrix for mass moment of inertia of muscular part of the rider model

$I_{\text{solid rod}}$ ……Matrix for mass moment of inertia of solid rod

k ……..spring constant (or stiffness of the rider-bike system)

L_1 ……Length of crank (Rod1)

L_2 ……..Length of lower leg (Rod2, shank)

L_3 ……...Length of upper leg (Rod3, thigh)

L_{12} ……A constant ($=L_1+L_2$)

$\overline{L}$ …….Leg length ($=L_2=L_3$)

$\overline{L}_{\min}$ ……Minimum leg length of rider ($= L_{2,\min} = L_{3,\min}$)

$\overline{L}_{\max}$ ……..….Maximum leg length of rider ($= L_{2,\max} = L_{3,\max}$)

ℓ …….Length of rod or cylinder (or Horizontal distance between front and rear axles)

ℓ_f ……..Horizontal distance between c.g. of entire rider-bike system and front axle

ℓ_r ……Horizontal distance between c.g. of entire rider-bike system and rear axle

m …….Effective mass of the entire rider-bike system

m_{bike} ……. Effective mass of bike

m_{rider} ……Effective mass of rider

R_c …….....Radius of crank ($= L_1$)

R_w ……...Radius of rear wheel

r ……Radius of disc

r_f ……..Radius of front sprocket

r_i ……...Inner radius of hollow circular cylinder

r_o ……..Outer radius of hollow circular cylinder

r_r …….Radius of rear sprocket

s_1, s_2 ……..Roots of the quadratic ($ax^2 + bx + c = 0$): $x = \left(-b \pm \sqrt{b^2 - 4ac}\right) / (2a)$

$T(t)$ ……...Torque developed by the crank at time t

T_f ……..Torque on front sprocket

T_p …….Period of the pedalling forces or strokes

T_r ……....Torque on rear sprocket

$T_z(t)$ ……...Reactive torque on rear wheel [$= F_x(t) \cdot R_w$]

t ……...……Time

t_1 ……Time for the responses of a dynamic system to be in steady state

$\bar{t}$ ……. ……..Time for the responses after steady state ($= t - t_1$)

Δt ……Step size of time for the analysis of dynamic responses (or time difference due to distance between front and rear axles $= d/v$)

Δt_b……Time duration from the rider-bike system meeting the left end of the bump to that leaving the right end of the bump

Δt_m ……Phase time interval at *meeting* left end of the bump

Δt_ℓ ……Phase time interval at *leaving* right end of the bump

V_t ……..Tangential velocity (of chain)

V_x ……...Forward velocity of rider-bike system in *x*-direction

$\overline{V_x}$ ……Average forward velocity of rider-bike system in *x*-direction

$|V_x|_{\min}$ ……..Minimum forward velocity of rider-bike system

$|V_x|_{\max}$ ……Maximum forward velocity of rider-bike system

ΔV_x ……Difference between $|V_x|_{\max}$ (or $|V_x|_{\min}$) and $\overline{V_x}$ $(=|V_x|_{\max \text{ or } \min} - \overline{V_x})$

VPP bike……Virtual pivot point bike

W ……...Work done by the rider in each half pedalling cycle

v ……..Horizontal moving velocity of bike

x ……Abscissa of the Cartesian coordinate system

$x(t)$ ……...displacement at time t

$\dot{x}(t)$ ……....velocity at time t

$\ddot{x}(t)$ ……acceleration at time t

x_c ……Horizontal distance between seat and bottom bracket

Δx ……Spacing for numerical integrations by using Simpson or trapezoidal rule

xyz ……Local Cartesian coordinate system

$\overline{xyz}$ ……..Global Cartesian coordinate system

y ……Ordinate of the Cartesian coordinate system

y_c ……Vertical distance between seat and bottom bracket

$\alpha(t)$ ……..Angle between Rod1 (crank) and Rod2 (shank) at time t $(=1.5\pi - \theta_1 - \theta_2)$

β ……Angle between Rod2 (shank) and upward *y*-axis

$\theta_1(t)$ ……Angle of crank (Rod1) with respect to its top dead centre (TDC) at time t

δ_x ……...Horizontal movement of rear axle

$|\delta_x|_{\max}$ ……..Maximum horizontal movement of rear axle

δ_y ……....Vertical movement of rear axle

$|\delta_y|_{\max}$ …….. Maximum vertical movement of rear axle

$\theta(t)$....……...Crank angle with its "origin" located at time $t = 0$

$\overline{\theta}(t)$……. Crank angle with its "origin" located at *reference* time ($t \neq 0$)

θ_1 …….Angle between Rod1 (crank) and upward *y*-axis

θ_1' ……Acute part of angle θ_1 (i.e., $\theta_1 = 0.5\pi + \theta_1'$ or $\theta_1 = \pi + \theta_1'$)

$\Delta\theta_1$ ……Step size of crank angle θ_1 for the analysis of dynamic responses

$\Delta\theta_{meet}$ …….. Phase angle between the time instant of meeting left end of the bump and beginning of the associated downstroke ($= \omega_e \Delta t_m$)

$\Delta\theta_{leave}$ …….. Phase angle between the time instant of leaving right end of the bump and beginning of the associated downstroke ($= \omega_e \Delta t_\ell$)

$\theta_2(t)$ ……..Angle between Rod2 (lower leg or shank) and *x*-axis at time *t*

$\theta_3(t)$ ……Angle between Rod3 (upper leg or thigh) and *x*-axis at time *t*

$\overline{\theta}_3$ ……..Amplitude of the rotational angle $\theta_3(t)$ ($= \theta_{3,L} - \theta_{3,U}$)

$\theta_{i,U}, \theta_{i,L}$ ……Critical angles of Rod i ($i = 1,2,3$) when Rod3 in its uppermost and lowermost positions, respectively

$\theta_{i,B}, \theta_{i,C}$ ….Critical angles of Rod i ($i = 1,2,3$) when Rod1 in its rightward (with Joint 1 at point *B*) and downward (with Joint 1 at point *C*) positions, respectively

θ_f ……..Rotational angle of front sprocket

θ_r ……Rotational angle of rear sprocket

ω_e ……..Circular exciting frequency of the external pedalling forces ($= 2\pi f_e$)

ω_f …….Circular rotational speed of front sprocket

ω_r ……..Circular rotational speed of rear sprocket (or rear wheel)

Chapter 1 Introduction

1.1 Introduction to Mountain Bikes

Bicycle riding is a globally popular sport and an economic transportation. Normal bicycles (road bikes) are good enough for a rider to ride on flat road surface. However, for a road bike to be ridden on rough terrains, the induced vibrations will cause the fatigue of its rider and the fracture of its frame structure (or related parts). Although a small part of the vibration can be absorbed by the pneumatic tyre, the most part of it is absorbed by the rider. Therefore, one requires a bike with stronger frame structure and better suspension systems, so that it can effectively reduce the vibration and increase the comfort for the rider. It is evident that the mountain bike belongs to this kind of bike.

The invention of mountain bike can be traced back to 1970's when a small group of people built bikes to race down Mount Tamalpais in California [1]. The mass production of mountain bikes began after 1977, and the first mass-produced mountain bike was Stumpjumper, made by the mountain bike manufacturer Specialized in 1981 [1]. Early mountain bikes had the similar frames to those of road bikes, but with wider frames and forks to allow for wider tyres [2]. In Europe, the population of mountain bike riders has grown up when the manufacturers began to mass produce the mountain bikes in the early 1990's [2], and the modern front suspension (front fork) for mountain bikes was introduced at that time. Rear suspension systems appeared soon after.

Mountain biking gained international recognition by UCI (Union Cycliste Internationale) in 1991 and became an Olympic event in Atlanta in 1996 [2~6]. An estimation by the IMBA in UK (International Mountain Biking Association UK) shows that 23% of the adult population in UK own a mountain bike [7].

1.2 Advantages and Disadvantages of Front and Rear Suspension Systems for Mountain Bikes

When one rides a bike, vibration caused by the surface irregularities is always an important issue, since the vibration will result in discomfort of the rider, the loss of traction control, the fatigue of frame structure, ...etc. One of the simplest ways of reducing bike vibration is the pneumatic tyre invented by Dunlop [1].

The first front suspension of bicycle was invented by Kenfield [8], in which a spring is mounted in the headset, and the rigid fork can move back and forth to absorb vibrations. The modern front and rear suspension systems for mountain bikes are introduced in 1990's. Current front suspension systems are adequate to absorb vibration when the bike is passing over rough terrains. Most advanced front suspension systems have not only springs in the front fork, but also fork (damping) oil in the fork tube to behave like a damping unit. Some of them even have the preloaded damping adjustment to be tuned according to the rider's weight and/or the terrain conditions. In addition, some forks are reversed (up-side-down) with thicker upper fork tube and thinner lower fork tube, which is introduced from current front suspension systems popularly used in sports motorbikes.

For rear suspension systems, the shock absorber looks like a spring-damper unit and is fitted between the front and rear parts of the bike frame. The rear shock absorber is mounted at different locations based on different configurations of bike frames. Some rear suspension designs are shown in Figure 1.1 [9,10].

Both front and rear suspension systems are used to absorb vibrations to increase the comfort of the rider in off-road riding conditions. Generally, suspension systems have four functions [4,10]: (a) isolate the rider from terrain irregularities, and reduce the discomfort of the rider; (b) absorb the energy and vibration caused by the bike hitting obstacles, and dissipate this effect; (c) keep the wheels on the ground while riding on rough terrains, so that the rider can have better control of traction, braking, and steering; (d) add no undesirable characteristics to the bikes. Undesirable characteristics here include chain-suspension interaction [9,10,13] and the bobbing

effect [2,4,12~16]. Chain-suspension interaction is an effect of compression of rear suspension due to the chain torque generated from the rider's pedalling motion (pushing the pedals) [10,13]. The bobbing effect is induced by the compression of rear suspension due to the inertial loading of the rider's legs spinning around (pedalling motion) and the other normal upper body motions [13]. Front suspension systems for mountain bikes have become a standard equipment [4,9] since they have no disadvantages except for a slight additional weight to the bike [4,11]. However, although current rear suspension systems can fulfil functions (a)-(c), none of them can satisfy function (d).

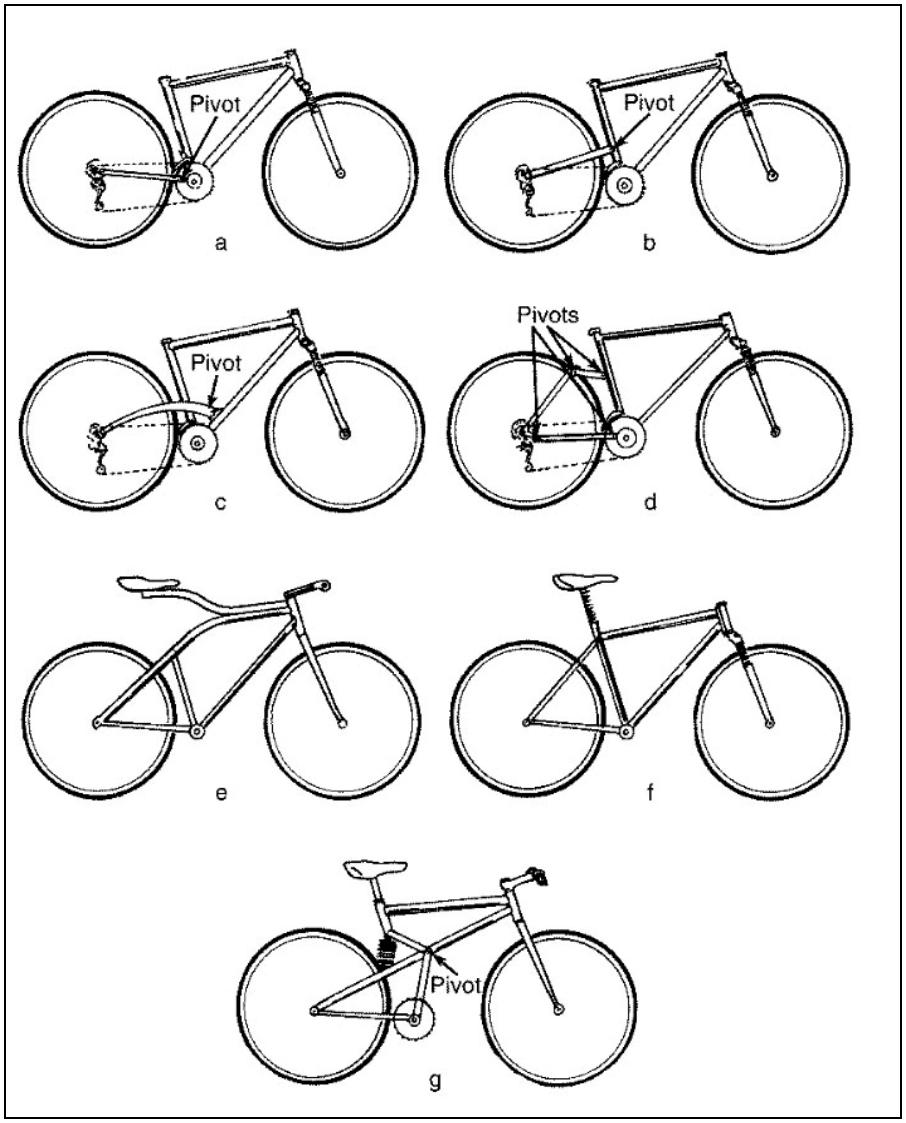

Figure 1.1 Illustration of various rear suspension designs [9,10] (a: low pivot; b: high pivot; c: low-forward pivot; d: four-bar linkage; e: cantilevered beam suspended saddle; f: telescopic seat post suspended saddle; g: unified rear triangle)

Numerous papers in the last two decades have studied the difference between performance of mountain bikes with and without suspension systems. A study presented by Nielens and Lejeune [15] shows that there is no significant difference in energy consumption between cyclists riding a bike either with or without suspension systems. In contrast, the study presented by Wang and Hull [17] indicates that there is power dissipation in the rear suspension when one rides a full suspension bike uphill.

1.3 Aim of this Thesis

The objective of this thesis is to study the experimental and numerical-simulation results to determining performance differences between the mountain bikes with and without suspension systems. For experimental studies, some researchers have designed indoor and field experiments and measured the rider's physiological and psychological state together with mechanical data from the bike. For numerical simulations, mathematical models of some rider-bike systems are developed using different software or programmes, and the dynamic response of the rider-bike systems are studied. Details will be introduced in Chapter 2 of this thesis.

However, all the existing studies are focused on one specific full suspension system, none of them analyze and compare differences between bikes with different kinds of rear suspension systems, except the report of Iturrioz [2] introduced in this thesis. Experimental results of Titlestad, Davie, and Whittaker et al. [3,4,18~20] confirm that during a simulated riding condition with bumps, the full suspension mountain bikes provide physiological and psychological advantages over those of hard tail bikes. However, a series of questionnaires with 260 respondents of mountain bikers ranging from amateur level to competition riders in the UCI World Championships are analyzed by Davie [4], and the results show that only 37% (95 respondents) of the participants have ridden full suspension mountain bikes.

The hard tail bike is a kind of mountain bike with only front suspension and no rear suspension. The most popular mountain bikes with rear suspension systems are: single pivot (swingarm type), four-bar-linkage, and VPP (virtual pivot point), which will be discussed in Chapter 3 of this thesis.

In this thesis, mathematical models of rider-bike systems with the different rear suspension systems mentioned above are developed using SimMechanics. The performance of each bike is analyzed and compared using the dynamic responses of each rider-bike system, including effective pedalling forces and powers, forward velocities, contact forces of front and rear wheels, fork and shock compressions, chain tension forces, and vertical accelerations at handle and seat.

1.4 Thesis Structure

Chapter 1:-Introduction. In this chapter, the general information regarding mountain bikes with suspension systems is presented, and the advantages and disadvantages of the suspension systems are introduced.

Chapter 2:-Mountain Bike Research. In this chapter, a general review regarding the reports on mountain bikes is performed, in which the studies on physiological responses of mountain bike riders, mechanical characteristics of bikes with and without suspension systems, and dynamic simulations of rider-bike systems, and the previous studies on this topic are introduced.

Chapter 3:-Hard-tail and full-suspension mountain bikes. In this chapter, the software used in this study is introduced: Simulink, SimMechanics, Linkage, BikeCAD, and AutoCAD. Following this, the configurations of the five mountain bikes studied in this thesis, hard tail, single pivot, horst link, faux bar, and VPP bikes, are presented.

Chapter 4:-A technique for evaluating the pedalling efficiency of a bike rider. In this chapter, the theoretical analysis of rider's pedalling efficiency is performed, including the determinations of critical angles of the crank and those of the rider's lower and upper legs. Two driving forces transmitted from the rider's upper legs with simple harmonic (SH) and non-simple harmonic (NSH) motions are studied.

Chapter 5:-Rider-bike system models developed in SimMechanics. In this chapter, the theoretical basis of this study and the mathematical model of the rider-bike systems developed in SimMechanics are discussed, then, a series of dynamic simulations are implemented to observe the dynamic characteristics of the rider-bike system of a hard tail bike.

Chapter 6:-Quasi-static and dynamic analyses of bare and loaded bikes in stationary and moving conditions. In this chapter, a quasi-static analysis is conducted to study the characteristics of the five bare bikes in stationary condition due to sinusoidal or rapidly applied external loads. In addition, the dynamic analyses are also implemented to investigate the dynamic responses of each of the five rider-bike systems moving on

the flat road surface with and without bumps in the steady condition. It is found that, for a rider-bike system, the “phase angle” between the beginning (or end) of each pedalling stroke and the position corresponding the instant of time for it to meet (or leave) a bump is one of the important factors affecting its dynamic responses.

Chapter 7:-Conclusions and future work. This chapter summarizes some conclusions obtained from the previous chapters and suggests some future works concerning the design of full suspension systems of mountain bikes.

Chapter 2 Mountain Bike Research

2.1 Introduction

Many reports concerning the performance of mountain bikes with and without suspension systems have been presented in the past two decades. Some of the studies implemented indoor or field experiments to measure the physiological variables of riders, and some of them implemented theoretical analyses to present better designs to reducing the bobbing effect. A literature review of both physiological experiments and theoretical analyses is carried out in this chapter. Since the abbreviations for hard tail bikes and full suspension bikes are different in the existing literature, in this study, the front suspension bike is called hard tail bike or HT bike, the full suspension bike is called FS bike, and the mountain bike without suspension systems is called rigid bike or RID bike.

2.2 Studies on Physiological Responses of Mountain Bike Riders

Generally, in comparison with road cycling competitions, the exercise intensity in off-road cycling races is much higher [6,21], since mountain bikers need to deal with rough terrains, such as gravel roads, uphill, and downhill. On the other hand, the air resistance in off-road biking competitions is much less than that in road cycling competitions [22] because the speed in the former is lower than that in the latter, and the riding strategies (such as the riding posture) are also different. In such high exercise-intensity races, the riders' HRs (heart rate) are close to their maxima soon after the races begin [5,6,21]. In addition, riders riding hard-tail mountain bikes have lower average (mean) HR than those riding rigid road bikes [21,23]. To investigate the difference between exercise intensities of the riders riding hard-tail bikes and full-suspension bikes, many studies have been performed, in which the physiological variables of the riders are measured, including CK (creatine kinase) [23], VO_2 (oxygen consumption) [15,16,18,22,23,24], RPE (rating of perceived exertion)

[16,18,22,24], HR (heart rate) [5,6,15,16,18,22,23,24], and blood lactate concentration [5,6,16,24].

In 1997, Seifert et al. [23] carried out a series of field experiments to investigate the effect of suspension systems on rider's muscular stress, energy expenditure, and time trials performance. Three bikes are used in this field study, including a rigid bike frame (RIG), a hard tail bike (HT), and a full suspension bike (FS) (Stumpjumper, Specialized). For the muscular stress, they found that the average variation in CK at 24 hours of RIG are greater than that of HT or FS. For the energy expenditure, they found that the average HR of RIG are higher than that of HT or FS, and the VO_2 of FS is lower than that of HT or RIG, but the difference (of average HR or VO_2) is not obvious. The cyclists participated in this study rated the FS to be most comfortable among the three bikes. For the time trials performance, they found that the time for each rider finishing the cross-country track with HT is shorter than that with RIG or FS. Finally, they concluded that FS may not increase the riding performance because the pedalling efficiency is decreased due to the rear suspension system.

In 2000, Macrae et al. [24] studied the effects of front(HT)/dual(FS) bike suspension systems on rider’s power output and the other physiological variables in uphill biking condition with an asphalt and an off-road courses, respectively, in which six male elite bikers are involved. The dual suspension system used in this experiment was a four-bar-linkage type with a Rock Shox Deluxe rear shock absorber. They found that the cardiovascular performance (VO_2 and HR) have no obvious differences between the asphalt and off-road courses by riding HT and FS bikes, this supports the findings of Reference [23]. However, the rider’s power output of the FS bike is obviously higher than that of the HT bike. Comparing with the HT bike in this experiment, at each time interval, the rider’s average power output required by the FS bike is about 80watt/min higher. They believed that the higher power output required by the FS bike is due to the rider needing to apply additional pedalling force to overcome the compression of the rear suspension. According to the last results, they conclude that the advantage values of VO_2 and HR of the FS bikes might be better than those of the HT bikes during downhill riding.

In 2000, Berry et al. [22] performed a study to investigate the influences of bicycle mass, speed, and grade on VO_2, HR, and RPE under a series of lab experiments. Three bike masses (11.6, 12.6, 13.6 kg), three speeds (2.7, 3.6, 4.5 m/s), and three grades (0, 2.5, 5 %) are randomly arranged for nine different testing conditions. The additional mass was added to a water bottle fixed on the bike with 1 kg or 2 kg lead shot. The bike used is Trek Y-22 with weight of 11.6 kg. The bike is ridden on a treadmill mounted by a bump with height of 3.8 cm, and the physiological variables were measured during the tests. They found that the effects of different bike masses on VO_2, HR, and RPE are negligible. The three physiological variables only obviously increase with the increments of speed and grade. They claimed that the limited indoor test did not represent a real field test of off-road riding. They suggested that future studies could investigate whether or not the additional mass has obvious effect on grades greater than 5%.

In 2001, Nielens and Lejeune [15] studied the effect of suspension systems on energy dissipation of mountain bikers. An indoor experiment is implemented in this study. They use an electromagnetically braked cycle ergometer to apply the braking force up to 250w. A four-bar-linkage full suspension mountain bike is used (FRM Be Active). Full suspended (FS), front suspended (HT), and no suspension (RIG) modes are considered in the test. Riders' energy dissipation is evaluated by VO_2, HR, and the relationship between VO_2 and power. The results showed that, during riding under the braking force of 250w, the relative difference between VO_2 of FS (44.4 ml/min/kg), HT (44.8 ml/min/kg), and RIG (43.6 ml/min/kg) is only 3 %. They claimed that there is no obvious difference on energy dissipation of the rider riding mountain bikes with and without suspensions. One possible reason for the bikers feeling the energy being dissipated by the rear suspension is because they use the technique of standing riding.

In 2001, Impellizzeri et al. [5] performed a study to analyze the exercise-intensity profile of off-road races. In this study, nine bikers participated in a lab test and four international off-road competitions using bikes with front suspensions. Their results showed that the bikers' HR are obviously lower than those of riding rigid bikes, this agrees with the results of Seifert [23]. Based on the HR and lap time during races,

they found that the bikers start the race at high exercise intensity in order to obtain the first position. They claimed that their results can be used (by trainers) to plan the training programme for off-road competitions.

In 2003, Ishii et al. [16] implemented an experiment on subjects riding the same bike (Trek Y-33) with different suspension modes, including rigid, front-suspension (HT), and full-suspension (FS) on a treadmill test and a field test. They measured the riders' VO_2 and blood lactate concentration, and showed that the average oxygen consumption of riding the FS bike during the field test was obviously bigger than that of riding the HT bike. However, the blood lactate concentration of riding the FS bike was lower than that of riding the HT bike. They claimed that the lower blood lactate concentration for a rider riding FS bike would be more advantageous during off-road competitions even though the VO_2 is bigger.

In 2004, Stapelfeldt et al. [6] performed a study to evaluate the exercise intensity of mountain bike racing. They recorded the HR and power output of eleven riders in 15 races, and found that the highest value of power output appeared soon after the start of the race (at first lap), which agrees with the findings of Impellizzeri [5]. In addition, the variation of power output during the whole races is high, but that of the HR is relatively stable. They indicated that, for the evaluation of exercise intensity, the measurement of power output is better than that of HR, because HR can be influenced by the physiological and psychological factors (such as mental stress), and thus the results of HR can be limited to some degree.

From 2003 to 2006, Titlestad, Davie, and Whittaker et al. [3,4,18,19,20] designed a lab experiment to test the physiological (VO_2 and HR) and psychological (RPE and comfort assessment) variables of twenty riders. A hard tail (HT) bike Marin Rocky Ridge and a full suspension (FS) bike Marin Mount Vision are used in this study. In this experiment, front fork of the bike is fixed on a front bracket and the rear wheel is rolling against a roller with and without a bump, as shown in Figure 2.1. From the test without a bump on the roller, they found that the measured values of VO_2 for riding the HT bike are lower than those for riding the FS bike, but the difference is small. In addition, from the test with bumps on the roller, they found that the values of VO_2,

HR, and RPE for riding the HT bike are higher than those for riding the FS bike, and the comfort assessment shows that all riders feel more comfortable while riding the FS bike. Titlestad et al. [3,4,18,19,20] suggested that, under the controlled test conditions, the physiological cost of riding the HT bike is greater than that of riding the FS bike.

Following the rolling rig experiment presented in References [3,4,18,19,20], Davie and Whittaker [4] improved the test platform to a rolling road rig (treadmill), as shown in Figure 2.2, in which the handlebar of the bike is fixed, and the bump can be hit by both the front and rear wheels. Only the FS bike Marin Mount Vision is used in this test, but a specially designed steel spacer is used to replace the rear shock absorber to switch to the HT mode. Eight riders took part in the test, and the same physiological (VO_2 and HR) and psychological (RPE and comfort assessment) variables are measured. In this roller road rig test, they found that no significant differences between VO_2 and HR of the riders riding the FS bike and those riding the HT bike in the test either with or without bumps, but both the RPE and comfort assessment reveal that, comparing with riding the HT bike, the riders feel more comfortable during riding the FS bike. In addition, Davie and Whittaker [4] designed an indoor track (see Figure 2.3) to do the same physiological tests on 10 riders. They found that the measured values of VO_2, HR, and RPE of the riders riding the FS bike are lower than those riding the HT bike. The comfort assessment also shows that, comparing with riding the HT bike, the riders feel more comfortable during riding the FS bike. Davie and Whittaker [4] indicated that the energy cost of a rider riding the FS bike is less than that riding the HT bike.

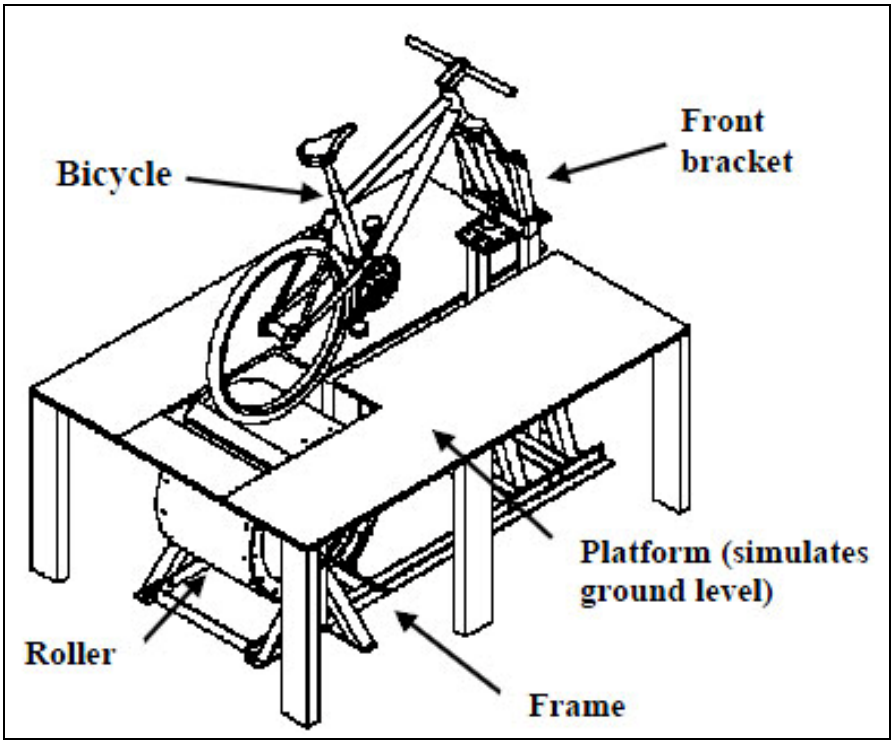

Figure 2.1 Platform of roller rig test [3,4,18,19,20]

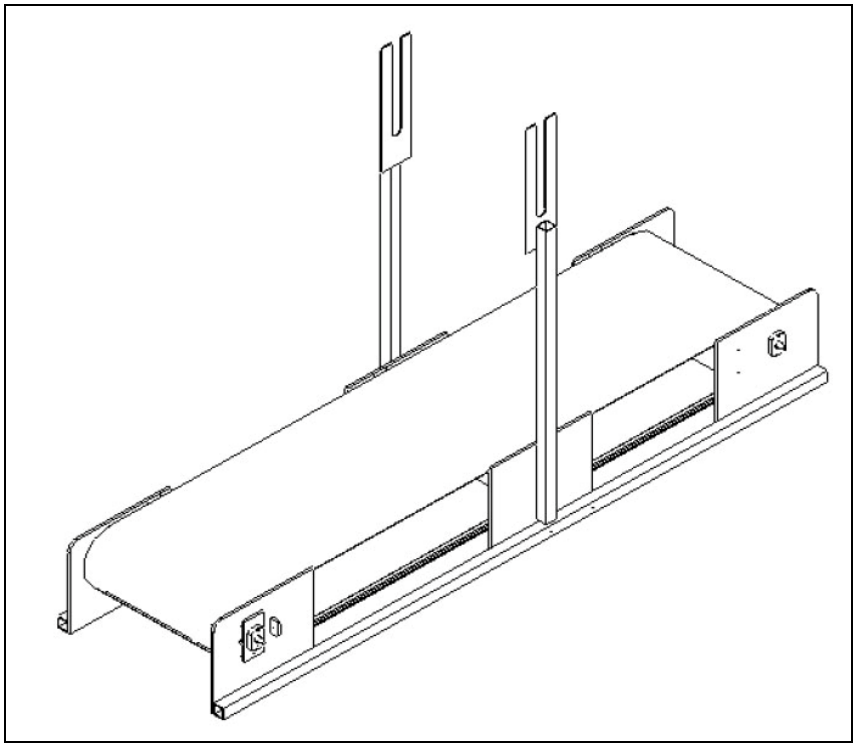

Figure 2.2 Rolling road rig [4]

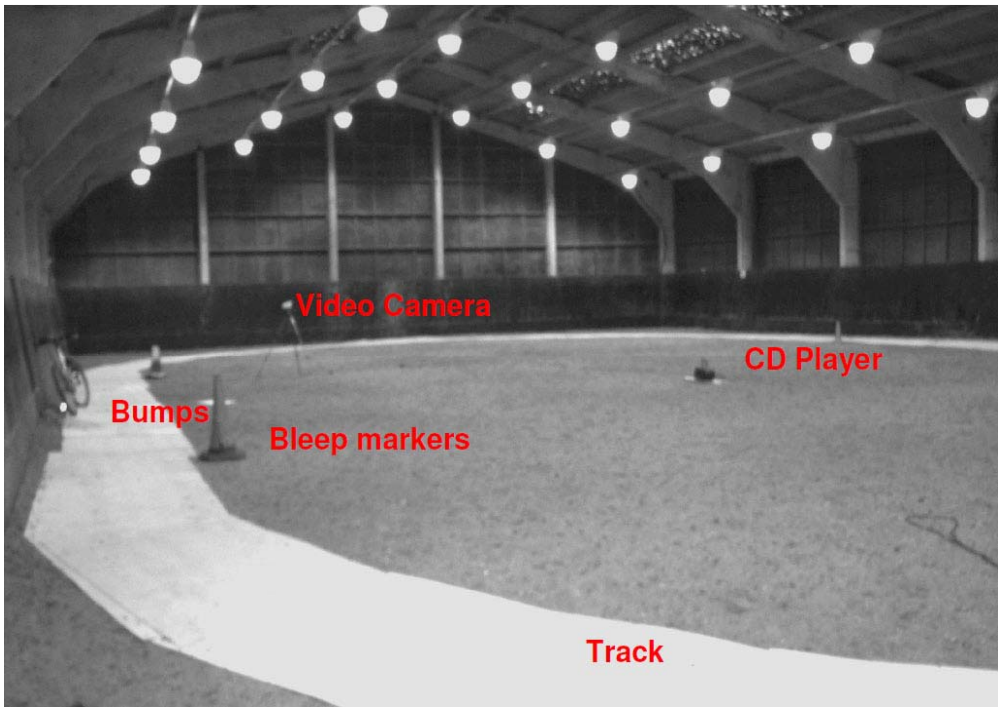

Figure 2.3 Indoor track presented by Davie and Whittaker [4]

2.3 Studies on Dynamic Responses of Mountain Bike Riders and Dynamic Simulations of Rider-Bike Systems

In addition to the physiological experiments of mountain bikers, many researchers have investigated the dynamic responses of rider-bike systems, and also presented different mathematical models for the theoretical analyses. Some of them study the location of optimal pivot point for single pivot full suspension bikes to minimize the bobbing effects or chain-suspension interactions [9,10,12,13,17,25,26,27], some of them study the vibrations of the road bike and mountain bikes [28,29,30], and some of them used bond graph model to study the dynamic characteristics of mountain bikes [31,32].

The sources of loads generated on rider-bike system can be classified as two kinds [33]. The first kind is called rider-induced loads, which come from the rider via his muscular action while pedalling and his static weight. The second kind is called surface-induced loads, which are generated by the surface irregularities when the rider-bike system passes over them.

In 1995, Stone and Hull [33] studied the rider-induced loads, and measured the loads on pedal, handlebar, and seat post in three riding conditions, including seated cruising, seated climbing, and standing climbing. Five riders, with their weights ranged from 547N to 894N, took part in this study by using the Trek 1500 racing bicycle. From the measured rider-induced loads, they found a linear relationship between the rider weight and rider-induced loads (such as the normal pedal forces and the average power output).

In 1996, in order to satisfy a design in which the bicycle rear suspension responds to bumps instead of rider-induced forces, Padilla and Brennan [25] presented an analysis of the free-body diagram of a bike to study the forces applied to the bike and suspension, and to determine the frame configuration and pivot location. They found that the ideal pivot point should be located at the point of intersection of the contact force of rear wheel and the pedal force, in which the direction of the temporary contact force of rear wheel is always acting at about 45 degrees, which is similar to

the results presented by Olsen [10]. They showed that a unified rear triangle (URT) (similar to model g in Figure 1.1 in Chapter 1) can simplify the design problem of the rear suspension with the chain force to be isolated from the suspension.

In 1996, Wang and Hull [17] presented a dynamic model to study the rider's power input dissipated by the suspension, also called rider-induced energy loss, while riding on a smooth uphill surface (with no terrain-induced energy loss). The computer programme AUTOLEV was used to develop the dynamic model. The rider-bike system consists of six rigid bodies: the rider, bike frame with main triangle, bike frame with rear triangle, fork, front wheel, and rear wheel. The bike model is based on a full suspension bike with single pivot rear suspension. This model of rider-bike system integrated the effects of front and rear suspensions (spring stiffness and viscous dampers), wheel force with rolling resistance, and pedal loads with chain force together. The wind resistance is modelled as a force applied on handlebar and opposite to the moving velocity. The results showed that the average dissipation was 1.3% (6.9w) of the rider's power input (530w) while riding on the smooth uphill surface with grade 6%, velocity 6.5m/s, gear ratio 32:14 and cadence 84 rpm, and the average compression of rear suspension is 6.6mm with variation ±2.7mm. They suggest that a practical approach to designing the rear suspension by changing the location of the pivot point should be developed.

A discussion on the ideal pivot point for a full suspension bike with the single pivot rear suspension (as shown in Figure 2.4) is presented by Olsen [10]. In the discussion, Olsen [10] showed that the ideal pivot point can be found by drawing a line 45° up and forward from the ground contact point of rear wheel (GRL in Figure 2.4) to the intersection with the top point of the chain ("intersection of GRL with top run of chain" in Figure 2.4), and then draw another line from the rear axle to this intersection point (the chain line in Figure 2.4). However, Olsen [10] also showed that the ideal pivot point is varied with different front gears used. It is noted that the ideal pivot point can minimize the chain-suspension interaction as one may see from [9,10,13].

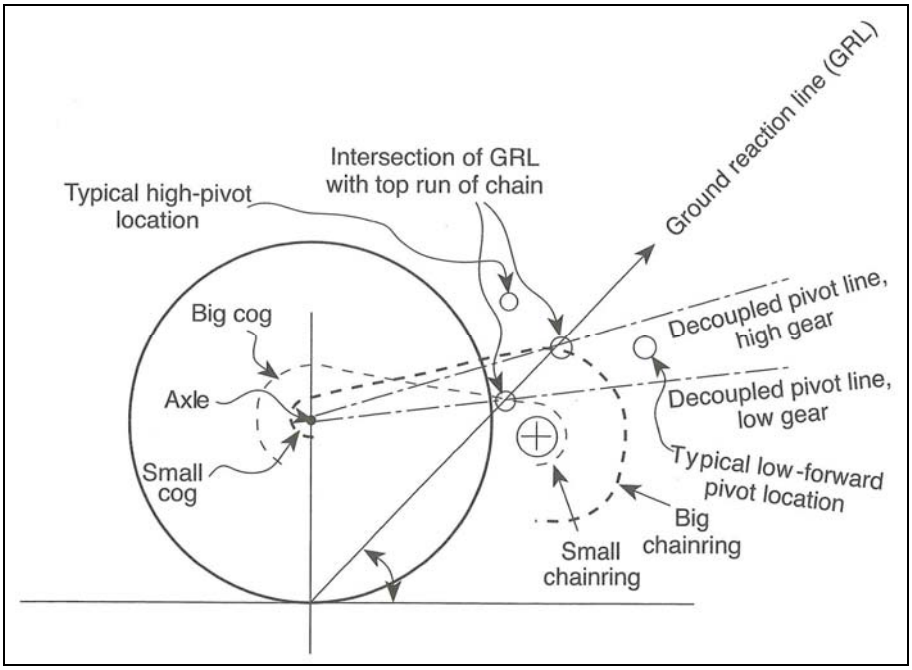

Figure 2.4 Illustration of location of ideal pivot point for single pivot bike [10]

In 1997, the same model presented by Wang and Hull [17] is used to study the optimal pivot point for a full suspension mountain bike with single pivot rear suspension in [13] with the same testing condition as that in [17]. The optimization parameters are assumed to be the pivot point coordinates (η,ξ), where η is the height above the bottom bracket measured along the seat tube, and ξ is the horizontal distance with respect to the seat tube. In the optimization analysis, it was found that the power dissipation depends on η, but not on ξ. Therefore, Wang and Hull [17] focused their attentions on the optimal pivot point located on the seat tube and studied the dependence of optimal location on pedalling mechanics (rider's body mass), spring rate, compression and extension damping parameters, and chainring (the front sprocket) size. Their results showed that the damping parameters have no effect on the optimal pivot point location. In addition, the effects of different riders' masses and spring rates on the optimal pivot point location are quite small. However, the optimal pivot point height η linearly rises as the chosen chainring has larger number of teeth (larger diameters). With the same model and testing condition as those in [17], Wang and Hull found that the optimal pivot point location is 11.0 cm above the bottom bracket along the seat tube and this can decrease the power dissipation from 6.9w to 1.2w. However, the last optimal pivot point location is only suitable for the riding condition with a particular grade (6%), speed (6.5m/s), and gear ratio (32:14). For the

other riding conditions, they suggested that a sub-optimal pivot point location can be used which is slightly above or below the optimal one.

In 1997, Needle and Hull [12] presented a design of a single pivot bike with adjustable pivot point. The pivot point is fixed on a collar which can be clamped along the seat tube from 0.0 to 22.0 cm above the bottom bracket. An experiment is implemented to find the optimal pivot point, in which a rider with weight 750N rides the bike in the seated position on a treadmill with the grade 6% at 23.3km/hr (corresponding to the cadence 84 rpm) and the gear ratio 39:14. They found that the minimum energy dissipation can be reached when the pivot point is arranged at the height of 8.4 cm above the bottom bracket.

In 1999 and 2000, Good and McPhee [9,26] developed a simplified four-body dynamic model with Maple algorithms based on the model presented by Wang and Hull [17] to investigate the chain-suspension interaction. This model is composed of front and rear wheels, main frame (front triangle) and rear triangle. Since the rider part is integrated into the bike frame, the determination of interface loads between the rider and the seat, handlebars and pedals are not considered. The rider-bike system is only excited by a chain tension force varying with crank angle. With the same simulation conditions as those in [17], Good and McPhee [9] validated their developed model with the results of compression of rear suspension presented in [17], and showed that their difference is only 1.0 mm less than that in [17].

In 2000, with the dynamic model presented in [9], Good and McPhee [26] implemented an optimization analysis with genetic algorithm search routine MECHAGEN to study the optimal pivot point for minimizing the pitching motion of the rider. The design variables in this analysis are the x-axis and y-axis positions of the spring-damper attaching point on the rear frame, and those of the pivot point relative to the centre of mass of frame and rider. It is different from the study of Wang and Hull [17] in that Good and McPhee [26] studied the location of the pivot point on seat tube and the forward or rearward position relative to the seat tube. Their results show that the pitching motion of the rider will be minimized when the pivot point is located at 11.6cm above and 2.7cm rearwards the bottom bracket.

In addition to conducting the physiological experiments, Titlestad, Whittaker, and Davie et al. [3,4,18,19,20] also measured some mechanical variables and presented a dynamic model of the rider-bike system [3,4,19]. During the roller rig test with and without bumps (see Figure 2.1), the pedal forces and vertical accelerations at handlebar and at saddle were measured. The experimental results show that, during the test with no bump, the measured accelerations have only small differences between the hard tail bike and full suspension bike. However, during the test with bump, the vertical accelerations at handlebar and at saddle of the full suspension bike are significantly lower than those of the hard tail bike. In addition, the average pedal force required by full suspension bike to maintain the same average speed over bumps is also lower than that required by hard tail bike. Titlestad, Whittaker, and Davie et al. [3,4,19] also presented a dynamic model of rider-bike system by using DADS (Dynamic Analysis and Design Systems [34]) to compare the numerical results with the experimental ones. In this, the properties of human body model is adapted from the one presented by Wilczynski and Hull [35]. The entire model of rider-bike system consists of 2 parts. The rider model consists of the head, upper arm, lower arm, torso, hip, one upper leg, and one lower leg, while the bike model consists of the rear wheel, bike frame, handlebar, front and rear suspension. The two ends of a spring are connected to the rider's shoulder and handlebar, respectively. The numerical results obtained from DADS simulation are similar to those obtained from the experiment. Therefore, Titlestad, Whittaker, and Davie et al. concluded that the full suspension bike has a significant advantage over the hard tail bike in a controlled experimental environment.

Following the study of Titlestad, Whittaker, and Davie et al. [3,4,19], Davie and Whittaker [4] measured the same mechanical variables and implemented the numerical simulation in DADS for the rolling road rig tests [see Figure 2.2(a)]. In the experiment of rolling road rig test with or without bumps, the mechanical results show that there is no significant difference between hard tail bike and full suspension system bike. The numerical results obtained from the DADS simulation show that, during the test with no bumps, the hard tail bike has a slight advantage over the full suspension bike, because the displacements of handlebar, saddle and rider of the hard

tail bikes are lower than those of the full suspension bikes. However, during the simulation of test with bumps, the advantage of the full suspension bike is significant over that of the hard tail bike, because the displacements and velocities of handlebar and saddle, and the displacements of rider of the former are lower than the corresponding ones of the latter.

In 2002, Karchin and Hull [27] implemented an experiment with the bike designed by Needle and Hull [12] to study the optimal pivot point height with respect to three objectives : (1) the influence of interaction between front and rear suspensions on the pivot point height; (2) the sensitivity of the optimal pivot point height to the rider's pedalling mechanics in seated and standing riding conditions; (3) the dependence of the optimal pivot point height on the rider posture. Eleven riders are involved in this experiment, in which each rider is asked to ride on a treadmill with the grade 6%, constant velocity 24.8 km/hr, the gear ratio 38:14, and the cadence of 84 rpm. For the first objective, the riders ride the bike with the front suspension active (no lockout) and inactive (lockout), and it is found that, at the optimal pivot point height, the power loss from the rear suspension has no obvious effect on the interaction between front and rear suspensions. For the second and the third objectives, Karchin and Hull [30] found that the average optimal pivot point height for seated riding is 9.8cm and ranged from 8.0-12.3cm, and that for standing riding is 5.9cm and ranged from 5.1-7.2cm. In addition, the optimal pivot point height is not sensitive to the pedalling mechanics in either seated or standing ridings.

In 2005, Levy and Smith [28] performed a study to compare the vibration damping of five different suspension conditions, including a rigid frame with three different front forks (air-oil fork, elastomer fork, and linkage fork), and a rear-suspended frame with two different front forks (air-oil fork and linkage fork). Where a rigid frame with rigid fork (full rigid) is selected as the benchmark. Only one rider is involved in this experiment, and two road conditions of gravel surface (similar to railway tracks) and trail surface (similar to an off-road racing track) are tested. The vibration damping of those suspension conditions were investigated by quantifying accelerations at the front axle and frame using spectral analysis. The results showed that, in a low

frequency range between 0 and 100 Hz, all the suspension systems can effectively reduce the vibration at the frame in comparison with the axle, while the full-rigid frame has only modest low-frequency attenuation of vibration. The attenuation of vibration of rear suspended frame with air-oil fork on the gravel surface is 66.2%, and that on the trail surface is 64.8%, and both are highest among the five suspension systems. In a range of higher frequencies between 300 – 400 Hz, the vibration can be effectively attenuated for all conditions. The high-frequency vibration in this study is unexpected, and Levy and Smith [28] think that it is resulted from the rubber knobby tyres used by the mountain bikes. Moreover, it is suggested that the data of rider should be input in the future assessment of the effectiveness of suspension systems.

In 2004, Champoux et al. [29] developed a fully instrumented mountain bike, in which all principal dynamic loads applied on the bike can be *in situ* (real-time) measured. The front and rear axles, and the front and rear brakes are equipped with commercial force transducers to measure the applied forces. The handlebar, seat, and pedals are equipped with strain gauges to measured the horizontal and vertical applied force components. Electric linear position transducers are used to measure the displacements of front and rear suspensions. A potentiometer is used to measure the pedal position. Electric cables of all transducers are fixed along the frame tubes and form an umbilical cable to connect to the data acquisition system in a backpack. With instrumented mountain bike, they achieve the goal of real-time measurement of all dynamic loadings applied on the bike when a rider rides it in the field or in the lab test.

The weight, stiffness and comfort are three important factors directly affecting the dynamic characteristics of a rider-bicycle system. Since the dynamic behaviour of a bike can directly influence the bike lifetime, maneuverability, efficiency and rider's comfort, Champoux et al. [30] indicated that the more manufacturers can realize about the dynamic response of their products, the more they can benefit both current and potential riders. They have shown that the rider comfort can be categorized into static comfort and dynamic comfort. The quality of the road surface and the vibration transmitted from the five contact points of the rider (the hands, the feet and the

buttock) are all involved in the perceived dynamic comfort to be directly related to the dynamic behaviour of bike. In their study a series of experiments, including SIMO (Single input multiple output) without a rider and MIMO (Multiple input multiple output) tests with a rider were implemented to investigate the dynamic behaviour of road bikes. In the SIMO test, a shaker was used to generate excitations to the front axle, and in the MIMO test, an additional shaker was used to generate excitations to the handlebar. The related natural frequencies and mode shapes were obtained in the experiments. The results showed that the biker strongly affect the dynamics of a bike. For the road bike with a rider, only the mode of front-to-back motion of the forks at a natural frequency of 27.8Hz is similar to one at a natural frequency of 33.5Hz for the road bike without a rider. In addition, for the road bike with a rider, only the 3 modes with natural frequencies in the band 10-100Hz can be obtained.

In 2005, Redfield [31] presented a mathematical model of rider-bike system to study the extreme manoeuvres of mountain biking. The model is developed by bond graphs, which is a series of graphical representations of physical systems based on energy domain [36]. In this study, the rider was assumed to be attached rigidly to a hard tail mountain bike, and the test condition was simulated by the rider passing through a steep drop of 1m. Several manoeuvres, including normal riding, applying maximum brake force, shifting the centre of mass of rider (nearly seated posture), and performing a "bunny hop" (jumping) to pass the steep drop (may be used by the professional mountain bikers), were investigated to assess the velocities of centre of gravity, shock forces, tyre forces, and torques. He indicated that the result of the simulation with the rider rigidly connected to the bike was reasonable comparing with a new rider carefully controlling the bike due to fearing the steep drop.

In 2006, Redfield and Sutela [32] presented a bond graph model of a rear shock absorber for mountain bikes based on the fluid pressure and the flow through orifices, in which the pressures and volumes of air, oil, and nitrogen are all considered. They implemented an experiment to compare the measured results with the ones from the world. In the experiment, the rear shock eye of the shock (the one connecting to rear part of the bike frame) is fixed, and an input sinusoidal force with peak-to-peak stroke

length 25mm with varying frequency is applied on the front shock eye (the one connecting to the front part of the bike frame), and the applied shock force is measured from the front shock eye. The applied shock forces and the relative velocities are observed. By adjusting the model parameters, it is found that the model results correspond to the experimental results well. They indicate that the bond graph model can be provided to the design engineers to identify which physical parameters influence the performance of shock absorber significantly, so that the design cycle time can be reduced.

In 2008, González et al. [11] performed an optimization analysis of a four-bar-linkage full suspension mountain bike. First, they present a dynamic model of rider-bike system by using Matlab, in which the human body model has right and left, upper and lower legs, and the bike is a single pivot bike similar to the one presented by Good and McPhee [9] and Wang and Hull [17]. Then, they used the same simulation conditions (uphill grade 6%, moving velocity 6.5m/s, gear ratio 38:14, and cadence 84rpm) as those in [9,17], and compare the results of compression of rear suspension as a function of crank angles to the ones presented by Wang and Hull [17], and Good and McPhee [9] and it was found that the difference is very small. González et al. [11] also found that the rider's body (pedalling) motion affects the power dissipation in rear suspension significantly and was not considered in [9,17], in addition, the power dissipation increases with the maximum crank torques developed by the rider. González et al. [11] then developed a model of four-bar-linkage bike with the same rider model developed for validation by them, and implemented an optimization analysis. The design variables considered in this analysis are: the position of shock eye on seat tube, the main pivot near the bottom bracket, the position of the rocker fix pivot, the length of chain stay, the length of horst link, the length of seat stay, the distance between horst link pivot and rocker pivot, the distance between rocker pivot and rocker fix pivot, the distance between rocker pivot and upper shock eye, the distance between rocker fix pivot and upper shock eye (all parts mentioned above are introduced in Chapter 4). The results of this optimization analysis show that the power dissipation in rear suspension will reduce from 10.8w to 0.8w, and the optimized rear triangle (rear part of bike frame) is only 20g heavier than the original one.

In a research report presented by Enright in 2007 [37], several packages were assessed to determine the most suitable one to be used to study the dynamics of mountain bikes. Finally, SimMechanics, an add-on to Matlab and Simulink, was selected. With SimMechanics, hard tail and full suspension mountain bike models were developed, in which several parts were modelled, including the bike frame, the suspension system, the tyres, the crank, and the gears. The chain was not included in the model. In order to easily adjust the parameter values of the bike model, a calculation programme was written as a Matlab m-file. In addition, the rider's mass was included in the model by adding two point masses [66.7% (of the rider's mass) on the seat post and the other 33.3% on the handlebars], and the point masses were added to the calculation of frame COG. The pedalling forces on the bike were simulated by inputting a sine wave force applied to one pedal. The pedalling motion was controlled by a proportional controller controlling the forces to the pedal depending on the speed of the bike comparing with the value of desired speed. Without the proportional controller, the sine wave force could not make the crank turn in complete revolutions and oscillated randomly, because the frequency of sine wave is fixed but the crank accelerates and the speed changes with time. The natural frequency and the deflections of the bike simulation under static loads were investigated to validate the mountain bike model with the pedalling controller and force removed. As a result, it was claimed that the numerical analysis results are close to the simulated results (around 80%).

Another report presented by Iturrioz in 2008 [2] was an extension study based on the one done by Enright [37]. In this project, the bump model was added to the bike model developed by Enright [37], and it was based on the example of bouncing ball model in SimMechanics [38]. A human body model was developed and integrated into the bike model. The body model used in this project was adapted from the one used by Titlestad [3]. The human body consisted of six segments, including the torso, the head, the upper and lower arms, and the upper and lower legs. All parts of the human body were supposed to be cylinders except the head being a sphere. A body spring-damper unit is connected with the handlebar and the shoulder to prevent the upper body from falling down due to gravity. Four bike models with different suspensions were studied in this project, including hard tail, single pivot, four-bar-linkage, and VPP (virtual pivot point). Due to the bump model being were

considered in this project, some models developed by Enright [37] were modified. The pedal force was simulated by two half sine waves applying on each crank in the second and third quadrants. The model of transmission between crank axle and rear hub were developed by using a chain force and a velocity driver instead of using a gear constraint used in the work of Enright [37]. A model for simulating the chain tension was developed in this project. After the four detailed mountain bike models were developed, situations for each bike passing over four different bumps, including flat bump (flat road), the fall of the bike due to a drop, vertical obstacle, and slope, were investigated. The angular velocity of COG, x and y velocity components of COG, x and y position components of COG, x and y velocity components of rear wheel, angular velocities of crank and rear wheel, pedalling force, chain force, torque, and power were analyzed. Some unexpected results occurred probably due to the incorrect definition of frame key points, because coordinates of frame key points are determined by approximate calculation, and the modification of these key points influence the numerical results significantly.

In 2010, Cangley et al. [39] presented a 3D mathematical model of rider-bike system by using SimMechanics to simulate competitive road cycling in forward dynamics. The positive directions of the three axes are: forward (x-axis), left (y-axis), and upward (z-axis) when the rider-bike system is viewed from the rear. The bicycle model is based on the Trek Madone. The rider model consisted of fourteen rigid bodies, and the pedalling motion is modelled as symmetrical two-legged pedalling. Wind resistance, rolling resistance, and gravitational resistance are taken into consideration. Balancing of the rider-bike system is controlled by using a PID controller. The full cycling model is simulated from rest to accelerates forward and will reach the steady condition at a velocity of 11.1m/s after $t \approx 7.5$sec. They conducted an experiment, in which fourteen riders are asked to ride in a time trial course, and the time, power, speed and distance data are recorded and compared to the numerical results. The finishing time predicted in the numerical analysis is only 1.4% higher than the actual time.

2.4 Studies on Rider's Pedalling Efficiency

In the works of Enright [37] and Iturrioz [2], the pedalling force is simulated as the sine wave with its maximum and minimum occurring at the moment that the crank is at the horizontal and vertical positions, respectively. It is obvious that the above assumption for the pedalling force does not agree with the actual situations, because the maximum pedalling force should occur when the angle between the crank and rider's lower leg, α, is near 90° (i.e., $\alpha \approx 90°$), and the minimum pedalling force occurs when $\alpha \approx 180°$. Note that, if θ_1 represents the rotational angle of the crank with respect to its top dead centre (TDC) at any instant of time t, then $\alpha \approx 90°$ does not occur at the moment that the crank is at the horizontal position (with $\theta_1=90°$) and $\alpha \fallingdotseq 180°$ does not occur at the moment that the crank is at the vertical position (with $\theta_1=180°$) as one may see from Chapter 4 of this thesis. Besides, in some studies [40~46], the rider's pedalling motion was investigated and the performance of the rider-bike system subjected to rider's pedalling force was estimated.

Broker [40] has shown that, with the strong growth of mountain biking, the questions and issues surrounding the biomechanics of cycling have become more complex and multifaceted. For this reason, a lot of researchers devoted themselves to the study of cycling biomechanics. For example, Neptune and Hull [41] examined the accuracy of three methods to indicate the hip joint centre (HJC) in seated stead-state cycling: trochanter method (TRO), fixed hip method (FIX) and anterior superior iliac spine method (ASIS). To perform a comparative analysis of errors inherent in the three methods, a standard method (STD) for locating the true HJC was developed. Quantified results reveal that the peak power obtained from TRO (43.2W) is much greater than that from STD (12.2W) with 254% error and the hip joint force work obtained from TRO (10J) is also much greater than that from STD (2.5J) with 300% error. Neptune and Hull [42] also developed a forward dynamic model of cycling and an optimization framework to simulate pedalling during submaximal steady-state conditions to identify the experimentally collected kinetic and kinematic data. Their model was driven by 15 individual musculotendon actuators per leg and the foot is assumed to be rigidly attached to the pedal. Neptune and Bogert [43] assessed the

utility of four experimental methods to quantify the mechanical energy expenditure (MEE) in human movement: metabolic energy method, external work method, kinematic method and kinetic method. They found that the kinematic (internal energy) method is theoretically flawed and should not be used in the cycling analyses, and the external work method has the potential to vastly improve our understanding of muscle function. Hansen et al [44] studied the influence of crank inertial load on freely chosen pedal rate and gross efficiency, and found that a considerable increase in crank inertial load would cause: (1) freely chosen pedal rate to increase, (2) gross efficiency to decrease and (3) peak crank torque to increase (for keeping a constant pedal rate). Sanderson and Black [45] studied whether the cyclists will modify the pattern of force application to become more effective during a prolonged ride to exhaustion and found that the peak effective force of the cyclist in the final minute ride is significantly increased compared with his first minute ride (to maintain the pedal cadence). Duc et al. [46] investigated the muscular activity of eight lower and four upper limb muscles across various laboratory pedalling exercises to simulate the uphill cycling conditions. They found that the increase of treadmill slope from 4% to 10% in uphill cycling did not significantly change the muscular activity of lower and upper limbs. In contrast, the change of pedalling posture from seated to standing affected largely the intensity and the timing of electromyography (EMG) activity of muscles crossing elbow, pelvis, hip and knee joint.

2.5 Summary

A general literature review on research in mountain biking and pedalling efficiency is given in this chapter. Researches in the past two decades have investigated the performance of mountain bike with and without suspension systems. Some projects are focused on measuring the physiological variables of the rider in laboratory or field tests and analyzing the performance of hard tail bike and full suspension bike from the point of view of physiology. Some reports are focused on rider's power dissipation resulting from the compression of rear suspension and presentation of some methods to improve the design of rear suspension by developing the experimental tools or implementing the dynamic simulations.

From the experimental evidences presented in Section 2.2, one can see that under various experimental environments, including lab tests and field tests, when the rider rides a RIG bike, a HT bike, or a FS bike, the difference of VO_2 or HR is not obvious [4,15,23,24]. In addition, Berry et al. [22] and Nielens and Lejeune [15] concluded that there is no evidence to indicate the performance of a FS bike to be worse than a HT bike. On the other hand, in most of the experimental studies with the comfort assessment taken into consideration, the FS bikes are more advantageous than HT bikes [3,4,18,19,20,23]. More studies also conclude that FS bikes may be more beneficial than HT bikes during off-road riding conditions [3,4,16,18,19,20,24].

In Section 2.3, most of reports concerning dynamic simulations only investigated the optimal location of pivot points for single pivot bikes, and only one study investigated the optimization design of the four-bar-linkage bike [11].

In addition, it is found that most of the researchers study the cycling problems from the viewpoint of biomechanics and statistics theory and incorporating with various complicated experiments, and the literature for tackling the problems with the engineering mechanics and deterministic theory is rare. Thus, in this thesis, the pedalling efficiency of a bike rider is evaluated by using the conventional engineering mechanics incorporating with computer simulations. To this end, the rider-bike system is modelled by a two-dimensional mechanism consisting of crank, shank (lower leg),

thigh (upper leg) and a stationary segment (framework) joining hip to the crank spindle. Then five rider-bike systems (including one hard tail bike and four of the most popular full suspension bikes) are used to investigate the quasi-static responses of the stationary bare bikes due to applied forces and the dynamic responses of the moving loaded bikes passing over bumps.

Chapter 3 Hard Tail and Full Suspension Mountain Bikes

3.1 Introduction

In order to study the influence of different full suspension systems of mountain bikes on the bike and rider performance, numerical models of five rider-bike system have been developed. In this chapter, the software used to develop the models are introduced and the details of all bike models are discussed.

3.2 Software Used in Thesis

In this thesis, numerical models of all rider-bike system are developed in SimMechanics and Matlab. The full suspension bikes are drawn with Linkage and AutoCAD so as to obtain the precise dimension of bike frames. The dimension of the rider model is measured and obtained from BikeCAD and [17].

3.2.1 Matlab, Simulink, and SimMechanics

The rider-bike mechanical models are developed in SimMechanics in this study, which was also used by Enright [37] and Iturrioz [2], and the control system in rider-bike models is developed by using Simulink.

SimMechanics [38] is one of the toolboxes among Simscape, which is the platform used for physical modelling in the Matlab and Simulink simulation environment. With SimMechanics, one can focus on defining the mechanics of a system since SimMechanics derives the equation of motion automatically [39]. A mechanical system developed in SimMechanics is represented graphically by connected blocks. All objects in the mechanical system are rigid bodies and defined with Body Block, in which the mass property, mass moment of inertia, relative coordinate systems (called CS), and initial orientations are defined. Each rigid body is connected to others with

different kind of Joint Block, and kinematic constraints can be defined. Standard Newtonian dynamics of force and torque are used to do the analysis in SimMechanics. As SimMechanics becomes popular, many researchers have begun to use SimMechanics in their studies [2,37,39,47~58].

In this thesis, all parameters required by SimMechanics are defined and calculated in an “m-file” written by the user. This is more convenient when many parameters must be modified at the same time. In the simulation, the results can either directly be observed in SimMechanics or output to the Matlab workspace for further observation.

SimMechanics provides both forward and inverse dynamics analyses. In the forward dynamics analysis, the driving forces are given to the mechanical system and the resulting motion can be observed; in the inverse dynamics analysis, the motion of the mechanical system is given and the forces required to generate the motion are calculated [59]. In this thesis, forward dynamics analysis is used.

In the simulation of Simulink and SimMechanics models, different types of solver (including variable time step and fixed time step) can be used. In this thesis, two solvers are used. For fixed time step, the solver ODE 14x (extrapolation) is used, and the time step size is 0.01s. With this solver, the animation of the simulation is much faster than variable time step solver, and the response of rider-bike system can be observed easily. Since the numerical results obtained from last fixed time step solver are rough, the numerical results shown and discussed in this thesis are obtained from the variable time step solver ODE 45 (Dormand-Prince), in which the maximum time step is 0.01s and the relative tolerance is 1×10^{-5}.

3.2.2 Linkage - Bike Suspension Simulation Software

Linkage is a software which can simulate the motion of full suspension system of mountain bikes [60]. One of the sample interfaces is shown in Figure 3.1. By importing pictures of different mountain bikes into Linkage, and choosing the patterns of different suspension systems provided in Linkage, the models can be developed including drawing the contour of bike frames and defining the key pivot points. The full dimensions can be calculated automatically if a reference data is set. The reference data used here is the wheelbase. However, the dimensions calculated in Linkage are approximate, so AutoCAD is used to produce the more accurate dimensions.

In Linkage, a vertical force can be applied on head tube and seat post simultaneously or one at a time to observe the responses of both front and rear suspensions.

There are many other functions available in Linkage, such as customizing the parameters of the front fork and rear shock absorbers so that the behaviour of the suspension system will be affected directly. However, in this thesis only the motion of the rear suspension system is considered and the other functions are not used.

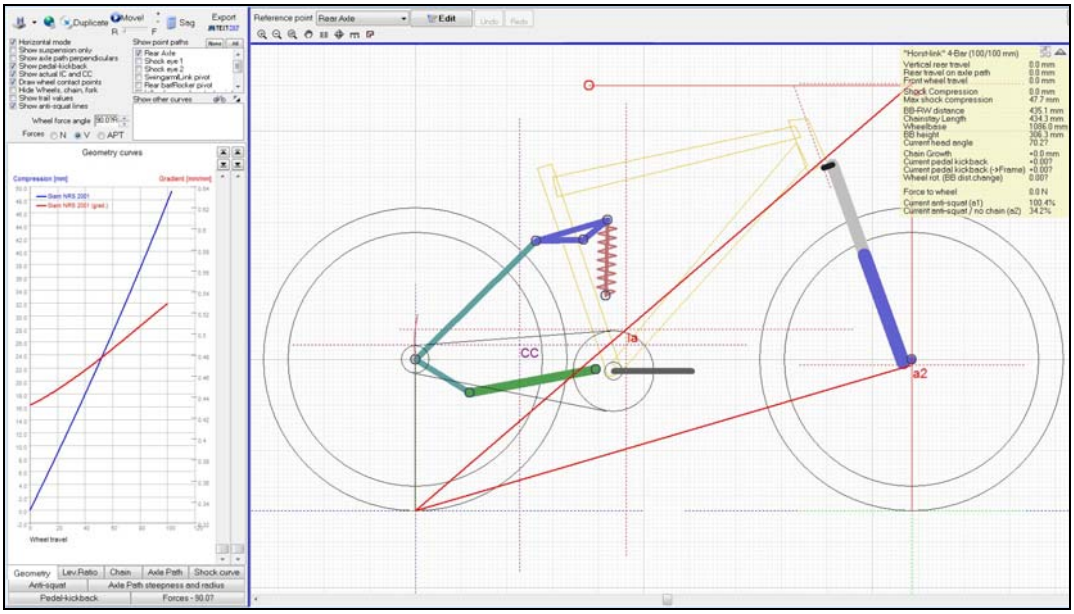

Figure 3.1 A sample interface of Linkage software [60]

3.2.3 BikeCAD

BikeCAD [61] is a software for bike enthusiasts to design bicycles and rider models. It can be used to design both road and mountain bikes. However, only a hard tail mountain bike is provided in BikeCAD. In this software, one can customize every length, diameter, angle of each frame tube. One of the sample interfaces of the software is shown in Figure 3.2.

In this thesis BikeCAD is used because the rider model can be customized as well. While the angle of rider's upper body is difficult to measure during real experiments, BikeCAD can provide the central line of each body part and labels the length and angle of every rider's body part. Based on the clearly defined lengths and angles of rider model in BikeCAD, the improved rider model in SimMechanics has been developed. Details will be given in Chapter 5.

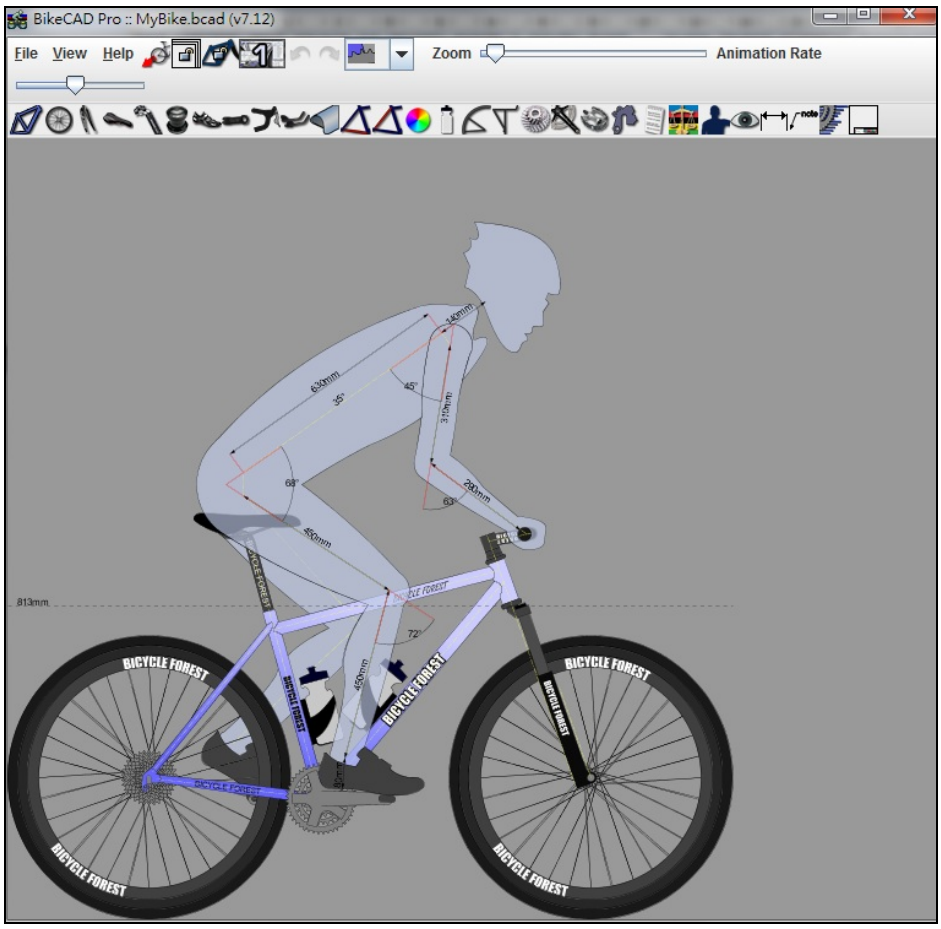

Figure 3.2 A sample interface of BikeCAD software [61]

3.2.4 AutoCAD

AutoCAD is a very useful tool for engineering design. An example for the detailed design of a road bike is shown in Figure 3.3 [62], in which all detailed dimensions of the bike are labelled.

In this thesis, the pictures of the full suspension mountain bikes are imported into AutoCAD then the central lines of each tube is drawn. The origin (0,0) of the coordinate system is set at the rear axle, the wheelbase is set as the reference length. From this the relative length and angle of each tube is determined. The ling drawing of the single pivot mountain bike is shown in Figure 3.4.

Comparing the dimension of line drawings of the full suspension mountain bikes obtained from AutoCAD with the specification provided by the manufacturers, it is found that the maximum error for lengths and angles between line drawings and real bikes is less than 6cm and 2°, respectively. Mountain bike models developed in SimMechanics in this thesis are therefore based on the line drawings obtained from AutoCAD.

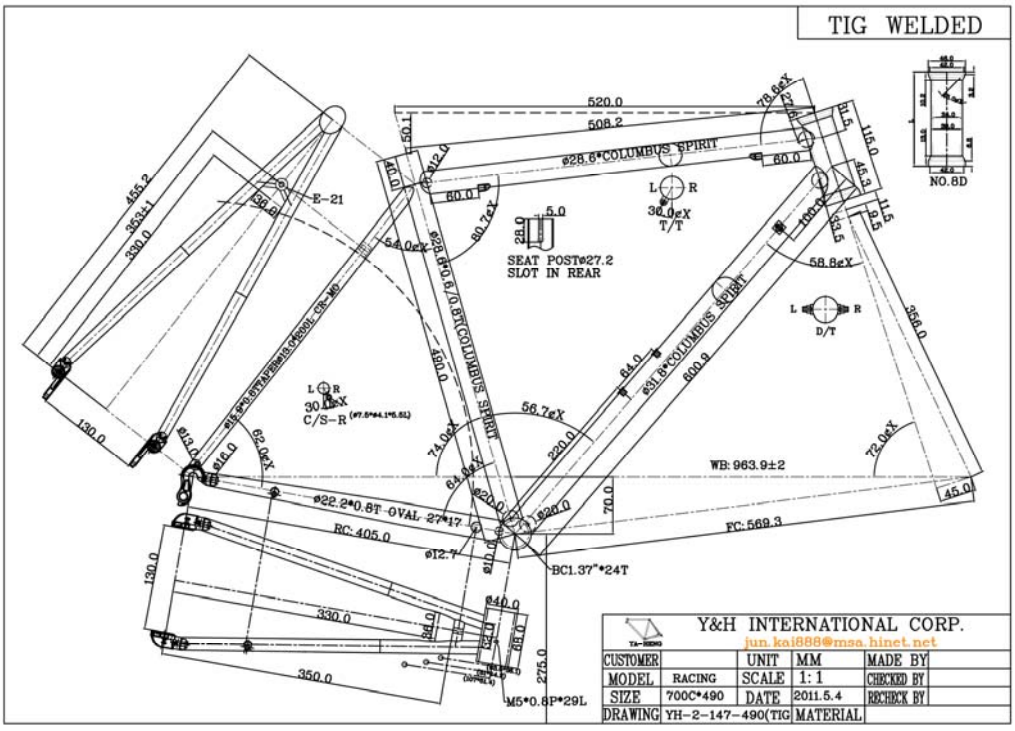

Figure 3.3 Example for the detailed design of a road bike [62]

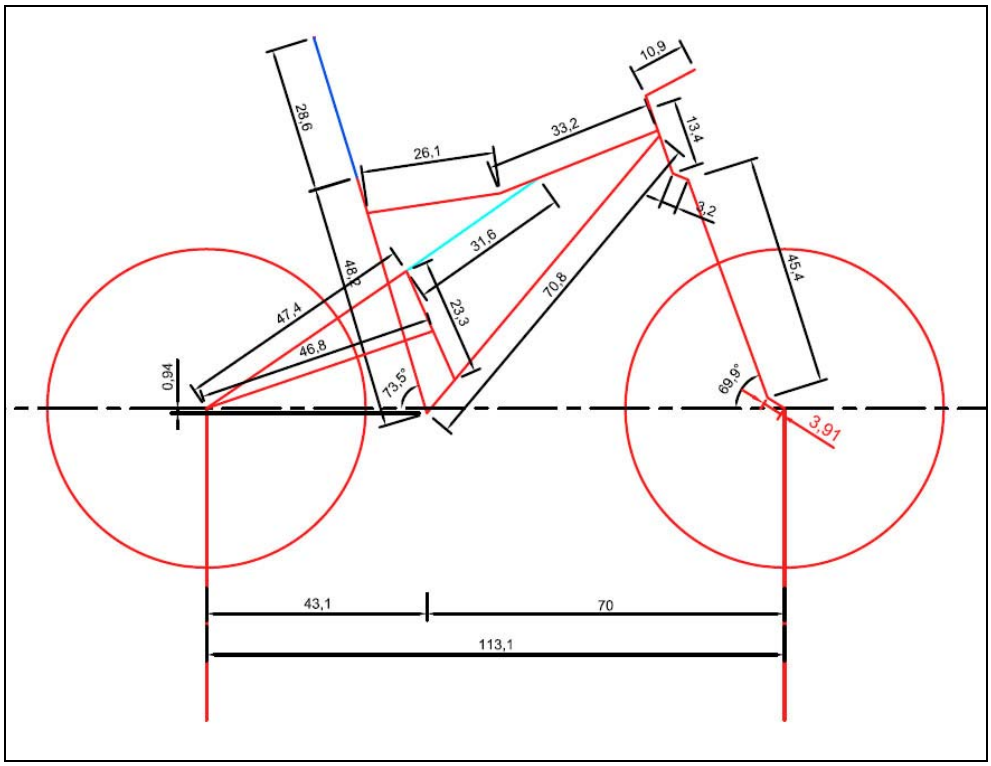

Figure 3.4 Line drawing for a single pivot bike studied in this thesis

3.3 Model of Hard Tail Bike and Full Suspension Bikes

A sample basic geometry of a mountain bike frame is shown in Figure 3.5, which is taken from the mountain bike magazine MBR [63]. The specification includes head angle, seat angle, bottom bracket (BB) height, lengths of chain stay, front centre, wheelbase, and down tube. From a book about the science of cycling, written by Burke [64], one obtains the geometry of a road bike frame as shown in Figure 3.6. From Figures 3.5 and 3.6, it is found the head angle, seat angle, and BB height affect the geometry of the bike frame significantly, and the three parameters affect the stiffness of the bike frame, the performance of steering, and the comfort of rider as well.

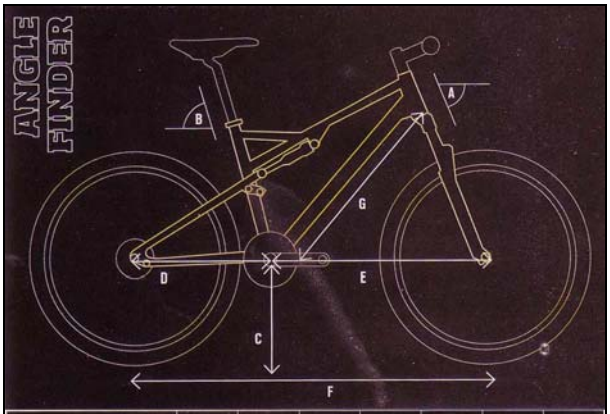

	A HEAD ANGLE	B SEAT ANGLE	C BB HEIGHT	D CHAIN-STAY	E FRONT CENTRE	F WHEEL-BASE	G DOWN TUBE
Specialized	70.4°	72.8°	300mm	425mm	650mm	1075mm	655mm
Whyte	67.4°	68°	325mm	425mm	680mm	1105mm	650mm

Figure 3.5 Specification of a bike frame of Whyte 905 [63]

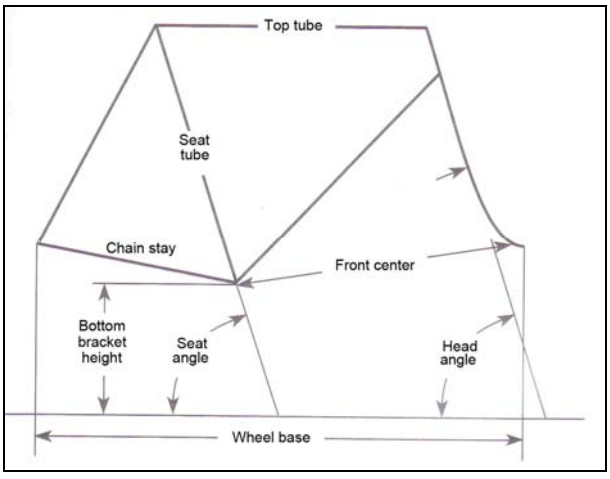

Figure 3.6 Basic geometry of a bike frame based on [64]

In this thesis, five mountain bike models are developed and analyzed. One of them is the hard tail bike, which only has front suspension (front fork) and no rear suspension system. The other four mountain bikes have both front and rear suspension systems, and also called full suspension bikes.

In the current mountain bike market, the most popular rear suspension systems can be categorized in four types: single pivot, four-bar-linkage horst link, four-bar-linkage faux bar, and virtual pivot point (VPP).

The developed bike models are based on Marin Rocky Ridge (hard tail) [65], Orbea Occam (single pivot) [66], Specialized Pitch (four-bar-linkage horst link) [67], Kona Tanuki (four-bar-linkage faux bar) [68], and Santa Cruz Blur (VPP) [69]. Except the Marin Rocky Ridge is an old (hard tail) bike frame in the dynamics lab, all four full suspension bikes chosen are the 2011 models, as shown in Figures 3.7-3.11 obtained from the manufacturers websites. Details of each bike model developed in this thesis will be shown in the following sections.

Figure 3.7 Marin Rocky Ridge [65]

Figure 3.8 Orbea Occam [66]

Figure 3.9 Specialized Pitch [67]

Figure 3.10 Kona Tanuki [68]

Figure 3.11 Santa Cruz Blur [69]

3.3.1 Hard Tail Bike

The Linkage model of the hard tail bike is shown in Figure 3.12. Hard tail bikes are the most common type of mountain bike in the market. Its frame is composed of front and rear triangles, and has only a front suspension with no rear suspension, thus, the bobbing effect is negligible. The absence of rear suspension system will result in less riding comfort since the terrain-induced load [13] and the vibration resulted from passing through bumps must be absorbed by the rider's body.

Another kind of hard tail bike is called soft tail, which has a chain stay made of special material to increase the flexibility for absorbing the vibrations. Since materials are not the subject of this thesis, no soft tail bikes have been included in this study.

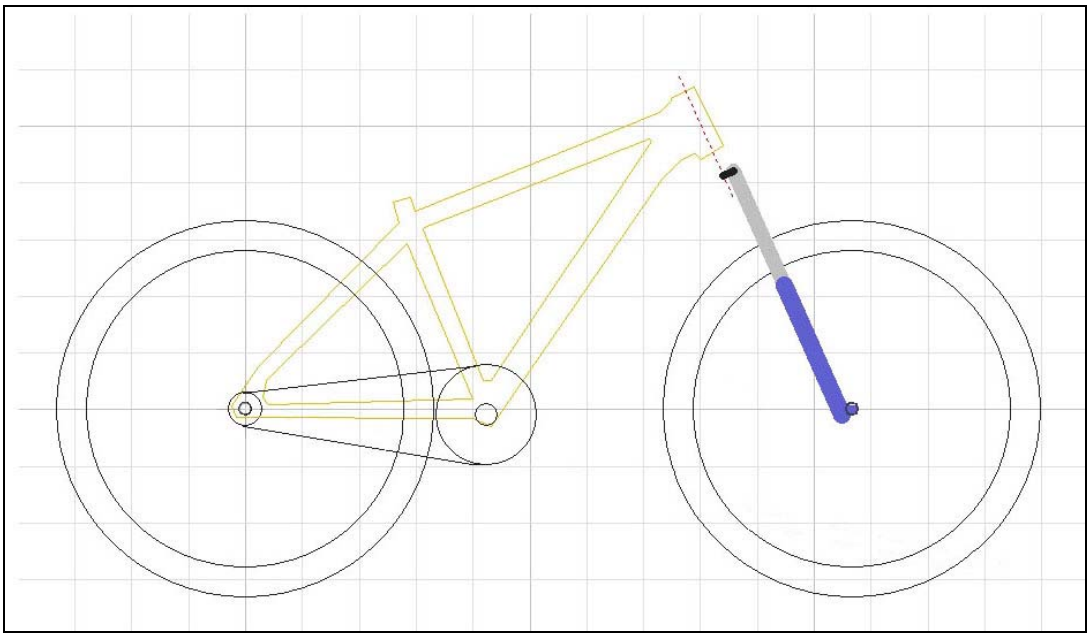

Figure 3.12 Linkage model of Marin Rocky Ridge, a Hard Tail bike

3.3.2 Full Suspension Bike - Single Pivot

The Linkage model of this single pivot bike is shown in Figure 3.13 and some important points are defined and shown in Table 3.1.

The rear suspension system of a single pivot bike is the simplest, its main pivot is located above the bottom bracket on the down tube near the bottom bracket. Some bikes have the main pivot point located on seat tube.

When a vertical force is applied on the seat post, the rear shock absorber is activated. It is found that the travel path of the rear wheel is similar to an arc when the rear shock absorber is compressed, which results in the bobbing effect. Therefore, the rider's pedalling efficiency is reduced since part of rider's pedalling force is absorbed by the rear suspension.

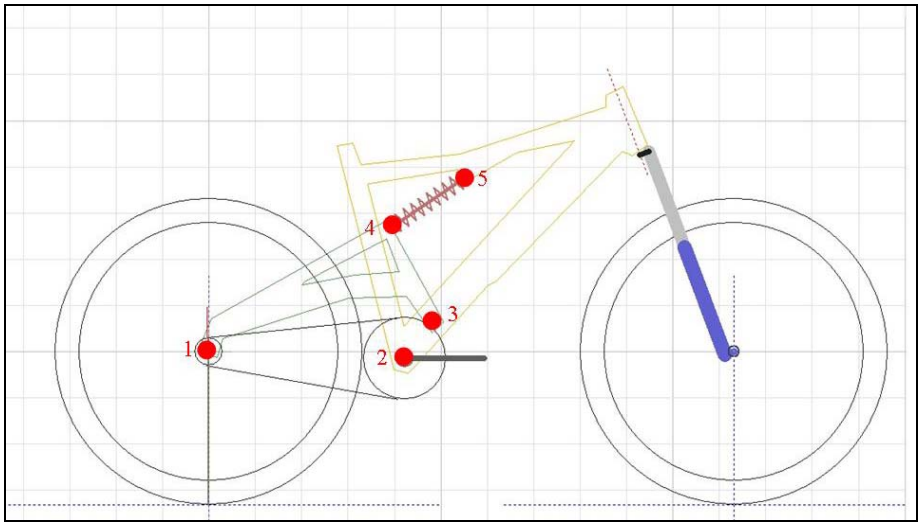

Figure 3.13 Linkage model of Orbea Occam, single pivot bike

Table 3.1 Definition of important points of a single pivot bike

Point No.	Definition of Point
1	Rear Axle
2	Bottom Bracket
3	Main Pivot
4	Shock Eye 1
5	Shock Eye 2

3.3.3 Full Suspension Bike - Four-Bar-Linkage Horst Link

The Linkage model of this four-bar-linkage horst link mountain bike is shown in Figure 3.14, and the important points are defined and shown in Table 3.2. It can be seen the four-bar-linkage is consisted of seat stay, rocker (the triangle part), rear shock absorber, and chain stay. The horst link type rear suspension is also called chain stay pivot, which has a pivot point in front of the rear axle, and connected to rear axle by a small link, called horst link. The horst link is a patent owned by the mountain bike manufacturer Specialized, and the inventor is Horst Leitner [70].

With the four-bar-linkage mechanism, the travel path of rear wheel is more vertical than single pivot rear suspension when the rear shock absorber is activated. Thus, less pedalling force is absorbed by the rear suspension, which results in better performance of pedalling, climbing, accelerating, and braking.

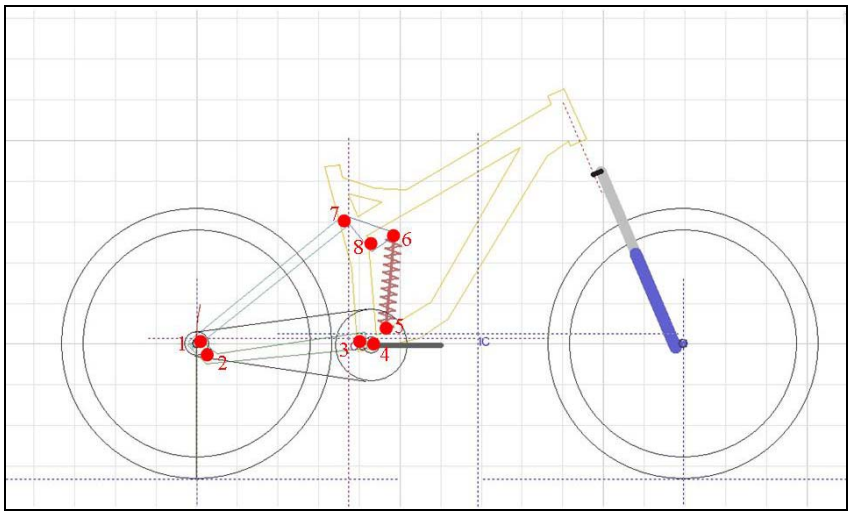

Figure 3.14 Linkage model of Specialized Pitch, four-bar-linkage horst link

Table 3.2 Definition of important points of a four-bar-linkage horst link mountain bike

Point No.	Definition of Point
1	Rear Axle
2	Horst Link Pivot
3	Main Pivot
4	Bottom Bracket
5	Shock Eye 1
6	Shock Eye 2
7	Rocker Pivot
8	Rocket Fix Pivot

3.3.4 Full Suspension Bike - Four-Bar-Linkage Faux Bar

The linkage model of this faux bar mountain bike is shown in Figure 3.15, and the important points are summarized in Table 3.3. Faux bar design is similar to horst link design, both have the four-bar-linkage mechanism. However, the faux bar design does not have a small link to connect rear axle and chain stay. Instead, there is a pivot at the end of seat stay, and a small link is connected to rear axle, which is the so-called faux bar. Therefore, faux bar design is also called seat stay pivot.

When the rear absorber is activated, the motion of the faux bar rear suspension is slightly similar to that of a single pivot mountain bike, so the travel path of rear wheel is also like an arc. However, faux bar design can provide better performance on braking.

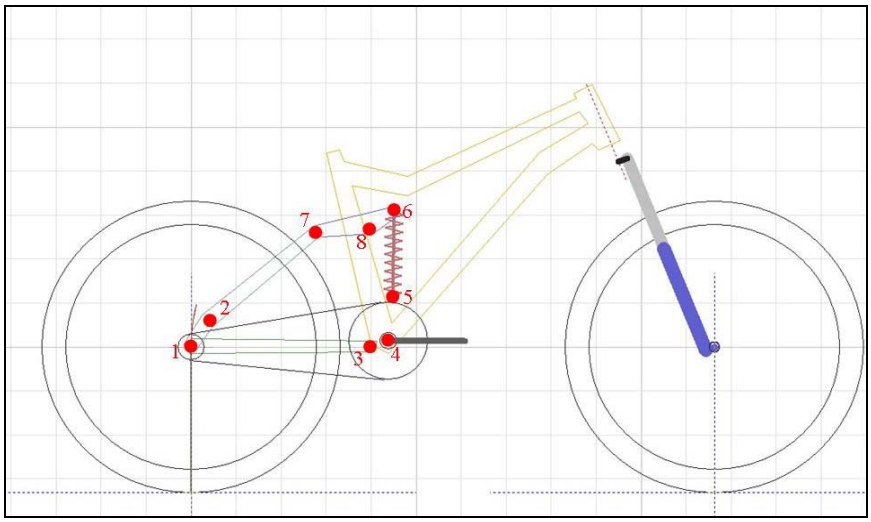

Figure 3.15 Linkage model of Kona Tanuki, four-bar-linkage faux bar

Table 3.3 Definition of important points of a four-bar-linkage faux bar mountain bike

Point No.	Definition of Point
1	Rear Axle
2	Faux Bar Pivot
3	Main Pivot
4	Bottom Bracket
5	Shock Eye 1
6	Shock Eye 2
7	Rocker Pivot
8	Rocket Fix Pivot

3.3.5 Full Suspension Bike - Virtual Pivot Point (VPP)

The linkage model of this VPP mountain bike is shown in Figure 3.16 with the important points summarized in Table 3.4. Unlike four-bar-linkage type rear suspension system, VPP bike has two individual triangles to compose the bike frame, and two links are used to connect the front and rear triangles. Although the real pivot points must be located on the bike frame, the effective virtual pivot point (VPP) is not constrained to be on the frame. In Figure 3.16, points 2 and 7 are located outside the bike frame, while two links, the rocker and a small link are used to connect the front and rear triangles.

VPP design allows the travel path of rear wheel to be vertical when the rear shock absorber is under compression. Thus, the bobbing effect is decreased. VPP technology is a patent owned by the mountain bike manufacturer Santa Cruz. An illustration captured from their official website is shown in Figure 3.17 [69].

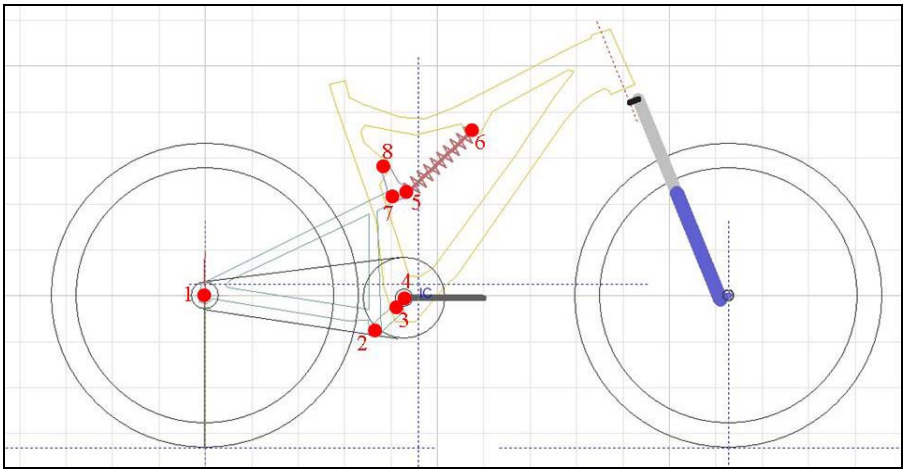

Figure 3.16 Linkage model of Santa Cruz Blur, virtual pivot point (VPP)

Table 3.4 Definition of important points of a VPP mountain bike

Point No.	Definition of Point
1	Rear Axle
2	Small Link Pivot
3	Main Pivot
4	Bottom Bracket
5	Shock Eye 1
6	Shock Eye 2
7	Rocker Pivot
8	Rocket Fix Pivot/Second Link Pivot

Figure 3.17 Illustration of Santa Cruz VPP technology on the mountain bike Blur [69]

3.4 Procedure for Development of Rider-Bike System Model

Five mountain bike models, including one hard tail (HT) bike and four full suspension (FS) bikes, and one rider model are developed in SimMechanics in this thesis. The procedure for developing the bike and rider models is shown in Figure 3.19.

For the bike models, the pictures of the five bikes are obtained from the manufacturer's websites [65-69]. Then, the bike pictures are imported into AutoCAD to develop the line drawings to derive the dimensions of frame tubes for developing the SimMechanics bike models. (Comparing the dimensions derived from AutoCAD with the ones provided by manufacturers, the maximum errors for lengths and angles between line drawings and real bikes are less than 6 cm and 2°, respectively.)

On the other hand, the pictures of the five bikes are imported into Linkage as well to develop the linkage models to observe the motion of rear suspension systems. The SimMechanics bike models are then tested to observe the motion of rear suspension systems and the results are compared with the ones from Linkage. If the motions of both results are consistent, then the SimMechanics model is integrated with the rider model for the numerical analysis.

For the rider model, the dimensions of rider are obtained from [17]. Then the rider model is developed in BikeCAD, in which the angles of the rider's limbs and trunk can be precisely obtained. Afterwards, the SimMechanics rider model can be developed by using the information from [17] and BikeCAD rider model. Finally, the SimMechanics rider model is integrated with the bike model.

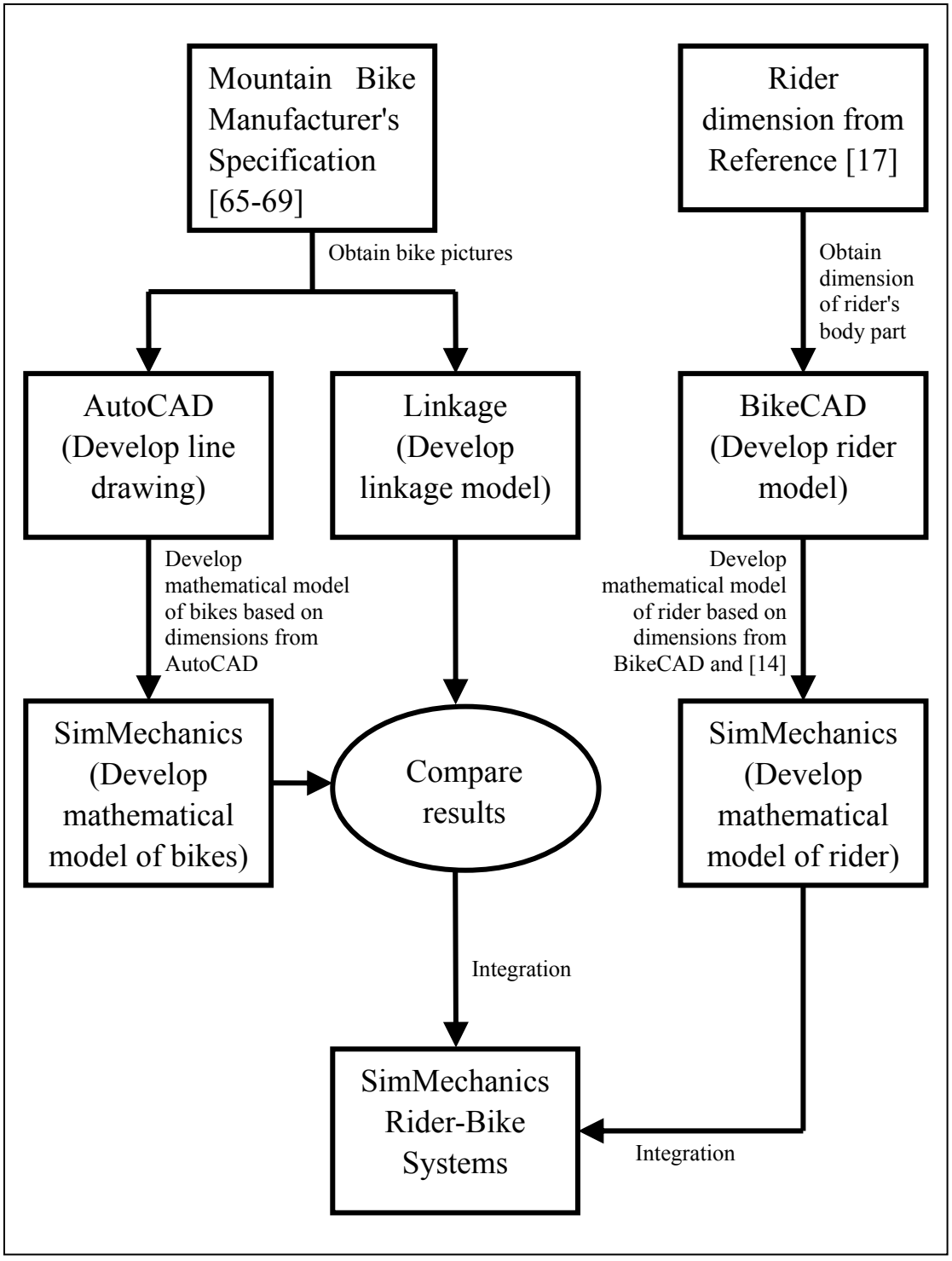

Figure 3.18 Procedure for developing rider-bike system models

3.5 Summary

The steps required to develop the models detailed in this thesis can be summarized as follows. For each bike, with the help of Linkage, the motion of the rear suspension system is observed, and key pivot points of the bikes are defined.

Using BikeCAD, the length and angles of each rider's body part are clearly defined. The SimMechanics model of rider and bikes are then developed based on the dimensions obtained from BikeCAD.

The line drawings of mountain bikes studied in this thesis are generated by using AutoCAD. Since the errors between the AutoCAD line drawings and real specifications provided by the (mountain bike) manufactures are small, the SimMechanics models of mountain bikes are developed based on the dimensions of the line drawings obtained from AutoCAD. Detailed works will be shown in Chapter 5.

Chapter 4 A Technique for Evaluating Pedalling Efficiency of a Bike Rider

4.1 Introduction

It is a common sense that a good match between a rider and his bike is an important factor affecting the pedalling efficiency of the bike rider. In other words, it is impossible that a bike can match with every rider appropriately and, on the contrary, a rider can match with every bike with different dimensions. This is recognized implicitly by manufacturers of bikes who produce the same model in a variety of frame sizes. However, there does not appear to be any publications concerning evaluation of the appropriate match between a rider and his bike, thus, this Chapter presents a technique to the address.

For the right (or left) leg of a bike rider, the crank, the lower leg and upper leg are the three members constituting a mechanism for transmitting the forces applied by the rider's right (or left) leg, they are called Rod1, Rod 2 and Rod3, respectively. Furthermore, the angle between Rod1 and upward y-axis is designated as θ_1, while the angle between Rod2 and x-axis and that between Rod3 and x-axis are designated as θ_2 and θ_3, respectively. Because the mathematical expressions for determining the instantaneous positions of the foregoing three members are dependent on the associated positions of Rod1 in the three angular intervals bounded by four "critical positions", for convenience, the angles of Rod1 corresponding the two critical positions, *uppermost* and *lowermost* positions of Rod3, are denoted by $\theta_{1,U}$ and $\theta_{1,L}$, respectively, and those corresponding to the other two critical positions, *rightward* (with θ_1=90°) and *downward* (with θ_1=180°) positions of Rod1, are denoted by $\theta_{1,B}$ and $\theta_{1,C}$, respectively, where the subscripts U and L represent *uppermost* and *lowermost* positions of Rod3, while B and C represent the positions of Joint 1 with θ_1= 90° and 180°, respectively, as one may see from Figure 4.1. The last angles ($\theta_{1,U}$, $\theta_{1,L}$, $\theta_{1,B}$ and $\theta_{1,C}$) associated with the four "critical positions" are called "critical angles" of Rod1. For the last reason, this Chapter begins with the determination of

critical angles of the three members corresponding to each critical position. Next, two types of driving forces are investigated: (i) The first type of driving forces are transmitted by the "simple" harmonic (SH) motions of the rider's right (or left) upper leg, this leads to non-constant rotating (angular) speed of the crank and "non-simple" harmonic (NSH) external loads; (ii) The second type of driving forces are transmitted by the "non-simple" harmonic (NSH) motions of the rider's right (or left) upper leg leading to *constant* rotating (angular) speed of the crank so that external loads are near "simple" harmonic (SH). In order to find the time history of *external loads* due to first type of driving forces, one must determine the instantaneous positions of Rod1 and Rod2 defined by the associated angles $\theta_1(t)$ and $\theta_2(t)$ based on the specified time-dependent position of Rod3 defined by the given angle $\theta_3(t)$. On the other hand, in order to find the time history of *external loads* due to second type of driving forces, one must determine the instantaneous positions of Rod2 and Rod3 defined by the associated angles $\theta_2(t)$ and $\theta_3(t)$ based on the specified time-dependent position of Rod1 defined by the given angle $\theta_1(t)$.

Finally, from the dimensions (or geometric configuration) of Rod1, Rod2 and Rod3 along with the relative positions of seat centre and bottom bracket, one finds that the angle between Rod1 and Rod2 at any instant of time t is given by $\alpha(t)=1.5\pi-\theta_1(t)-\theta_2(t)$ with $\theta_1(t)$ and $\theta_2(t)$ denoting the instantaneous angles of Rod1 and Rod 2, respectively. Thus, at any instant of time t, the external torque $T(t)$ developed by the crank due to driving forces $F_2(t)$ transmitted from Rod2 is given by $T(t)=L_1F_2(t) \cdot \sin\alpha(t)$ with L_1 denoting the radius of the bike crank (Rod1). It is obvious that, in each half cycle, the effective work W done by the rider's right (or left) leg is determined by the integrations of $T(\theta_1) \cdot d\theta_1$ through the angles from $\theta_{1,U}$ to $\theta_{1,L}$, where $\theta_{1,U}$ and $\theta_{1,L}$ are the (critical) angles between Rod1 and upward y-axis when Rod3 are in its uppermost and lowermost positions, respectively. The above-mentioned integrations are performed numerically by using the trapezoid rule for the first type of (NSH) external torques and the Simpson's rule for the second type of (SH) external torques.

Two cases are studied. For the first case, the dimensions of a bike are kept unchanged and the lengths of upper and lower legs of the riders are varied. For the second case,

the dimensions of the bikes are different and the leg lengths of the rider are kept constant. Because the effective work done by the riders are different from case to case, the appropriate match between a rider and his bike will affect the pedalling efficiency significantly.

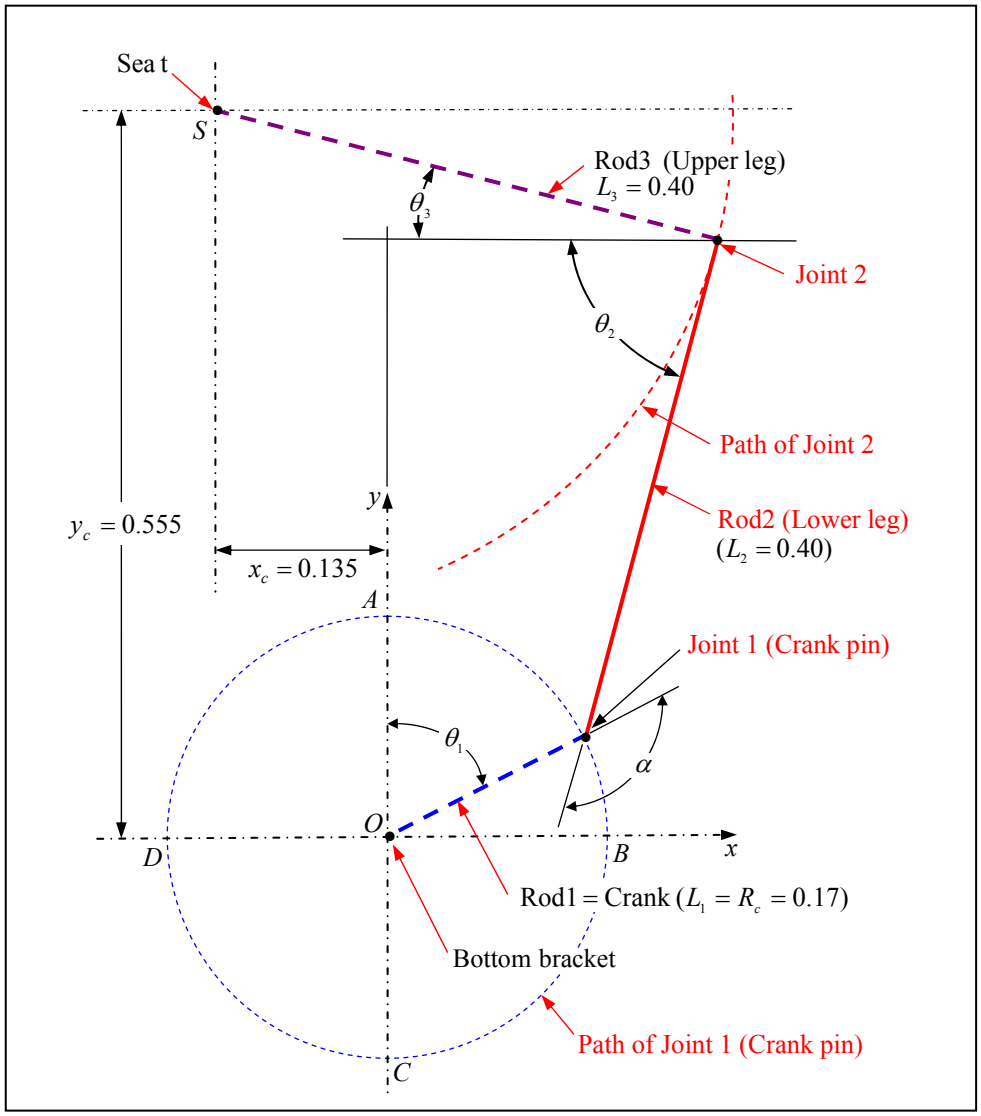

Figure 4.1 Relative positions between the rider's legs (lengths $L2$=$L3$=0.4m) and the crank (length $L1$=R_c=0.17m) with seat-to-bottom bracket distance x_c=0.135m and y_c=0.555m, where the crank, lower leg (shank) and upper leg (thigh) are designated as Rod1, Rod2 and Rod3, respectively.

From the literature reviews shown in Section 2.4, one sees that most of the researchers study the cycling problems from the viewpoint of biomechanics and statistics theory and incorporating with various complicated experiments, and the literature for

tackling the problems with the engineering mechanics and deterministic theory is rare. Thus, this chapter tries to study the pedalling efficiency of a bike rider by using the conventional engineering mechanics incorporating with computer simulations. For convenience, the following assumptions are made: (1) The functions of the rider's muscles are neglected; (2) The performance of left leg is the same as that of right leg; (3) The applied force $F_2(t)$ of each leg during its upstroke is zero, so is the "negative work" produced by the reverse (retarding) pedalling force. It is noted that the similar simple assumptions are also used by the software SimMechanics, such as, each elastic member is assumed to be rigid, the continuous mass is modelled with lumped mass, the functions of the rider's muscles are either neglected or modelled by the springs, … Furthermore, based on the foregoing simple assumptions, the theoretical results obtained from this chapter are very close to the experimental values of literature [45] as one may see from Figures 4.9 and 5.42.

4.2 Determination of Critical Positions of Rod1, Rod2 and Rod3

For convenience, the crank, lower leg (shank) and upper leg (thigh) are called Rod1, Rod2 and Rod3, respectively, as shown in Figure 4.1. In general, the length of a rider's "right" leg is identical with his "left" leg, thus, either lower leg or upper leg may refer to his "right" one or "left" one dependent on the situations concerned. This section determines the critical angles of Rod1, Rod2 and Rod3 for the following critical positions of Rod3 and those of Rod 1: (i) The upper leg (Rod3) is in its uppermost position; (ii) The upper leg (Rod3) is in its lowermost position; (iii) The crank (Rod1) is in its rightward position (with $\theta_1=\theta_{1,B}=90°$); (iv) The crank (Rod1) is in its downward position (with $\theta_1=\theta_{1,C}=180°$). These situations are detailed in Sections 4.2.1 - 4.2.4.

4.2.1 Critical Angles when Upper Leg (Rod3) in its Uppermost Position

From Figure 4.2 one sees that Rod3 (upper leg) is in its uppermost position when the angle between Rod1 (crank) and Rod2 (lower leg) are equal to π(=180°) (i.e., on a straight line). Thus, from Figure 4.2 one sees that

$$(L_1 + L_2)\cos\theta_{1,U} + L_3 \sin\theta_{3,U} = y_c \tag{4.1}$$

$$L_3 \cos\theta_{3,U} - (L_1 + L_2)\sin\theta_{1,U} = x_c \tag{4.2}$$

or

$$L_{12} \cos\theta_{1,U} + L_3 \sin\theta_{3,U} = y_c \tag{4.1'}$$

$$L_3 \cos\theta_{3,U} - L_{12} \sin\theta_{1,U} = x_c \tag{4.2'}$$

where

$$L_1 + L_2 = L_{12} \tag{4.3}$$

It is noted that the subscripts "U" of θ_1 and θ_3 refer to the "uppermost" position of Rod3.

Eliminating $\theta_{1,U}$ from Equations (4.1)' and (4.2)' and then re-arranging the equations, one obtains

$$(x_c^2 + y_c^2)\sin^2\theta_{3,U} - 2C_1 y_c \sin\theta_{3,U} + (C_1^2 - x_c^2) = 0 \tag{4.4}$$

where

$$C_1 = (x_c^2 + y_c^2 + L_3^2 - L_{12}^2)/(2L_3) \tag{4.5}$$

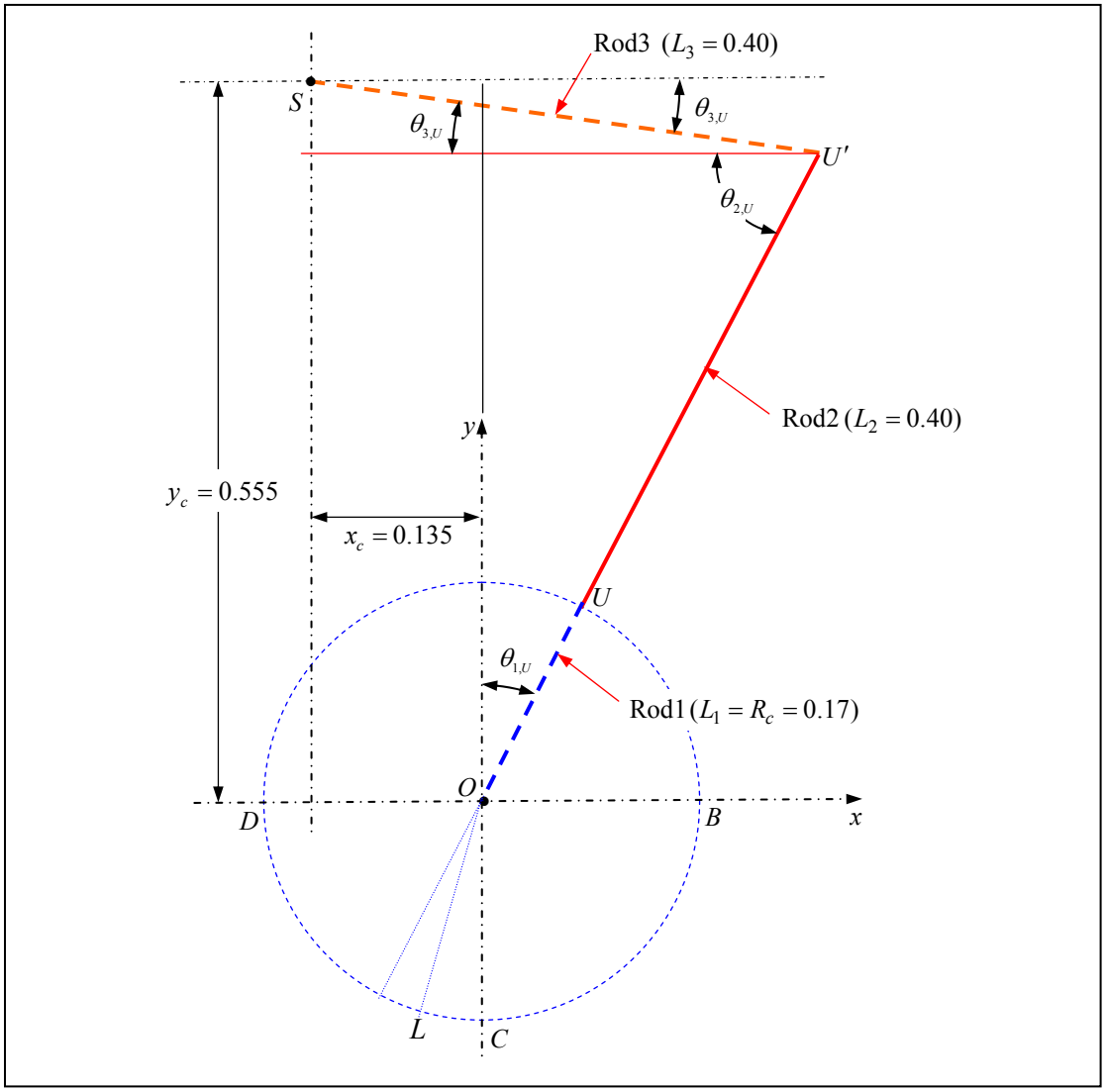

Figure 4.2 Diagram for determining the critical angles of Rod1, Rod2 and Rod3 ($\theta 1_{,U}$, $\theta 2_{,U}$ and $\theta 3_{,U}$) when the upper leg (Rod3) is in its "uppermost" position.

From the foregoing equations one obtains

$$\sin\theta_{3,U} = \frac{C_1 y_c \pm \sqrt{(C_1 y_c)^2 - (x_c^2 + y_c^2)(C_1^2 - x_c^2)}}{x_c^2 + y_c^2} = s_2 \tag{4.6}$$

or

$$\theta_{3,U} = \sin^{-1} s_2 \tag{4.6'}$$

and

$$\theta_{1,U} = \cos^{-1}[(y_c - L_3 \sin\theta_{3,U})/L_{12}] \tag{4.7}$$

$$\theta_{2,U} = \tfrac{1}{2}\pi - \theta_{1,U} \tag{4.8}$$

Besides, from Figure 4.1 one sees that the angle between Rod1 and Rod2 is given by

$$\alpha = 360^\circ - 90^\circ - \theta_1 - \theta_2 = 270^\circ - \theta_1 - \theta_2 \tag{4.9}$$

For the details regarding Equations (4.6)-(4.8) one may refer to Equations (A.6)-(A.10) in Appendix A at the end of this thesis.

4.2.2 Critical Angles when Upper Leg (Rod3) in its Lowermost Position

From Figure 4.3 one sees that upper leg (Rod3) is in its *lowermost* position when the path of Joint 1 of Rod1 is tangential to the path of Joint 1 of Rod2 with centre L' on path of Joint 2 and radius to be L_2. If the tangential point between the above-mentioned two paths (arcs) is denoted by L, then $\overline{L'L}$ must pass through the centre "O" of the circle of crank pin (i.e., bottom bracket) because the radius of the circle must be perpendicular to the tangential line at point L. Where the symbol $\overline{L'L}$ denotes the line connecting points L' and L.

Thus, from Figure 4.3 one sees that

$$\overline{SP} + \overline{PN} = \overline{SM} + \overline{MN} \tag{4.10}$$

$$\overline{QR} = \overline{PR} - \overline{PQ} = \overline{PR} - (\overline{PL'} - \overline{QL'}) \tag{4.11}$$

Thus,

$$L_3 \sin\theta_{3,L} + L_2 \sin\theta_2 = y_c + L_1 \sin\theta_2 \tag{4.12a}$$

$$L_1 \cos\theta_2 = x_c - (L_3 \cos\theta_{3,L} - L_2 \cos\theta_2) \tag{4.12b}$$

Eliminating θ_2 from Equations (4.12a) and (4.12b), one obtains

$$(x_c^2 + y_c^2)\sin^2\theta_{3,L} - 2y_c E_2 \sin\theta_{3,L} + (E_2^2 - x_c^2) = 0 \tag{4.13}$$

where

$$E_2 = [x_c^2 + y_c^2 + L_3^2 - (L_2 - L_1)^2] / (2L_3) \tag{4.14}$$

From Equations (4.12)-(4.14) and referring to Equations (A.19)-(A.23), one obtains

$$\sin\theta_{3,L} = \frac{y_c E_2 \pm \sqrt{(y_c E_2)^2 - (x_c^2 + y_c^2)(E_2^2 - x_c^2)}}{x_c^2 + y_c^2} = s_2 \tag{4.15}$$

or

$$\theta_{3,L} = \sin^{-1} s_2 \tag{4.15'}$$

and

$$\theta_2 = \theta_{2,L} = \sin^{-1}[(y_c - L_3 \sin\theta_{3,L})/(L_2 - L_1)] \tag{4.16}$$

$$\theta_{1,L} = \pi + \theta'_{1,L} = \pi + (0.5\pi - \theta_2) = 1.5\pi - \theta_2 \tag{4.17}$$

It is noted that the subscripts "L" of θ_1, θ_2, and θ_3 refer to the "lowermost" position of Rod3.

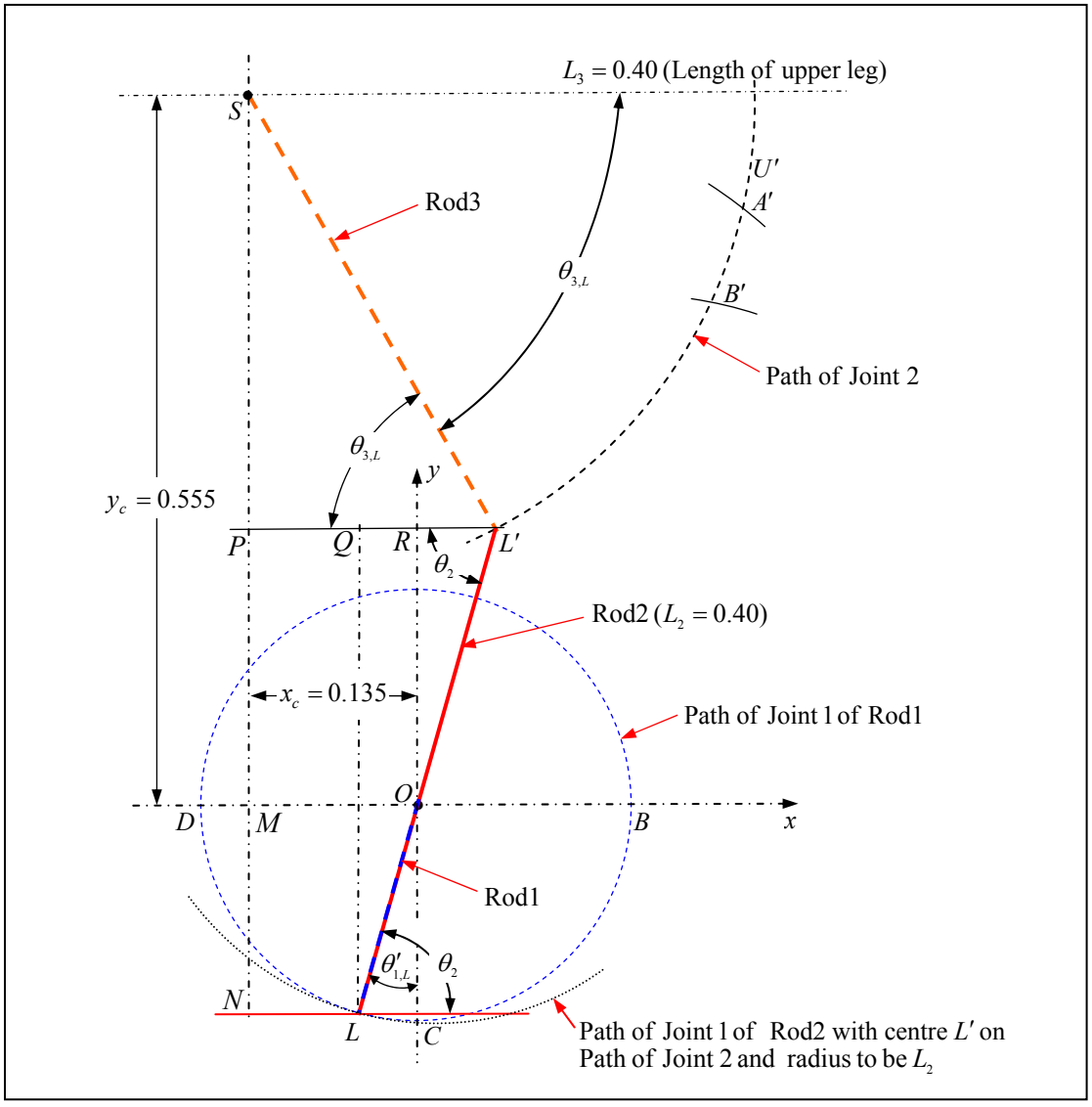

Figure 4.3 Diagram for determining the critical angles of Rod1, Rod2 and Rod3 ($\theta 1_{,L}$, $\theta 2_{,L}$ and $\theta 3_{,L}$) when the upper leg (Rod3) is in its "lowermost" position. Note that $\overline{OL}$ and $\overline{L'L}$ are overlapped, and L is the tangential point between the two paths (arcs).

4.2.3 Critical Angles when Crank (Rod1) in Rightward Position ($\theta_1=\theta_{1,B}=90°$)

When Rod1 is in its horizontal position with Joint 1 at point B and $\theta_1=\theta_{1,B}=90°$ as shown in Figure 4.4, one has

$$\overline{SM}=\overline{SP}+\overline{PM}\ ,\ \ \overline{PB'}=\overline{PQ}+\overline{QR}+\overline{RB'} \tag{4.18a,b}$$

Thus,

$$y_c=L_3\sin\theta_{3,B}+L_2\sin\theta_2\ ,\ \ L_3\cos\theta_{3,B}=x_c+L_1+L_2\cos\theta_2 \tag{4.19a,b}$$

Eliminating θ_2 from Equations (4.19a) and (4.19b), one obtains

$$(C_3^2+y_c^2)\sin^2\theta_{3,B}-2D_3y_c\sin\theta_{3,B}+(D_3^2-C_3^2)=0 \tag{4.20}$$

where

$$C_3=x_c+L_1\ ,\ \ D_3=(C_3^2+y_c^2+L_3^2-L_2^2)/(2L_3) \tag{4.21a,b}$$

From Equations (4.19)-(4.21) and referring to Equations (A.29)-(A.32), one obtains

$$\sin\theta_{3,B}=\frac{D_3y_c\pm\sqrt{(D_3y_c)^2-(C_3^2+y_c^2)(D_3^2-C_3^2)}}{(C_3^2+y_c^2)}=s_2 \tag{4.22}$$

or

$$\theta_{3,B}=\sin^{-1}s_2 \tag{4.23}$$

and

$$\theta_2=\theta_{2,B}=\sin^{-1}[(y_c-L_3\sin\theta_{3,B})/L_2] \tag{4.24}$$

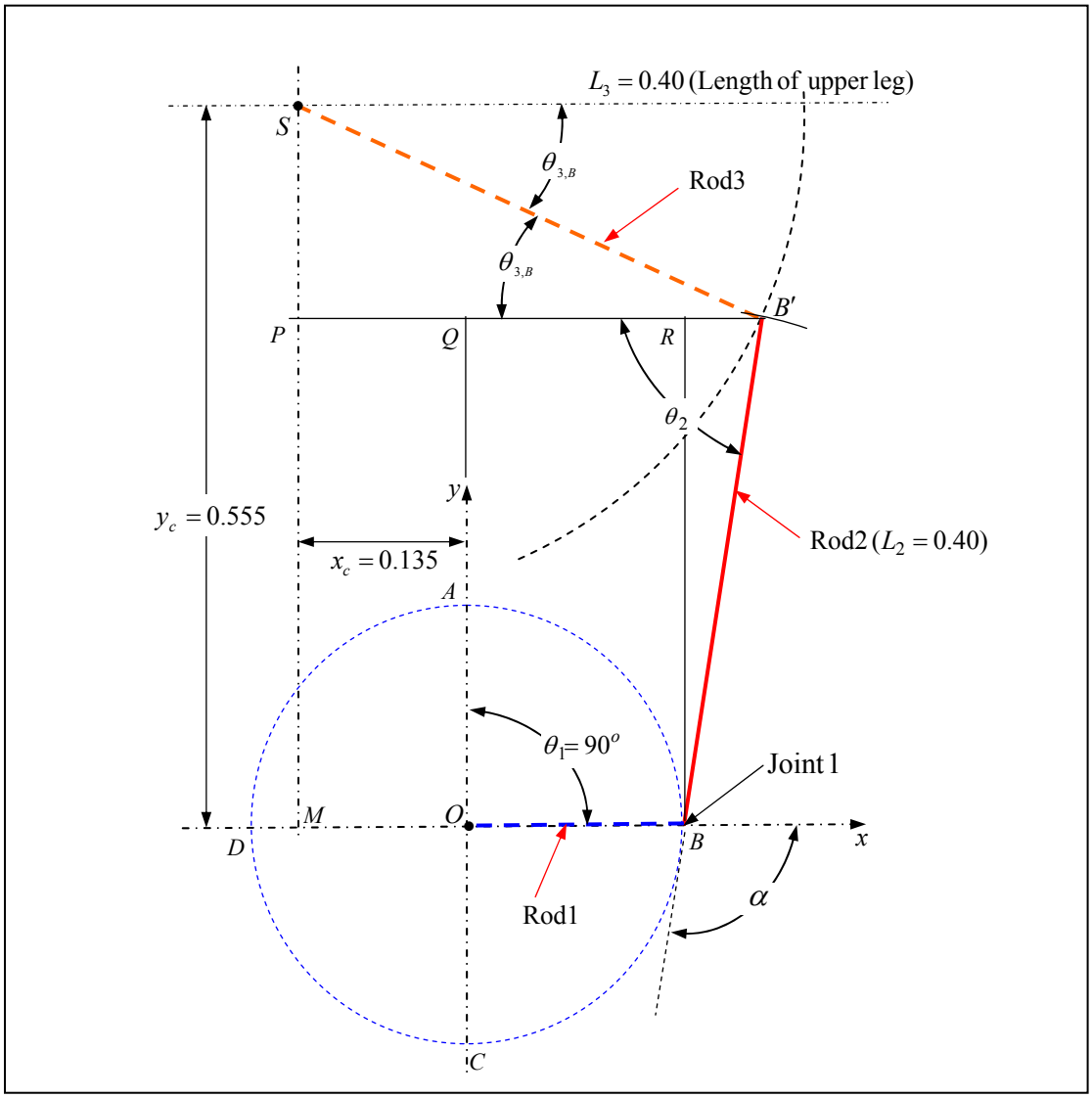

Figure 4.4 Diagram for determining the critical angles of Rod2 and Rod3 ($\theta 2_{,B}$ and $\theta 3_{,B}$) when the crank (Rod1) is in *rightward* position with Joint 1 at point *B* and $\theta 1 = \theta 1_{,B} = 90°$.

4.2.4 Critical Angles when Crank (Rod1) in Downward position ($\theta_1=\theta_{1,C}=180°$)

When Rod1 is in vertical position with Joint 1 at point C and $\theta_1=\theta_{1,C}=180°$ as shown in Figure 4.5, one has

$$\overline{SM} = \overline{SP} + \overline{PN} - \overline{NM}\ ,\ \ \overline{PC'} = \overline{PQ} + \overline{QC'} \tag{4.25a,b}$$

Thus,

$$y_c = L_3 \sin\theta_{3,C} + L_2 \sin\theta_2 - L_1\ ,\ \ L_3 \cos\theta_{3,C} = x_c + L_2 \cos\theta_2 \tag{4.26a,b}$$

Eliminating θ_2 from Equations (4.26a) and (4.26b) produces

$$(x_c^2 + C_4^2)\sin^2\theta_{3,C} - 2C_4 D_4 \sin\theta_{3,C} + (D_4^2 - x_c^2) = 0 \tag{4.27}$$

where

$$C_4 = y_c + L_1\ ,\ \ D_4 = (x_c^2 + C_4^2 + L_3^2 - L_2^2)/(2L_3) \tag{4.28a,b}$$

From Equations (4.26)-(4.28) and referring to Equations (A.37)-(A.40), one obtains

$$\sin\theta_{3,C} = \frac{C_4 D_4 \pm \sqrt{(C_4 D_4)^2 - (x_c^2 + C_4^2)(D_4^2 - x_c^2)}}{(x_c^2 + C_4^2)} = s_2 \tag{4.29}$$

or

$$\theta_{3,C} = \sin^{-1} s_2 \tag{4.29'}$$

and

$$\theta_2 = \theta_{2,C} = \sin^{-1}[(C_4 - L_3 \sin\theta_{3,C})/L_2] \tag{4.30}$$

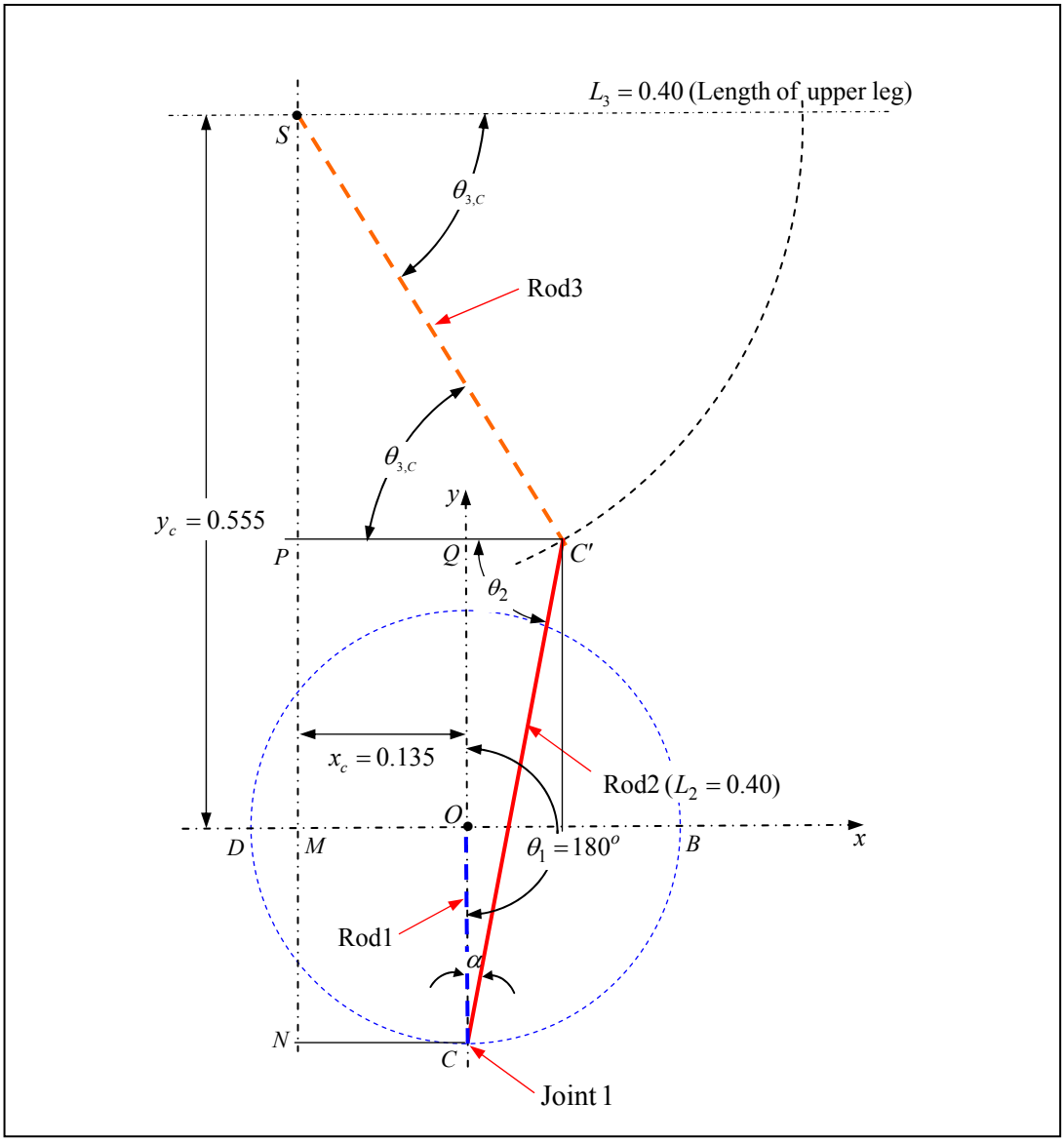

Figure 4.5 Diagram for determining the critical angles of Rod2 and Rod3 ($\theta 2_{,C}$ and $\theta 3_{,C}$) when the crank (Rod1) is in *downward* position with Joint 1 at point *C* and $\theta 1 = \theta 1_{,C} = 180°$.

4.3 Positions of Rod1 and Rod2 Associated with any Specified Positions of Rod3

When the driving forces are transmitted by the "simple" harmonic (SHM) motions of the rider's right (or left) upper leg, the rotating (angular) speed of the crank is "non-constant" and the external loads are "non-simple" harmonic (NSHM). In order to determine the instantaneous external loads, one requires to find the angles of Rod1 and Rod2 corresponding to the (given) prescribed angle of Rod3 at any instant of time t. The relevant mathematical expressions must be derived based on the position of Rod3, $\theta_3(t)$, within the following three angular intervals: (i) $\theta_{3,U} \le \theta_3(t) < \theta_{3,B}$, (ii) $\theta_{3,B} \le \theta_3(t) < \theta_{3,C}$ and (iii) $\theta_{3,C} \le \theta_3(t) < \theta_{3,L}$.

4.3.1 Positions of Rod1 and Rod2 Associated with $\theta_{3,U} \le \theta_3(t) < \theta_{3,B}$

When upper leg (Rod3) is in the arbitrary position within the interval $\theta_{3,U} \le \theta_3(t) < \theta_{3,B}$, the position of crank (Rod1) must be in the interval $\theta_{1,U} \le \theta_1(t) < 0.5\pi$ as shown in Figure 4.6. From the figure one obtains

$$\overline{SN} = \overline{SP} + \overline{PM} + \overline{MN}, \quad \overline{PT} = \overline{PQ} + \overline{QR} + \overline{RT} \tag{4.31a,b}$$

Thus,

$$y_c = L_3 \sin\theta_3 + L_2 \sin\theta_2 + L_1 \cos\theta_1, \quad L_3 \cos\theta_3 = x_c + L_1 \sin\theta_1 + L_2 \cos\theta_2 \tag{4.32a,b}$$

Eliminating θ_2 from Equations (4.32a) and (4.32b), one obtains

$$(C_5^2 + D_5^2)\sin^2\theta_1 - 2E_5 D_5 \sin\theta_1 + (E_5^2 - C_5^2) = 0 \tag{4.33}$$

where

$$C_5 = y_c - L_3 \sin\theta_3, \quad D_5 = -x_c + L_3 \cos\theta_3 \tag{4.34a,b}$$

$$E_5 = (C_5^2 + D_5^2 + L_1^2 - L_2^2)/(2L_1) \tag{4.34c}$$

From Equations (4.32)-(4.35) and referring to Equations (A.47)-(A.50), one obtains

$$\sin\theta_1 = \frac{E_5 D_5 \pm \sqrt{(E_5 D_5)^2 - (C_5^2 + D_5^2)(E_5^2 - C_5^2)}}{(C_5^2 + D_5^2)} = s_1 \tag{4.35}$$

or

$$\theta_1 = \sin^{-1} s_1 \tag{4.35'}$$

and

$$\theta_2 = \sin^{-1}[(C_5 - L_1 \cos\theta_1)/L_2] \tag{4.36}$$

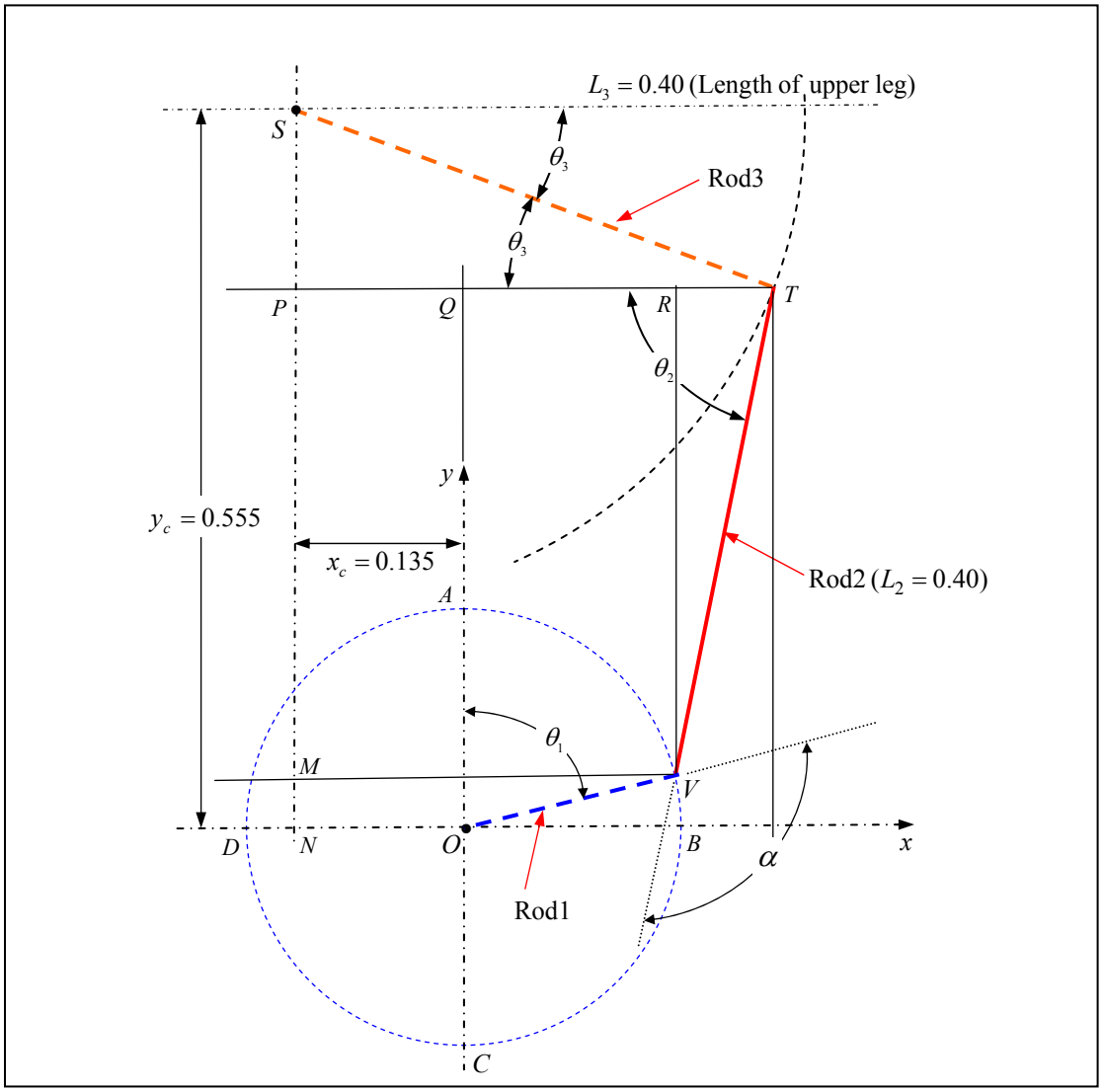

Figure 4.6 Diagram for determining the angle of Rod1, $\theta 1_{,U} \le \theta 1(t) < 0.5\pi$, when the position of upper leg (Rod3) is in the interval $\theta 3_{,U} \le \theta 3(t) < \theta 3_{,B}$.

4.3.2 Positions of Rod1 and Rod2 Associated with $\theta_{3,B} \le \theta_3(t) < \theta_{3,C}$

When upper leg (Rod3) is in the arbitrary position within the interval $\theta_{3,B} \le \theta_3(t) < \theta_{3,C}$, the position of crank (Rod1) must be in the interval $0.5\pi \le \theta_1(t) < \pi$ as shown in Figure 4.7. In such a case, from the figure one sees that

$$\overline{SM} = \overline{SP} + \overline{PN} - \overline{MN}, \quad \overline{PT} = \overline{PQ} + \overline{QR} + \overline{RT} \tag{4.37a,b}$$

Thus,

$$y_c = L_3 \sin\theta_3 + L_2 \sin\theta_2 - L_1 \sin\theta_1', \quad L_3 \cos\theta_3 = x_c + L_1 \cos\theta_1' + L_2 \cos\theta_2 \tag{4.38a,b}$$

Eliminating θ_2 from Equations (4.38a) and (4.38b) leads to

$$(C_5^2 + D_5^2)\cos^2\theta_1' - 2E_5 D_5 \cos\theta_1' + (E_5^2 - C_5^2) = 0 \tag{4.39}$$

Where C_5, D_5 and E_5 take the same forms as those given by Equations (4.34a,b,c), i.e.,

$$C_5 = y_c - L_3 \sin\theta_3, \quad D_5 = -x_c + L_3 \cos\theta_3 \tag{4.40a,b}$$

$$E_5 = (C_5^2 + D_5^2 + L_1^2 - L_2^2)/(2L_1) \tag{4.40c}$$

From Equations (4.38)-(4.40) and referring to Equations (A.55)-(A.59), one obtains

$$\cos\theta_1' = \frac{E_5 D_5 \pm \sqrt{(E_5 D_5)^2 - (C_5^2 + D_5^2)(E_5^2 - C_5^2)}}{(C_5^2 + D_5^2)} = s_1 \tag{4.41}$$

or

$$\theta_1' = \cos^{-1} s_1 \tag{4.41'}$$

$$\theta_1 = 0.5\pi + \theta_1' \tag{4.42}$$

$$\theta_2 = \sin^{-1}[(C_5 + L_1 \sin\theta_1')/L_2] \tag{4.43}$$

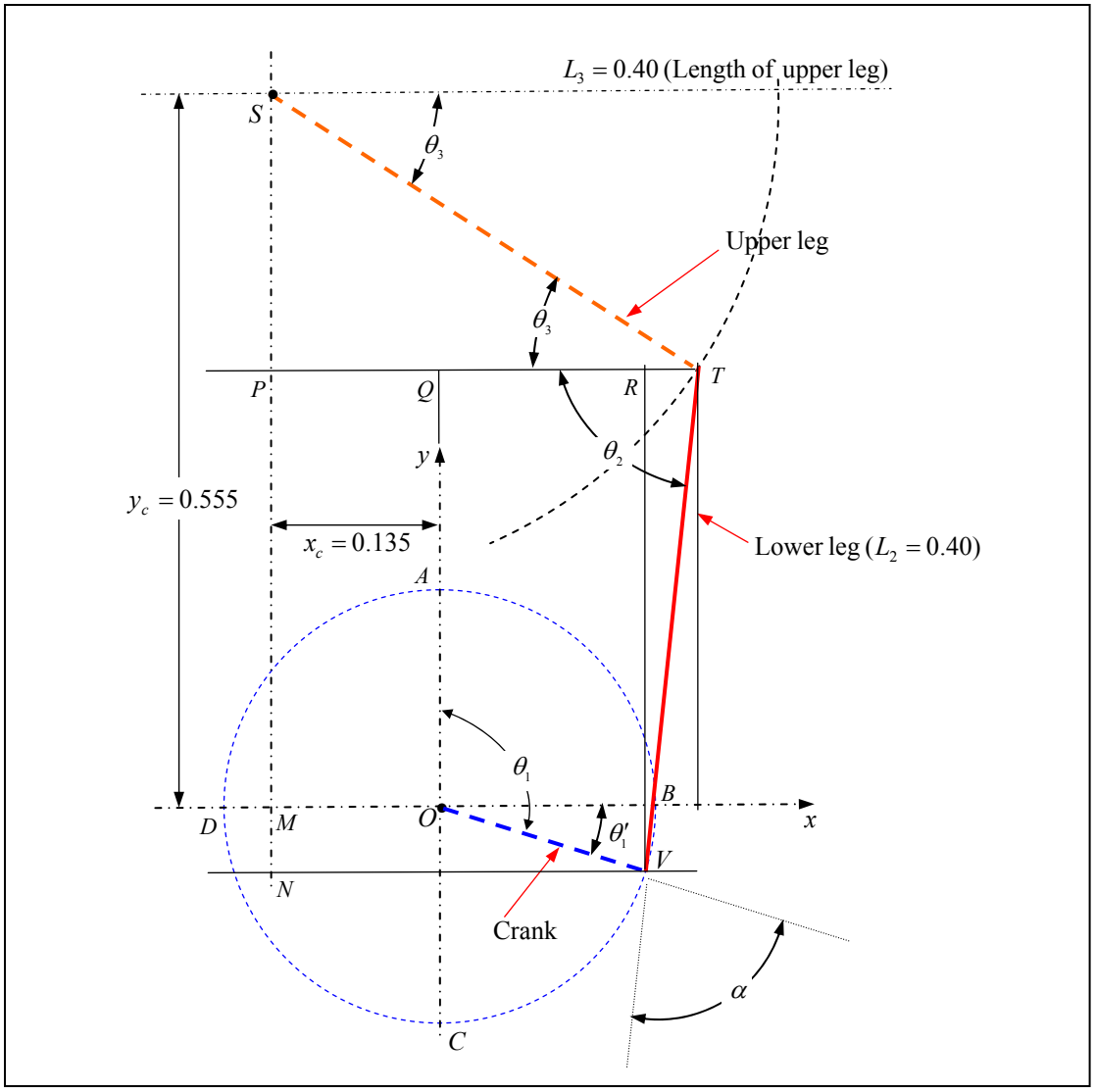

Figure 4.7 Diagram for determining the position of Rod1, $0.5\pi \le \theta 1(t) < \pi$, when the position of upper leg (Rod3) is in the interval $\theta 3_{,B} \le \theta 3(t) < \theta 3_{,C}$.

4.3.3 Positions of Rod1 and Rod2 Associated with $\theta_{3,C} \le \theta_3(t) < \theta_{3,L}$

When the upper leg (Rod3) is in the arbitrary position $\overline{SG'}$ within the interval $\theta_{3,C} \le \theta_3(t) < \theta_{3,L}$, the position of crank (Rod1) must be in the interval $\pi \le \theta_1(t) < \theta_{1,L}$ as shown in Figure 4.8 denoted by $\overline{OG}$. In such a case, from the figure one sees that

$$\overline{SM} = \overline{SP} + \overline{PN} - \overline{MN}, \quad \overline{PG'} = (\overline{PR} - \overline{QR}) + \overline{QG'} \tag{4.44a,b}$$

Thus,

$$y_c = L_3 \sin\theta_3 + L_2 \sin\theta_2 - L_1 \cos\theta_1', \quad L_3 \cos\theta_3 = (x_c - L_1 \sin\theta_1') + L_2 \cos\theta_2 \tag{4.45a,b}$$

Eliminating θ_2 from the above two equations, one obtains

$$(C_6^2 + D_6^2)\sin^2\theta_1' - 2D_6E_6 \sin\theta_1' + (E_6^2 - C_6^2) = 0 \tag{4.46}$$

where

$$C_6 = -y_c + L_3 \sin\theta_3, \quad D_6 = x_c - L_3 \cos\theta_3 \tag{4.47a,b}$$

$$E_6 = (C_6^2 + D_6^2 + L_1^2 - L_2^2)/(2L_1) \tag{4.47c}$$

From Equations (4.45)-(4.47) and referring to Equations (A.64)-(A.68), one obtains

$$\sin\theta_1' = \frac{D_6E_6 \pm \sqrt{(D_6E_6)^2 - (C_6^2 + D_6^2)(E_6^2 - C_6^2)}}{(C_6^2 + D_6^2)} = s_1 \tag{4.48}$$

or

$$\theta_1' = \sin^{-1} s_1 \tag{4.48'}$$

and

$$\theta_1 = \pi + \theta_1' \tag{4.49}$$

$$\theta_2 = \sin^{-1}[(L_1 \cos\theta_1' - C_6)/L_2] \tag{4.50}$$

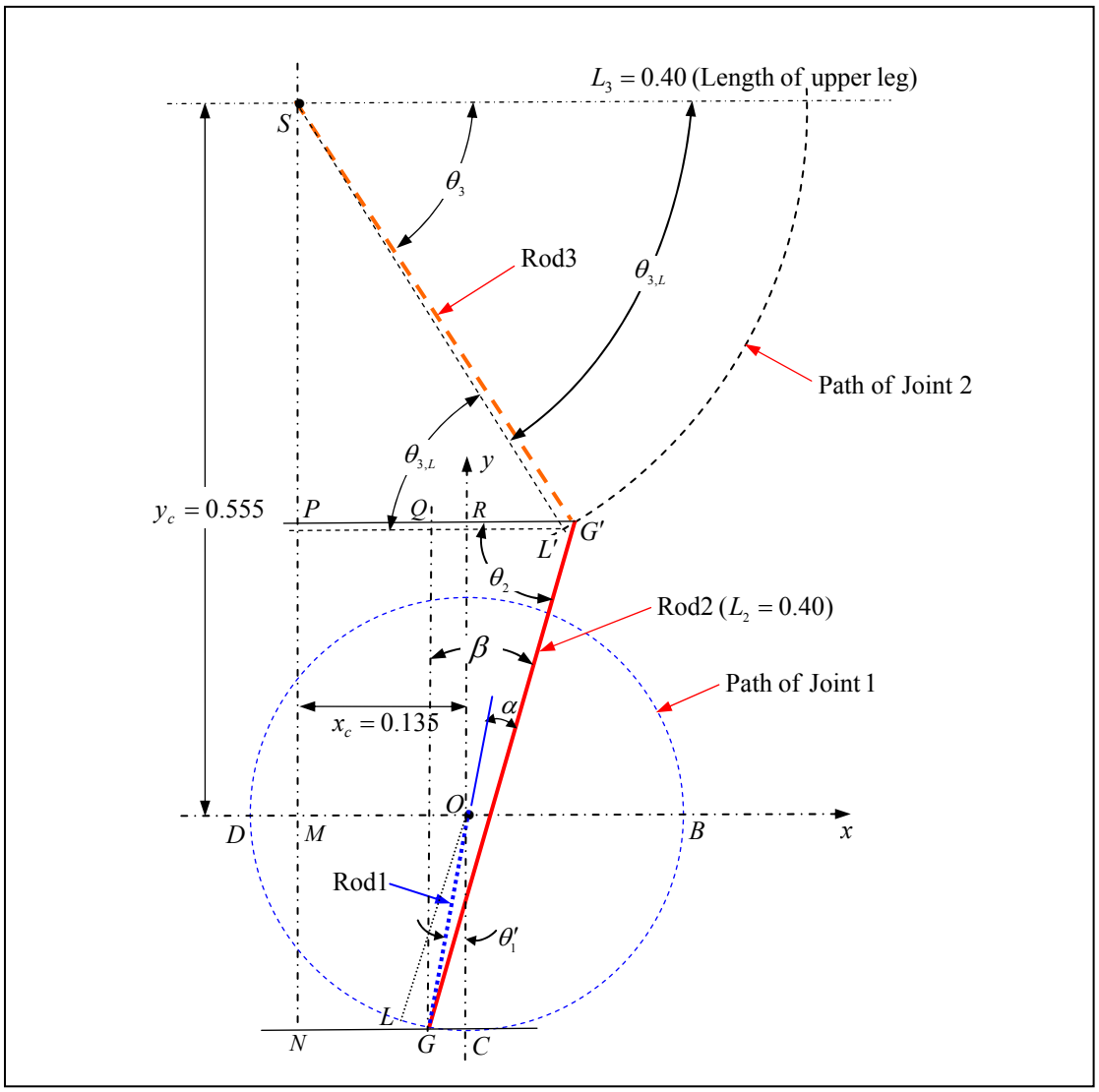

Figure 4.8 Diagram for determining the position of Rod1, $\pi \leq \theta 1(t) < \theta 1_{,L}$, when the position of upper leg (Rod3) is in the interval $\theta 3_{,C} \leq \theta 3(t) < \theta 3_{,L}$.

4.4 Positions of Rod2 and Rod3 Associated with any Specified Positions of Rod1

If the driving forces are transmitted by the "non-simple" harmonic (NSHM) motions of the rider's right (or left) upper leg and the rotating (angular) speed of the crank is constant, then the external loads are "simple" harmonic (SHM). It is obvious that, in order to determine the instantaneous external loads, one requires to find the angles of Rod2 and Rod3 corresponding to the (given) prescribed angle of Rod1 at any instant of time t. In such situations, the relevant mathematical expressions must be derived based on the position of Rod1, $\theta_1(t)$, within the following three angular intervals: (i) $\theta_{1,U} \le \theta_1(t) < 0.5\pi$, (ii) $0.5\pi \le \theta_1(t) < \pi$ and (iii) $\pi \le \theta_1(t) < \theta_{1,L}$. The formulation of this section is similar to that of the last section, the main difference is that $\theta_3(t)$ is given with $\theta_1(t)$ and $\theta_2(t)$ being determined in the last section, however, $\theta_1(t)$ is given with $\theta_2(t)$ and $\theta_3(t)$ being determined in the present section.

4.4.1 Positions of Rod2 and Rod3 Associated with $\theta_{1,U} \le \theta_1(t) < 0.5\pi$

For the current case, the configuration of the crank (Rod1), the rider's right (or left) lower leg (Rod2) and his upper leg (Rod3) is the same as that shown in Figure 4.6. From Equations (A.74)-(A.77) of Appendix A at end of this thesis, one obtains

$$\sin\theta_3 = \frac{C_5' E_5' - \sqrt{(C_5' E_5')^2 - (C_5'^2 + D_5'^2)(E_5'^2 - D_5'^2)}}{(C_5'^2 + D_5'^2)} = s_2 \tag{4.51a}$$

Thus,

$$\theta_3 = \sin^{-1} s_2 \tag{4.51b}$$

In addition,

$$\theta_2 = \sin^{-1}[(C_5' - L_3 \sin\theta_3)/L_2] \tag{4.52}$$

4.4.2 Positions of Rod2 and Rod3 Associated with $0.5\pi \le \theta_1(t) < \pi$

For the current case, the configuration of the crank (Rod1), the rider's right (or left) lower leg (Rod2) and his upper leg (Rod3) is the same as that shown in Figure 4.7.

From Equations (A.81)-(A.85), one obtains

$$\cos\theta_3 = \frac{D_5''E_5'' + \sqrt{(D_5''E_5'')^2 - (C_5''^2 + D_5''^2)(E_5''^2 - C_5''^2)}}{(C_5''^2 + D_5''^2)} = s_1 \tag{4.53a}$$

Thus,

$$\theta_3 = \cos^{-1} s_1 \tag{4.53b}$$

In addition,

$$\theta_2 = \sin^{-1}[(C_5'' - L_3 \sin\theta_3)/L_2] \tag{4.54}$$

$$\theta_1 = 0.5\pi + \theta_1' \tag{4.55}$$

4.4.3 Positions of Rod2 and Rod3 Associated with $\pi \le \theta_1(t) < \theta_{1,L}$

For the current case, the configuration of the crank (Rod1), the rider's right (or left) lower leg (Rod2) and his upper leg (Rod3) is the same as that shown in Figure 4.8, thus, from Equations (A.89)-(A.93), one obtains

$$\cos\theta_3 = \frac{-D_6'E_6' + \sqrt{(D_6'E_6')^2 - (C_6'^2 + D_6'^2)(E_6'^2 - C_6'^2)}}{(C_6'^2 + D_6'^2)} = s_1 \tag{4.56a}$$

Thus,

$$\theta_3 = \cos^{-1} s_1 \tag{4.56b}$$

In addition,

$$\theta_2 = \sin^{-1}[(C_6' - L_3 \sin\theta_3)/L_2] \tag{4.57}$$

$$\theta_1 = \pi + \theta_1' \tag{4.58}$$

$$\theta_2 = 0.5\pi - \beta \tag{4.59}$$

$$\alpha = 1.5\pi - \theta_1 - \theta_2 = 1.5\pi - (\pi + \theta_1') - (0.5\pi - \beta) = \beta - \theta_1' \tag{4.60}$$

The last result agrees with that appearing in Figure 4.8.

4.5 Simple Harmonic and Non-Simple Harmonic Motions of Upper Leg (Rod3)

In this chapter, two types of driving forces are investigated: (i) The first type of driving forces are transmitted by the "simple harmonic" (SH) motions of the rider's right (or left) upper leg, this leads to non-constant rotating (angular) speed of the crank (Rod1) and "non-simple harmonic" (NSH) external loads; (ii) The second type of driving forces are transmitted by the "non-simple harmonic" (NSH) motions of the rider's right (or left) upper leg leading to constant rotating (angular) speed of the crank so that external loads are near "simple harmonic" (SH).

(i) Simple Harmonic (SH) Motions of Upper Leg (Rod3)

The angle $\theta_{3,U}$ associated with the uppermost position of a rider's right (or left) upper leg (Rod3) has been determined by Equations (4.6) and (4.6)', and the angle $\theta_{3,L}$ associated with the lowermost position of the same upper leg has been determined by Equations (4.15) and (4.15)'. Thus, if the motion of a rider's upper leg is "simple harmonic" (SH) with circular frequency ω_e rad/sec, the angle between his "right" upper leg (Rod3) and x-axis (in horizontal direction) at any instant of time t during the downward half cycle is given by

$$\theta_3(t) = \theta_{3,U} + \overline{\theta}_3 \sin(0.5\omega_e t) \tag{4.61}$$

Where $\overline{\theta}_3$ is the amplitude of Rod3 given by

$$\overline{\theta}_3 = \theta_{3,L} - \theta_{3,U} \tag{4.62}$$

It is noted that the instantaneous position of the rider's "left" upper leg during the other half cycle is also determined by Equation (4.61). Once the instantaneous position of Rod3, $\theta_3(t)$, is obtained from Equation (4.61), the corresponding angles of Rod1 and Rod2 can be determined by using the associated equations presented in Section 4.3, and the angle $\alpha(t)$ between Rod1 and Rod2 is determined by Equation (4.9), $\alpha(t)=1.5\pi-\theta_1(t)-\theta_2(t)$. Finally, the external torque $T(t)$ developed by the crank (Rod1) is given by Equation (4.64) in the next section.

(ii) Non-Simple Harmonic (NSH) Motions of Upper Leg (Rod3)

If non-simple harmonic (NSH) motions of the rider's right (or left) upper leg lead to constant rotating (angular) speed of the crank (Rod1), then the angle between Rod1 and positive *y*-axis (in upward direction) at any instant of time *t* during the downward half cycle of the rider's right (or left) upper leg is given by

$$\theta_1(t) = \theta_{1,U} + \omega_e t \tag{4.63}$$

where $\theta_{1,U}$ is the angle between crank (Rod1) and positive *y*-axis when the upper leg (Rod3) is in its uppermost position, as one may see from Figure 4.2 and Equation (4.7). Once the instantaneous position of Rod1, $\theta_1(t)$, is obtained from Equation (4.63), the corresponding angles of Rod2 and Rod3 can be determined by using the associated equations presented in Section 4.4, and the angle $\alpha(t)$ between Rod1 and Rod2 is determined by Equation (4.9). Finally, the external torque $T(t)$ developed by the crank (Rod1) is given by Equation (4.64) in the next section.

4.6 Effective Work Done by the Rider

If the driving force transmitted from the rider's right (or left) lower leg (Rod2) is represented by $F_2(t)$, then the external torque developed by the crank (Rod1) with radius R_c=L_1 is given by (refer to Figure 4.6)

$$T(t) = L_1 F_t(t) = L_1 F_2(t) \cdot \sin\alpha(t) \tag{4.64}$$

Where $F_t(t) = F_2(t) \cdot \sin\alpha(t)$ represents the tangential component of $F_2(t)$ normal to the crank. In such a case, $T(t)$ is a function of $\alpha(t)$ and the latter is a function of instantaneous positions of Rod1 and Rod2 defined by the angles, $\theta_1(t)$ and $\theta_2(t)$, as one may see from Equation (4.9).

The time history for the tangential pedalling forces $F_t(\theta_1) = F_2(t) \cdot \sin\alpha(t)$ (normal to crank) takes the form as shown in Figure 4.9(a) and that for the external torques given by Equation (4.64) takes the form as shown in Figure 4.9(b). Since the ordinate of Figure 4.9(b) represents the torques $T(\theta_1)$ associated with the abscissa for the rotational angles of crank (Rod1), θ_1, the effective work W done by a rider during the down-stroke of each pedalling cycle is given by

$$W = \int_{\theta_{1,U}}^{\theta_{1,L}} T(\theta_1) \cdot d\theta_1 \tag{4.65}$$

From Figure 4.9(a) of this paper and Figure 4.9(c) of Reference [45], one sees that the "profile" of normal pedalling forces $F_t(\theta_1)$ (tangential to the circular path of crank pin) in the down-stroke (with crank angles $\theta_1 = \theta_{1,U} = 27.366^o$ to $\theta_1 = \theta_{1,L} = 199.808^o$) for each pedalling cycle of this thesis (obtained from engineering mechanics and computer simulations) takes the same form as that of the mean normal pedalling forces (subtracting 125N for the retarding force of the other leg due to muscular function) of Reference [45] (obtained from biomechanics and experiments). This result reveals that the mathematical model and the theory presented in this thesis should be significant. Note that, although the "profile" of Figure 4.9(b) is the same as that of Figure 4.9(a), the ratio between their ordinates is given by $T(\theta_1)/F_t(\theta_1) = 0.17 = L_1$ = constant. (Please see Section 5.6 and Figure 5.42

for the details.)

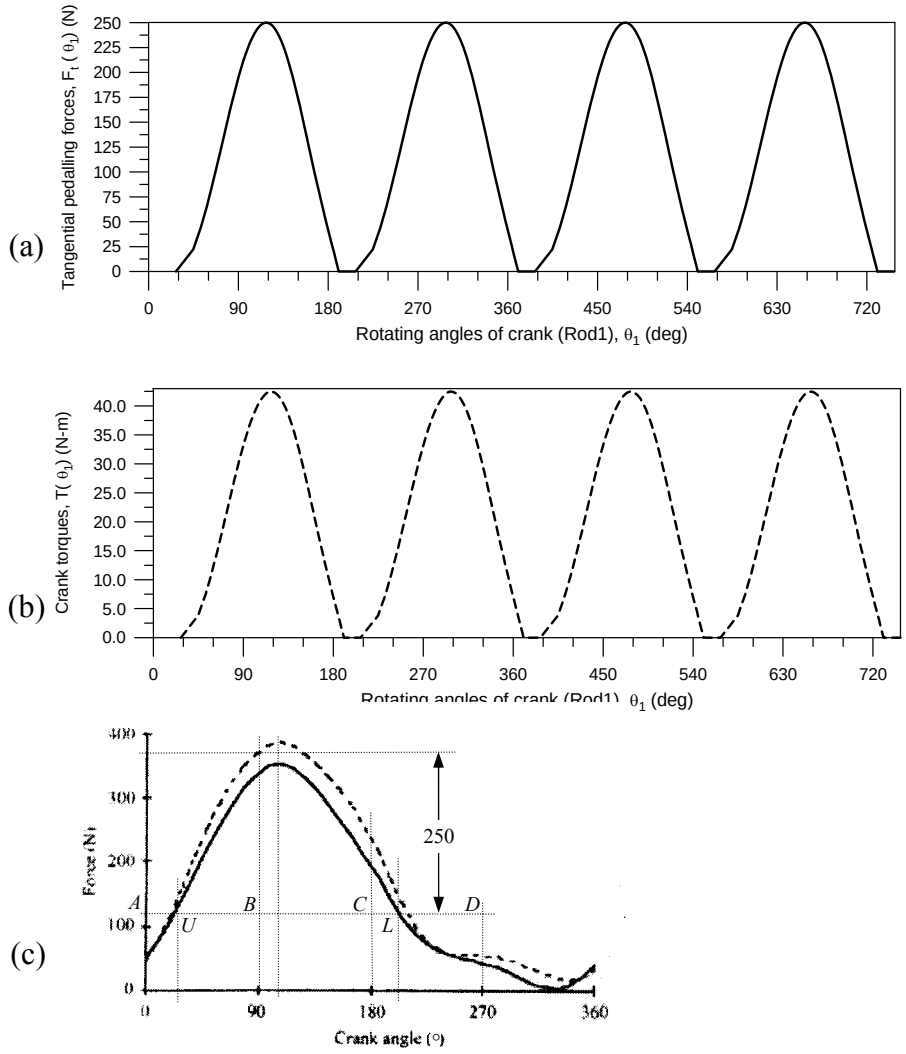

Figure 4.9 Time histories of (a) normal pedalling forces $F_t(\theta_1)$ (tangential to the circular path of crank pin) and (b) crank torques $T(\theta_1)$ due to alternative pedalling of a rider's two legs with constant force $F_2 = 250\,\text{N}$ and cyclic frequency (cadence) $f_e = 1$ Hertz, and (c) normal pedalling forces $F_t(\theta_1)$ based on Reference [45].

It is noted that, in Equation (4.65), the work W represents the "area" under each curve of "T vs. θ_1" and the horizontal axis. Since, in SI units, the unit of torque is "N-m" and the unit of θ is "radian", thus, the unit for Equation (4.65) is "N-m" (unit of work), because "radian" is a dimensionless unit.

From Sections 4.1-4.5, one sees that the angle between crank (Rod1) and a rider's lower leg (Rod2), $\alpha(t)$, is a function of some parameters from the discussions of the rider (L_2 and L_3) and those from the discussions of the bike itself (R_c, x_c and y_c). Therefore, for the "same bike" (with R_c, x_c and y_c keeping constant) the time history of external torque $T(t)$ given by Equation (4.64) along with the associated effective work W given by Equation (4.65) due to "different rider" (with L_2 and L_3 being variable) will be different. Of course, for the "same rider" (with L_2 and L_3 keeping constant), the external torque $T(t)$ and the associated effective work W will be also different when he rides "different bikes" (with R_c, x_c and y_c being variable). Therefore, Equations (4.64) and (4.65) provide a practical theory for evaluating the appropriateness of match between a rider and his bike.

In practice, it is very difficult to calculate the effective work W from Equation (4.65) by using an analytical method. In such a case, the numerical approach, such as trapezoidal rule or Simpson rule, is popularly used [71,72].

4.6.1 Calculation of Effective Work Using Trapezoid Rule

When the driving forces are transmitted through SH motions of the rider's upper leg (Rod3), the angular speed of crank (Rod1), ω_1, is not a constant, so is the angle corresponding to each time interval, $\Delta\theta=\omega_1\Delta t$, even if Δt=constant. For the case of $\Delta\theta \neq$ constant, the area under a curve (such as that shown in Figure 4.9(b)) can be obtained from the trapezoid rule, using step-by-step calculations. From Figure 4.10, one sees that the area of the trapezoid $C_iD_iE_iF_i$ is given by $A_i=\frac{1}{2}\Delta x_i(y_{i-1}+y_i)$, thus, the total area under the curve can be evaluated by

$$\text{Area}=\sum_{i=1}^{n}A_i=\sum_{i=1}^{n}\tfrac{1}{2}(x_i-x_{i-1})(y_{i-1}+y_i)=\sum_{i=1}^{n}\tfrac{1}{2}\Delta x_i(y_{i-1}+y_i)\quad(i=1\sim n)\qquad(4.66)$$

where

$$\mathrm{A_i}=\tfrac{1}{2}(x_i-x_{i-1})(y_{i-1}+y_i)=\tfrac{1}{2}\Delta x_i(y_{i-1}+y_i)\qquad(4.67)$$

$$\Delta x_i=x_i-x_{i-1}\qquad(4.68)$$

From the above formulation one sees that, in the trapezoidal rule, the curve segment between the two points, D_i and E_i, as shown in Figure 4.10 is replaced by a straight line $\overline{D_iE_i}$.

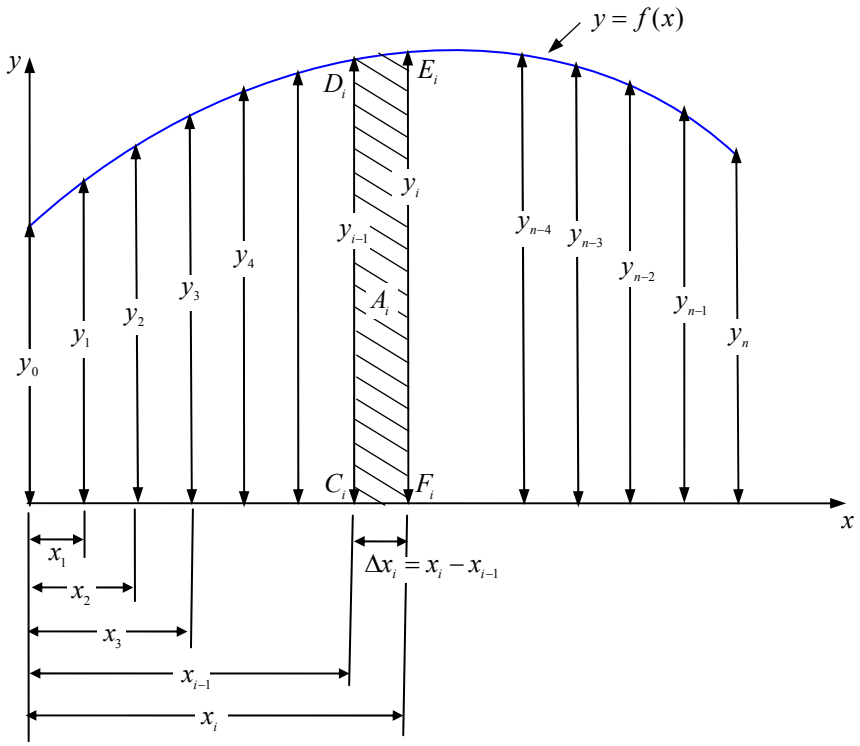

Figure 4.10 For the trapezoid rule, the area under the curve $y=f(x)$ is subdivided into n small area by the ordinates y_i, $i = 0,1,2,...,n$, with arbitrary spacing Δx_i and arbitrary number n.

4.6.2 Calculation of Effective Work Using Simpson Rule

If the driving forces are transmitted through NSH motions of the rider's upper leg (Rod3) leading to constant rotating (angular) speed of the crank (Rod1), ω_1, then the angle corresponding to each time interval, $\Delta\theta=\omega_1\Delta t$, is constant. In such a case, one of the simplest ways for calculating the area under a curve is the Simpson rule. According to the theory shown in Appendix B at the end of this thesis, if the area under the curve $y=f(x)$ and the horizontal axis as shown in Figure 4.11 is subdivided into n small areas by the ordinates $y_i,\ i=0,1,2,...,n$, with identical spacing Δx and even number n, then the total area under the curve is given by

$$\begin{aligned} Area &= \frac{\Delta x}{3}[y_0+4y_1+2y_2+4y_3+...2,4,2,4,2...+4y_{n-3}+2y_{n-2}+4y_{n-1}+y_n] \\ &= \frac{\Delta x}{3}[(y_0+y_n)+4(y_1+y_3+y_5+...+y_{n-1})+2(y_2+y_4+y_6+...+y_{n-2})] \end{aligned} \tag{4.69}$$

From Figure B.1 (in Appendix B) one sees that, in the Simpson rule, the "3-point" curve segment passing through the three points, $i-1$, i and $i+1$, is represented by a "quadratic" equation.

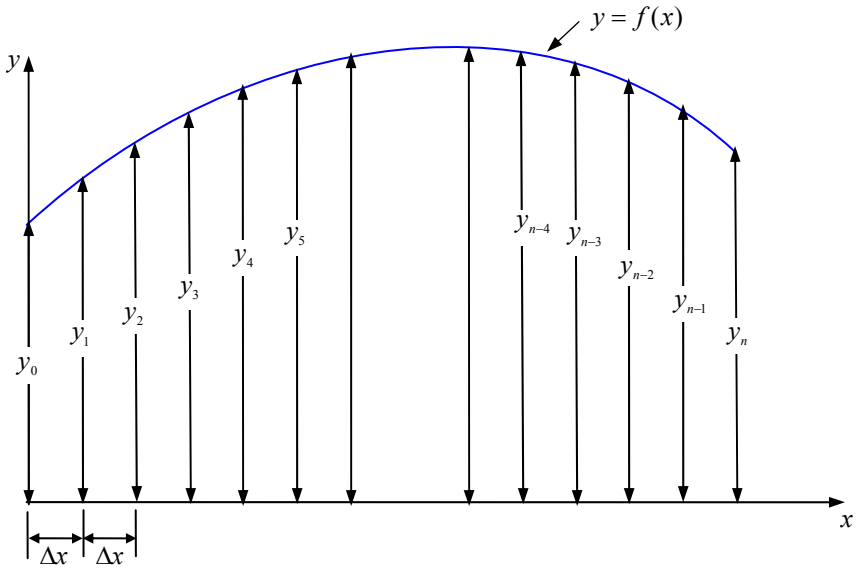

Figure 4.11 For the Simpson rule, the area under the curve $y=f(x)$ is subdivided into n small areas by the ordinates $y_i,\ i=0,1,2,...,n$, with identical spacing Δx and even number n.

4.7 Limitations of Lengths of a Rider's Legs for this Study

It is a fundamental requirement that the length of a rider's upper leg (Rod3) plus that of his lower leg (Rod2) must be long enough so that his heel can touch the bike's pedal. This limiting configuration is shown in Figure 4.12 by the dashed lines. In which, $\overline{SH}$, $\overline{HK}$ and $\overline{OK}$ denote the upper leg (Rod3), lower leg (Rod2) and crank (Rod1), respectively, and it is noted that they are on a straight line with Joint 2 and Joint 1 located at points *H* and *K*, respectively.

From the point of view of natural and comfortable posture so that a rider does not feel tired after long-time riding, it is required that each upper leg (Rod3) should be lower than the horizontal line passing through seat centre as shown by the solid line in Figure 4.12. In which, $\overline{SH'}$, $\overline{H'K'}$ and $\overline{OK'}$ denote the upper leg (Rod3), lower leg (Rod2) and crank (Rod1), respectively, and it is noted that lower leg (Rod2) and crank (Rod1) are on a straight line with Joint 2 and Joint 1 located at points H' and K', respectively.

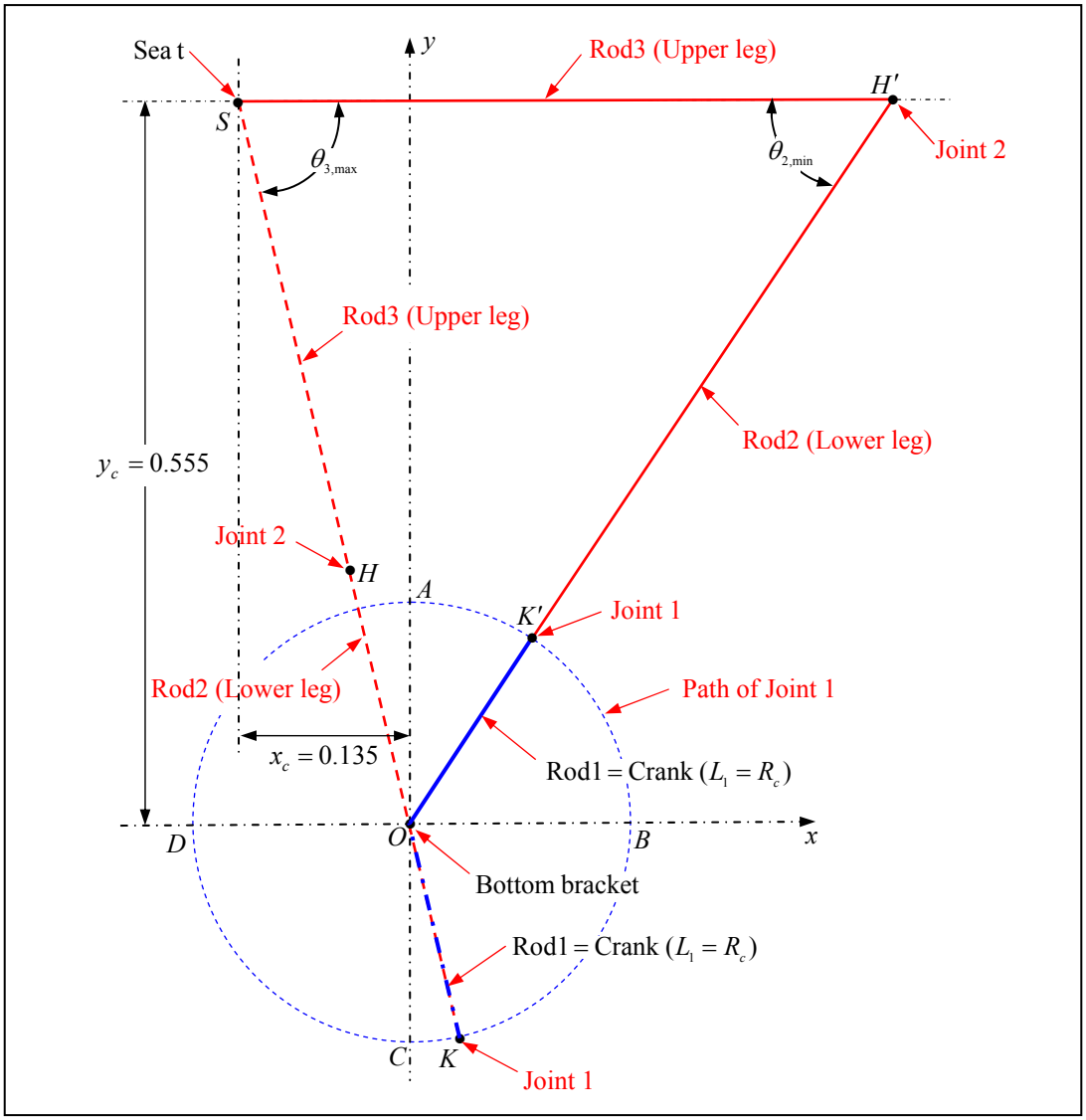

Figure 4.12 Limitations for lengths of a rider's legs: the shortest leg lengths are that the heel of each lower leg (Rod2) can touch the bike's pedal as shown by the dashed lines, while the longest leg lengths are that each upper leg (Rod1) should be lower than the horizontal line passing through seat centre as shown by the solid lines

(i) ***Determination of Shortest Leg Lengths***

Based on the dashed lines shown in Figure 4.12, one obtains

$$\tan\theta_{3,\max} = y_c / x_c \tag{4.70a}$$

$$(L_2 + L_3)\cos\theta_{3,\max} - L_1\cos\theta_{3,\max} = x_c \tag{4.70b}$$

In general, it is assumed that the length of upper leg is equal to that of lower leg, i.e.,

$$L_3 = L_2 = \overline{L} \tag{4.71a,b}$$

From Equations (4.70) and (4.71) one has

$$L_{3,\min} = L_{2,\min} = \overline{L}_{\min} = (x_c + L_1\cos\theta_{3,\max})/(2\cos\theta_{3,\max}) \tag{4.72a,b}$$

(ii) ***Determination of Longest Leg Length***

Based on the solid lines shown in Figure 4.12, one obtains

$$L_3 - (L_1 + L_2)\cos\theta_{2,\min} = x_c \tag{4.73}$$

$$(L_1 + L_2)\sin\theta_{2,\min} = y_c \tag{4.74}$$

From the above two equations one obtains

$$y_c^2 + (L_3 - x_c)^2 = (L_1 + L_2)^2 \tag{4.75}$$

If $L_3 = L_2 = \overline{L}$ as shown by Equation (4.71a,b), then the last equation reduces to

$$y_c^2 + \overline{L}^2 - 2x_c\overline{L} + x_c^2 = L_1^2 + 2L_1\overline{L} + \overline{L}^2 \rightarrow x_c^2 + y_c^2 - L_1^2 = 2(L_1 + x_c)\overline{L} \rightarrow$$

$$L_{1,\max} = L_{2,\max} = \overline{L}_{\max} = (x_c^2 + y_c^2 - L_1^2)/[2(L_1 + x_c)] \tag{4.76}$$

4.8 Numerical Results and Discussions

The configurations shown in Figures 4.1-4.8 are obtained based on the leg lengths of a *reference* rider, L_2=L_3=0.40m, and the relevant dimensions of a *reference* bike, R_c=L_1=0.17m, x_c=0.135m and y_c=0.555m. Where L_2 and L_3 are lengths of the rider's lower leg and upper leg, respectively, R_c=L_1 is the radius of bike crank, while x_c and y_c are the horizontal and vertical distances between seat and bottom bracket of the bike, respectively. In this section, the influence of different leg lengths of riders riding the same reference bike is studied first, and then the influence of different dimensions of bikes ridden by the same reference rider is investigated.

4.8.1 The Influence of Different Leg Lengths of Riders Riding Reference Bike

Based on relevant dimensions of the *reference* bike (R_c=L_1=0.17m, x_c=0.135m and y_c=0.555m) and limitations of the rider's leg lengths given by Equations (4.72) and (4.76), one obtains the minimum leg length is $L_{2,\min} = L_{3,\min} = \overline{L}_{\min} = 0.371\,\text{m}$ and the maximum one is $L_{2,\max} = L_{3,\max} = \overline{L}_{\max} = 0.487\,\text{m}$. For the last reason, the leg lengths of three different riders are assumed to be L_2=L_3=0.375m, 0.4m and 0.48m, respectively.

(i) ***The Influence on Critical Angles of Rod1, Rod2 and Rod3***

In order to determine the positions of Rod1, Rod2 and Rod3 at any instant of time t, one requires the critical positions of the last three members as one may see from Sections 4.3 and 4.4. Thus, the critical positions of Rod1, Rod2 and Rod3 for the three riders riding the reference bike are determined first and shown in Table 4.1. Where the subscripts U and L of θ_i refer to the positions of Rod i (i =1,2,3), when the upper leg (Rod3) is in its uppermost and lowermost positions, respectively, while the subscripts B and C of θ_i refer to those when the crank (Rod1) is in the rightward and downward positions with Joint 1 located at points B (with θ_1=$\theta_{1,B}$=90°) and C (with θ_1=$\theta_{1,C}$=180°), respectively. From Table 4.1 one sees that the critical angles of Rod1

corresponding to the uppermost and lowermost positions of upper leg (Rod3), $\theta_{1,U}$ and $\theta_{1,L}$, increase with the increase of leg lengths (L_2=L_3) and the trend of associated critical angles of Rod2 and Rod3, ($\theta_{2,U}$, $\theta_{2,L}$) and ($\theta_{3,U}$, $\theta_{3,L}$), is reversed. Furthermore, the critical angles of Rod2 and Rod3 corresponding to θ_1=$\theta_{1,B}$=90° andθ_1=$\theta_{1,C}$=180°, ($\theta_{2,B}$, $\theta_{2,C}$) and ($\theta_{3,B}$, $\theta_{3,C}$), decrease with the increase of leg lengths (L_2=L_3). The last results agree with those observed from Figures 4.2-4.5.

Table 4.1 Influence of rider's leg lengths (L_2=L_3) on the critical angles of Rod1, Rod2 and Rod3 for the *reference* bike (with L_1=0.17m, x_c=0.135m and y_c=0.555m)

Leg lengths L_2=L_3 (m)	Members Rod i	*Critical angles, $\theta_{i,X}$ (degrees)				Limitations of leg lengths $\overline{L}_{\min}$, $\overline{L}_{\max}$ (m)
		$\theta_{i,U}$	$\theta_{i,B}$	$\theta_{i,C}$	$\theta_{i,L}$	
0.375	Rod1	25.50281	90.00000	180.00000	180.10390	$\overline{L}_{\min}=0.371$
	Rod2	64.49719	86.39656	89.94327	89.89610	$\overline{L}_{\max}=0.487$
	Rod3	9.68744	28.81461	68.96061	68.96068	
0.40	Rod1	27.36598	90.00000	180.00000	199.80839	
	Rod2	62.63402	81.12686	77.74277	70.19161	
	Rod3	7.00603	23.54491	56.64664	57.83539	
0.48	Rod1	32.05562	90.00000	180.00000	223.50694	
	Rod2	57.94438	70.06584	60.73965	46.49306	
	Rod3	0.48981	12.48389	39.64352	43.45881	

* X = U, B, C or L.

(ii) ***The Influence on Effective Works Done by the Riders***

Because the effective work W done by a rider is dependent on the time history curves of external torques $T(\theta_1)$ developed by the bike crank (see Figures 4.13-4.15), and these curves are dependent on the types of motions of the rider's upper leg (Rod3), the influence of "simple harmonic" (SH) and "non-simple harmonic" (NSH) motions of upper leg is also studied in addition to the rider's leg lengths, in this subsection. Furthermore, the effective work W given by Equation (4.65) is determined by the numerical integration, and the latter is usually performed by using the Simpson rule and trapezoid rule, both of the two numerical integration methods are used in this subsection for inter checking. However, for the type of SH motions of upper leg (Rod3), the integration spacing $\Delta\theta_1$ is varied from $\Delta\theta_{1,\min}$=0.003° to $\Delta\theta_{1,\max}$=5.502° for the current example, this is "not available" for the Simpson rule so that the associated numerical results are removed from Table 4.2 to avoid misunderstanding, in this subsection. For the present example, the exciting frequency is ω_e=1Hertz=2π rad/sec with period $t_e=2\pi/\omega_e$=1sec, thus, if the time interval is Δt= 0.001sec, then the total time intervals in each "half cycle" is given by $n=0.5(t_e/\Delta t)$=500. It is noted that the work done by a rider's "right" leg in a "half cycle" is equal to that by his "left" leg in the other "half cycle".

According to the last statements, the effective works done by the three riders (with leg lengths $L_2=L_3$=0.375m, 0.4m and 0.48m, respectively) are shown in Table 4.2. For the type of NSH motions of the rider's upper leg (Rod3), the rotating speed of the crank (Rod1) is a constant and so is the integration spacing $\Delta\theta_1=\pi/n_e$=180°/500=0.36°. In such situation, either Simpson rule or trapezoid rule is available for the numerical integration of Equation (4.65), this is the reason why the values of effective work W obtained from trapezoid rule shown in the 6th row of Table 4.2 are very close to the corresponding ones obtained from Simpson rule shown in the adjacent (5th) row of Table 4.2. However, the last statement is not true for the type of SH motions of the rider's upper leg (Rod3), because the rotating speed of the crank (Rod1) is "not" a constant and so is not the integration spacing $\Delta\theta_1$. In such situation, only the trapezoid rule is available for the numerical integration of Equation (4.65), this is the reason

why the values of effective work W obtained from Simpson rule are removed from the 3rd row of Table 4.2 (to avoid misunderstanding) and only those obtained from trapezoid rule are shown in the 4th row of Table 4.2. Since the values of W obtained from trapezoid rule listed in 4th row of Table 4.2 associated with SH motions of the rider's upper leg (Rod3) are very close to the corresponding ones listed the final row of the table associated with NSH motions of the rider's upper leg (Rod3), the influence of types of motions (simple or non-simple harmonic) of the rider's upper leg on the effective work W is negligible.

It is noted that both trapezoidal rule and Simpson rule are the "approximate" methods, and their formulations are different as one may see from Subsections 4.6.1, 4.6.2 and Appendix B, in general, the effective works obtained from the two methods cannot be equal to each other "exactly". However, the difference between them will become smaller if the integration spacing $\Delta\theta_1$ is reduced from 3.6° (with $\Delta t = 0.01$sec) to 0.36° (with $\Delta t = 0.001$sec) as one may see from the final six rows of Table 4.2. For better accuracy, all numerical results concerned are based on $\Delta t = 0.001$sec (with $\Delta\theta_1 = 0.36°$) unless particularly stated.

Table 4.2 Effective works W (N-m) in a "half pedalling cycle" done by three riders with leg lengths, L_2=L_3=0.375m, 0.4m and 0.48m, respectively, and riding the same reference bike (L_1=0.17m, x_c=0.135m, y_c=0.555m) with pedalling force F_2=10N and frequency ω_e=1Hertz=2π rad/sec.

Motions of upper leg (Rod3)	Integration methods	Lengths of rider's leg, L_2=L_3			Spacing $\Delta\theta_1$ (deg)
		0.375m	0.40m	0.48m	
Simple harmonic (SH)	Simpson rule	—	—	—	Not available*
	Trapezoid rule	2.9284 N-m	3.1045 N-m	3.5090 N-m	Varied*
Non-simple harmonic (NSH)	Simpson rule	3.0388 N-m	3.0962 N-m	3.4729 N-m	3.6
	Trapezoid rule	3.0379 N-m	3.0952 N-m	3.4920 N-m	
	Simpson rule	3.0373 N-m	3.0962N-m	3.4932N-m	1.8
	Trapezoid rule	3.0371 N-m	3.0959N-m	3.5014N-m	
	Simpson rule	3.0370 N-m	3.0961N-m	3.5063N-m	0.36
	Trapezoid rule	3.0370 N-m	3.0961N-m	3.5077N-m	

* For simple harmonic motions of upper leg (Rod3), $\Delta\theta_1$ is varied from $\Delta\theta_{1,min}$=0.003° to $\Delta\theta_{1,max}$=5.502°, thus, it is "not available" for Simpson rule.

(iii) ***The Influence on Time Histories of External Torques***

The influence of rider's leg lengths on the time histories of external torques $T(\theta_1)$ due to "simple harmonic" motions of upper leg (Rod3) with "non-constant" rotating speed of Rod1 is shown in Figure 4.13, and that due to "non-simple harmonic" motions of upper leg (Rod3) with "constant" rotating speed of Rod1 is shown in Figure 4.14. Where the solid lines (——) are obtained based on the rider's leg lengths L_2=L_3=0.375m, dashed lines (——) are based on L_2=L_3=0.40m and the dashed-dotted lines (— · —) are based on L_2=L_3=0.48m. For the type of "non-simple harmonic" motion of upper leg leading to "constant" rotating speed of crank (Rod1), the time-history curve in each half cycle looks like the sine wave as one may see from Figure 4.14. However, this is not true for the curves shown in Figure 4.13, in which, each curve deviates from the sine wave to some degree, particularly for the case of rider's leg lengths L_2=L_3=0.375m near the minimum values $L_{2,\min} = L_{3,\min} = \overline{L}_{\min} = 0.371\,\text{m}$. From Figures 4.13 and 4.14 one also sees that the longer the rider's leg the larger the critical angle of Rod1 ($\theta_{1,U}$) and the larger the "area under each corresponding curve" (i.e., the effective work W). These results agree with those shown in Tables 4.1 and 4.2.

For comparisons, the time history curves for the types of SH and NSH motions of the rider's upper leg with L_2=L_3=0.375m, L_2=L_3=0.40m and L_2=L_3=0.48m are shown in Figures 4.15(a), (b) and (c), respectively, where the solid lines (——) are for the type of SH motions of upper leg and the dashed lines (– – – –) for the type of NSH motions of upper leg. Although the area under the solid curve in each half cycle is very close to that under the dashed one as one may see from the effective works W shown in Table 4.2, the dashed one should be better because the associated motions are more smooth. Furthermore, for the present example, the radius of crank is R_c=L_1= 0.17m and the external force transmitted from lower leg (Rod2) is F_2= 10N, thus, from Equation (4.64) one obtains the external torques to be $T(t) = L_1 F_2 \cdot \sin\alpha(t) = 1.7 \cdot \sin\alpha(t)$. This is the reason why the "amplitude" for each time-history curve of external torques is very close to 1.7 N-m as one may see from Figures 4.13-4.15.

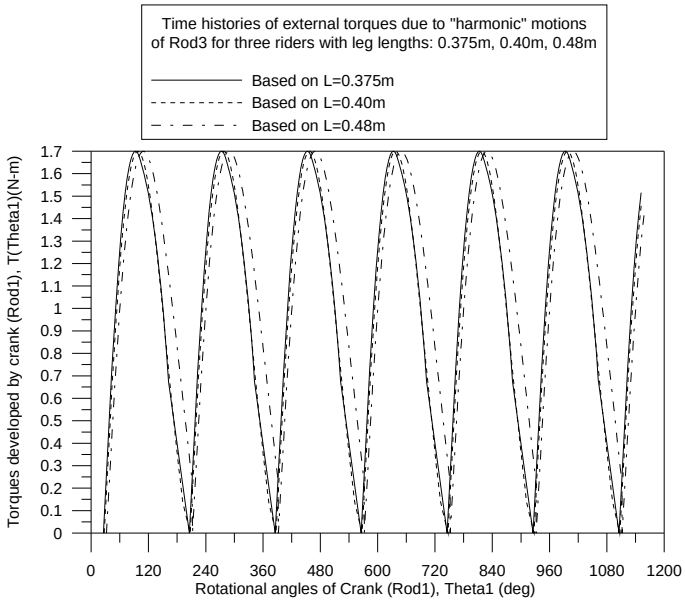

Figure 4.13 The influence of rider's leg lengths on the time histories of external torques $T(\theta 1)$ based on "simple harmonic" motions of the rider's upper leg (Rod3) with "non-constant" rotating speed of Rod1: (a) $L2$=$L3$=0.375m (denoted by solid lines ———), (b) $L2$=$L3$=0.40m (denoted by dashed lines ——), (c) $L2$=$L3$=0.48m (denoted by dashed-dotted lines — · —).

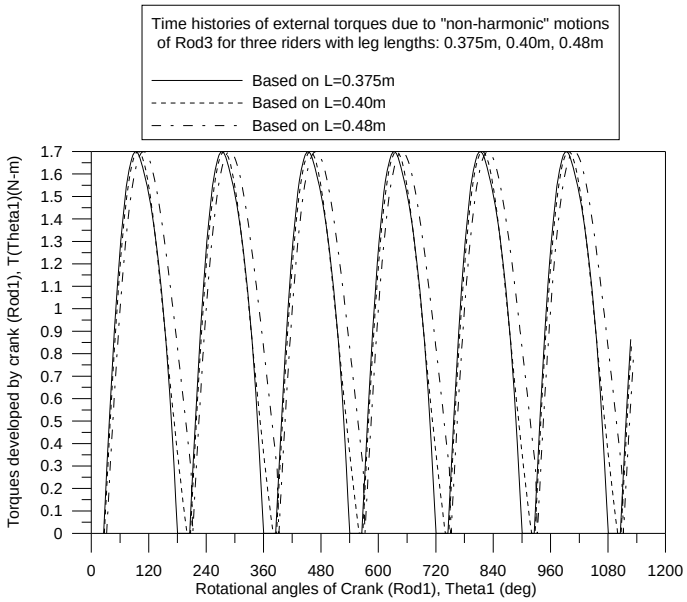

Figure 4.14 The influence of rider's leg lengths on the time histories of external torques $T(\theta 1)$ based on "non-simple harmonic" motions of the rider's upper leg (Rod3) with "constant" rotating speed of Rod1: (a) $L2$=$L3$=0.375m (denoted by solid lines ———), (b) $L2$=$L3$=0.40m (denoted by dashed lines ——), (c) $L2$=$L3$=0.48m (denoted by dashed-dotted lines — · —).

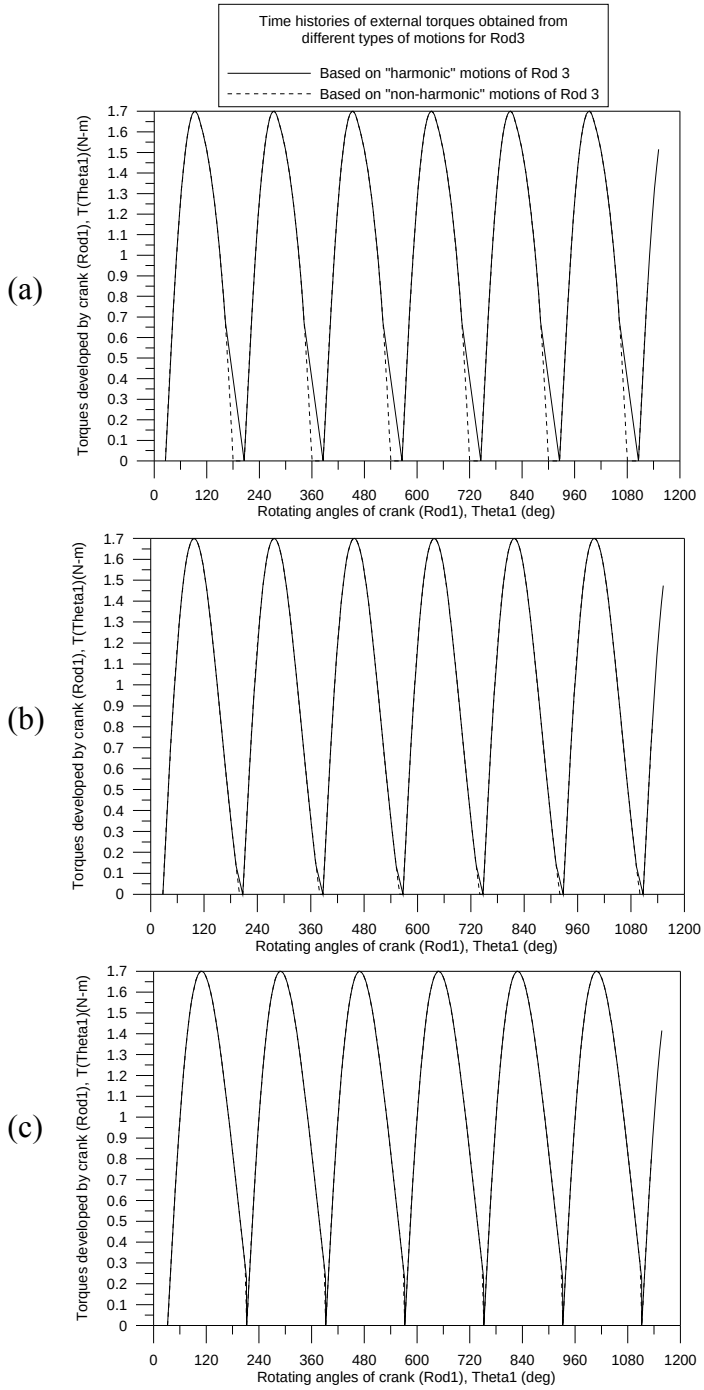

Figure 4.15 Comparisons between time histories of external torques $T(\theta 1)$ due to "simple harmonic" motions (denoted by solid lines ——) and "non-simple harmonic" motions (denoted by dashed lines – – –) of the rider's upper leg (Rod3) with: (a) $L2$=$L3$=0.375m, (b) $L2$=$L3$=0.40m, (c) $L2$=$L3$=0.48m.

4.8.2 Influence of Different Dimensions of Bikes Ridden by Reference Rider

The purpose of this subsection is to investigate the influence of different seat-to-bottom bracket distances of the bike. In addition to the reference bike (with R_c=L_1=0.17m, x_c=0.135m and y_c=0.555m), two more bikes are considered. One of them has "shorter" centre distance with x_c=0.115m and y_c=0.535m, and the other has "longer" centre distance with x_c=0.155m and y_c=0.575m. Comparing with the reference bike, the differences between horizontal and vertical centre distances for the two new bikes are $\Delta x_c = \Delta y_c$ =0.02m.

The influence on the critical angles ($\theta_{i,U}$, $\theta_{i,B}$, $\theta_{i,C}$ and $\theta_{i,L}$ with i=1,2,3) is shown in Table 4.3 and that on the effective works W is shown in Table 4.4. Since the minimum rider's leg lengths $L_{2\min} = L_{3\min} = \overline{L}_{\min}$ given by Equation (4.72) and the maximum ones $L_{2\max} = L_{3\max} = \overline{L}_{\max}$ given by Equation (4.76) are functions of seat-to-bottom bracket distances, x_c and y_c, the values of $\overline{L}_{\min}$ and $\overline{L}_{\max}$ are different for the three bikes as one may see from the final column of Table 4.3. It is noted that the leg lengths of the reference rider, L_2=L_3=0.40m, do not exceed the limitations for each bike.

From rows 3-8 of Table 4.3 one sees that reducing the seat-to-bottom bracket distances will increase the value of $\theta_{1,U}$ and decrease those of $\theta_{2,U}$ and $\theta_{3,U}$. Since reducing the seat-to-bottom bracket distances and keeping the rider's leg lengths unchanged as shown in Table 4.3 is equivalent to increasing the rider's leg lengths and keeping the seat-to-bottom bracket distances unchanged as shown in Table 4.1, thus, the last conclusion agrees with that obtained from Table 4.1. On the other hand, from rows 6-11 of Table 4.3 one sees that increasing the seat-to-bottom bracket distances will decrease the value of $\theta_{1,U}$ and increase those of $\theta_{2,U}$ and $\theta_{3,U}$. This trend is the same as the case of decreasing the rider's leg lengths and keeping the seat-to-bottom bracket distances unchanged as shown in Table 4.1. For the same reason, decreasing the seat-to-bottom bracket distances (x_c and y_c) can increase the values of effective works W and increasing the seat-to-bottom bracket distances (x_c and y_c) has the reverse effect as one may see from Table 4.4. This result agrees with that obtained

from Table 4.2.

The influence on the time-history curves of external torques $T(\theta_1)$ of different seat-to-bottom bracket distances for the three bikes ridden by the same reference rider is shown in Figures 4.16-4.18. Those shown in Figure 4.16 are based on the type of "simple harmonic" motions of the rider's upper leg (Rod3) with "non-constant" rotating speed of Rod1, where the solid line (———) is for the case of x_c=0.115m and y_c=0.535m, the dashed line (——) is for x_c=0.135m and y_c=0.555m and the dashed-dotted line (— · —) is for x_c=0.155m and y_c=0.575m. All legends for Figure 4.17 are the same as those for Figure 4.16, the only difference is that the time-history curves of external torques $T(\theta_1)$ are based on "non-simple harmonic" motions of the rider's upper leg (Rod3) with "constant" rotating speed of Rod1.

For comparisons, the time history curves associated with the types of SH and NSH motions for the seat-to-bottom bracket distance with (x_c=0.115m and y_c=0.535m), (x_c=0.135m and y_c=0.555m) and (x_c=0.155m and y_c=0.575m) are shown in Figures 4.18(a), (b) and (c), respectively, where the solid lines (———) are for the type of SH motions of upper leg and the dashed curves (– – – –) for the type of NSH motions of upper leg. The effective work W shown in Table 4.4 indicates that the area under each solid curve in each half cycle is very close to the corresponding one under the dashed one.

Table 4.3 Influence of seat-to-bottom bracket distances (x_c and y_c) on the critical angles of Rod1, Rod2 and Rod3 for three bikes (with R_c=L_1=0.17m) ridden by the reference rider with leg lengths L_2=L_3=0.40m.

Seat-to-bottom bracket distance x_c, y_c (m)	Members Rod i	*Critical angles, $\theta_{i,X}$ (degrees)				Limitations of leg lengths $\overline{L}_{\min}$, $\overline{L}_{\max}$ (m)
		$\theta_{i,U}$	$\theta_{i,B}$	$\theta_{i,C}$	$\theta_{i,L}$	
x_c=0.115 y_c=0.535	Rod1	29.76520	90.00000	180.00000	208.03825	$\overline{L}_{\min}=0.359$ $\overline{L}_{\max}=0.475$
	Rod2	60.23480	77.30836	72.50414	61.96175	
	Rod3	5.76821	21.21898	53.97509	56.09725	
x_c=0.135 y_c=0.555	Rod1	27.36598	90.00000	180.00000	199.80839	$\overline{L}_{\min}=0.371$ $\overline{L}_{\max}=0.487$
	Rod2	62.63402	81.12686	77.74277	70.19161	
	Rod3	7.00603	23.54491	56.64664	57.83539	
x_c=0.155 y_c=0.575	Rod1	24.98140	90.00000	180.00000	190.27022	$\overline{L}_{\min}=0.383$ $\overline{L}_{\max}=0.501$
	Rod2	65.01860	85.12682	83.77802	79.72978	
	Rod3	8.38453	26.17504	60.27215	60.65829	

* X = U, B, C or L.

Table 4.4 Effective works W (N-m) in a "half pedalling cycle" done by the reference rider with leg lengths L_2=L_3= 0.40m and riding three bikes with the same crank radius R_c=L_1= 0.17m and different seat-to-bottom bracket distances (x_c and y_c) with pedalling force F_2=10N and frequency ω_e=1Hertz=2π rad/sec.

Motions of upper leg (Rod3)	Integration methods	Seat-to-bottom bracket distances, x_c and y_c (m)			Spacing $\Delta\theta_1$ (deg)
		x_c=0.115 y_c=0.535	x_c=0.135 y_c=0.555	x_c=0.155 y_c=0.575	
Simple harmonic	Simpson rule	—	—	—	Not available*
	Trapezoid rule	3.2088N-m	3.1045 N-m	2.9525N-m	Varied*
Non-simple harmonic	Simpson rule	3.2093N-m	3.0961 N-m	2.9790N-m	0.36
	Trapezoid rule	3.2093N-m	3.0961 N-m	2.9790N-m	0.36

* For simple harmonic motions of upper leg (Rod3), $\Delta\theta_1$ is varied from $\Delta\theta_{1,\min}$=0.007° to $\Delta\theta_{1,\max}$=5.460°, thus, it is not available for Simpson rule.

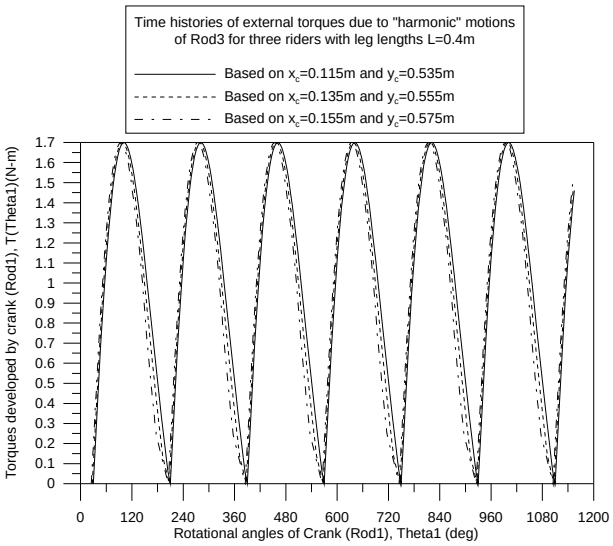

Figure 4.16 Influence of seat-to-bottom bracket distances (x_c and y_c) on the time histories of external torques $T(\theta 1)$ based on "simple harmonic" motions of the rider's upper leg (Rod3) with "non-constant" rotating speed of Rod1 for three bikes (with R_c=$L1$=0.17m) ridden by the reference rider with leg lengths $L2$=$L3$=0.40m for: (a) x_c=0.115m and y_c=0.535m (denoted by solid lines ————); (b) x_c=0.135m and y_c=0.555m (denoted by dashed lines ——); (c) x_c=0.155m and y_c=0.575m (denoted by dashed-dotted lines — · —).

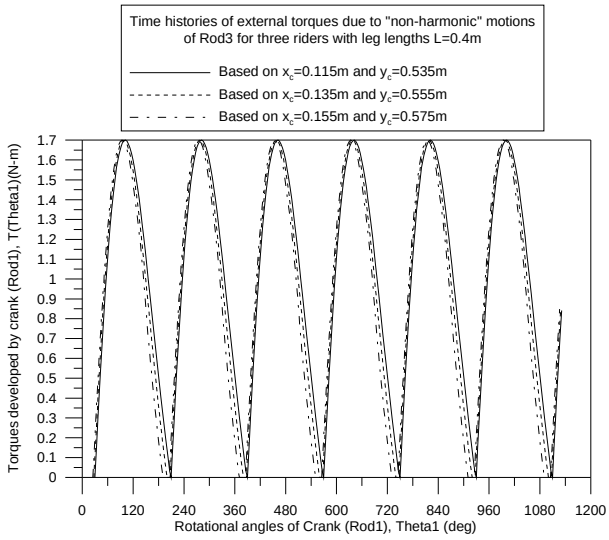

Figure 4.17 Influence of seat-to-bottom bracket distances (x_c and y) on the time histories of external torques $T(\theta 1)$ based on "non-simple harmonic" motions of the rider's upper leg (Rod3) with "constant" rotating speed of Rod1 for three bikes (with R_c=$L1$=0.17m) ridden by the reference rider with leg lengths $L2$=$L3$=0.40m for: (a) x_c=0.115m and y_c=0.535m (denoted by solid lines ————); (b) x_c=0.135m and y_c=0.555m (denoted by dashed lines ——); (c) x_c=0.155m and y_c=0.575m (denoted by dashed-dotted lines — · —).

(a)

(b)

(c)

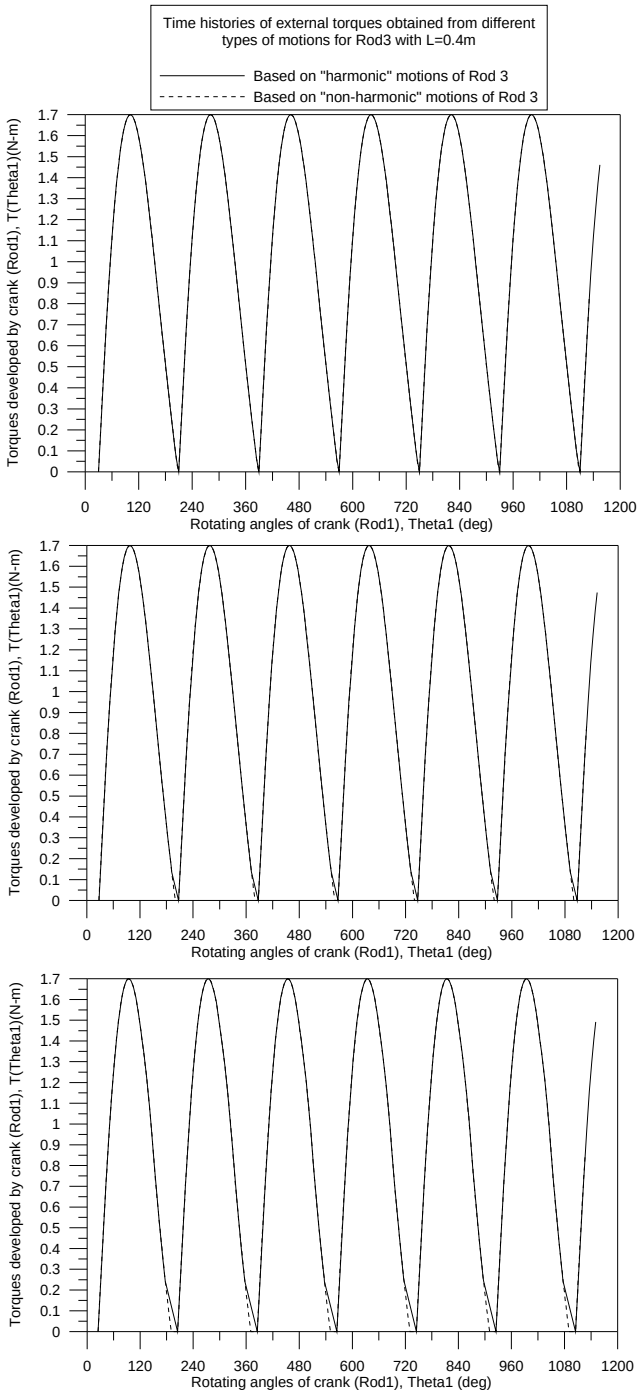

Figure 4.18 Comparisons between time histories of external torques $T(\theta 1)$ due to "simple harmonic" motions (denoted by solid lines ———) and "non-simple harmonic" motions (denoted by dashed lines — — —) of the rider's upper leg (Rod3) with R_c=$L1$=0.17m and leg lengths $L2$=$L3$=0.40m for: (a) x_c=0.115m and y_c=0.535m; (b) x_c=0.135m and y_c=0.555m; (c) x_c=0.155m and y_c=0.575m.

4.9 Pedalling Efficiency of a Long-Leg Rider Riding a High-Seat Bike

In the anthropometric studies, researchers have found that the leg length is approximately equal to half of the adult human height [73]. Therefore, in this section, for the tall rider with height 200cm, the length for each of his legs is approximated by 100cm (i.e., L_2=L_3=50cm=0.5m). In such a case, the seat-to-bottom bracket distance must be adjusted to accommodate the tall rider, thus, the horizontal and vertical distances between the seat and bottom bracket are assumed to be x_c=0.190m and y_c=0.605m, respectively.

The critical positions of Rod1, Rod2 and Rod3 for the tall rider riding the high-seat bike are determined first and shown in Table 4.5. Where the subscripts U and L of θ_i refer to the positions of Rod i (i =1,2,3), when the upper leg (Rod3) is in its uppermost and lowermost positions, respectively, while the subscripts B and C of θ_i refer to those when the crank (Rod1) is in the rightward and downward positions with Joint 1 located at points B (with θ_1=$\theta_{1,B}$=90°) and C (with θ_1=$\theta_{1,C}$=180°), respectively. The effective work W done by the tall rider is shown in Table 4.6 and the crank torque developed by him is shown in Figure 4.19. Comparing with Table 4.2, it is found that the effective work done by the current tall rider (W=3.4229N-m obtained from Simpson rule) is slightly smaller than that of the rider (with L_2=L_3=0.48m) shown in Table 4.2 (W=3.5063N-m obtained from Simpson rule) in spite of the fact that the leg lengths of the current rider (with L_2=L_3=0.50m) are slightly longer than those of the rider studied in Table 4.2. This is because the horizontal and vertical distances between the seat and bottom bracket for the current case (x_c=0.190m and y_c=0.605m) are greater than those for Table 4.2 (x_c=0.135m and y_c=0.555m). From the present example one sees that the pedalling efficiency of a rider is dependent on the parameters regarding both the rider and his bike and is a complicated problem. Thus, the technique presented in this chapter provides an efficient approach.

Table 4.5 The critical angles of Rod1, Rod2 and Rod3, and the limitations of leg lengths for the long-leg rider riding the high-seat bike (with L_1=0.17m, x_c=0.190m and y_c=0.605m)

Leg lengths L_2=L_3 (m)	Members Rod i	*Critical angles, $\theta_{i,X}$ (degrees)				Limitations of leg lengths $\overline{L}_{\min}$, $\overline{L}_{\max}$ (m)
		$\theta_{i,U}$	$\theta_{i,B}$	$\theta_{i,C}$	$\theta_{i,L}$	
0.50	Rod1	27.5490	90.00000	180.00000	213.98020	$\overline{L}_{\min} = 0.402$
	Rod2	62.4510	75.50372	66.70985	56.01980	$\overline{L}_{\max} = 0.518$
	Rod3	1.25689	13.99493	39.15981	41.50670	

* $X = U$, B, C or L.

Table 4.6 Effective work W (N-m) in a half pedalling cycle done by the tall rider with leg lengths L_2=L_3=0.50m and riding the high seat bike (L_1=0.17m, x_c=0.190m, y_c=0.605m) with pedalling force F_2=10N and frequency ω_e=1Hertz= 2π rad/sec.

Motions of upper leg (Rod3)	Integration methods	Works done by the rider, W	Spacing $\Delta\theta_1$ (deg)
Non-simple harmonic	Simpson rule	3.4229N-m	0.36
	Trapezoid rule	3.4237N-m	0.36

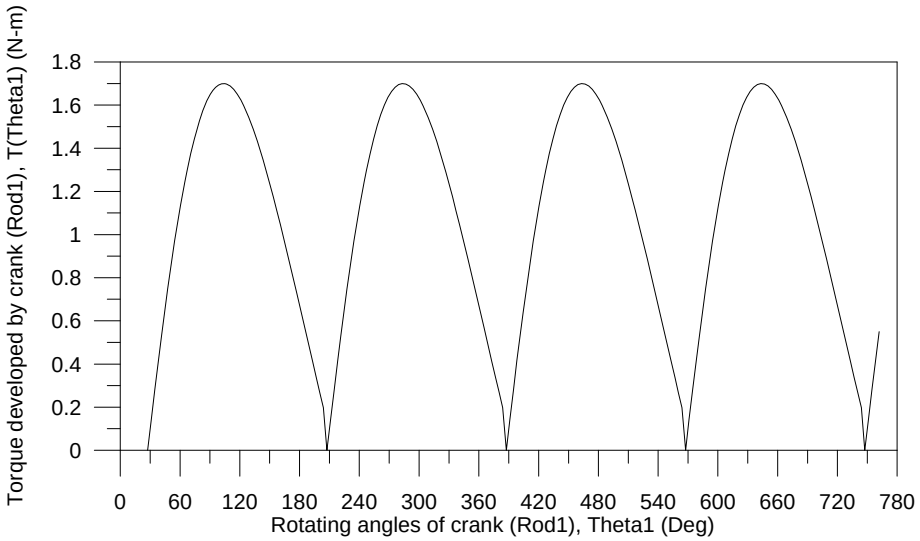

Figure 4.19 Crank torque developed by the tall rider (with leg lengths $L2$=$L3$=0.50m) riding the high-seat bike (with x_c=0.190m, y_c=0.605m).

4.10 Conclusion

1. For the mechanism composed of Rod1, Rod2 and Rod3, studied in this Chapter, one can obtain only two "independent" equations based on the next two requirements: (i) the summation of projections of Rod1, Rod2 and Rod3 on x-axis is equal to x_c and (ii) that on y-axis is equal to y_c. Where x_c and y_c denote the horizontal and vertical distances between seat centre and bottom bracket, respectively. Thus, if θ_1 denotes the angle between Rod1 and y-axis, θ_2 denotes that between Rod2 and x-axis, and θ_3 denotes that between Rod3 and x-axis, then one of the three unknowns, θ_1, θ_2 and θ_3, must be given for the other two unknowns to be obtainable. For the cases studied in Section 4.3, the angle θ_3 is given with the angles θ_1 and θ_2 being determined. On the other hand, for those studied in Section 4.4, the angle θ_1 is given with the angles θ_2 and θ_3 being determined.

2. For the cases that the critical positions of Rod1 (with angles $\theta_{1,U}$, $\theta_{1,L}$, $\theta_{1,B}$ and $\theta_{1,C}$) are given and the critical positions of Rod2 (with angles $\theta_{2,U}$, $\theta_{2,L}$, $\theta_{2,B}$ and $\theta_{2,C}$) and those of Rod3 (with angles $\theta_{3,U}$, $\theta_{3,L}$, $\theta_{3,B}$ and $\theta_{3,C}$) are determined as studied in Section 4.2, the "negative (-)" sign is "correct" for the roots of the quadratic equation, $x = \left(-b \pm \sqrt{b^2 - 4ac}\right) / (2a)$. However, for the cases that the arbitrary position of Rod3 (with angle θ_3) is given and the corresponding positions of Rod1 and Rod2 (with angles θ_1 and θ_2) are determined as studied in Section 4.3, the "positive (+)" sign is "correct" for the last roots.

3. Under the assumptions that the length of a rider's upper leg (Rod3) plus that of his lower leg (Rod2) must be long enough so that his heel can touch the bike's pedal and the upper leg (Rod3) must be lower than the horizontal line passing through the bike's seat centre, for the same specified bike, the longer the rider's legs the larger the effective work W done by the rider in each half pedalling cycle. Furthermore, the influence of types of motions (simple or non-simple harmonic) of the rider's upper leg on the effective work W is negligible.

4. Under the same assumptions made in the last conclusion 3, for the same

specified rider, the smaller the seat-to-bottom bracket distances (x_c and y_c) of the bike, the larger the effective work W done by the rider in each half cycle. In other words, the effect of decreasing the seat-to-bottom bracket distances (x_c and y_c) of the bike with the rider's leg lengths keeping unchanged is equivalent to increasing the rider's leg lengths with the seat-to-bottom bracket distances (x_c and y_c) of the bike keeping unchanged.

5. For the type of "non-simple harmonic" motion of upper leg leading to "constant" rotating speed of crank (Rod1), the time history curve in each half cycle looks like the sine wave, however, this is not true for the curves associated with "simple harmonic" motions, in which, each curve deviates from the sine wave to some degree, particularly for the case of rider's leg lengths (L_2=L_3) near the minimum values ($L_{2\min} = L_{3\min} = \overline{L}_{\min}$).

6. According to the theory of this chapter, for a given bike dimensions, the longer the lengths of its rider's legs, the higher the rider's pedalling efficiency, however, the longest lengths of the rider's legs must be "practical". On the contrary, for a rider with given leg lengths, the smaller the distances (x_c and y_c) between the seat and bottom bracket of his bike, the higher the rider's pedalling efficiency, of course, the minimum values of x_c and y_c must also be "practical".

Chapter 5 Rider-Bike System Models Developed in SimMechanics

5.1 Introduction

All bikes studied in this chapter have been introduced in Chapter 3. In order to study the influence of various full suspension systems of mountain bike on the bike and rider performance, numerical models of five rider-bike systems have been developed in SimMechanics. In this chapter, details of all bike models and the rider models are discussed.

5.2 Matrices for Mass Moments of Inertias (Inertia Tensors)

In SimMechanics, the various parts of a rider-bike system are modelled by the cylindrical tubes, solid rods and/or circular discs. Since the mass moments of inertias of each rigid body are dependent upon its configuration (or shape), the inertia tensors of some rigid bodies are introduced here for convenience of the subsequent descriptions. In general, it is assumed that the centre of gravity (CG) of a rigid body is coincident with its centroid. Thus, if the centroidal coordinate axes (x, y and z) are the principal axes, then its inertia tensor takes the form

$$I = \begin{bmatrix} I_{xx} & I_{xy} & I_{xz} \\ I_{yx} & I_{yy} & I_{yz} \\ I_{zx} & I_{zy} & I_{zz} \end{bmatrix} = \begin{bmatrix} I_{xx} & 0 & 0 \\ 0 & I_{yy} & 0 \\ 0 & 0 & I_{zz} \end{bmatrix} \tag{5.1}$$

Where the diagonal elements, I_{xx}, I_{yy}, and I_{zz}, denote the mass moment of inertia about x, y and z axes, respectively.

For a thin solid rod with length l (m) and mass m (kg) as shown in Figure C.1, the matrix for its mass moments is given by (see **Appendix C**)

$$I_{\text{solid rod}} = \begin{bmatrix} 0 & 0 & 0 \\ 0 & \frac{1}{12}ml^2 & 0 \\ 0 & 0 & \frac{1}{12}ml^2 \end{bmatrix} \tag{5.2}$$

For a hollow circular cylinder with length l, mass m, inner radius r_i and outer radius r_o as shown in Figure C.2, the matrix for its mass moments of inertias is given by

$$I_{\text{hollow circular cylinder}} = \begin{bmatrix} \frac{1}{12}m\left[3\left(r_i^2 + r_o^2\right) + l^2\right] & 0 & 0 \\ 0 & \frac{1}{2}m\left(r_i^2 + r_o^2\right) & 0 \\ 0 & 0 & \frac{1}{12}m\left[3\left(r_i^2 + r_o^2\right) + l^2\right] \end{bmatrix} \tag{5.3}$$

For a solid disc with radius r and mass m as shown in Figure C.3, the matrix for its mass moments of inertias is given by

$$I_{\text{solid disc}} = \begin{bmatrix} \frac{1}{4}mr^2 & 0 & 0 \\ 0 & \frac{1}{4}mr^2 & 0 \\ 0 & 0 & \frac{1}{2}mr^2 \end{bmatrix} \tag{5.4}$$

For the muscular parts of a rider model, including shanks, thighs, torso, upper and lower arms, the inertia tensor is modified from Equation (5.2) and takes the form

$$I_{\text{muscular part}} = \begin{bmatrix} \frac{1}{12\times 8}ml^2 & 0 & 0 \\ 0 & \frac{1}{12}ml^2 & 0 \\ 0 & 0 & \frac{1}{12}ml^2 \end{bmatrix} \tag{5.5}$$

By adding the mass moment of inertia about x-axis, $I_{xx}=ml^2/(8\times 12)$, in Equation (5.5), the shape of a thin solid rod shown in Figure C.1 will be similar to an ellipsoid and can represent the muscular part better.

Based on Equations (5.1) ~ (5.5), various bike models and the rider models are developed in SimMechanics, and will be discussed in the following sections.

5.3 SimMechanics Models of Five Bikes in this Thesis

The mass of bike frame is divided into two parts, including front and rear triangles. The front triangle is composed of head tube, top tube, down tube, and seat tube. The rear triangle is varied dependent on the different rear suspension systems, but basically, seat stay and chain stay are included. In order to study the influence of different rear suspension systems on rider's pedalling efficiency, all bike frames are assumed to have the same masses. Thus, only the geometric difference between the bikes is considered. In addition, a series of lab experiments done by Berry, Koves, and Benedetto [22] has shown that the effect of different bike masses on rider's VO_2, HR, and RPE is negligible. It is obvious that the three physiological variables increase with the increase of speed and grade.

The specification of the five bikes developed in this thesis is listed in Table 5.1. All dimensions are obtained from the AutoCAD line drawings. The seat tube angle of most common mountain bikes is between 71° to 73° [64]. Bike mass and other common variables used in the five bikes are also summarized in Table 5.1. Among the common variables, only the effect of different geometry of bike frames will be analyzed.

Each member (or component) is modelled by a rigid body with the mass to be equal to ρAL (or $\rho\forall$) located at CG of the member and mass moments of inertias determined by the formulas given in Appendix C. Where ρ is mass density, A is cross-sectional area, L is length and $\forall$ is volume of the member. In Table 5.1, BB height is the distance between bottom bracket and ground. Swingarm pivot tube refers to the tube connecting the shock eye on swingarm and the main pivot point on down tube for single pivot bike, as shown in Figure 3.13. Horst link is a small link connecting the seat stay and rear axle for horst link bike, as shown in Figure 3.14. Faux bar is a small bar connecting the chain stay and rear axle for faux bar bike, as shown in Figure 3.15. Small link is the link connecting the bottom of rear triangle and the main pivot point near bottom bracket for VPP bike, and the rear triangle tube is a tube connecting chain stay, seat stay, and small link for VPP bike as well, as shown in

Figure 3.16. Offset at crown refers to the distance between the bottom of head tube and the top of front fork, and offset at front axle refers to the distance between the bottom of front fork and front axle. Forks of all five bikes are assumed to be identical in their masses and to be different in their lengths only.

Table 5.1 Specification of bike frames studied in this thesis

Item \ Bike	Hard Tail	Single Pivot	Horst Link	Faux Bar	VPP
Base Model	Marin RockyRidge	Orbea Occam	Specialized Pitch	Kona Tanuki	Santa Cruz Blur
Head Angle	69°	69.5°	66°	68°	68°
Seat Angle	72°	73.5°	72°	74°	73°
Wheelbase	1.0668m	1.131m	1.196m	1.16332m	1.12776m
BB Height	0.29246m	0.3208m	0.31458m	0.32278m	0.32521m
Chain Stay	L:0.42711m M:0.5918kg	L:0.468m M:0.478kg	L:0.40343m M:0.4635kg	L:0.42507m M:0.5174kg	L:0.3706m M:0.353kg
Seat Stay	L:0.43888m M:0.6082kg	L:0.474m M:0.4841kg	L:0.46427m M:0.5334kg	L:0.3169m M:0.3857kg	L:0.45844m M:0.4367kg
Seat Tube	L:0.40206m M:1.3911kg	L:0.482m M:1.5493kg	L:0.46819m M:1.4796kg	L:0.46542m M:1.4733kg	L:0.490m M:1.5814kg
Top Tube	L:0.56025m M:1.9384kg	L:0.593m M:1.9061kg	L:0.59437m M:1.8783kg	L:0.63042m M:1.9956kg	L:0.61237m M:1.9764kg
Down Tube	L:0.69295m M:2.3976kg	L:0.708m M:2.2758kg	L:0.7517m M:2.3754kg	L:0.70727m M:2.2389kg	L:0.68754m M:2.2190kg
Head Tube	L:0.12569m M:0.4349kg	L:0.134m M:0.4307kg	L:0.13565m M:0.4287kg	L:0.14351m M:0.4543kg	L:0.11936m M:0.3852kg
Swingarm Pivot Tube	N/A	L:0.233m M:0.238kg	N/A	N/A	N/A
Horst Link	N/A	N/A	L:0.04612m M:0.053kg	N/A	N/A
Faux Bar	N/A	N/A	N/A	L:0.06114m M:0.0744kg	N/A
Small Link	N/A	N/A	N/A	N/A	L:0.09477m M:0.0903kg
Rear Triangle Tube	N/A	N/A	N/A	N/A	L:0.26938m M:0.2566kg
Rocker	N/A	N/A	L:0.13059m M:0.15kg	L:0.18275m M:0.2224kg	L:0.06661m M:0.0634kg
Front Suspension	M:1.546kg [17] Stiffness=73600N/m [4] Damping=975N · s/m [4]				
	L:0.46109m	L:0.454m	L:0.45374m	L:0.42048m	L:0.4367m
Offset at Crown	0.0365m	0.032m	0.03154m	0.0325m	0.03769m
Offset at Front Axle	0.02982m	0.0391m	0.06487m	0.0755	0.05021m
Rear Suspension	N/A	Stiffness=73900N/m [4] Damping=7776N · s/m [4]			
		L:0.316m	L:0.2308m	L:0.20447m	L:0.19701m
Total Bike Mass	Front frame=6.162kg Rear frame=1.2kg [17]				
Front Wheel	Diameter=26in=0.6604m Mass=1.755kg [17] Stiffness=90000N/m [35] Damping=10000 N · s/m (tested)				
Rear Wheel	Diameter: 26in=0.6604m Mass: 2.535kg [17] Stiffness=90000N/m [35] Damping=10000 N · s/m (tested)				
Frame Tube Radius	Inner=0.006m Outer=0.012085m				
Fork Tube Radius	Upper Tube: Inner: 0.0145m Outer: 0.016m Lower Tube: Inner: 0.016m Outer: 0.02m				
Crank	Length: Right=Left=0.17m Mass:1kg				

5.3.1 Block Diagrams and Mathematical models of Bike Frames

The SimMechanics block diagrams, mathematical models of the five mountain bike frames are shown as follows:

(a) Hard Tail Bike

The block diagram and mathematical of the hard tail bike based on Marin Rocky Ridge are shown in Figure 5.1 and Figure 5.2, respectively. Since the hard tail bike is the simplest kind of mountain bike (without rear suspension), its main frame is composed of front and rear triangle only, in which the adjacent frame tubes are welded together by weld joints. The mass moments of inertias of every frame tube are shown in Table 5.2.

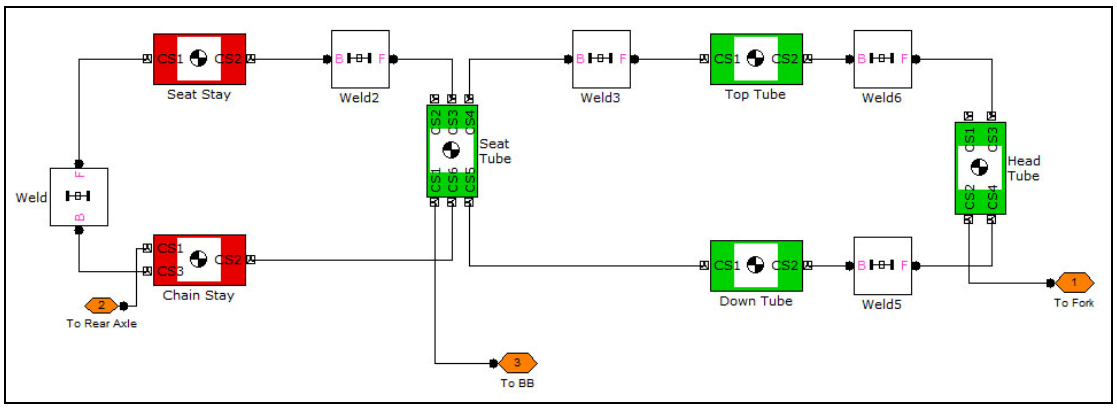

Figure 5.1 Block diagram of the hard tail bike frame

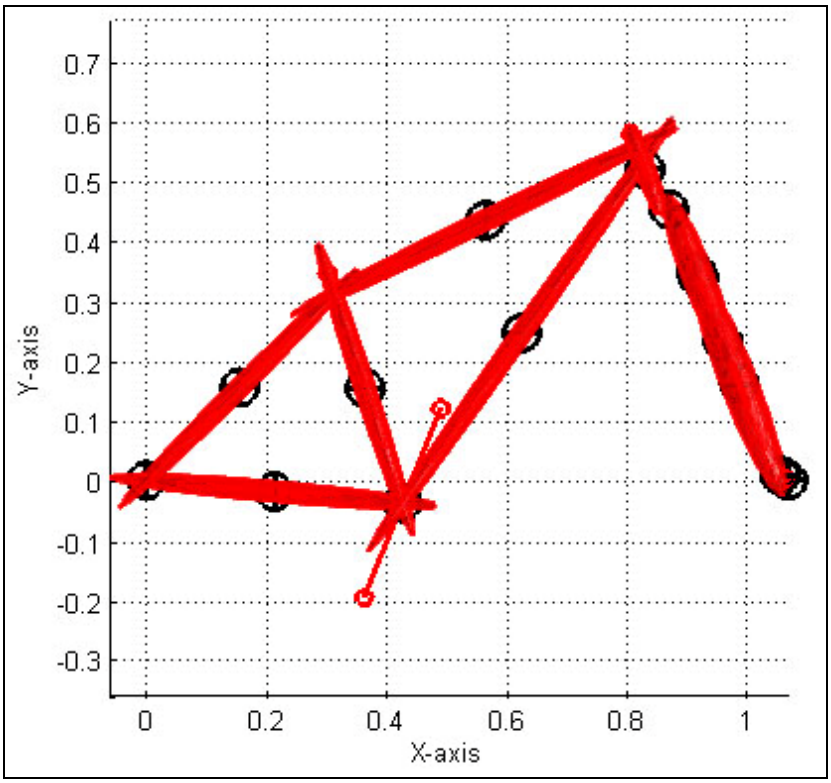

Figure 5.2 Mathematical model of the hard tail bike frame (comes from the output of SimMechanics)

Table 5.2 Mass moments of inertias for tubes of the hard tail bike frame

Tube	Mass moments of inertias ($kg \cdot m^2$)		
	I_{xx}	I_{yy}	I_{zz}
Chain Stay	5.387×10^{-5}	9.024×10^{-3}	9.024×10^{-3}
Seat Stay	5.535×10^{-5}	9.789×10^{-3}	9.789×10^{-3}
Seat Tube	1.266×10^{-4}	1.880×10^{-2}	1.880×10^{-2}
Top Tube	1.764×10^{-4}	5.079×10^{-2}	5.079×10^{-2}
Down Tube	2.182×10^{-4}	9.604×10^{-2}	9.604×10^{-2}
Head Tube	3.958×10^{-5}	5.923×10^{-4}	5.923×10^{-4}

(b) Single Pivot Bike

The block diagram and mathematical model of the single pivot bike based on Orbea Occam 2011 are shown in Figure 5.3 and Figure 5.4, respectively. The mass moments of inertias of the frame tubes are summarized in Table 5.3. From the block diagram shown in Figure 5.3, one can find that the swingarm pivot tube is welded to seat stay and chain stay, and the end of this tube is connected to down tube with a revolute joint which is the main pivot point.

The rear suspension (shock absorber) of the single pivot bike is modelled as a "body spring & damping block". It is connected to swingarm pivot tube and the top tube, in which the natural spring length, stiffness, and damping constants are defined, but the rear shock absorber does not appear in the mathematical model shown in Figure 5.4, because in SimMechanics, "body spring & damper" is a force element to model the force of a damped spring between two bodies.

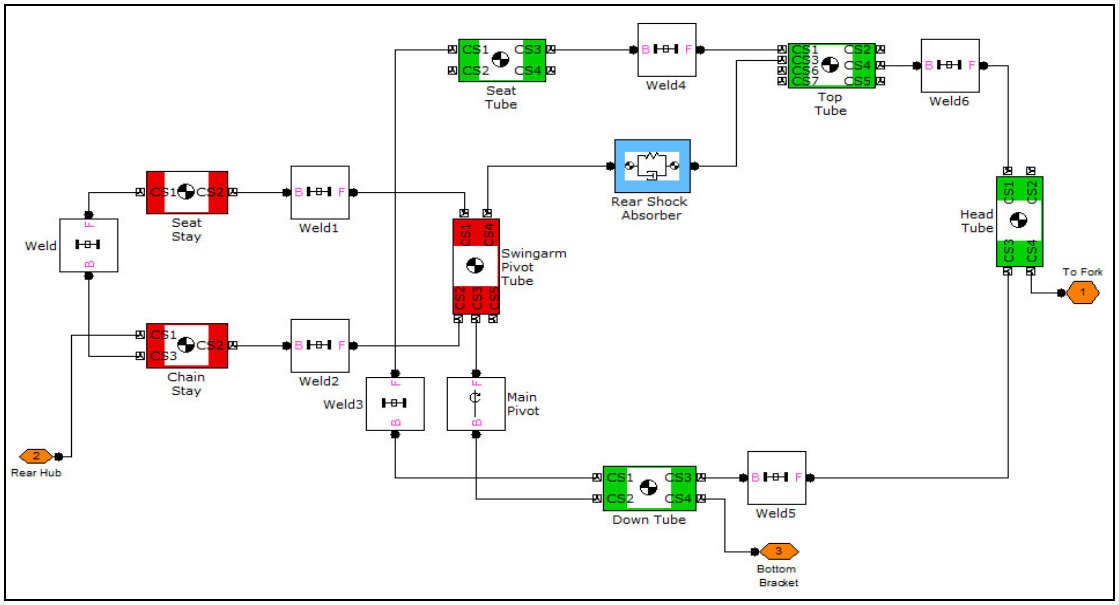

Figure 5.3 Block diagram of the single pivot bike frame

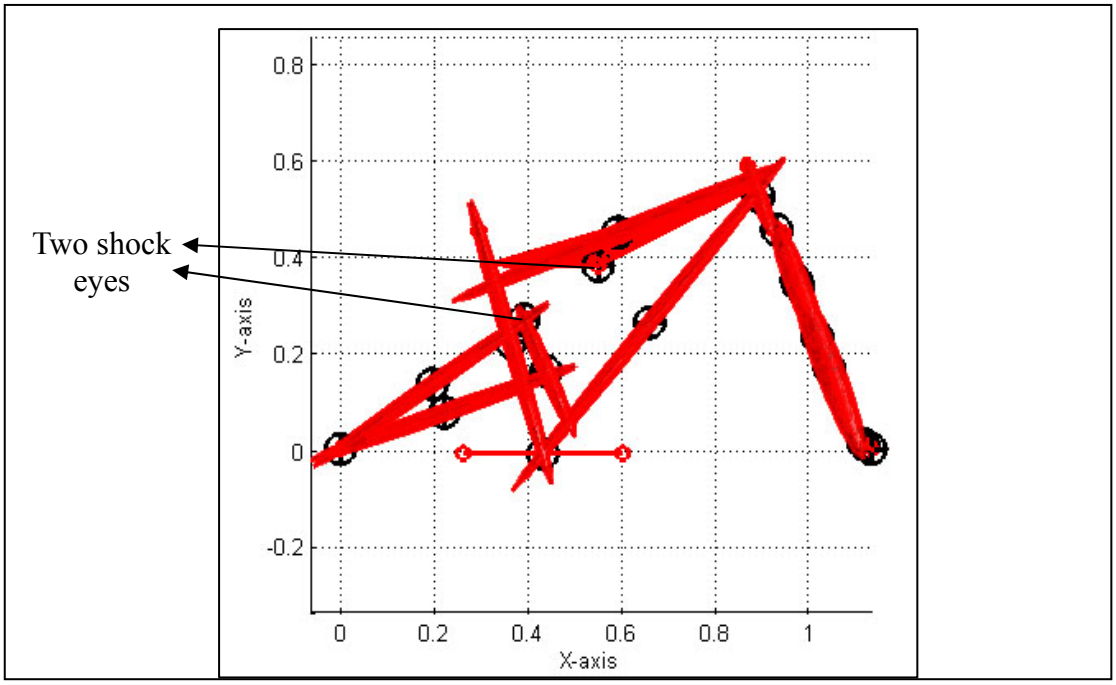

Figure 5.4 Mathematical model of the single pivot bike frame (damper unit is connected between two shock eyes)

Table 5.3 Mass moments of inertias for tubes of the single pivot bike frame

Tube	Mass moments of inertias ($kg \cdot m^2$)		
	I_{xx}	I_{yy}	I_{zz}
Chain Stay	4.350×10^{-5}	8.745×10^{-3}	8.745×10^{-3}
Seat Stay	4.406×10^{-5}	9.085×10^{-3}	9.085×10^{-3}
Swingarm Pivot Tube	2.165×10^{-5}	1.087×10^{-3}	1.087×10^{-3}
Seat Tube	1.410×10^{-4}	3.006×10^{-2}	3.006×10^{-2}
Top Tube	1.735×10^{-4}	5.594×10^{-2}	5.594×10^{-2}
Down Tube	2.071×10^{-4}	9.516×10^{-2}	9.516×10^{-2}
Head Tube	3.920×10^{-5}	6.641×10^{-4}	6.641×10^{-4}

(c) Four-Bar-Linkage Horst Link Bike

The block diagram and mathematical model of the four-bar-linkage horst link bike based on Specialized Pitch 2011 are shown in Figures 5.5 and 5.6, respectively. The mass moments of inertias of the frame tubes are summarized in Table 5.4. From Figure 5.5 one sees that the horst link bike model developed in SimMechanics has four revolute joints to model the main pivot, horst link pivot, rocker pivot, and rocker fix pivot. The two shock eyes are located on rocker and down tube, and connected with the shock absorber. The horst link pivot is between chain stay and rear axle.

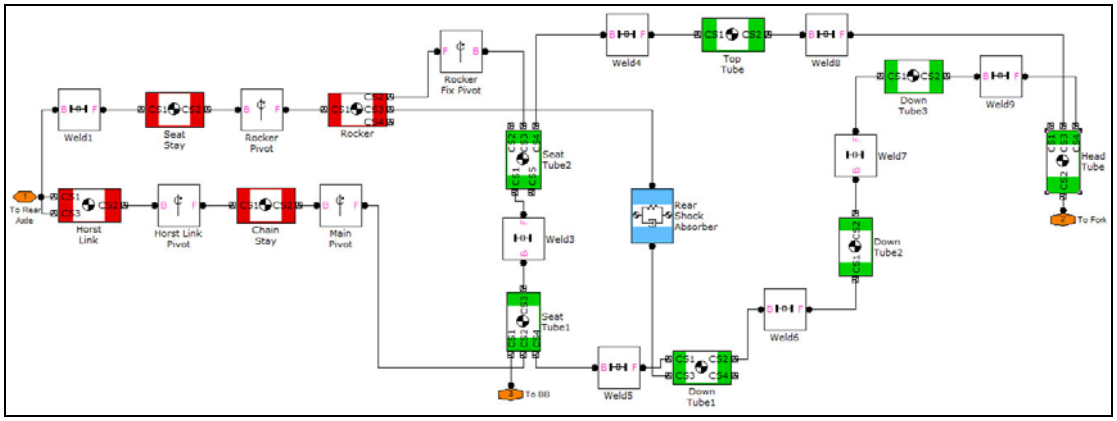

Figure 5.5 Block diagram of the horst link bike frame

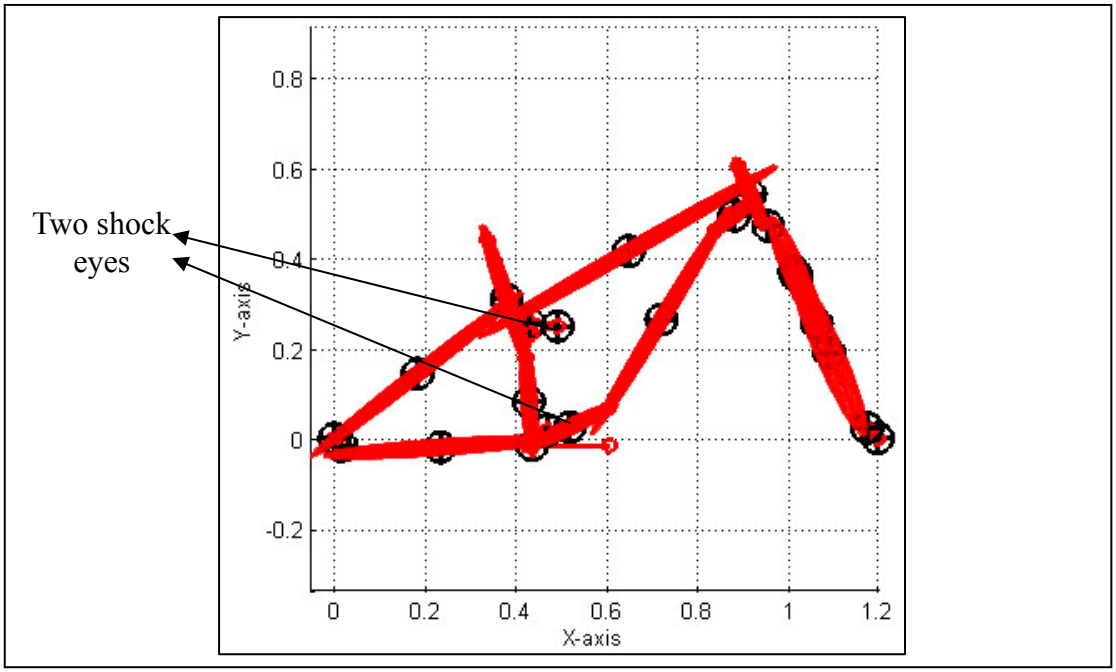

Figure 5.6 Mathematical model of the horst link bike frame (damper unit is connected between two shock eyes)

Table 5.4 Mass moments of inertias for tubes of the horst link bike frame

Tube	Mass moments of inertias ($kg \cdot m^2$)		
	I_{xx}	I_{yy}	I_{zz}
Horst Link	0	9.392×10^{-6}	9.392×10^{-6}
Chain Stay	4.219×10^{-5}	6.307×10^{-3}	6.307×10^{-3}
Seat Stay	4.855×10^{-5}	9.605×10^{-3}	9.605×10^{-3}
Rocker	0	2.132×10^{-4}	2.132×10^{-4}
Seat Tube	7.902×10^{-5}	5.500×10^{-3}	5.500×10^{-3}
Top Tube	1.709×10^{-4}	5.538×10^{-2}	5.538×10^{-2}
Down Tube	2.162×10^{-4}	1.119×10^{-1}	1.119×10^{-1}
Head Tube	3.901×10^{-5}	6.768×10^{-4}	6.768×10^{-4}

(d) Four-Bar-Linkage Faux Bar Bike

The block diagram and mathematical model of the four-bar-linkage faux bar bike based on Kona Tanuki 2011 are shown in Figures 5.7 and 5.8, respectively. The mass moments of inertias for the tubes of bike frame are summarized in Table 5.5.

It has been mentioned in Section 3.3.4 that the faux bar design is very similar to horst link design, and the only difference is the faux bar pivot to be between the rear axle and seat stay instead of between rear axle and chain stay.

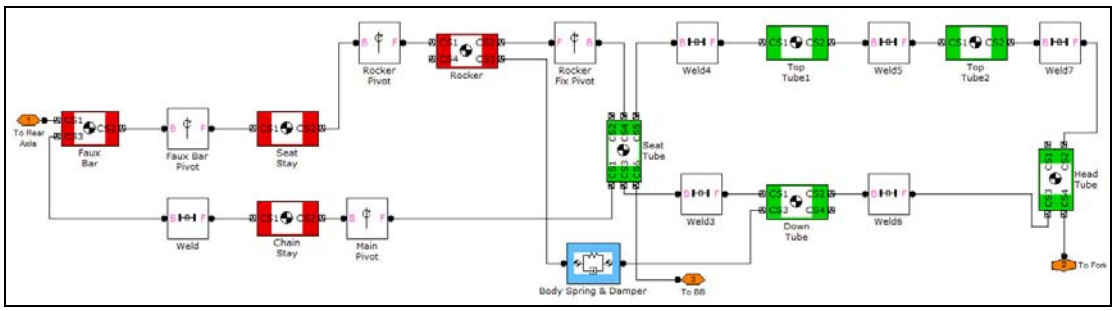

Figure 5.7 Block diagram of the faux bar bike frame

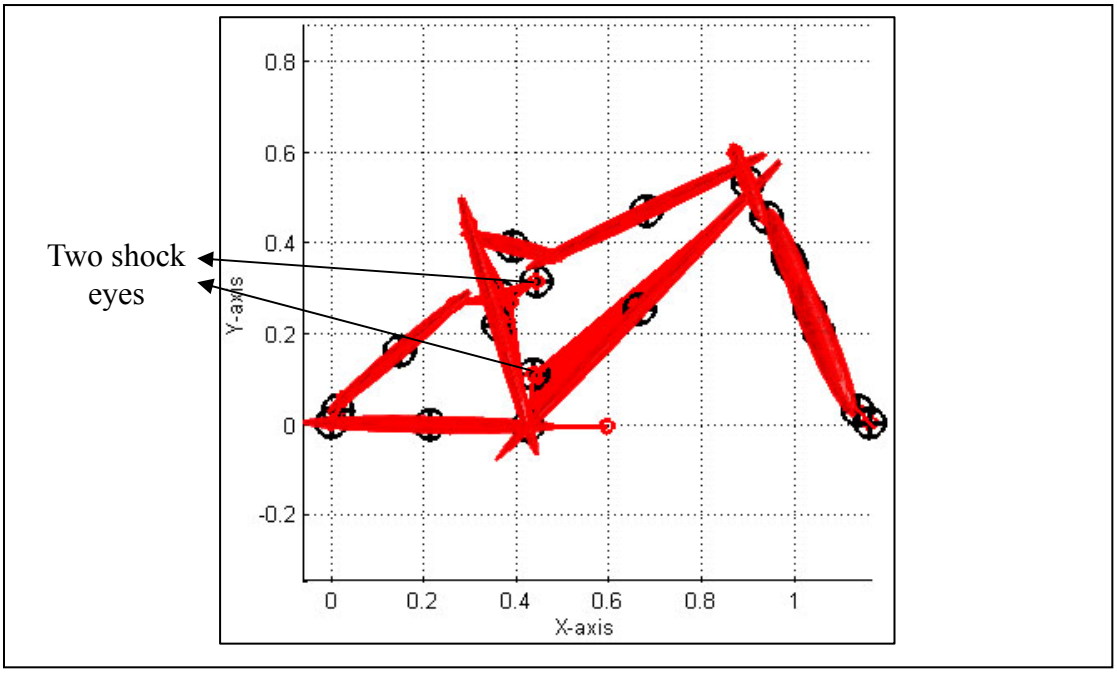

Figure 5.8 Mathematical model of the faux bar bike frame (damper unit is connected between two shock eyes)

Table 5.5 Mass moments of inertias for tubes of faux bar bike frame

Tube	Mass moments of inertias ($kg \cdot m^2$)		
	I_{xx}	I_{yy}	I_{zz}
Faux Bar	0	2.318×10^{-5}	2.318×10^{-5}
Chain Stay	4.709×10^{-5}	7.814×10^{-3}	7.814×10^{-3}
Seat Stay	3.511×10^{-5}	3.245×10^{-3}	3.245×10^{-3}
Rocker	0	2.783×10^{-5}	2.783×10^{-5}
Seat Tube	1.341×10^{-4}	2.666×10^{-2}	2.666×10^{-2}
Top Tube	1.816×10^{-4}	6.618×10^{-2}	6.618×10^{-2}
Down Tube	2.037×10^{-4}	9.343×10^{-2}	9.343×10^{-2}
Head Tube	4.135×10^{-5}	8.003×10^{-4}	8.003×10^{-4}

(e) Virtual Pivot Point Bike

The block diagram and mathematical model of the virtual pivot point (VPP) bike based on Santa Cruz Blur 2011 are shown in Figures 5.9 and 5.10, respectively. The mass moments of inertias of frame tubes are summarized in Table 5.6. As has been introduced in Section 3.3.5, the VPP bike has individual front and rear triangles, so in the SimMechanics model, one tube is used to weld with seat stay and chain stay, and is named “rear triangle tube”, as shown in Figure 5.9. The rear triangle is connected with front triangle by two small links and named small link and rocker, respectively, in Figure 5.9.

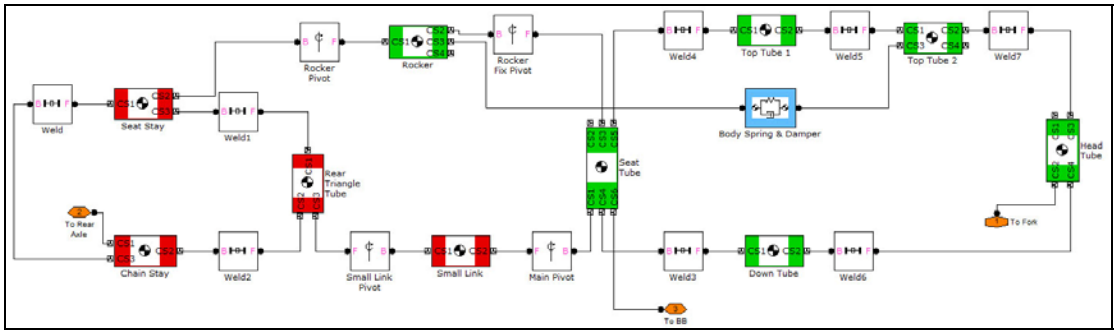

Figure 5.9 Block diagram of the VPP bike frame

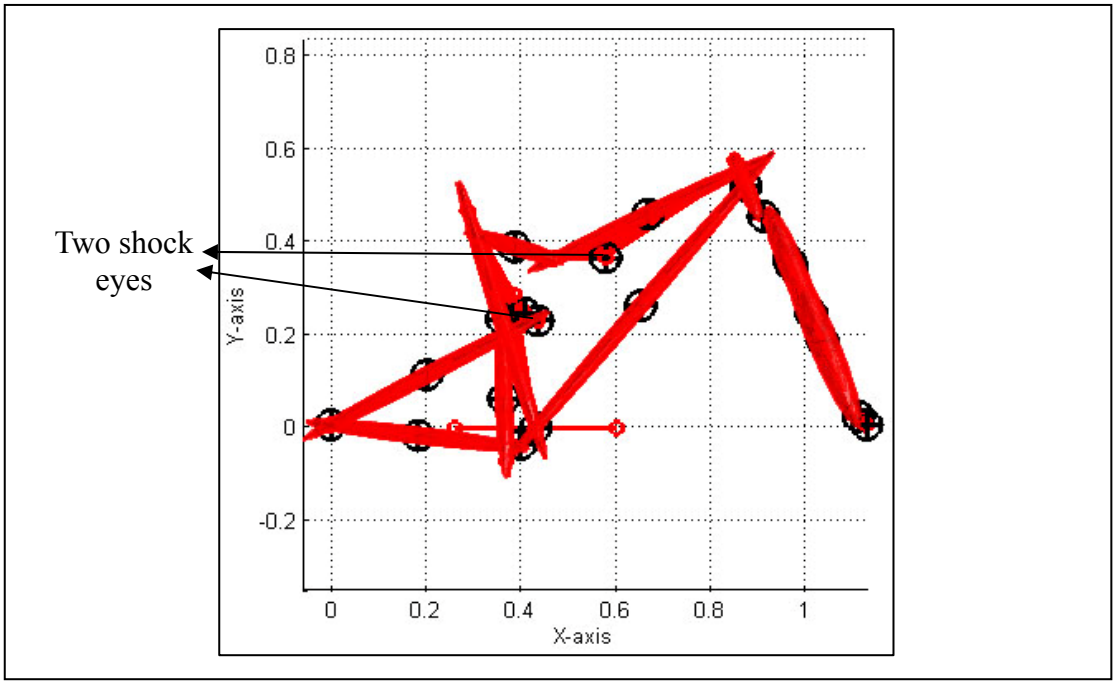

Figure 5.10 Mathematical model of the VPP bike frame (damper unit is connected between two shock eyes)

Table 5.6 Mass moments of inertias for tubes of the VPP bike frame

Tube	Mass moments of inertias ($kg \cdot m^2$)		
	I_{xx}	I_{yy}	I_{zz}
Chain Stay	3.213×10^{-5}	4.056×10^{-3}	4.056×10^{-3}
Seat Stay	3.974×10^{-5}	7.667×10^{-3}	7.667×10^{-3}
Rear Triangle Tube	2.335×10^{-5}	1.563×10^{-3}	1.563×10^{-3}
Rocker	0	2.345×10^{-5}	2.345×10^{-5}
Small Link	0	6.756×10^{-5}	6.756×10^{-5}
Seat Tube	1.439×10^{-4}	3.171×10^{-2}	3.171×10^{-2}
Top Tube	1.798×10^{-4}	6.185×10^{-2}	6.185×10^{-2}
Down Tube	2.019×10^{-4}	8.751×10^{-2}	8.751×10^{-2}
Head Tube	3.506×10^{-5}	4.748×10^{-4}	4.748×10^{-4}

5.3.2 Block Diagrams Concerning Wheel

In the work of Itturioz [2], the wheel is modelled as a rigid ball, which is used in the demo model of bouncing ball from SimMechanics [38]. This demo model uses a contact force system to apply a bouncing force to the ball when the ball hits the ground from the air. The contact force system is available for the wheel model moving on the ground. However, the shape of the rigid ball must be modified.

In [39] and [47], the wheel models are represented by the two-dimensional knife edge rigid discs, which are better than a three-dimensional rigid ball. Therefore, the wheel models are represented by the rigid discs in this study.

This subsection uses the parameters of the "hard tail bike" with wheels shown in Figure 5.11 and the mass moments of inertias of the front and rear wheels shown in Table 5.7. The models developed here are easily applied to other bikes.

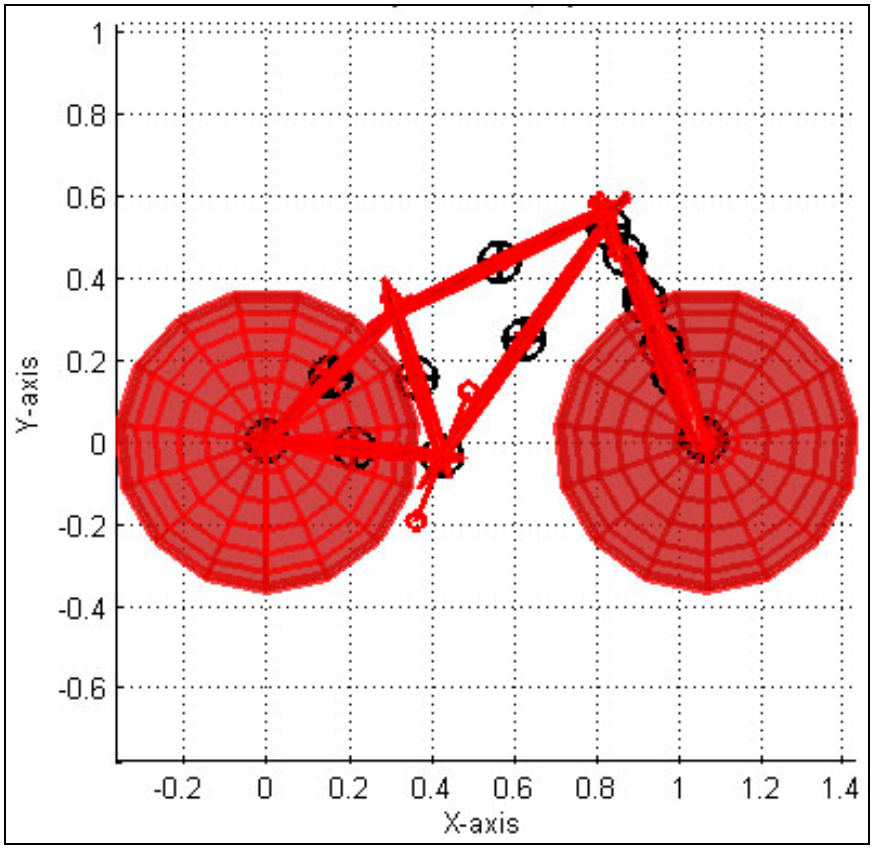

Figure 5.11 Mathematical model of the hard tail bike with wheels

Table 5.7 Mass moments of inertias of front and rear wheels

Wheel	Mass moments of inertias ($kg \cdot m^2$)		
	I_{xx}	I_{yy}	I_{zz}
Front Wheel	4.783×10^{-2}	4.783×10^{-2}	9.567×10^{-2}
Rear Wheel	6.909×10^{-2}	6.909×10^{-2}	1.381×10^{-1}

The block diagram of rear wheel is shown in Figure 5.12. The most popular diameter of bike wheel used for mountain bikes is 26 inch (660.4 mm), so this value is used to construct the wheel model. Other information about the wheel can be found in Table 5.1. In Figure 5.12, the contact point between ground and wheel is modelled by a planar joint with 2 translational degrees of freedom (in x and y directions) and one rotational degree of freedom (about z-axis). Since the wheel falls down due to gravity, a contact force subsystem is introduced as in the bouncing ball model [46].

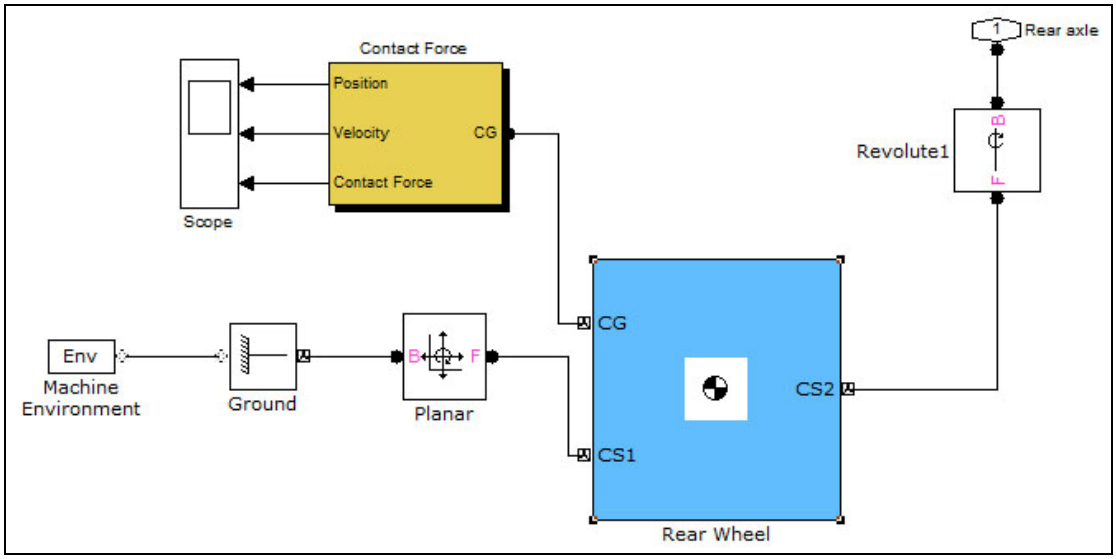

Figure 5.12 Block diagram of the rear wheel

The contact force subsystem is a closed-loop control system as shown in Figure 5.13. First of all, the position and velocity of the centre of gravity of the wheel are measured and the associated signals are sent into the force law system shown in Figure 5.14, where the position of CG is subtracted by the block "bump", in which the instantaneous y-axis position and the corresponding time are obtained from the

“m-file” written by the user. The bump model will be discussed later. Then, the selector block selects the *y*-axis component and sent it to the logical if block to check if the numerical value of *y*-axis position is larger or less than 0.

If the numerical value of position is less than 0, which means the wheel is lower than ground, then the signal is sent to the penalty force block, as shown in Figure 5.15(a). In Figure 5.15(a), the value of position is multiplied by a negative spring constant (-90000N/m), and the velocity is multiplied by a negative damping constant (-10000 N · s/m). Then the two amplified values are added together and the result is sent to a saturation block to ensure the value is larger than 0. After that, the signal is sent out back to the force law subsystem. The spring and damping constants used in this model are similar to a spring-damper system to bounce back and forth when it is applied by a force. In real riding condition, the pneumatic tyres can absorb some part of vibration dependent on the different tyre pressures.

In contrast, if the numerical value of position is larger than 0, the signal is sent to the other block with no force being applied, as shown in Figure 5.15(b), and then sent back to the force law system.

Returning to the force law system shown in Figure 5.14, where both penalty force and zero force are merged in the merge block and then a signal is sent back to the contact force subsystem shown in Figure 5.13. Finally, the signal of force is sent to the body actuator block to apply force on the centre of gravity of wheel.

A “contact force system” is added to both front and rear wheels to support the wheels on the ground for preventing them from falling down.

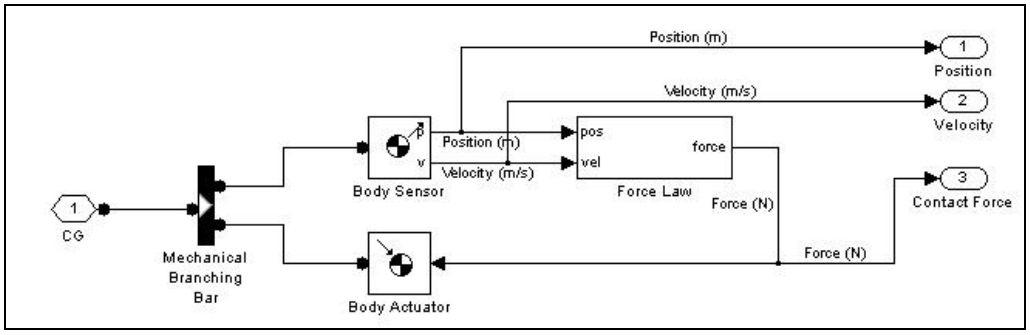

Figure 5.13 Block diagram of contact force subsystem

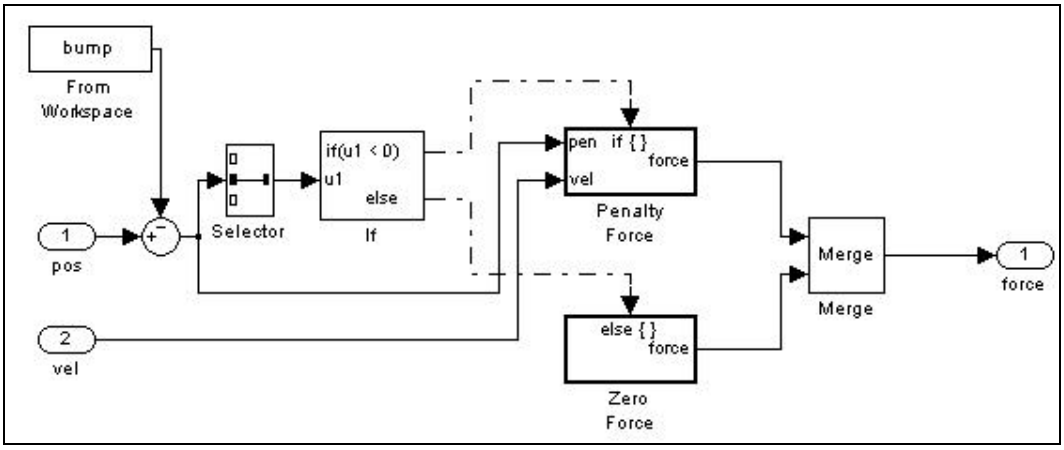

Figure 5.14 Force law system of wheel model

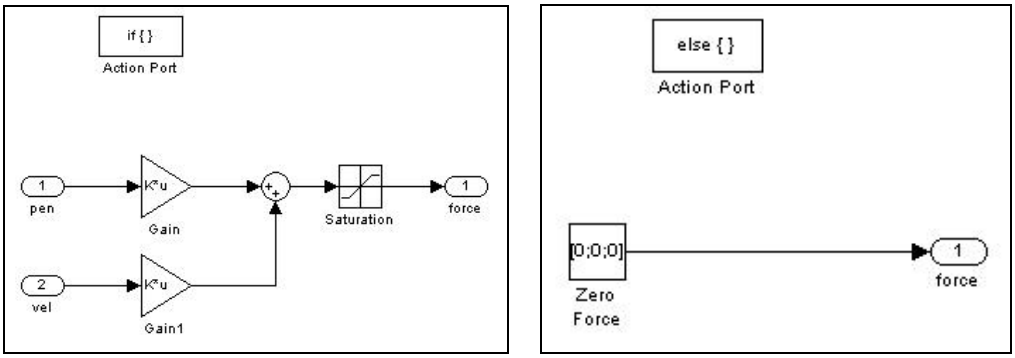

(a) Penalty Force (b)Zero Force

Figure 5.15 Block diagram of penalty force and zero force system

5.3.3 Front Fork

The current front suspension systems of mountain bikes are adequate to absorb vibration when the bike is passing over rough terrain. Most advanced front suspension systems have not only springs in the front fork, but also fork oil (damping oil) in the fork tube to behave like a damping unit. Some of them even have the preloaded damping adjustment to be tuned according to the rider's weight and/or the road condition. Some front suspensions are made of the reversed (up side down) forks similar to the ones used on racing motorcycles, which have an upper tube with a thicker diameter and a lower tube with a thinner diameter.

The front suspension system developed in this study is a simple model with a body spring & damper unit being added between the upper and lower fork tubes. The block diagram is shown in Figure 5.16. The CG of upper tube is connected to the top of lower tube with a prismatic joint which has a degree of freedom along *y*-axis based on the lower tube, so that the upper tube can move back and forth along the lower tube when the bike passes through obstacles. The body spring & damper unit is equipped in the middle of the front fork. The spring constant and damper constant used in this model are shown in Table 5.1. The length of spring is 0.125m. Although different bike models have different fork lengths, the length, spring constant, and damper constant of each "spring & damper unit" are the same, thus, the analysis can be focused on different rear suspension systems. It is noted that the only factor affecting the characteristics of front fork is the different head angle among the five bike models.

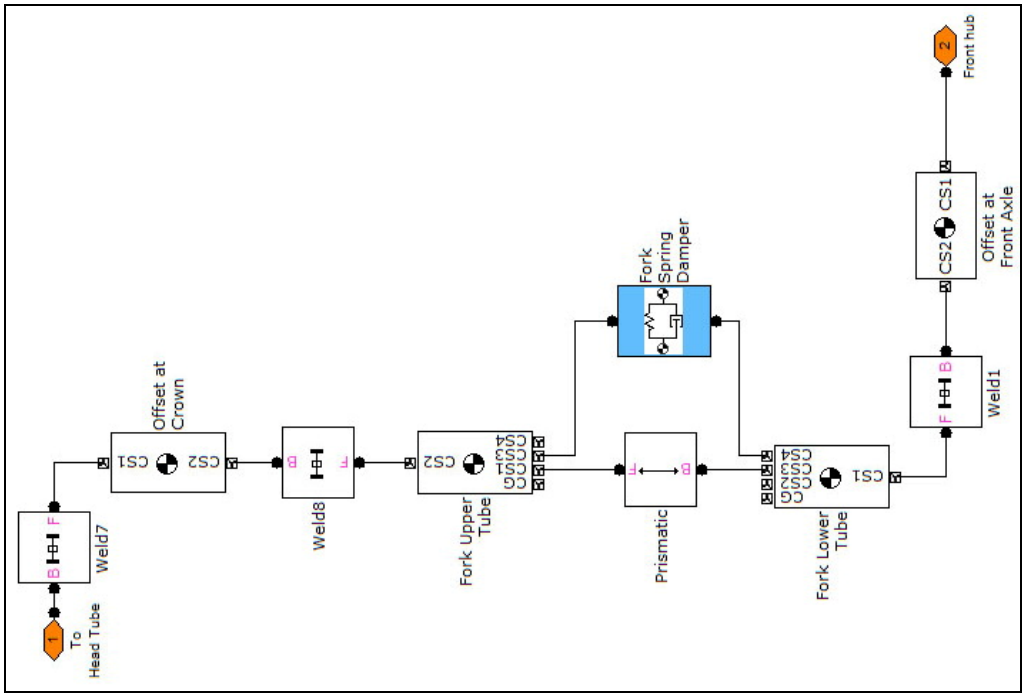

Figure 5.16 Block diagram of the front fork

5.3.4 Chain Tension

In real riding conditions, the length of chain will be varied when the bike passes through bumps. Although the change is small for the hard-tail bike, it will produce the pedal kick-back effect [9,26] when one rides a mountain bike with the rear suspension system and the latter is activated due to hitting bumps of the bike or pedalling of the rider. When the length of chain is varied, the chain tension is maintained by the derailleur. Therefore, it is necessary to develop a model to tackle the chain tension force. This system is based on Itturioz's study [2].

The relationship between chain and its sprockets is shown in Figure 5.17, where the "sprocket distance" is defined as the distance between bottom bracket and the centre of rear wheel. During riding a bike, if the instantaneous chain length is larger than the initial distance, then the derailleur will expand the chain to make it longer, just like a spring. To simulate this effect, a pair of forces are applied to the bottom bracket and the centre of rear wheel, as shown in Figure 5.17.

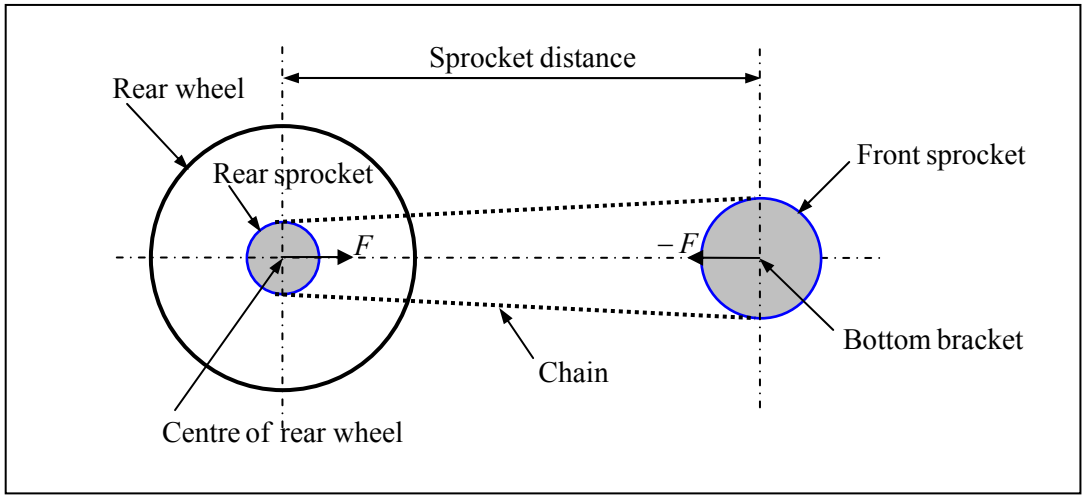

Figure 5.17 Definition for sprocket distance

The block diagram of chain tension system is shown in Figure 5.18. In which the *x* coordinates of bottom bracket and CG of rear wheel are measured and subtracted first. This signal gives the instantaneous sprocket distance and is then subtracted by the initial chain distance. The signal for the last result is sent to a logical if block to check if the signal is larger or less than 0m. If it is larger than 0m, then it will be multiplied

by the spring constant (chain stiffness block in the system). Then the signal is sent to the force actuator to apply force on the centre of rear wheel. Meanwhile, the signal is multiplied by a constant -1 and sent to another force actuator to apply force at the bottom bracket, because the direction of the two forces are opposite (see Figure 5.17). If the signal is less than 0m, then no force is applied.

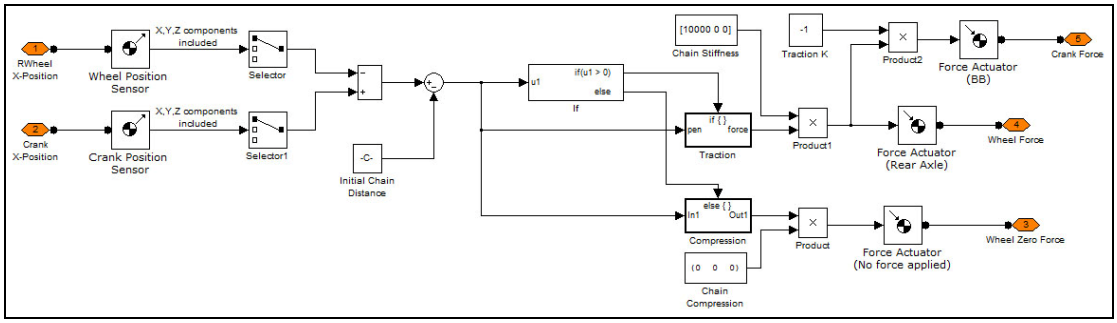

Figure 5.18 Block diagram for chain tension system

5.4 SimMechanics Model of Rider and PID Controller

With the help of BikeCAD introduced in Section 3.2.3, the angles of all body parts of the rider's upper body can be well measured. The positions of rider's lower body, including upper and lower legs are calculated with the method discussed in Chapter 4. In Chapter 4, every possible position of rider's upper and lower legs are discussed and the calculations have been written into a programme in the "m-file". The two points significantly influencing the instantaneous configurations of the rider's upper and lower legs are the positions of seat post and bottom bracket. As long as the horizontal and vertical distances x_c and y_c, between them are known, the programme can calculate the positions of the rider's upper and lower legs automatically. The lengths of upper and lower legs can also be modified.

The rider-bike system model (for hard tail bike) is shown in Figure 5.19. The information for the rider's body parts are summarized in Table 5.8. The lengths and masses of all rider's body parts are obtained from [17], which is a rider with height of 1.88m and weight 778N (including hands and feet), but in this study, the weight 778N does not include hands and feet. The horizontal and vertical distances between seat post and bottom bracket (x_c, y_c), the initial angles of rider's upper and lower legs on each mountain bike are summarized in Table 5.8, where the definitions for the symbols, $\theta_{2,U}$, $\theta_{2,L}$, $\theta_{3,U}$ and $\theta_{3,L}$, are defined in Figures 4.2 and 4.3.

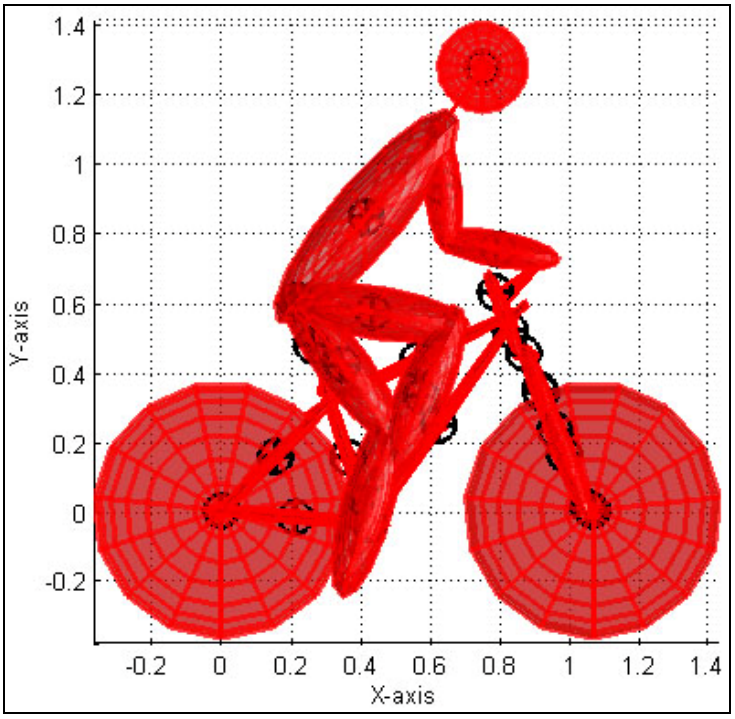

Figure 5.19 Mathematical model of rider and hard tail bike

Table 5.8 Physical quantities for the rider's body parts

Items	Length (m)	Mass (kg)	Mass moments of Inertia (kg · m^2)		
			I_{xx}	I_{yy}	I_{zz}
Lower leg (Shank)	0.45	3.19	6.728×10^{-3}	5.383×10^{-2}	5.383×10^{-2}
Upper leg (Thigh)	0.45	8.4	1.771×10^{-2}	1.417×10^{-1}	1.417×10^{-1}
Torso	0.63	41.69	1.723×10^{-1}	1.378	1.378
Upper arm	0.31	2.18	2.182×10^{-3}	1.745×10^{-2}	1.745×10^{-2}
Lower arm	0.29	1.47	1.287×10^{-3}	1.030×10^{-2}	1.030×10^{-2}
Head	0.23 (Diameter)	4.54	1.501×10^{-2}	1.501×10^{-2}	3.002×10^{-2}

Table 5.9 Distances between seat and bottom bracket, and initial angles of upper and lower legs for each mountain bike

Bike	x_c(m)	y_c(m)	Lower leg		Upper leg	
			Right($\theta_{2,U}$)	Left($\theta_{2,L}$)	Right($\theta_{3,U}$)	Left($\theta_{3,L}$)
Hard Tail	0.21218	0.64074	67.93°	74.96°	8.45°	53.91°
Single Pivot	0.186	0.62793	65.27°	69.82°	8.27°	53.11°
Horst Link	0.1553	0.61915	62.20°	64.86°	9.03°	53.58°
Faux Bar	0.17595	0.61359	64.12°	66.78°	7.11°	51.66°
VPP	0.19934	0.63222	66.60°	72.11°	8.07°	53.12°

The block diagram of rider model is shown in Figure 5.20. It is seen that every body part is connected with a revolute (hinged) joint, except the neck joint being welded (rigid) joint. Furthermore, the elbow joint is connected with an angle controller subsystem. In the work of Iturrioz [2], a spring is connected between shoulder and hand to prevent the rider's upper body from falling down due to gravity. It is not adequate since no spring is attached on human body in real condition.

In normal riding condition, the elbow joint can be considered as the middle point from shoulder to hand, and the angle of elbow joint is changed when the bike passes through bumps. Therefore, it is decided to attach a feedback control system at elbow joint to control the angle of elbow.

The block diagram of the elbow angle control system is shown in Figure 5.21. In which the joint sensor senses the angle of elbow first and then sends the signal to the PID controller.

In control engineering, PID controller is also called three-term control [76], because it includes the three terms, proportional, integral, and derivative. The P term deals with the "present error" and gives a proportional amplified signal to output. The I term senses the "past error" and sends an integral signal to output. The D term predicts the "future errors" and gives a derivative signal to output. The three summed output is then given to a certain system to do feedback control. The transfer function of PID controller takes the form given by Equation (5.6) [38,76], where K_p is the proportional gain, K_i is the integral gain, and K_d is the derivative gain. Sometimes PI only or PD only controllers are used as well.

$$C(s) = K_p + \frac{K_i}{s} + K_d s \tag{5.6}$$

The PID controller is shown in Figure 5.22. In this controller, the desired angle 0º is subtracted by the actual angle, and the error signal is sent to amplify with proportional, integral, and differential gains, then three amplified signals are added together and sent to the joint actuator to apply torque at the elbow joint to make the angle of elbow at the desired angle. The desired angle is set as 0º because the initial angle is set as 0º in SimMechanics.

A test is implemented to observe the functions of the PID controller. PI mode is used in this test with K_p=100 and K_i=70. The simulation is implemented under the assumed condition that the rider sits on the bike and keeps stationary. The results for the angle and reaction torque at the elbow joint are shown in Figure 5.23. It is seen that, initially, the elbow angle has a slight fluctuation (or variation) about 0.56º with reaction torque to be 57.5 N·m, and then the angle decreases to 0º gradually due to the action of PI controller, just as expected. Since the PI controller gives feedback control to the elbow angle, the angle gradually decreases to 0º, and the reaction torque decreases to 35N·m also gradually.

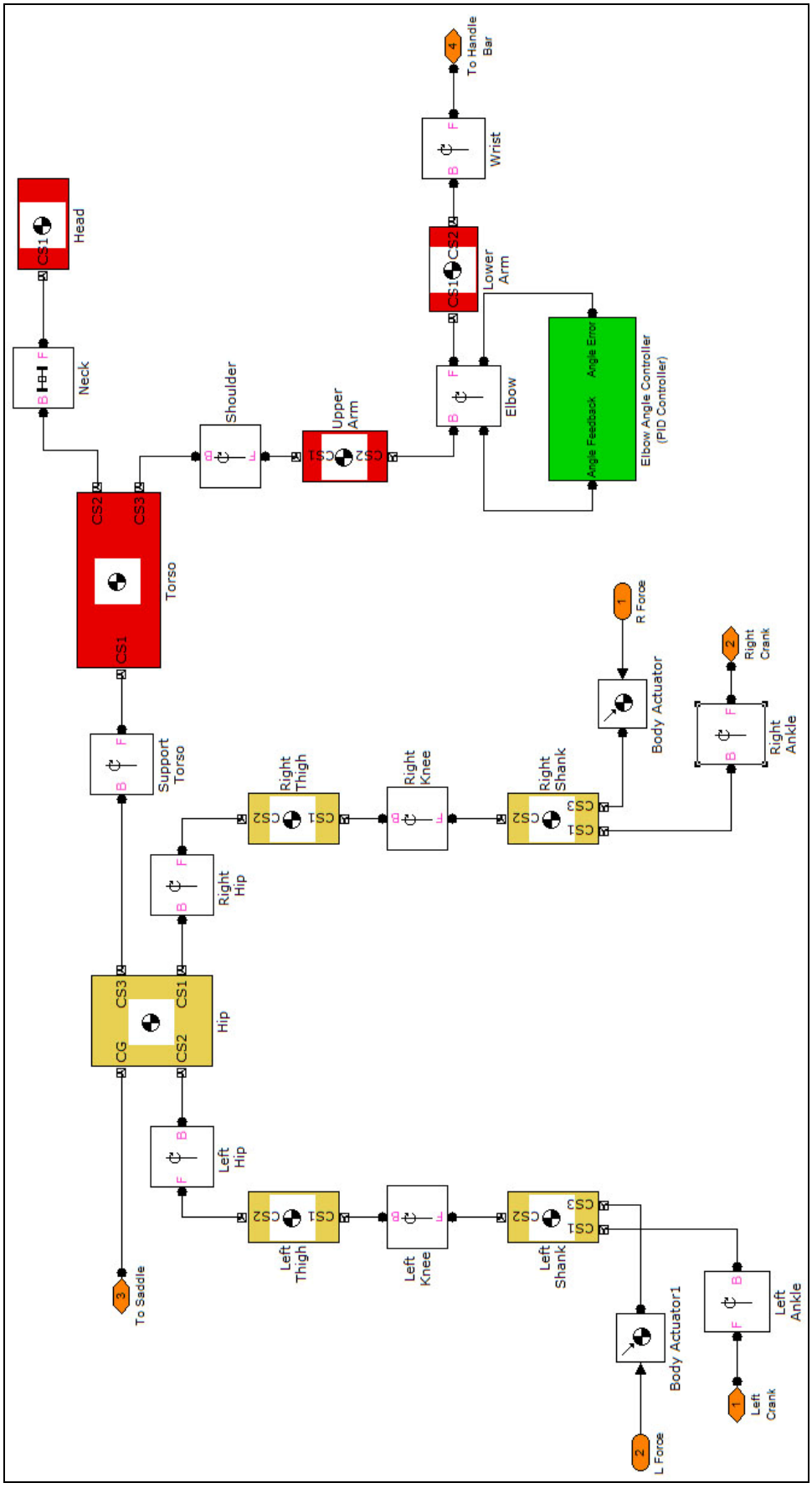

Figure 5.20 Block diagram for a rider

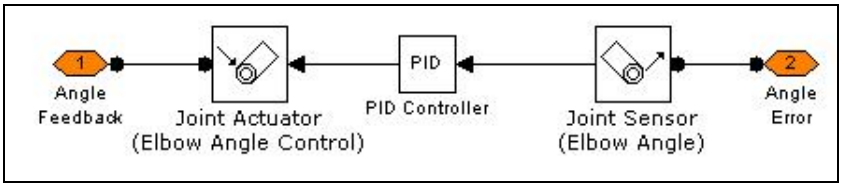

Figure 5.21 Block diagram for the elbow angle control system

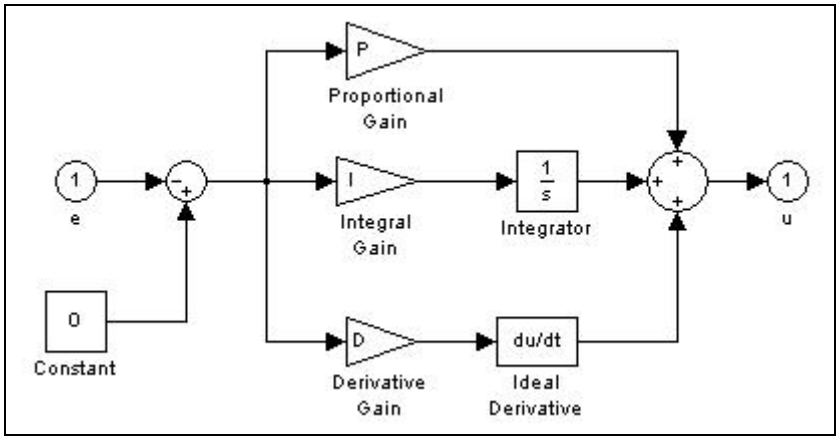

Figure 5.22 Block diagram for the PID controller in elbow angle control system

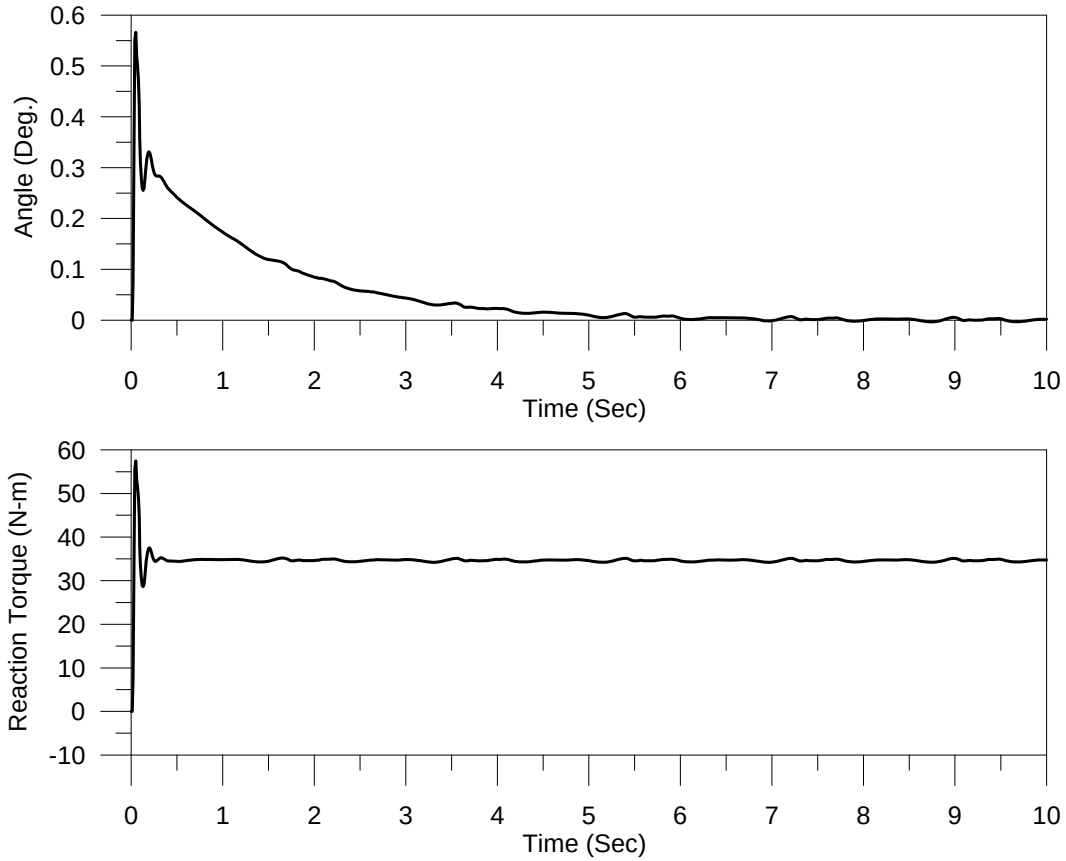

Figure 5.23 Time histories for the angles and reaction torques at the elbow joint

5.5 Rider-Bike System

When the models for a human body and all parts of a bike are developed, they are integrated and connected together as a whole rider-bike system as shown in Figure 5.24. Since movement of a bike requires the pedalling force from the rider, a pedalling controller is developed in Section 5.5.2 for this purpose and the theory used is introduced in Section 5.5.1. In Figure 5.24, the rider-bike system consists of several subsystems, including "hard-tail bike frame", "rear wheel", "front wheel", "front fork", "chain model", "rider" and "crank, pedalling controller, and transmission". The "hard-tail bike frame" is discussed in Section 5.3.1 with block diagram shown in Figure 5.1 and mathematical model shown in Figure 5.2, and the block diagrams and mathematical models for other 4 full suspension bikes are shown in Figures 5.3-5.10, respectively. The "rear wheel" is discussed in Section 5.3.2 with mathematical model and block diagram shown in Figures 5.11 and 5.12, respectively, and the "front wheel" is the same as "rear wheel". The "front fork" is discussed in Section 5.3.3 with block diagram shown in Figure 5.16. The "chain model" is discussed in Section 5.3.4 and shown in Figure 5.18. The "rider" is discussed in Section 5.4 with associated mathematical model and block diagram shown in Figures 5.20 and 5.21, respectively. The "crank, pedalling controller, and transmission" will be discussed in Section 5.5.2 with associated block diagrams shown in Figures 5.25 and 5.26.

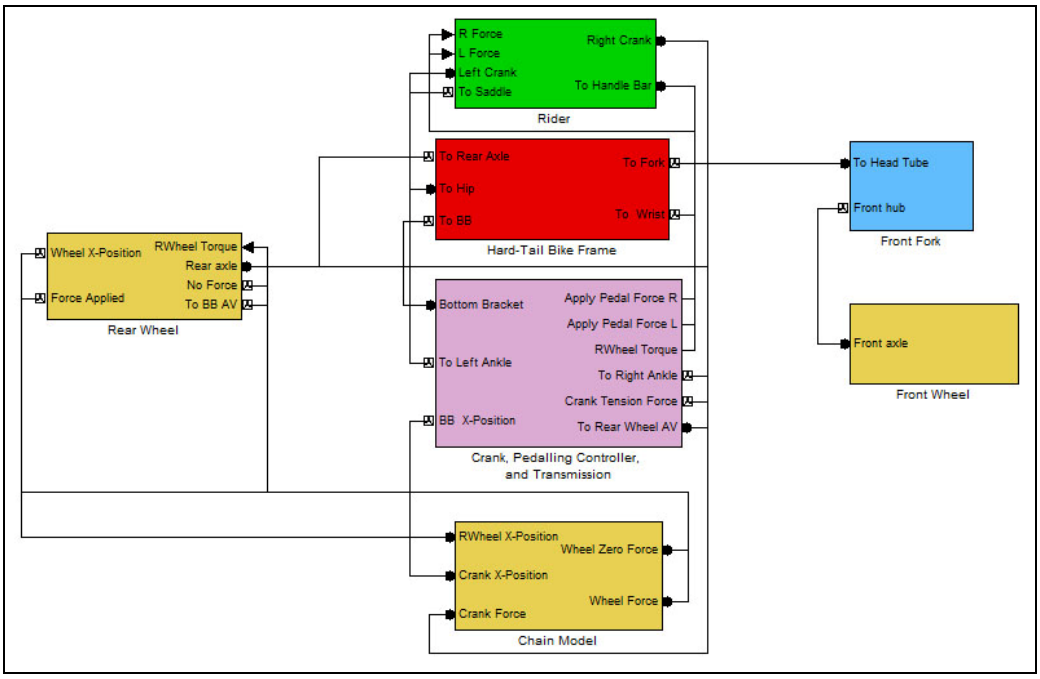

Figure 5.24 Block diagram of rider-bike system (for hard tail bike)

5.5.1 Theoretical Analysis for Parameter Transmission between Sprockets

If the radii of the front and rear sprockets are denoted by r_f and r_r, respectively, and the corresponding angular velocities by ω_f and ω_r, respectively, then, the tangential velocity of the chain is given by (see Figure D.1 in Appendix D)

$$V_t = r_f \omega_f = r_r \omega_r \tag{5.7}$$

Thus,

$$\omega_r = \left(\frac{r_f}{r_r} \right) \omega_f \tag{5.8}$$

If the torque applied on the front sprocket is $T_f(t)$, then the force in the chain is determined by

$$F_f(t) = \frac{T_f(t)}{r_f} \tag{5.9}$$

The force equilibrium in the chain requires that $F_r(t) = F_f(t)$, thus,

$$F_r(t) = F_f(t) = T_f(t) / r_f \tag{5.10}$$

Therefore, the torque applied on the rear sprocket is given by

$$T_r(t) = F_r(t) \cdot r_r = \left(\frac{r_r}{r_f} \right) T_f(t) \tag{5.11}$$

Since the power of a rotating shaft is given by $P = T\omega$, the power developed by the rear sprocket shaft is determined by

$$P_r = T_r \omega_r = \left(\frac{r_r}{r_f} \right) T_f \cdot \left(\frac{r_f}{r_r} \right) \omega_f = T_f \omega_f = P_f \tag{5.12}$$

In Equation (5.12), T_r and ω_r are given by Equations (5.11) and (5.8), respectively.

From Equation (5.8) one has

$$\theta_r = \omega_r t = \left(\frac{r_f}{r_r} \right) \omega_f t = \left(\frac{r_f}{r_r} \right) \theta_f \tag{5.13}$$

Therefore, for the case of $r_f/r_r = 4$, Equation (5.13) produces $\theta_r(t) = 4\theta_f(t)$.

If the external torque $T_r(t)$ on the rear sprocket given by Equation (5.11) can be transformed into external force $F_x(t)$ on the rear wheel (or on the rear axle) by using the next equation

$$F_x(t) = T_r(t)/R_w \tag{5.14}$$

then, from Figure D.3 (in Appendix D) one sees that the average moving speed $V_x(t)$ of the entire bike is given by

$$V_x(t) \approx R_w \omega_r \tag{5.15}$$

Where R_w is the radius of rear wheel and the subscript x of $F_x(t)$ denotes the force to be in the horizontal (x) direction. The actual value of $V_x(t)$ may be smaller than that given by Equation (5.15) due to inertia forces of the entire bike, frictions or sliding on the road surface, etc.

5.5.2 Transmission System and Pedalling Controller

In SimMechanics, one cannot find the function to simulate the chain transmission, although there exists a block Gear Constraint for the constraint between two "engaged" gears based on Equation (5.7). In other words, the two gears must rotate in the opposite directions. Therefore, much time has been spent to test how to simulate the power transmission between bottom bracket and rear wheel by using the other functions of the SimMechanics.

The block diagram of transmission subsystem of the rider-bike system is shown in Figure 5.25, in which, a velocity driver is introduced with one of its ends connected to the crank (CG) and the other end connected to the rear axle. In SimMechanics, the velocity driver can be used to constrain the relative translational and rotational velocities of the two attached bodies [38]. Here, in the velocity driver of the transmission system, the rotational velocities of crank and rear axle are defined, which are 4rpm and 1rpm, respectively. By doing so, when the crank rotates 1 revolution, the rear wheel rotates 4 revolutions, which represents the gear ratio 4:1 (front sprocket : rear sprocket) used in this study.

Three parameters are input the pedalling controller, including the crank angle with unit "degrees", crank angular velocity with unit "deg/sec", and crank angular velocity with the unit "rpm". The output of pedalling controller represents the force applied on right or left pedal. It is evident that when the last force is multiplied by the crank length 0.17m will produce the pedalling torque on the front sprocket, and when the latter is multiplied by 1/4 [see Equation (5.13)] will produce the torque transferred to the rear axle.

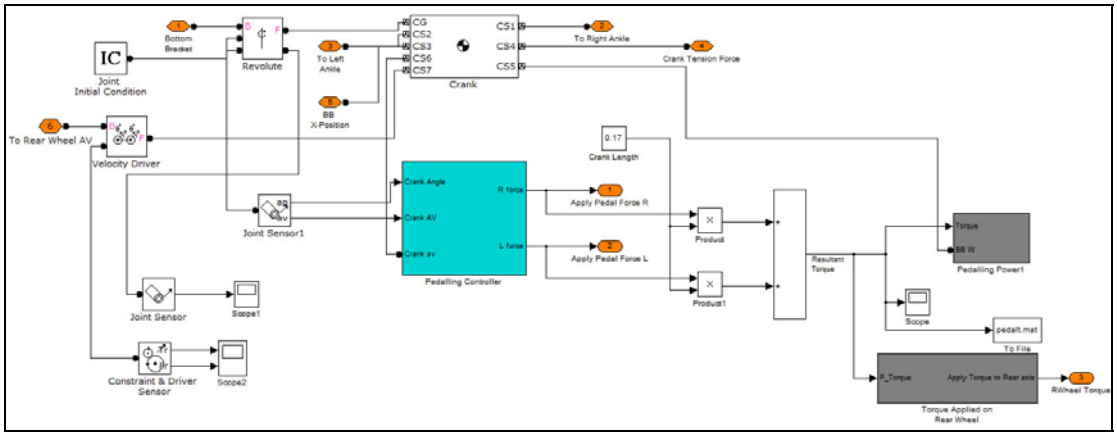

Figure 5.25 Block diagram of (torque) transmission system

The pedalling controller is shown in Figure 5.26. The crank angle with unit “degrees” and crank angular velocity with unit “deg/sec” are input the continuous angle block. In SimMechanics, the range of angle is between -180° and +180°, so when the crank angle reaches -180° (- means the clockwise direction), it jumps to +180° immediately and then decreases to -180° gradually. With the continuous angle block, the crank angle can be accumulated during the simulation. Thus, if the rider pedals 10 cycles, the final crank angle will be 3600°. The output signal from the continuous angle is then sent to the summation block and added by using a "constant block" named "Initial Crank Angle". In this study, the zero crank angle (i.e., θ=0°) is assigned at the position when the right crank is in the “upward” vertical (+ y-axis) direction (see point A in Figure 4.1.), also called top dead centre [17], and when the right crank reaches point C shown in Figure 4.1, the crank angle will be 180°, also called bottom dead centre [17].

In SimMechanics, the initial angle of any object is assumed to be 0°. Since the initial crank angle is given by $\theta_{1,U}$ = 90° - $\theta_{2,U}$ (see Figure 4.2), so the value given in the “constant block” is $-\theta_{1,U}$ = -(90° - $\theta_{2,U}$) (- means the clockwise direction). Then, the signal is sent to the "abs" block to obtain the “absolute value” of crank angle. Afterwards, the signal is divided by 360, and the remainder is obtained through the Math Function block in which the remainder mode is selected. Finally, the remainder is sent to the output block named "Crank Angle Output". Thus, the correct crank angle is obtained and can be output for drawing related figures. For convenience, the initial

crank angle $\theta_{1,U}$ of the five rider-bike systems are summarized in Table 5.10.

In Figure 5.26, the crank angle (before the Continuous Angle block) is transferred into two logical blocks, named “if condition for right pedal” and “if condition for left pedal”, in which the conditions $-180° \le \theta_{\text{right crank}} \le 0°$ and $0° \le \theta_{\text{right crank}} \le 180°$ are introduced, respectively.

The whole effective pedalling stroke is composed of the two half cycles by pedalling the right and left crank from point *U* to point *L* (instead of from point *A* to point *C*) in clockwise direction, respectively, as shown in Figures 4.2 and 4.3. Obtaining the angle α as shown in Figure 4.4, the instantaneous effective pedalling force is determined by $F \cdot \sin(\alpha)$ [with $F \equiv F_2(t)$ denoting the force given by the rider's lower leg (along Rod2) appearing in Equation (4.64)].

Therefore, the condition $-180° \le \theta_{\text{right crank}} \le 0°$ given in the block "if condition for right pedal" means that the rider begins to apply the right pedalling force at right crank angle $-\theta_{1,U}$ (0° in SimMechanics), and ends at the right crank angle $-(180°+\theta_{1,U})$ (-180° in SimMechanics). Then, the condition $0° \le \theta_{\text{right crank}} \le 180°$ given in the block "if condition for left pedal" represents the rider begins to apply the left pedalling force at right crank angle $-(180°+\theta_{1,U})$ (+180° in SimMechanics), and ends at the right crank angle $-\theta_{1,U}$ (0° in SimMechanics). The critical angles and points of the five rider-bike systems are summarized in Table 5.10.

In Chapter 4, the angle α between Rod1 and Rod2 (see Figure 4.4) is 180° when the rider's upper leg is in its uppermost position, as shown in Figure 4.2, and 0° when the rider's upper leg is in its lowermost position, as shown in Figure 4.3. Therefore, the angle α begins from 180° and then reduces to 0° gradually.

By defining the conditions for the two logical blocks "if condition for right pedal" and "if condition for left pedal", the instantaneous angle α is obtained.

After sensing the instantaneous angle of right crank in the two logical blocks, the signal is then transferred to two pairs of action blocks for deciding to apply force on right foot or left foot, or to take no action. Since the two pairs of action blocks are the same with 180° phase difference, only one pair of them is discussed below. The action

block “Right Force” is shown in Figure 5.27. First the instantaneous angle is added by 180° because the initial angle in SimMechanics is 0°, and the initial angle of α is 180° (i.e., $\alpha_{initial}$=180°). Then, the signal is transformed into radians and the sine value of the angle is determined. It is noted that one must transform the “degrees” into “radians”, because the trigonometric block in Simulink can only deal with “radians”. The sine value of the angle is used to determine the instantaneous force component in the tangential direction to produce the “effective” pedalling force. It is evident that the other force component in radial direction has no effect on pedalling [39,78]. In Figure 5.27 the sine value is multiplied by the force in right (or left) lower leg to produce the “effective” pedalling force. Furthermore, a constant named “Force applied”, [0 -10 0] N is used, which is a downward vertical force applied at Joint 1.

When the right crank passes the point L in Figure 4.3 (i.e. 180°+$\theta_{1,U}$), the upward stroke begins with no force being applied, so the signal is transferred to the "No Force" subsystem with the constant given by [0 0 0]N.

After running through each of the two pairs of action blocks, one can back to Figure 5.26 to merge the two signals together by using the merge block.

In Figure 5.26, a block named “Crank av” at the downward part of the pedalling controller is used to sense the angular velocity of crank first with the unit of rpm. The actual angular velocity of crank is then subtracted by the desired angular velocity 86rpm (a cadence adopted by elite mountain bikers during competition). The error signal then goes to the PID controller block, in which the PI mode is used with K_p=10 and K_i=0.1.

After the PID controller, the corrected signal is sent to multiply with the original given force given by [0 -10 0]N to amplify the pedalling force. Finally, two saturation blocks are added to the right and left pedalling forces, respectively, to make sure the applied force is not too big so that human cannot reach.

In the work of Soden and Adeyefa [77], it has been reported that a rider with weight 570N can apply the maximum pedalling force approximately equal to his body weight in an indoor experiment and another rider with weight 660N can apply a pedalling

force 1448N (more than twice of his body weight) in an outdoor experiment. In the outdoor experiment, the rider is to ride on level (uphill) ground with standing posture and the bike used in [77] is a road bike.

The standing (riding) posture is not studied in this thesis, and for convenience, the maximum pedalling force is assumed to be 1000N. Now based on the signals concerned the pedalling forces on right and left cranks are applied, respectively.

One problem occurs in the pedalling controller. The rider's right and left upper legs are located at their uppermost (α=180°) and lowermost (α=0°) positions at the start of simulation, respectively, so no “effective” pedalling force is applied because sin180°=sin0°=0, and the rider-bike system stays in stationary condition. To solve this problem, one block "Joint Initial Condition" is added to the Revolute Joint (the bottom bracket), as shown in Figure 5.25, in which a small initial angular velocity 1 rpm is given. Thus, the rider can pedal normally.

With the output data regarding the pedalling forces and the "Crank Angle Output", one can obtain the relationship between the effective pedalling forces and the crank angles successfully.

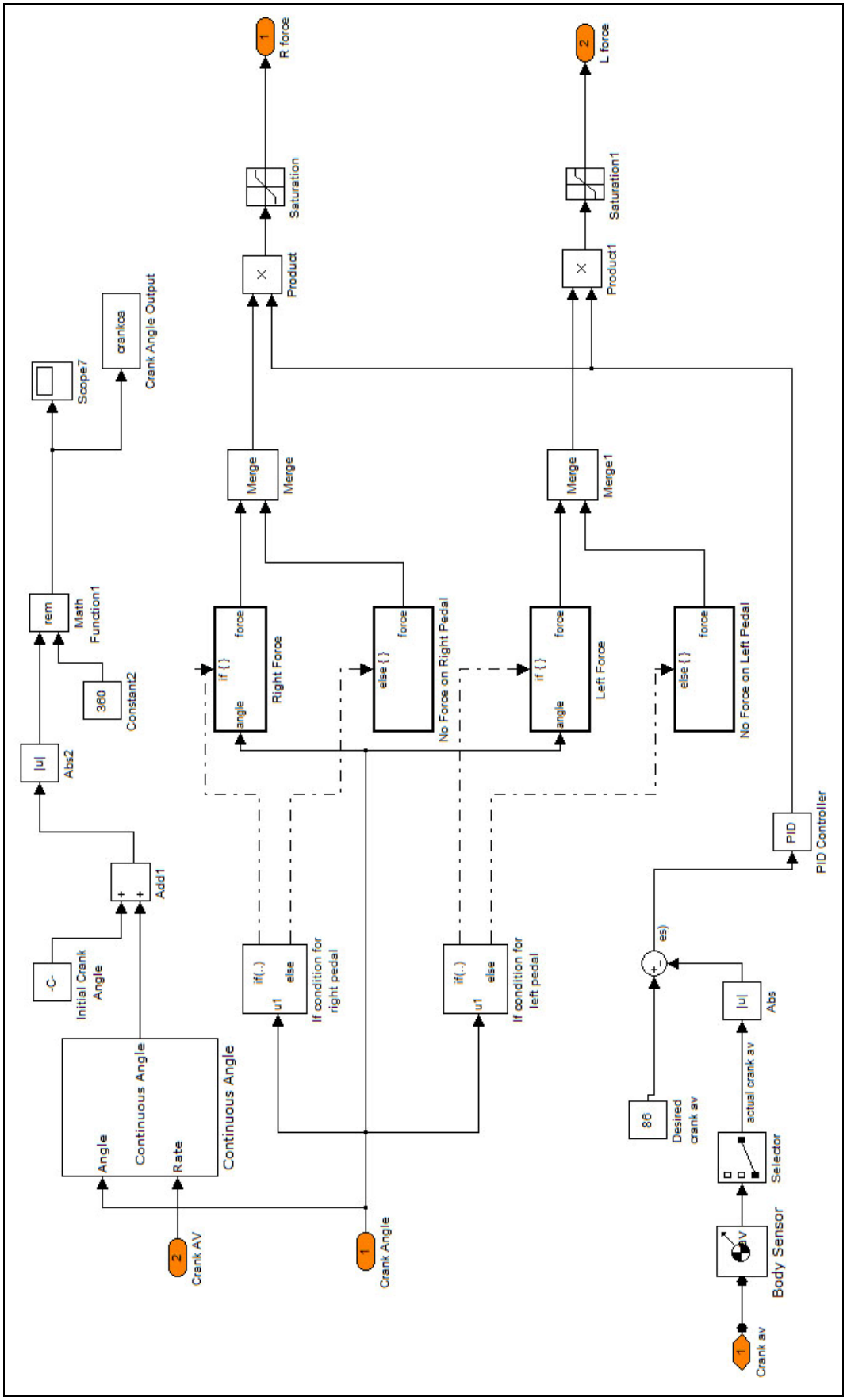

Figure 5.26 Block diagram of pedalling controller

Table 5.10 Critical angles and points of pedalling strokes

Angle	Hard Tail	Single Pivot	Horst Link	Faux Bar	VPP
TDC	0°				
$\theta_{1,U}$	22.067°	24.724°	27.795°	25.875°	23.396°
BDC	180°				
180°+$\theta_{1,U}$	202.067°	204.724°	207.795°	205.875°	203.396°
TDC: Top dead centre (see point *A* in Figure 4.1) BDC: Bottom dead centre (see point *C* in Figure 4.1) $\theta_{1,U}$: Beginning of pedalling (down) stroke (see point *U* in Figure 4.2) 180°+$\theta_{1,U}$: End of pedalling (down) stroke (see point *L* in Figure 4.3)					

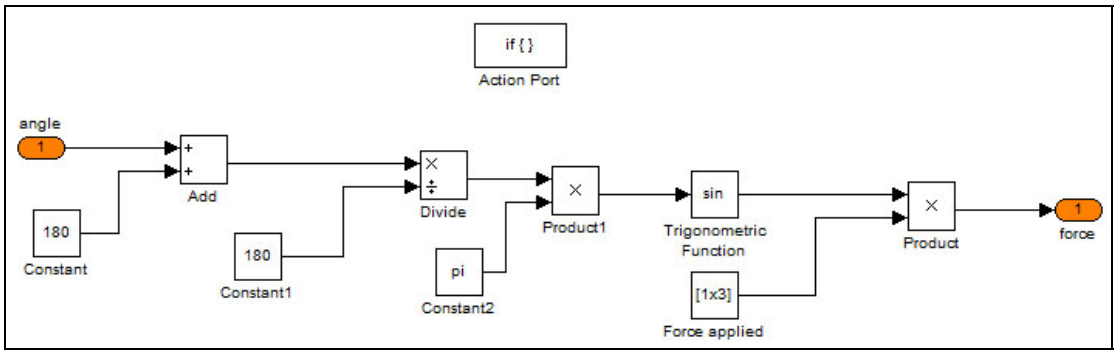

Figure 5.27 Block diagram for "Right Force" in the pedalling controller

With the pedalling controller, the simulation shows the rider's pedalling motion on the bike correctly, as shown in Figures 5.28 and 5.29. In order to move the bike forward on the ground, two velocity drivers are added to the front and rear wheels, respectively; and in order to constrain both the relative translational and rotational velocities between the wheels and ground, two constraints, V=1m/s and ω=0.3rad/s, are defined with V denoting the translational velocity and ω denoting the rotational velocity.

After developing the pedalling controller and the rolling constraints (the velocity drivers for constraining the motions between wheels and ground), the rider-bike system can move forward normally. However, the air resistance and friction resistance are not considered. Therefore, a joint damper is added to the rear axle to represent the total mechanical loss of the rider-bike system. The damping coefficient can be

adjusted according to the desired velocity of the rider-bike system. A discussion of using the damping force to represent the mechanical loss in the rider-bike system is shown in Appendix E. The damping constant used in this study is 3 N-sec/m.

5.5.3 Bump Model

As mentioned in Section 5.3.2, the bump model is a series of variables of the instantaneous positions of CG of the wheel in *y*-direction together with the corresponding time instants given in an “m-file”, represented by the block "bump" shown in Figure 5.14. If the *y*-axis position of CG of wheel keeps at 0m, then the last information indicates that road surface is flat.

In the complete rider-bike system, the front and rear wheels must be added, so two identical bump models are given to front and rear wheels, respectively. The only difference between the two bumps is due to the time instants. The front bump defines the *y*-axis position of CG of the front wheel and the corresponding time instant, and the rear bump is defined based on Reference [2]. Each time moment of the rear bump must be added by the time difference Δt given by Equation (5.16), where d is the distance between the front and rear axles (wheelbase), and v is the forward velocity of bike.

$$\Delta t = \frac{d}{v} \tag{5.16}$$

5.5.4 Simulation of Rider-Bike System Moving on Flat Road Surface

First of all, a simulation of the rider-bike system (for hard tail bike) moving on flat road surface is implemented to observe the dynamic response of the developed rider-bike model. The simulation condition of this section is that the rider-bike system with the hard tail (HT) bike moving on the flat road surface will lead to the steady pedalling cadence 86 rpm and result in the convergence of forward velocity to about 11.96 m/s at the instant $t \approx 11$sec.

For the first step, the time history for the original pedalling force obtained based on the two signals after "Merge" block shown in Figure 5.26 is presented, as shown in Figure 5.28. When the simulation begins, the rider applies right pedalling force first. The right pedalling force becomes bigger during the downward pedalling stroke and reaches maximum -10N at t=1.45sec with the angle α=90°. Then the force begins to decrease gradually and reaches to 0N at t=1.74sec, which is the time that right pedal reaches the point L in Figure 4.3. Immediately after t=1.74sec, the rider begins to apply force on left pedal. At t=2.22sec, the rider stops applying force on left pedal since the left pedal reaches the point L in Figure 4.3. After that, another pedalling cycle begins. Therefore, the alternate pedalling is achieved. In addition, as the angular velocity of crank reaches the desired value 86 rpm, the cycling time becomes shorter. The result shown in Figure 5.28 is not constrained by the saturation blocks to restrict the maximum pedalling force.

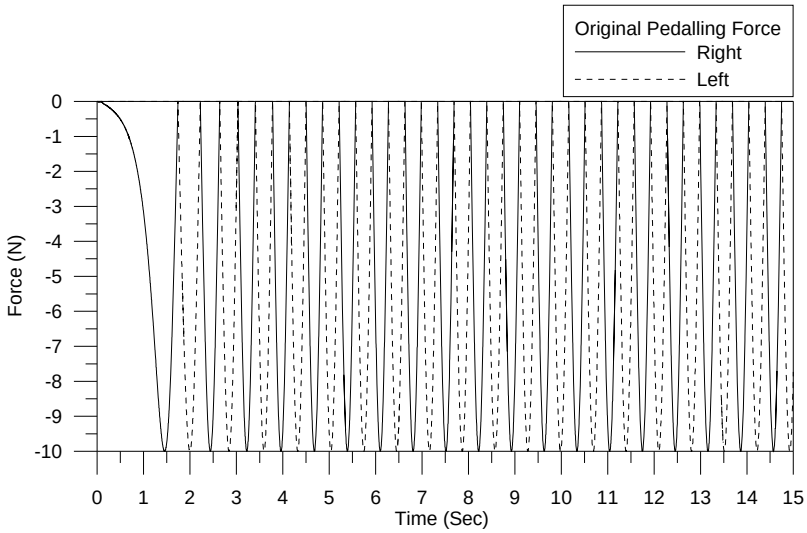

Figure 5.28 Time history for the original pedalling force

After the force signal is controlled by the PI controller, the result without constraint of the saturation blocks is shown in Figure 5.29. As one can see the maximum pedalling force is near 5000N (4630.34N), which is beyond capacity of the general strength of human. Therefore, the saturation block is used to constrain the pedalling force to be less than or equal to 1000N, and the result is shown in Figure 5.30. From Figure 5.30 one sees that for the first pair of pedalling forces, the right pedalling force ends at t=2.32sec and the left one ends at t=3.14sec, respectively, which are slower than the corresponding ones shown in Figure 5.29, but closer to the real riding condition.

In Figure 5.30, the pedalling force is near steady condition at about t=11sec when the angular velocity of crank reaches the desired value 86 rpm. The final pair of right and left pedalling forces in the time interval from t=13.72sec to t=14.42sec are shown in Figure 5.31 with the abscissa denoting the crank angle.

The crank angle of rider-bike system of hard tail bike has reached 5400° (i.e. 15 pedalling cycles) before t=13.72sec. For convenience, the crank angle shown in Figure 5.31 during the time interval between t=13.72sec and t=14.42sec is assigned to be between 0° and 360°, in which the two red chain lines are located at crank angles $\theta=\theta_{1,U}$ and $\theta=180+\theta_{1,U}$, respectively, and the three blue dashed lines are located at crank angles θ=90°, θ=180°, and θ=270°, respectively.

When the rider-bike system reaches the steady condition (with angular velocity of crank being 86 rpm), the right and left pedalling forces shown in Figure 5.31 are almost the same, in which the right pedalling force reaches the maximum 248.65N at the crank angle θ=100.96°, while the left pedalling force reaches the maximum 248.62N at the crank angle θ=280.47°. The two critical crank angles appear at the moment of the angle α=90° (i.e. the rider's lower leg is orthogonal to the crank). From Figure 5.31, one can see the right and left pedalling forces start at crank angles $\theta=\theta_{1,U}$ and $\theta=180+\theta_{1,U}$, respectively.

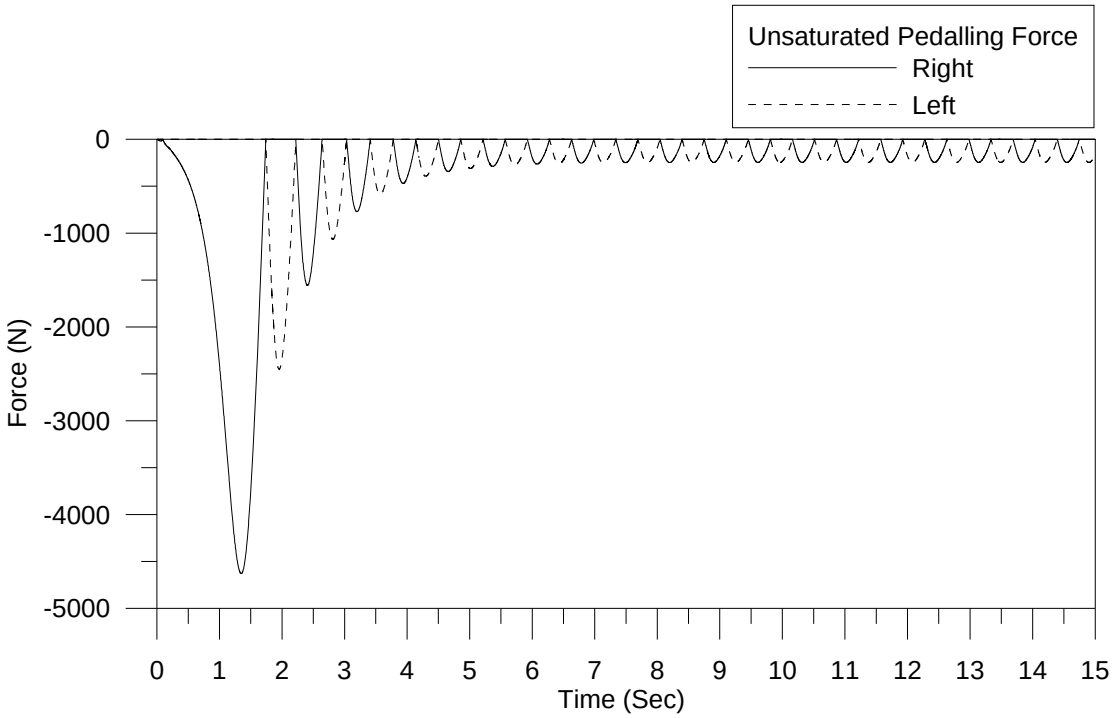

Figure 5.29 Time history for unsaturated pedalling forces

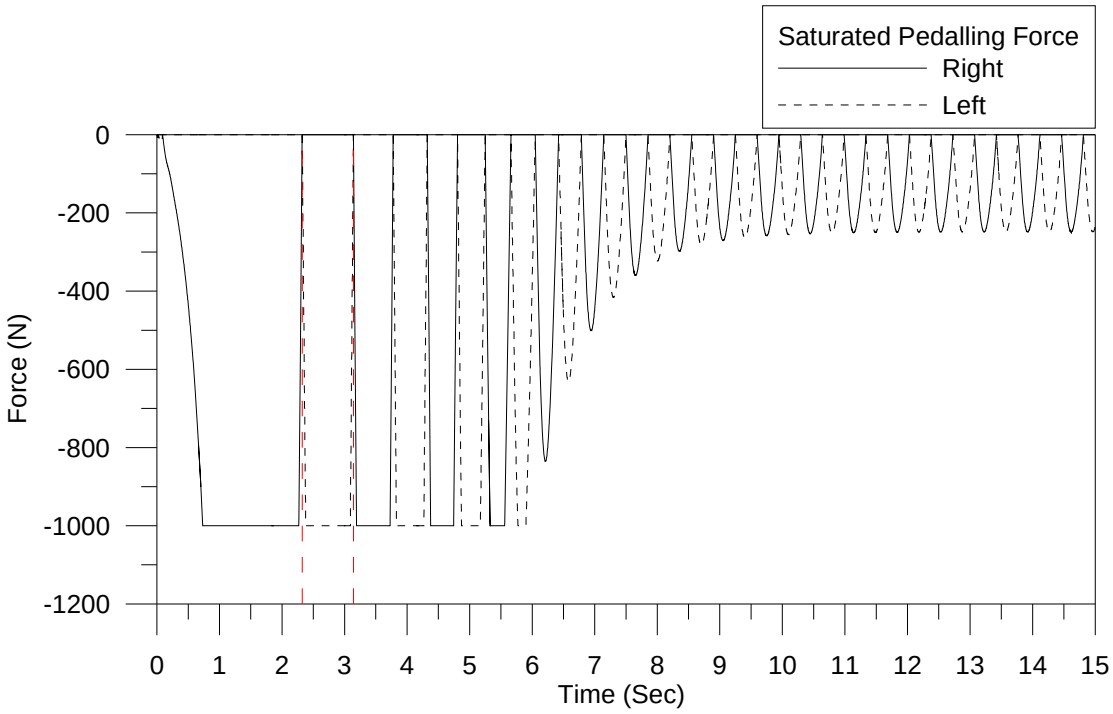

Figure 5.30 Time history for saturated pedalling forces

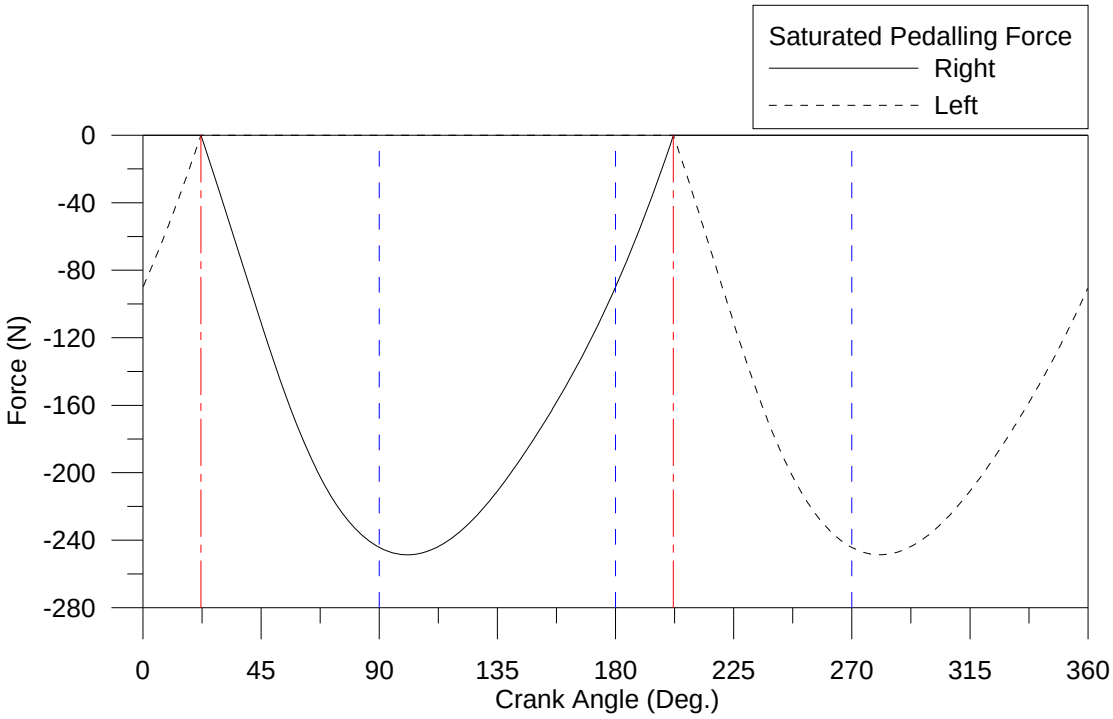

Figure 5.31 The relationship between the final pair of pedalling forces shown in Figure 5.30 and the corresponding crank angles θ with θ=0° at top dead centre

The angular velocities and torques for crank and rear wheel are shown in Figures 5.32 and 5.33, respectively. From Figure 5.32, one can see that the angular velocity of rear wheel is four times larger than that of crank during the simulation. By means of the PI controller, the actual angular velocity of crank reaches the desired value 86 rpm about at the moment t=8.39sec (the first moment for the crank and rear wheel reaching the desired angular velocity) and that of rear wheel reaches 344 rpm approximately, and then keep at the steady condition. Meanwhile, when the rider-bike system reaches the steady condition, the applied torque on rear wheel is 10.56N-m, which is four times smaller than that of the pedalling torque (42.27N-m) as one may see from Figure 5.33. The pedalling power and rear-wheel power are shown in Figure 5.34, it is seen that the power developed is about 382.05Watts when the rider-bike system reaches the steady condition. Since the foregoing results agree with the "theory" introduced in Section 5.5.1, the velocity driver added between bottom bracket and rear wheel is satisfactory for achieving the expected results.

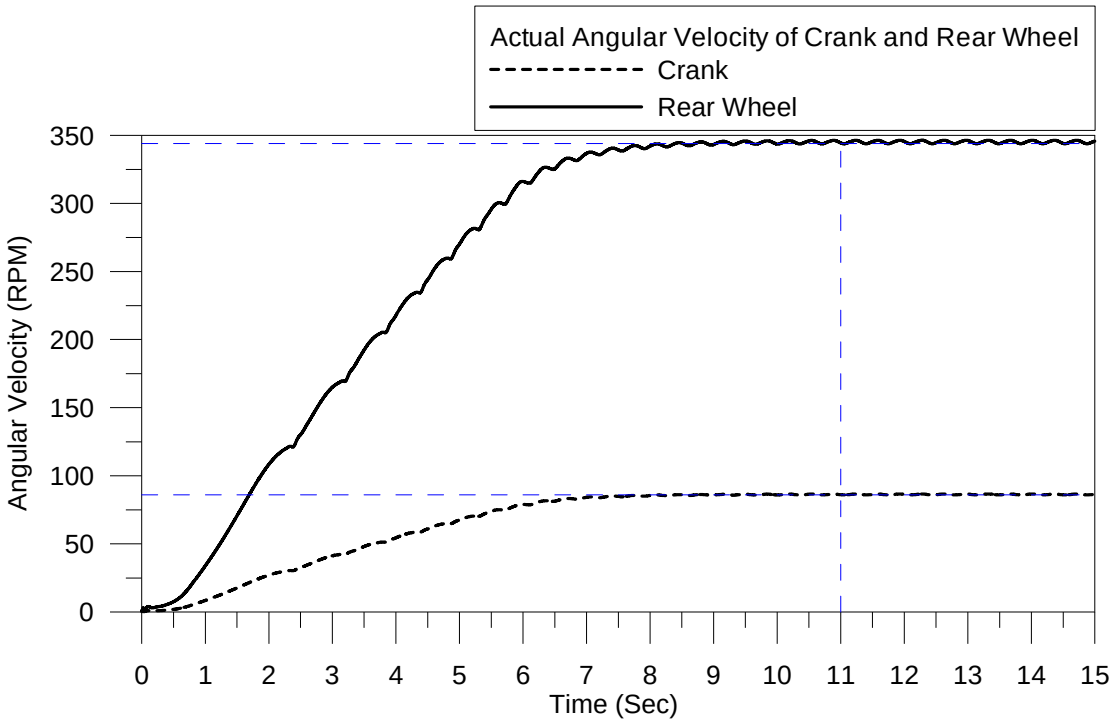

Figure 5.32 Time histories for actual angular velocities of crank and rear wheel

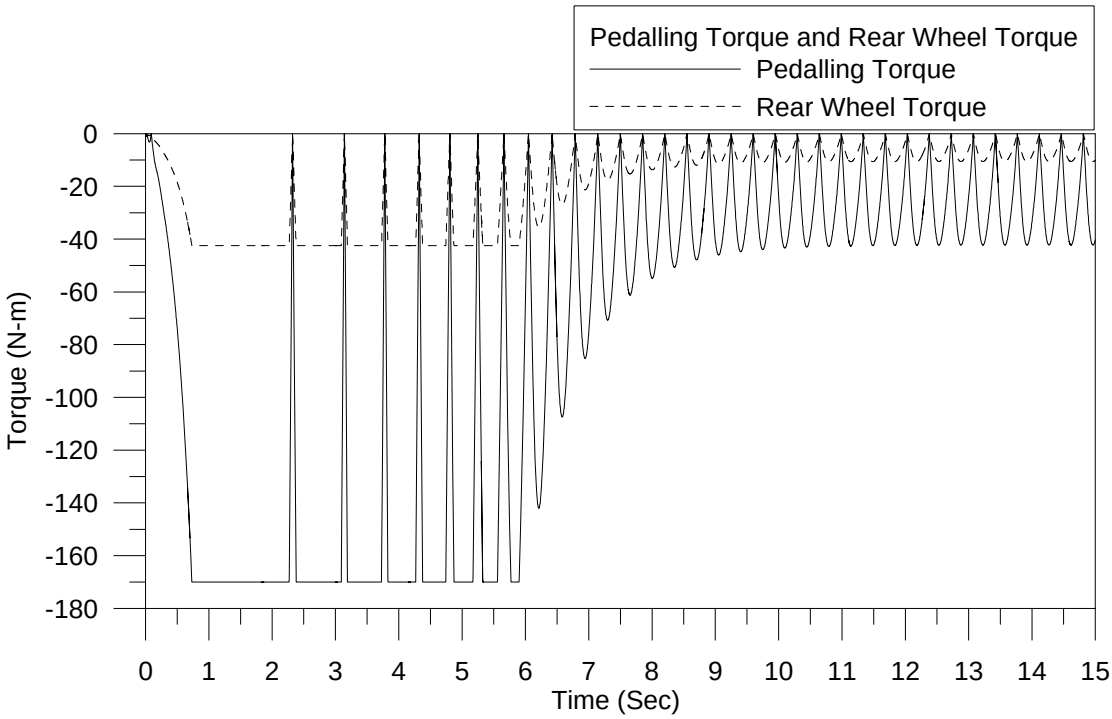

Figure 5.33 Time histories for pedalling torques and rear-wheel torques

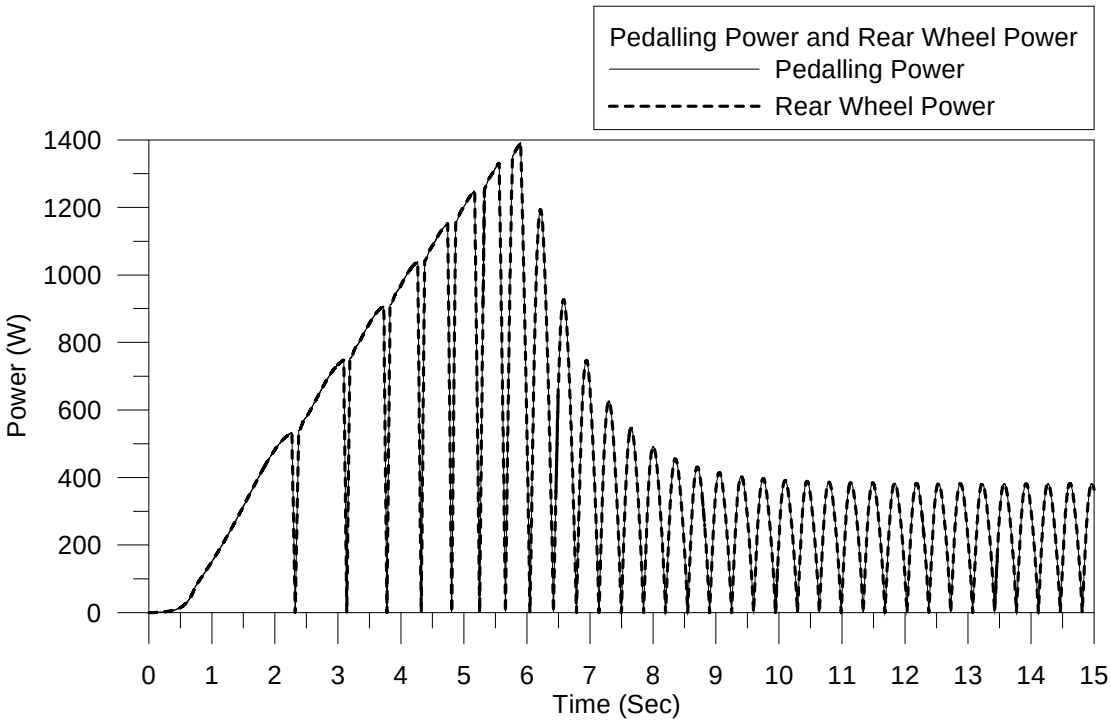

Figure 5.34 Time histories for pedalling power and rear-wheel power

The time history for the forward velocity of the rider-bike system in x-direction (V_x) is shown in Figure 5.35. Due to the joint damper added at rear axle, the moving velocity finally converges to about 11.96 m/s (43.056 km/hr) at about t=11sec.

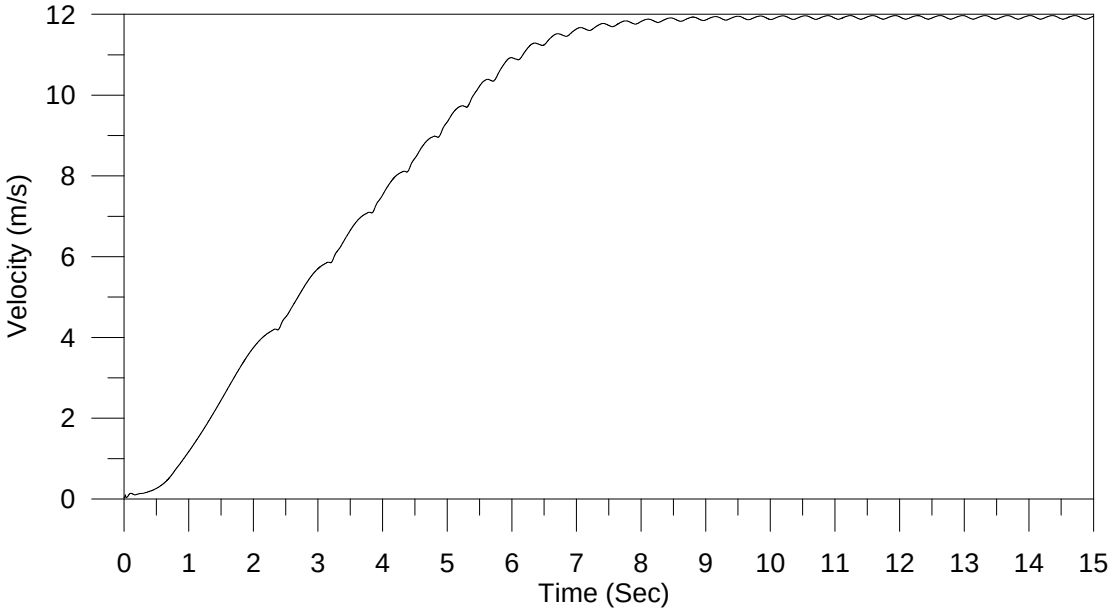

Figure 5.35 Time history for the forward velocity of rider-bike system in x-direction (V_x)

The time histories for the velocity components of front and rear wheels in y-direction (V_y) are shown in Figure 5.36. Both wheels have a slightly negative vertical velocities at the beginning due to the rider's weight applied on the bike (mainly at seat and handle bar). When the rider pedals to move the bike forward, the excitation resulting from the pedalling motion changes the contact force, so does the vertical velocity. However, it is seen that the vertical velocity of front wheel is smaller than that of rear wheel. This is due to not only the applied force on handle bar being less than the that on seat, but also the front fork absorbing some part of the excitation.

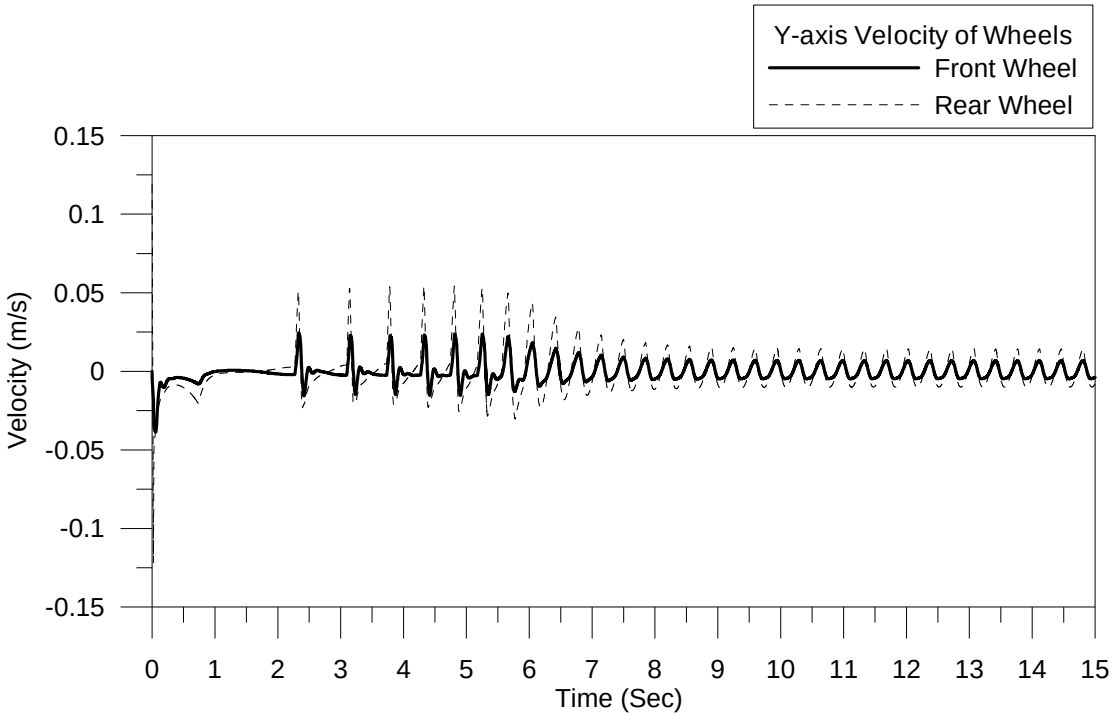

Figure 5.36 Time histories for the velocity components of front and rear wheels in the vertical (y-) direction (V_y)

The time histories for the contact forces between ground and wheels are shown in Figure 5.37. The front and rear wheels have big contact forces 535.49N and 1218.38N, respectively, at the start of simulation due to the same reason as the y-axis velocities. When the pedalling force decreases to the steady condition due to the angular velocity of crank reaching the desire value, the contact forces of front and rear wheels decrease to 496.08N and 694.19N (the maximum contact forces), respectively. Obviously, the contact force of rear wheel is bigger than that of front wheel due to the fact that the

CG of the rider's body is closer to the rear axle and the front fork absorbs some part of the pedalling force. Usually, a vehicle with bigger contact force between wheel and ground has more stable traction control. Therefore, although the main function of the suspension system is for the comfort of the vehicle's passengers, it must also be adjustable to produce adequate contact force between ground and wheel for achieving good traction control. Of course, the last requirements must also be satisfied by the suspension systems of the mountain bikes.

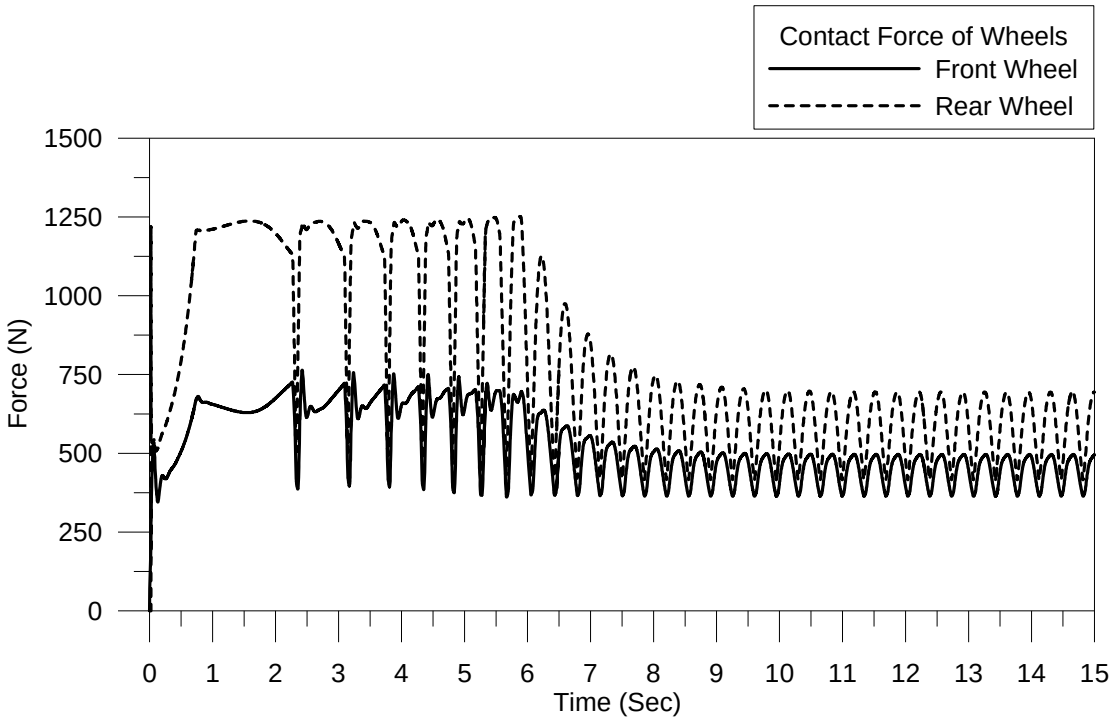

Figure 5.37 Time histories for the contact forces of front and rear wheels

The time history for the fork compression is shown in Figure 5.38. Based on the discussion of front fork in Section 5.3.3 and the defined stiffness constant and damping constant, the fork is compressed to the maximum -8.87mm at the moment t=2.27sec, and then gradually decreases as pedalling force lowers down. After the desired angular velocity of crank 86 rpm is reached, the fork has a slightly fluctuation between -5.96mm ~ -4.32mm, which means that the compression is only 1.64mm..

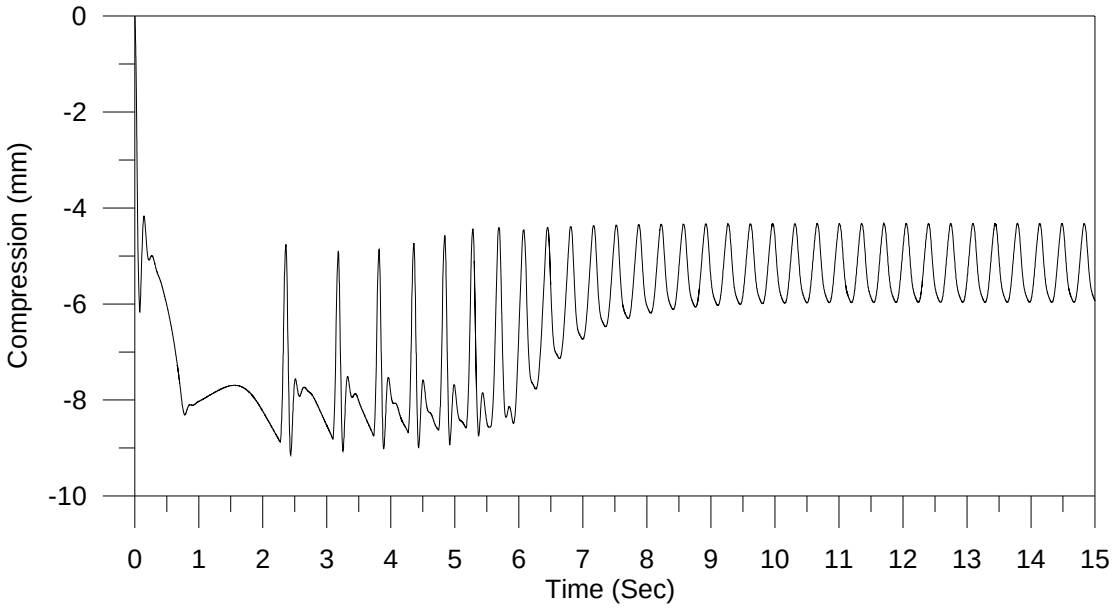

Figure 5.38 Time history for the fork compression

The time histories for the elbow angle and the reaction torque at elbow joint are shown in Figure 5.39(a) and (b), respectively. From Figure 5.39(a) one sees that, initially, the elbow angle has a big fluctuation due to falling down of the rider's upper body. Immediately, the PI controller begins to control the elbow joint to prevent the upper body from falling down. Due to the influence of the fork compression, the elbow angle has a slight fluctuation. After the rider-bike system reaches the stable condition, so that the elbow angle decreases to 0° gradually and the reaction torque remains at about 35N-m as in the static analysis.

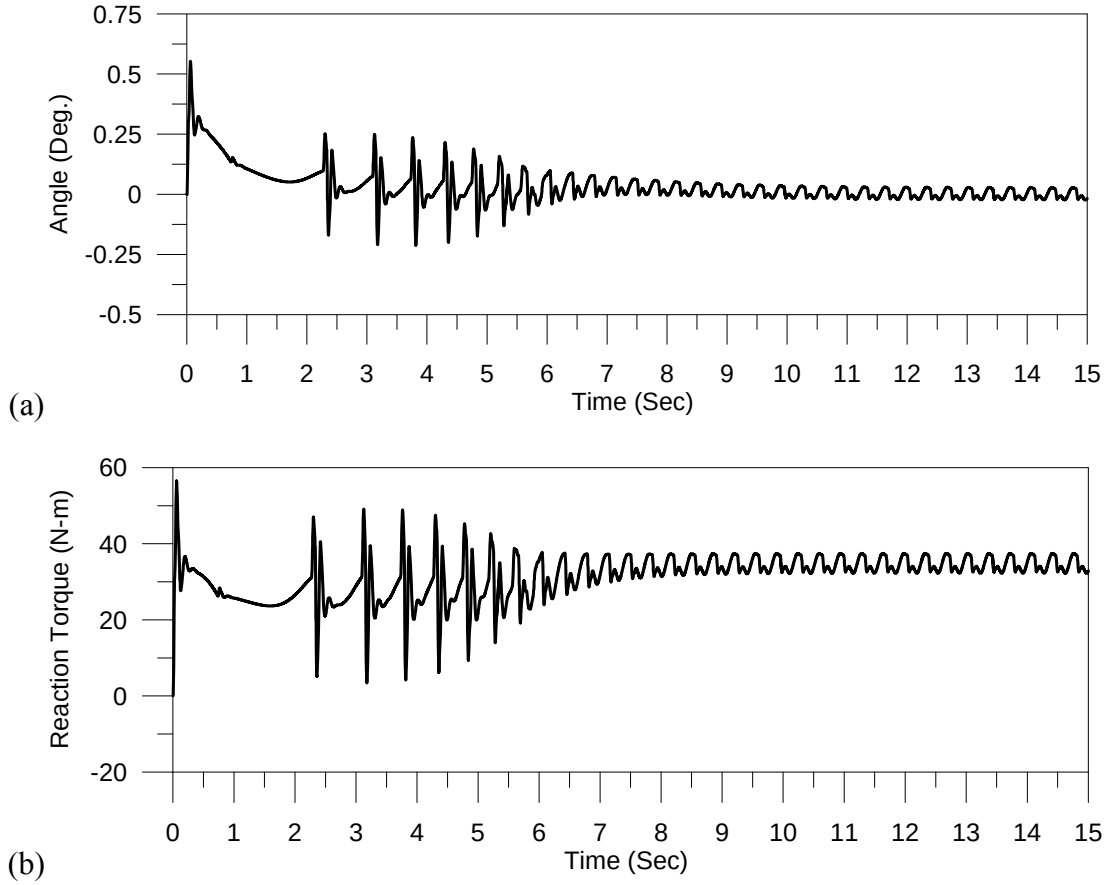

Figure 5.39 Time histories for (a) the elbow angle and (b) reaction torque of elbow joint for riding on flat road surface

The time history for the sprocket distance (between bottom bracket and rear axle) is shown in Figure 5.40. The initial sprocket distance of the hard tail bike is 0.42544m. From Figure 5.40 one sees that the biggest change of sprocket distance during the simulation is about 0.2mm. This change of sprocket distance is negligible, because there exists no rear suspension system in the hard tail bike. In addition, since the ordinates of curve shown in Figure 5.40 subtracted by the initial sprocket distance are always less than 0m, no forces are applied on the bottom bracket and the rear axle.

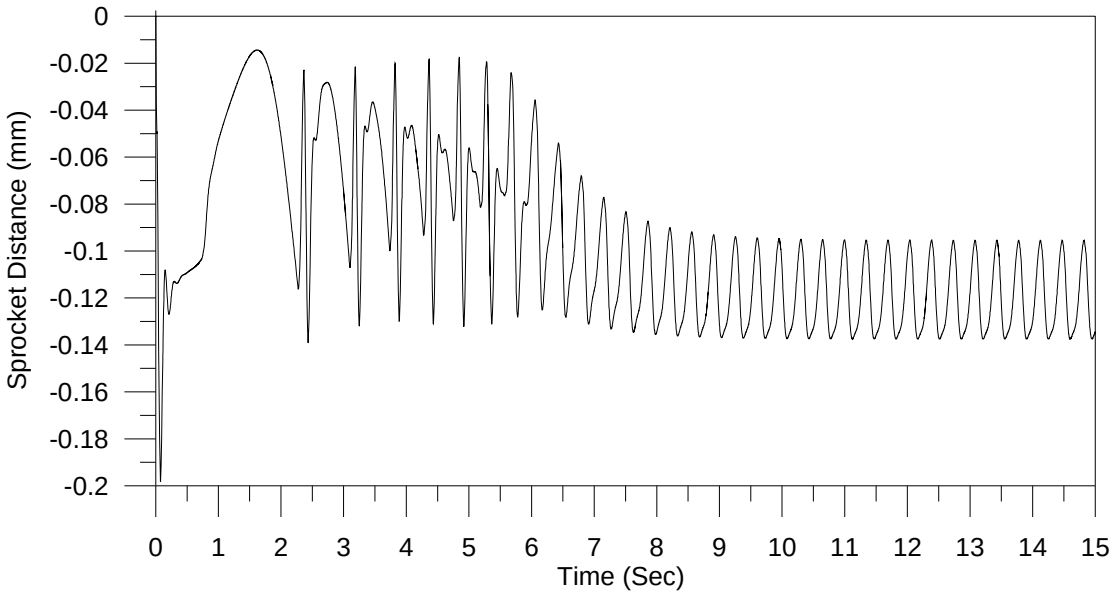

Figure 5.40 Time history for the sprocket distance

The time histories for the reaction force components at right and left ankle joints in the horizontal (x-) direction, $R_x(t)$, are shown in Figure 5.41(a) and the time histories for the corresponding ones in the vertical (y-) direction, $R_y(t)$, are shown in Figure 5.41(b). From the figures one sees that: (i) For either $R_x(t)$ or $R_y(t)$, the time histories of the right ankle joint are similar and not identical to those of the left one because of the time difference $\Delta t=\pi/\omega$ between them. (ii) Throughout the entire time histories, the amplitude of $R_y(t)$ is much greater than the corresponding one of $R_x(t)$, because the pedalling force is in the vertical (y-) direction. Furthermore, the increase of $R_x(t)$ is always accompanied by the decrease of the corresponding $R_y(t)$, because their resultant must be equal to the applied force. (iii) After time t=11 seconds, the rider-bike system reaches the steady condition gradually as one may see from Figure 5.35, so does the fluctuation of the time histories of $R_x(t)$ or $R_y(t)$. (iv) The smaller the moving speed of the bike in the horizontal (x-) direction, the greater the resistance of the ankle joint to the vertical force, thus, the magnitude of $R_y(t)$ is much greater than that of the corresponding $R_x(t)$ before time t=11 seconds (due to the smaller bike velocity).

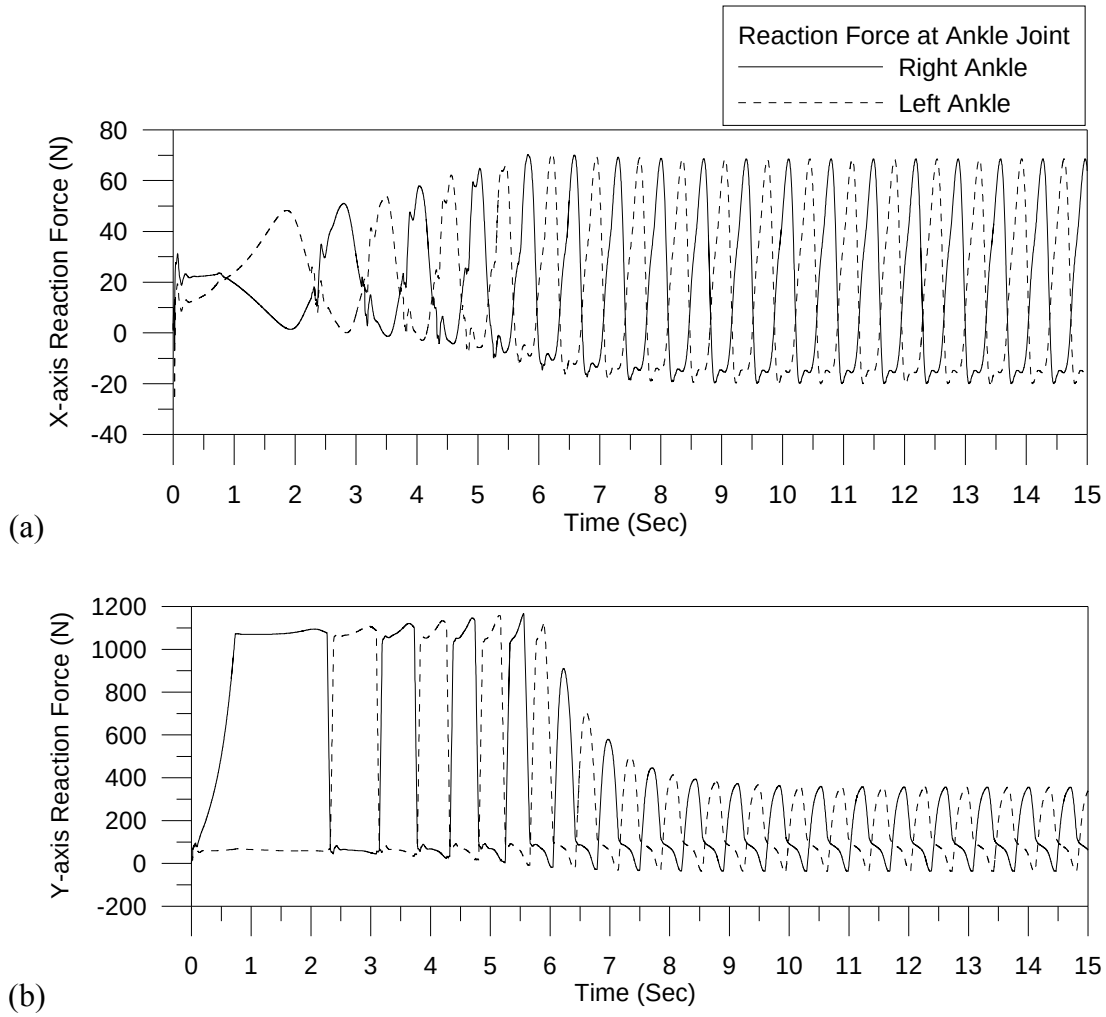

Figure 5.41 Time histories for the reaction force components at right and left ankle joints: (a) in the horizontal (*x*-) direction, (b) in the vertical (*y*-) direction.

5.6 Confirmation of Theoretical Results with Experimental Values of Literature

For the *reference rider* (with $L_2 = L_3 = 0.4$ m) riding the *reference bike* (with $L_1 = 0.17\,\text{m}$, $x_c = 0.135\,\text{m}$, $y_c = 0.555\,\text{m}$), according to the theory of Chapter 4 one obtains the crank angles corresponding to the *beginning* and *end* of "downstroke" of each pedalling cycle to be $\theta_{1,U} = 27.36598^o$ and $\theta_{1,L} = 199.80839^o$, respectively, as one may see from Table 4.1. Since Rod1 and Rod2 are on a *straight line* at the "beginning" of downstroke and they are *overlap each other* at the "end" of downstroke, the normal forces to the crank (Rod1) are equal to zero at those two points [see pints *U* and *L* in Figure 5.42]. Based on the last statement one sees that the retarding (or reverse) force due to the other leg (in the upstroke) in the time history curves shown in Figure 5.42 is (see line $\overline{UL}$ in the figure)

$$F_t' \approx 125\,\text{N} \tag{5.17}$$

From Figure 1(b) of Reference [45] one also sees that the average maximum pedalling forces is (see Figure 5.42)

$$|F_t'|_{\max} \approx 375\,\text{N} \tag{5.18}$$

(c)

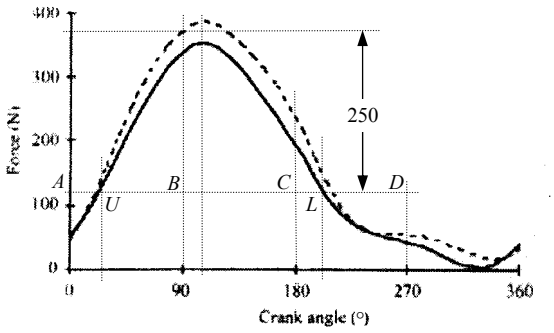

Figure 5.42 Time history of normal pedalling forces (tangential to the circular path of crank pin) $F_t(\theta_1)$ based on Figure 1(b) of Reference [45].

Thus, the average maximum "effective" pedalling force is given by

$$| \overline{F}_t |_{\max} \approx | F_t' |_{\max} - F_t' = 250 \text{ N} \tag{5.19}$$

Figure 5.31 or Table 6.4 reveals that the maximum effective pedalling force of the hard-tail bike is

$$| F_t |_{\max} = 248.65 \text{ N} \tag{5.20}$$

From Equations (5.19) and (5.20), one sees that the result of this thesis (obtained from engineering mechanics and computer simulations) is very close to that of Reference [45] (obtained from biomechanics and experiments).

Since the crank length is $L_1 = 0.17$ m and the corresponding rotating speed is $\omega_e = 9.0$ rad/sec, the peak crank torque $T_{\max}$ and peak power $P_{\max}$ are given by

$$T_{\max} = | F_t |_{\max} L_1 = 248.65 \times 0.17 = 42.27 \text{ Nm} \tag{5.21}$$

$$P_{\max} = T_{\max} \omega_e = 42.27 \times 9.0 = 380.43 \text{ Nm/sec} = 380.43 \text{ Watt} \tag{5.22}$$

The above values of $T_{\max}$ and $P_{\max}$ agree with those shown in Figures 5.33 and 5.34 or Table 6.5.

As shown on page 140 of the thesis, the crank angle corresponding to the maximum effective pedalling force is

$$\theta_{1,peak} = 100.96^o \tag{5.23}$$

The above value also agrees with that shown in Table 2 of Reference [45]: $103^o \pm 6.9^o$.

5.7 Conclusion

In this chapter, the mass moments of inertias for the members (or components) associated with the entire rider-bike system are determined. The details concerning the block diagrams and mathematical models of various rider-bike systems are presented. By using the SimMechanics, the rider-bike system models for a rider body and five types of mountain bikes are developed. A rider-bike system for a hard tail bike is used to test the dynamic response of the bike. Since the developed rider-bike system works well and the theoretical results are very close to the experimental values of literature, the behaviours of the rider-bike systems for different bikes passing through different bumps will be studied in the next chapter. In addition, in the developed rider-bike system model shown in Figure 5.24, the bike model is the hard tail. If a new bike frame model is developed in SimMechanics, the new bike model can be fitted into the rider-bike system model easily.

Chapter 6 Quasi-static and Dynamic Analyses of Bare and Loaded Bikes in Stationary and Moving Conditions without Bumps

6.1 Introduction

In order to compare the characteristics of different mountain bikes, both quasi-static and dynamic analyses are implemented and discussed in this chapter. For quasi-static analysis, the response of rear suspension systems due to a vertical downward sinusoidal force applied on the seat or handlebar of each bike is studied. For the dynamic analysis, the dynamic response of the rider-bike system for five different types of bikes passing through different terrains are discussed, where the mathematical model of each rider-bike system takes the form as shown in Figure 5.19, while the terrains indicate the flat road surfaces "without" bumps. As to the flat road surfaces "with" bumps, the characteristics of the five rider-bike systems are studied in the next chapter.

For convenience, a bike without the rider on its seat is called a "bare bike" and the one with the rider on its seat is called a "loaded bike", a bike with zero forward velocity is called a "stationary bike" and the one with non-zero forward velocity is called a "moving bike". Furthermore, the response of a stationary bike due to the "dynamic" or "impulsive" load is called "quasi-static" response and that due to the "static" load is called "real-static" response. For example, the (front) fork compression for a stationary bike due to a sinusoidal force applied on its seat or the weight of its rider applied on the seat gradually in a short time interval is called "quasi-static" fork compression and that due to the pure "static load" applied on the bike is called "real-static" fork compression. In other words, for a stationary bike, if its response is dependent on the time history (of the response), it is called the "quasi-static" response; otherwise, it is called the "real-static" response. All five bike frames in Chapters 6 and 7 are assumed to have the same masses and only the geometric differences between the five bikes are investigated.

6.2 Quasi-Static Analysis of the Stationary Bare Bike

In the quasi-static analysis presented in this section, each bike does not have any rider on its seat and is subjected to a vertical downward force on either the handlebar or the seat, in a stationary condition. The force is given by a sine wave signal [0 -1000 0]N with the exciting frequency ω_e=0.5 rad/sec and constrained by a saturation block to restrict the force to be less than 0 N to avoid lifting up of the bike.

When a vertical downward force is applied on the bike, the front fork and rear suspension system are activated, and the compressions are observed. Here, attention is paid to the travel path of the rear axle, the sprocket distance (distance between the bottom bracket and the rear axle), the chain tension force, the fork compression, and the shock compression.

6.2.1 Travel Path of Rear Axle

When the vertical downward sinusoidal force with amplitude 1000N is applied on the "seat" of the bike, the travel path of rear axle of each mountain bike is shown in Figure 6.1. For the hard tail bike, due to no rear suspension system, the vertical movement of the rear axle (in y-direction), δ_y, is the smallest (8.7mm) and so is the horizontal one (in x-direction), δ_x, to be (0.4mm), thus, the travel path of its rear axle is near a vertical line. However, due to the existence of rear suspension systems, the travel path of the rear axle for each of the four different full suspension (FS) bikes has greater vertical movement of the rear axle, δ_y, than that of the hard tail bike.

From Figure 6.1 one can see that the travel path of the single pivot bike is similar to that of the VPP bike, while those of horst link and faux bar are similar to each other. Besides, the travel path of the single pivot bike looks like a shallow circular arc, and those of the other three FS bikes look like the straight lines with the vertical movement of the rear axle, δ_y, of the VPP bike to be at a less inclined angle. Although the movements of the rear axle (δ_x and δ_y) for each bike presented in this quasi-static analysis are small and may be negligible, they influence the dynamic response of each

rider-bike system significantly since they have close relationship with the pedalling efficiency and the bobbing effect.

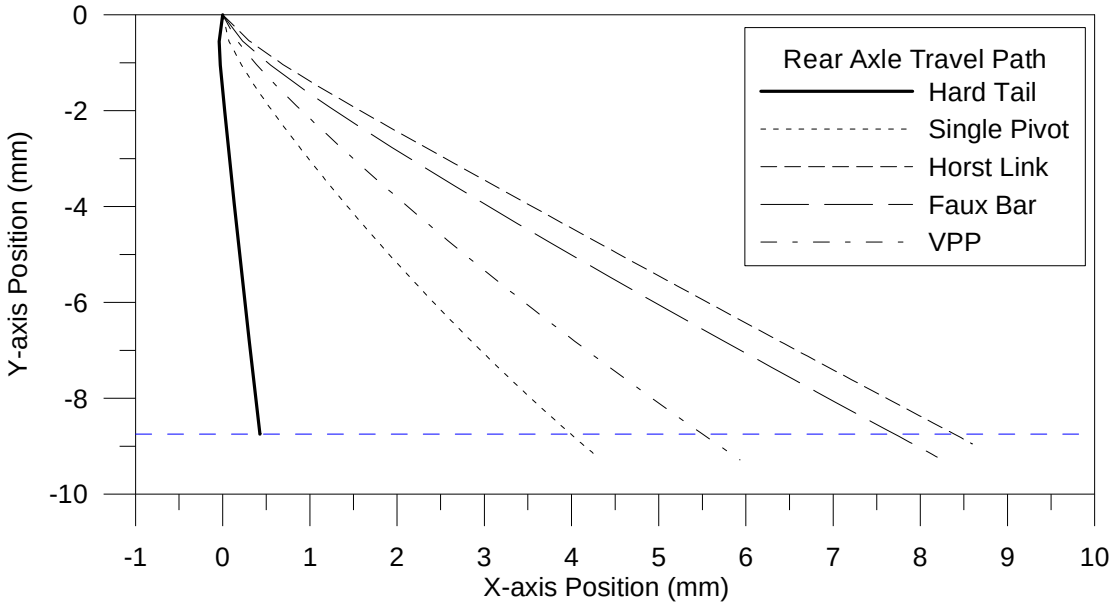

Figure 6.1 Travel path of rear axle for each bike due to a vertical downward force F_y=-1000sin$\omega_e t$ N applied on its seat in the time interval from t=0.0sec to t=6.5 sec with ω_e=0.5rad/sec

The maximum horizontal (x) and vertical (y) movements of the rear axle, $|\delta_x|_{max}$ and $|\delta_y|_{max}$, for each bike shown in Figure 6.1 is summarized in Table 6.1. Usually a good mountain bike should have bigger vertical (y) movement of rear axle, δ_y, and smaller horizontal (x) one , δ_x, so that a bike with larger ratio of $|\delta_y|_{max} / |\delta_x|_{max}$ would be better. As shown in Table 6.1, the ratio of $|\delta_y|_{max} / |\delta_x|_{max}$ for the hard tail bike is biggest because its horizontal movement δ_x is smallest. Among the four FS mountain bikes in this study, the order for the ratio $|\delta_y|_{max} / |\delta_x|_{max}$ is: single pivot, VPP, faux bar, horst link.

Table 6.1 The maximum "quasi-static" horizontal (x) movement of rear axle, $|\delta_x|_{max}$, and the maximum "quasi-static" vertical (y) one, $|\delta_y|_{max}$, for the five mountain bikes

Maximum movements (mm)	Hard Tail	Single Pivot	Horst Link	Faux Bar	VPP
$\|\delta_x\|_{max}$	0.42	4.24	8.59	8.19	5.93
$\|\delta_y\|_{max}$	8.74	9.14	8.95	9.22	9.28
$\|\delta_y\|_{max} / \|\delta_x\|_{max}$	20.80	2.15	1.04	1.12	1.56

The corresponding time history of contact force of rear wheel for each bike is shown in Figure 6.2. Since each wheel is supported by the contact force as discussed in Section 5.3.2, the contact forces is closely related to the maximum vertical movement of the rear axle, $|\delta_y|_{max}$. In Figure 6.1, the order of $|\delta_y|_{max}$ is: VPP, faux bar, single pivot, horst link, hard tail, thus, in Figure 6.2, the order of the maximum contact forces has the same trend. Since the $|\delta_y|_{max}$ of the VPP bike is 9.277mm and the wheel stiffness is 90000N/m (as shown in Table 5.1), the contact force of the VPP-bike rear wheel is given by $F=k \cdot x$=834.98N, which is near its peak contact force, 836.18N, appearing in Figure 6.2.

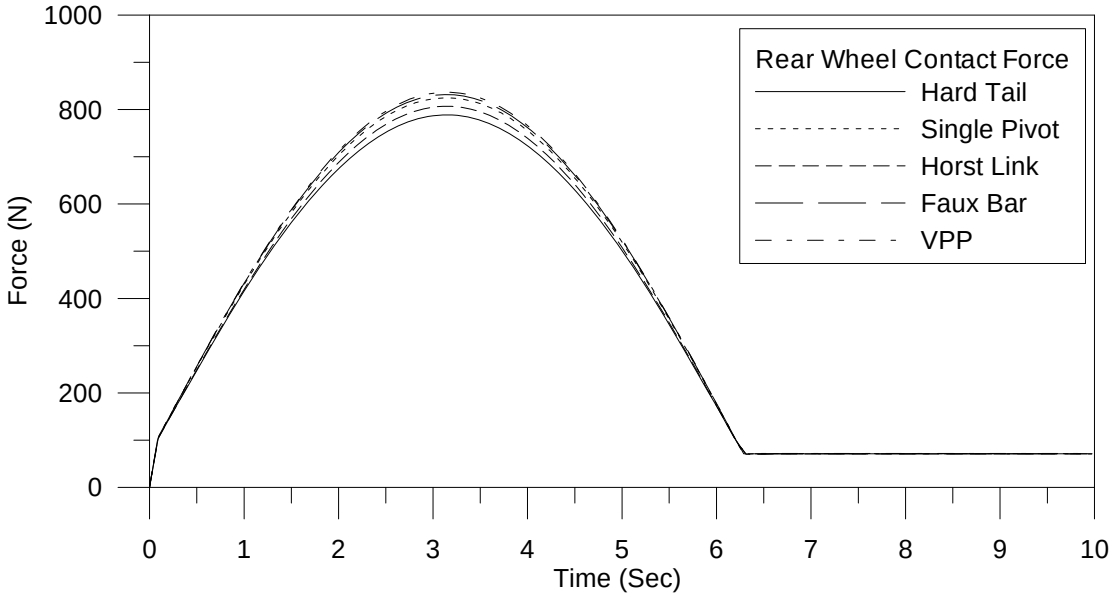

Figure 6.2 Time history of "quasi-static" contact force of rear wheel for each bike due to a vertical downward sinusoidal force with amplitude 1000N applied on its seat

6.2.2 Chain Tension

When a vertical downward sinusoidal force is applied on the seat of each bike, the variations of sprocket distance and the corresponding chain tension force applied on the rear sprocket are shown in Figures 6.3 and 6.4, respectively. Since the chain tension force is a pair of forces between the front and rear sprockets (with the same magnitudes and opposite directions), only the force applied on rear sprocket is shown.

From Figure 6.3 one sees that the variation of sprocket distance of the hard tail bike is 0.03mm, which is very small and negligible. The variation of sprocket distance of single pivot and VPP have the same trend, but the variation of VPP bike is bigger than that of the single pivot bike. The curves of VPP bike and single pivot bike look like the half-sine waves in the time interval from t=0 to t=6.5 seconds.

The variations of sprocket distances for the horst link bike and the faux bar bike (both with the four-bar-linkage frames) are much different from the other three types of bikes due to their rear axles being connected to either the horst link or the faux bar, as one may see from Figure 6.3. It is seen that when the amplitude of the applied sinusoidal force increases from 0.0N to 1000N gradually, the sprocket distance of the horst link bike increases from 0.0 to 0.45mm first and then reduces from 0.45mm to 0.0N. After that, the similar variation of the sprocket distance is repeated when the magnitude of the applied force decreases from 1000N to 0.0N gradually.

On the other hand, due to the configuration of faux bar design, the sprocket distance of the faux bar bike becomes smaller (negative) when a vertical downward sinusoidal force is applied on its seat. This is the reason why the chain tension forces applied on the rear sprocket of the faux bar bike are equal to zero, as shown in Figure 6.4. The maximum chain tension force on the rear sprocket of each bike shown in Figure 6.4 is summarized in Table 6.2.

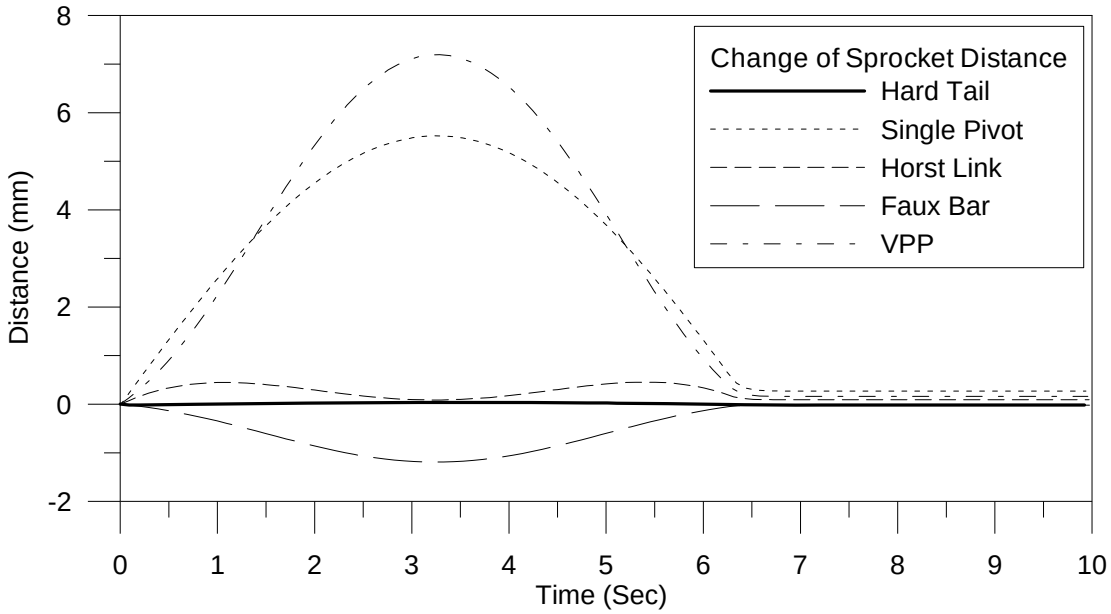

Figure 6.3 Time history for "quasi-static" sprocket distance of each bike due to a sinusoidal downward force with amplitude 1000N applied on its seat

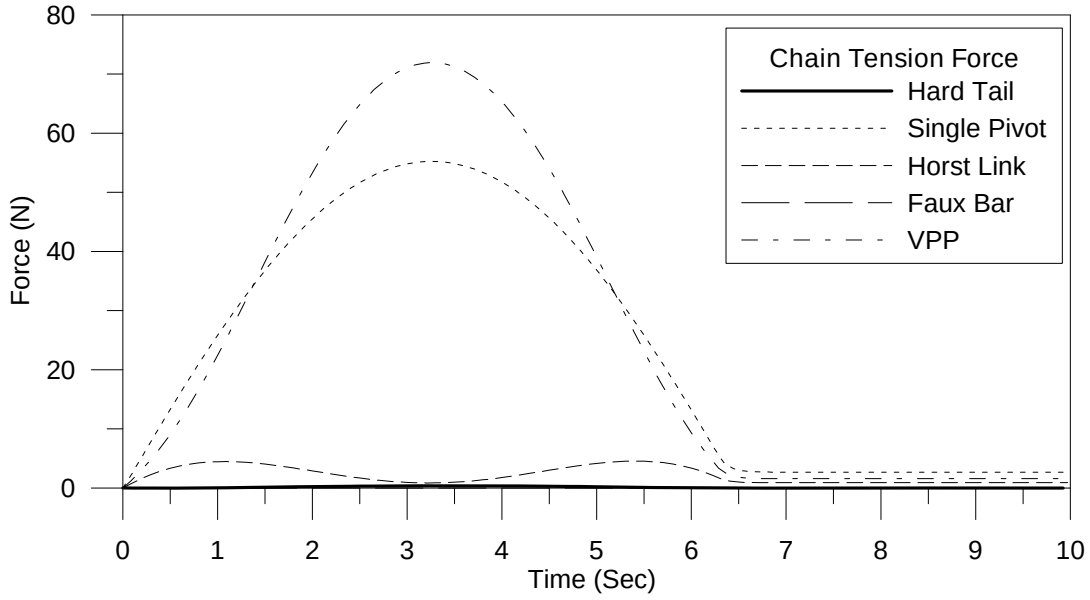

Figure 6.4 Time history for "quasi-static" chain tension force applied on the rear sprocket of each bike due to a vertical sinusoidal downward force with amplitude 1000N applied on its seat

Table 6.2 Maximum "quasi-static" chain tension force in the rear sprocket of each bike due to a vertical sinusoidal downward force with amplitude 1000N applied on its seat.

Types of bike	Hard Tail	Single Pivot	Horst Link	Faux Bar	VPP
Max. force (N)	0.374	55.366	4.473	0	71.957

6.2.3 Fork Compression

For each bike subjected to a vertical sinusoidal downward force with amplitude 1000N applied on its handlebar, the time history of its "quasi-static" fork compression is shown in Figure 6.5. As discussed in Section 5.3.3, the front forks of the five mountain bikes are the same and the only two differences are the total fork length and inclination due to head angle. This is the reason why the differences between the fork compressions of the five bikes are small as shown in Figure 6.5. From the figure one sees that the fork compression of hard tail bike and that of single pivot bike are almost the same, and so are the fork compression of faux bar bike and that of VPP bike. Among the five bikes, the horst link bike has the smallest fork compression.

Since the head angles of hard tail bike and single pivot bike are 69° and 69.5°, respectively, the head angle of either faux bar bike or VPP bike is 68°, and that of horst link bike is 66°, comparison between the foregoing head angles and fork compressions reveals that steeper head angle will result in greater fork compression as one's expectation. It is noted that the head angle affects the steering performance as well, but this effect is not considered in this study.

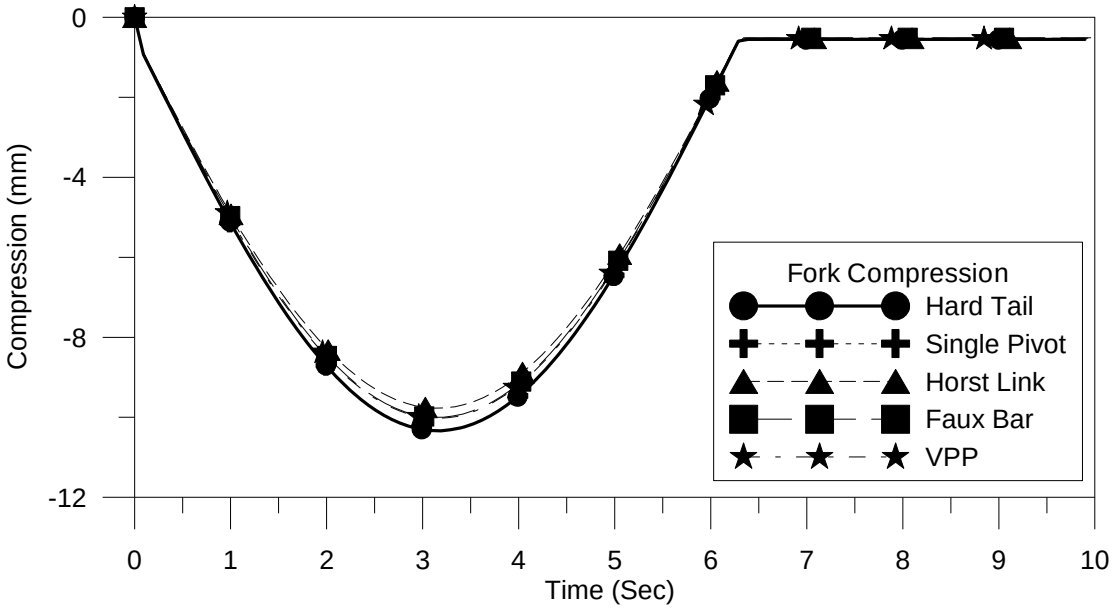

Figure 6.5 Time history of "quasi-static" fork compression for each bike due to a vertical sinusoidal downward force with amplitude 1000N applied on its handlebar

6.2.4 Shock Compression

When the vertical sinusoidal downward force with amplitude 1000N is applied on the seat of each bike, the time history for the compression of its rear shock absorber is shown in Figure 6.6. Since the hard tail bike has no rear suspension, its shock compression is not shown in the figure. The stiffness and damping constants for the rear shock absorber of each bike are the same, and the only difference is the length and the location equipped on the bike due to different type of rear suspension systems.

From Figure 6.6 one sees that, among the four FS bikes, VPP bike has the biggest shock compression (about 30mm), while the faux bar bike has the smallest one (about 21.3mm). In addition, the frame of the horst link bike and that of the single pivot bike have a similar shock compression, but the shock compression of the latter is slightly greater than that of the former.

If the foregoing “dynamic” (sinusoidal) downward force is replaced by a “static” one, then the “real-static” shock compression of each bike is shown in Table 6.3. Comparing with the maximum “quasi-static” shock compressions of the four FS bikes shown in Figure 6.6, one sees that each of the “real-static” shock compressions shown in Table 6.3 is only about one half of the corresponding one of the maximum “quasi-static” shock compressions. The last phenomenon indicates that the influence of inertia force due to each associated bike frame is significant, because one of the biggest differences between the static and dynamic characteristics is due to the “inertial effects”.

Table 6.3 The “real-static” shock compression of each bike due to the rider sits on the bike in the stationary condition

Bike	Hard Tail	Single Pivot	Horst Link	Faux Bar	VPP
Compression (mm)	N/A	13.7	14.5	12.5	16.5

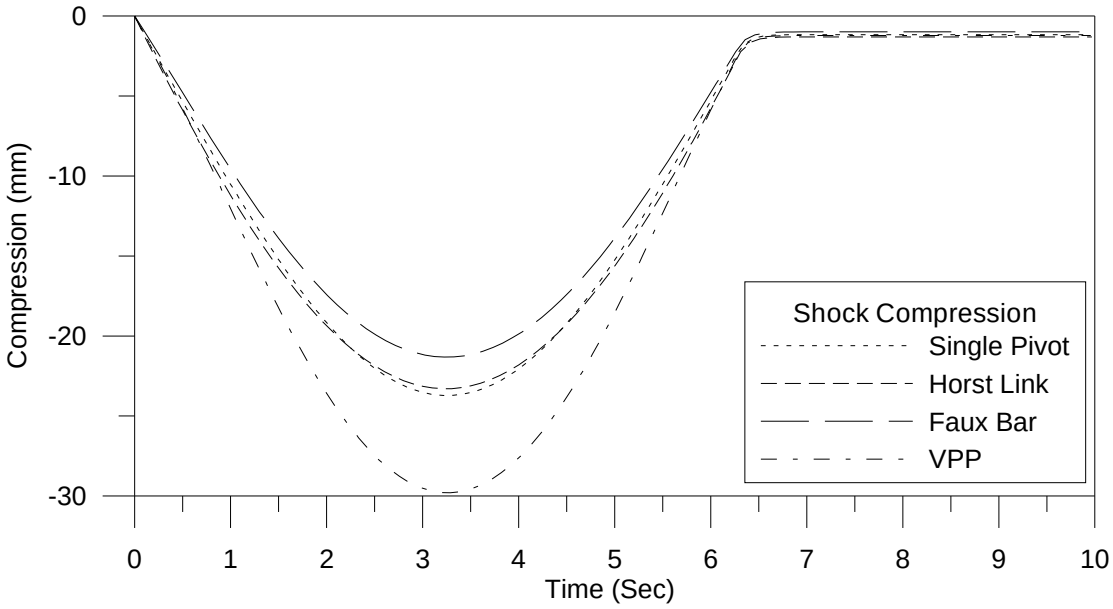

Figure 6.6 Time history of "quasi-static" compression of rear shock absorber for each bike due to a vertical downward sinusoidal force with amplitude 1000N applied on its seat

6.3 Dynamic Analysis of the Moving Loaded Bike on a Flat Road Surface

In the dynamic analysis presented in this section, the rider of the five bikes is the same person. Each of the five rider-bike systems is assumed to move on the flat road surface without small bumps and the pedalling cadence is 86 rpm which results in the convergence of forward velocity to 11.96 m/s at about t=11sec. The dynamic response, performance, bobbing effect, and comfort regarding each rider-bike system are studied. The theory concerned is given in Chapter 4 and Section 5.5.1.

6.3.1 Effective Pedalling Forces, Torques and Powers

For the rider-bike system of the hard tail bike moving on the flat road surface, the time histories for actual angular velocities of the crank and the rear wheel, and that of the forward velocity V_x are shown in Figures 5.39 and 5.42, respectively. Since each rider-bike system reaches the "steady condition" near time t=11secs (and V_x=11.96m/s), the time histories of the pedalling forces, torques and powers for each bike in the time interval from t=10sec to t=15sec are presented for observations.

First of all, the "effective" pedalling force of each bike (i.e., the force component perpendicular to the crank) is shown in Figure 6.7. As one can see from Figure 6.7, the difference between the "effective" pedalling forces of the five rider-bike systems is very small, in addition, when one right pedalling force ends at the (time) instant $t \approx 10.64$sec the next left pedalling force is applies successively.

In the steady condition, each pair of the right and left pedalling forces shown in Figure 6.7 are identical, thus, only the final pair of right and left pedalling forces appearing in the time interval from $t \approx 13.76$sec to $t \approx 14.46$sec are discussed and shown in Figure 6.8. The maximum pedalling forces for each rider-bike system is summarized in Table 6.4. From the table one sees that, among the five bikes, the maximum pedalling force of the hard tail bike is biggest due to no rear suspension system because the pedalling force is not absorbed by the rear shock absorber.

With the pedalling forces of the hard tail bike as the benchmark, the decrements of pedalling forces resulting from the activation of rear suspension systems of the bikes are shown in Table 6.4. It is seen that, based on the decrements of pedalling forces, that of the VPP bike is biggest and that of the faux bar bike is smallest. Where the "decrement" of a pedalling force of the "X bike" is defined as the difference of the maximum "effective" pedalling force of the hard tail bike minus the corresponding one of the "X bike" with X denoting single pivot, horst link, faux bar and VPP, respectively.

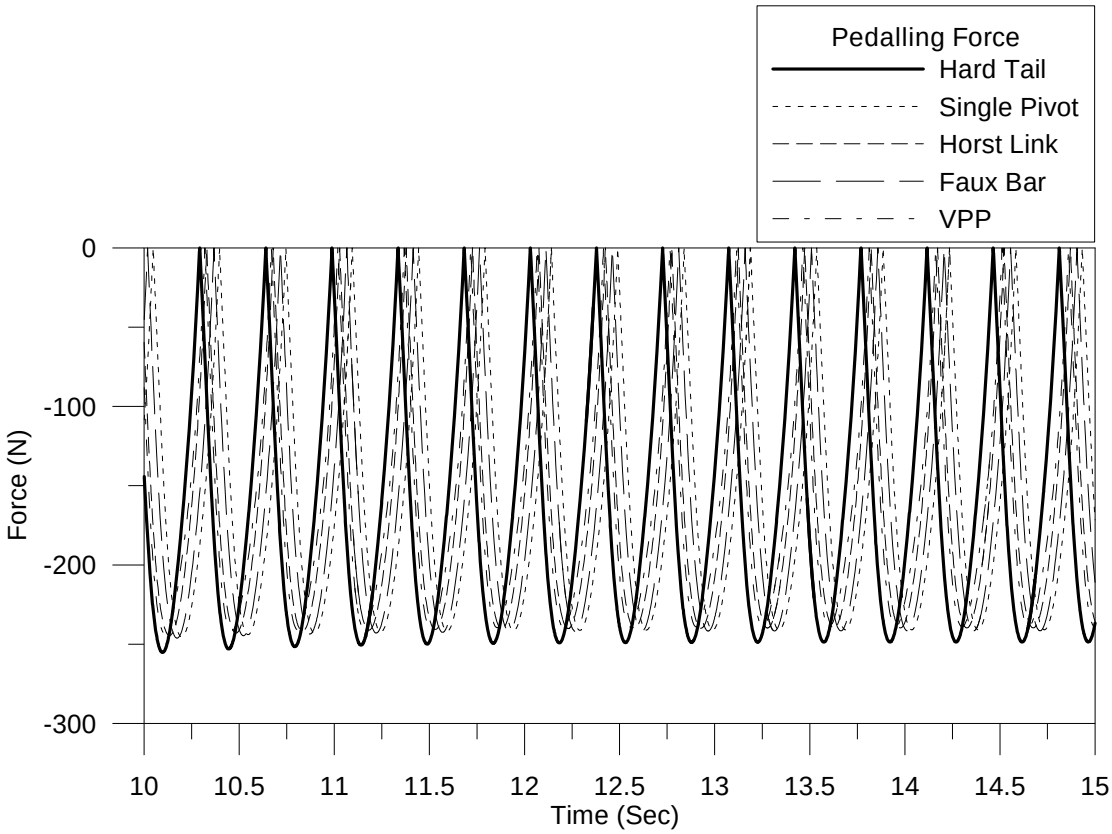

Figure 6.7 Time histories of "effective" pedalling forces for the five rider-bike systems moving on flat road surface.

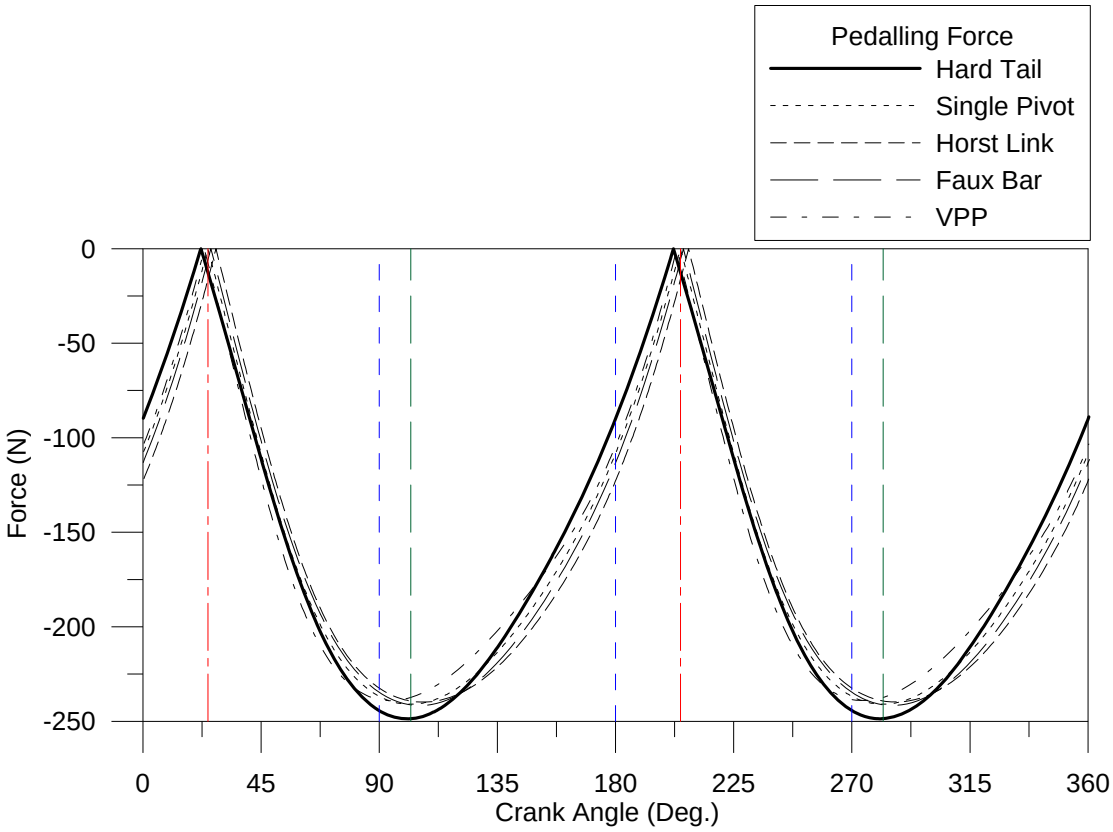

Figure 6.8 The relationship between the final pair of pedalling forces and the crank angles θ (with θ=0° at top dead centre) for the five bikes in the steady condition.

Table 6.4 Maximum "effective" pedalling forces, and their decrements (with respect to the hard tail bike) for the rider-bike systems moving on the flat road surface and in the steady condition

Bikes	Hard Tail	Single Pivot	Horst Link	Faux Bar	VPP
Max. pedalling forces (N)	248.65	240.95	239.81	241.63	239.05
Difference between FS bikes and HT bike (Pedalling force of HT bike minus the corresponding one of FS bikes)					
Decrements	—	7.7	8.84	7.02	9.6

The final pairs of "effective" pedalling torques and pedalling powers as a functions of crank angles are shown in Figures 6.9 and 6.10, respectively. It is obvious that the trend of either Figure 6.9 or 6.10 is the same as that of Figure 6.8, since the effective pedalling torque is equal to the effective pedalling force multiplied by the crank length (= 0.17m for the current example), and the effective pedalling power is equal to the effective pedalling torque multiplied by the angular velocity of crank (about

9.0rad/sec in the steady condition). The maximum effective pedalling torques and powers shown in Figures 6.9 and 6.10 are summarized in Table 6.5.

Comparing with the hard tail bike, one finds that, the “peak” power required by the hard tail bike is greater than that of the four FS bikes. Among the four FS bikes, the “peak” power required by faux bar bike is biggest, while that of single pivot bike is slightly smaller. The “peak” powers required by the two four-bar-linkage bikes are similar, while that of horst link bike is slightly smaller than that of faux bar bike. The "peak" power required by VPP bike is smallest. The bottom row of Table 6.5 is the percentage power decrements for each of four FS bikes with respect to the “peak” power required by the hard tail bike. It is seen that, among the four FS bikes, the percentage power decrement of faux bar bike is only 2.98%, while those of the other three FS bikes are bigger than 3%.

Based on the maximum pedalling powers shown in Table 6.5 one sees that the hard tail bike has the highest pedalling efficiency on the flat road surface. Furthermore, among the four FS bikes, the total power decrement of VPP bike is highest, but this is not necessary to mean that the VPP bike has the higher pedalling efficiency, because some part of the pedalling power may also be absorbed by the shock absorber of the rear suspension system of each FS bike due to the bobbing effect. In other words, the rider of a FS bike must apply more pedalling force to compensate the power decrement for achieving the same speed as the rider of a hard tail bike.

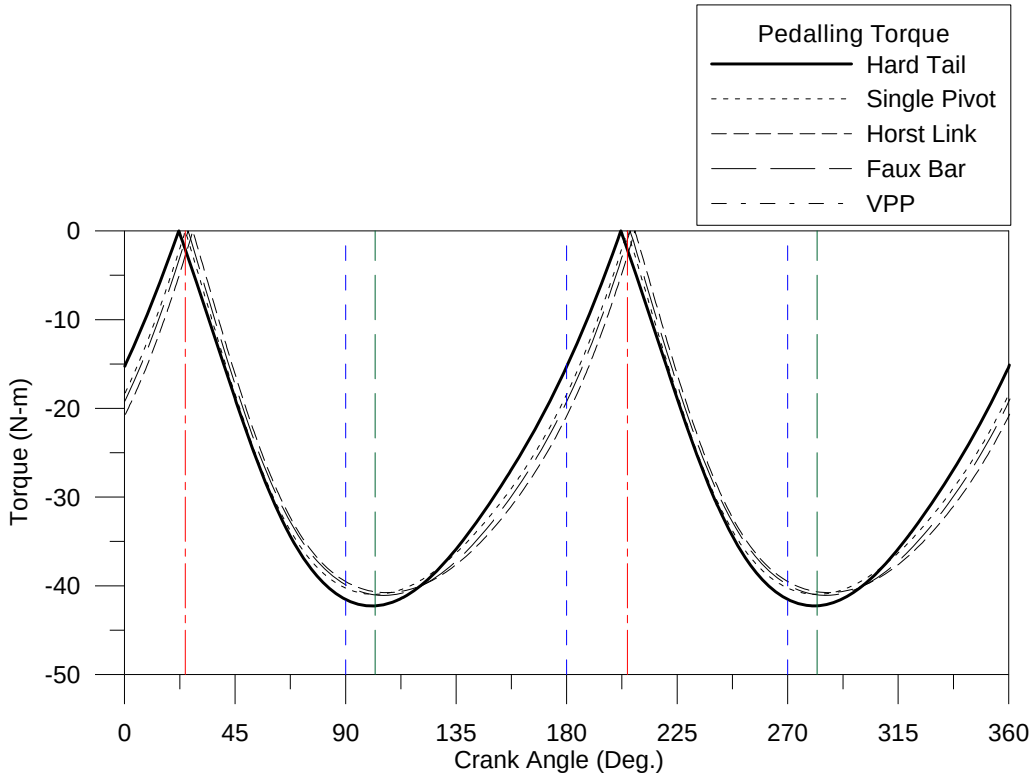

Figure 6.9 The relationship between the final pair of pedalling torques and the crank angles θ (with θ=0° at top dead centre) for the five bikes in the steady condition.

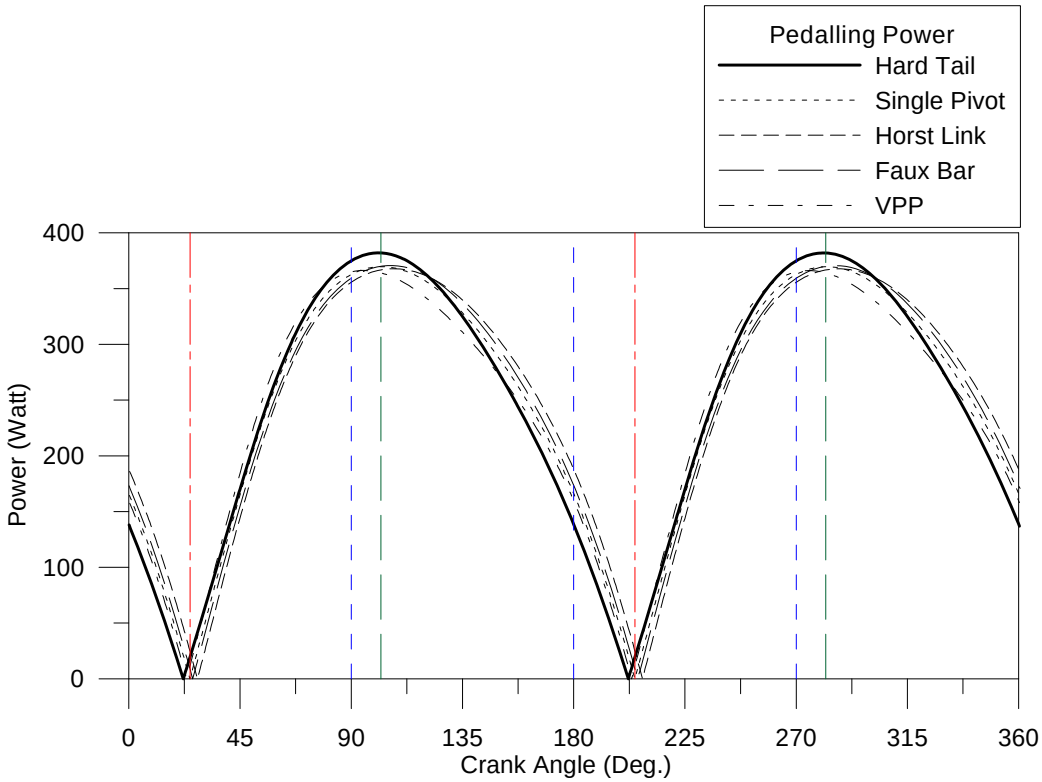

Figure 6.10 The relationship between the final pair of pedalling powers and the crank angles θ (with θ=0° at top dead centre) for the five bikes in the steady condition.

Table 6.5 Maximum pedalling torques and powers, and their decrements (with respect to the hard tail bike) for the rider-bike systems moving on the flat road surface and in the steady condition.

Max. pedalling Torque and Power	Hard Tail	Single Pivot	Horst Link	Faux Bar	VPP
Torque (N-m)	42.27	40.96	40.76	41.07	40.63
Power (Watt)	382.05	369.65	367.79	370.66	366.24
Difference between FS bikes and HT bike (Pedalling torque and power of HT bike minus the corresponding ones of FS bikes)					
Torque (N-m)	—	1.31	1.51	1.2	1.64
Power (Watt)	—	12.4	14.26	11.39	15.81
Power Decrements (%)	—	3.24	3.73	2.98	4.13

6.3.2 Forward Velocity

In the steady condition, the relationship between the forward velocity, V_x, and the crank angles θ is shown in Figure 6.11 and the maximum forward velocity, $|V_x|_{\max}$, and minimum one, $|V_x|_{\min}$, of the five bikes are summarized in Table 6.6. Figure 6.11 reveals that the values of $|V_x|_{\max}$ and $|V_x|_{\min}$ of the hard tail bike are biggest. The values of $|V_x|_{\min}$ for all FS bikes are smaller than that of hard tail bike, because the compression of rear shock absorber of the FS bikes causes the decrease of V_x. The value of $|V_x|_{\max}$ for the VPP bike is highest among the four FS bikes and that of the single pivot bike is next. It is noted that the values of $|V_x|_{\max}$ for the two four-bar-linkage bikes are almost the same.

In Table 6.6, for each of the bikes, the average of V_x (denoted by $\overline{V}_x$) represents the summation of $|V_x|_{\max}$ and $|V_x|_{\min}$ divided by two [i.e., $\overline{V}_x = \frac{1}{2}(|V_x|_{\max} + |V_x|_{\min})$], while the variation of V_x (denoted by ΔV_x) represents the difference between the $\overline{V}_x$ and the corresponding $|V_x|_{\max}$ or $|V_x|_{\min}$ (i.e., $\Delta V_x = |V_x|_{\max \text{ or } \min} - \overline{V}_x$). Among the five bikes, the hard tail bike has the highest value of $\overline{V}_x$ and the smallest value of ΔV_x, this means that the hard tail bike is least variable. Among the four FS bikes, the value of $\overline{V}_x$ for the horst link bike is lowest and that for the single pivot bike is highest, and the value of ΔV_x for the VPP bike is biggest.

From Figure 6.11 and Table 6.6, one can see that the bobbing effect will occur on each FS bike, because the compression of rear shock absorber due to the rider's pedalling motion will cause the decrement of V_x.

Although the differences between average speeds in Table 6.6 are very small [with the biggest difference to be 11.925-11.8625 = 0.0625(m/s)], they will become significant if the same rider rides each of the two bikes for more than 60 seconds, because the difference between the distance may reach 3.75m for the same rider riding the hard tail bike and the horst link bike, respectively. In other words, the bobbing effect will influence the rider’s performance significantly in the long competitions. It is noted that the foregoing discussion is based on the rider-bike system moving on the flat road surface and the influence of bumps on the road surface is not considered.

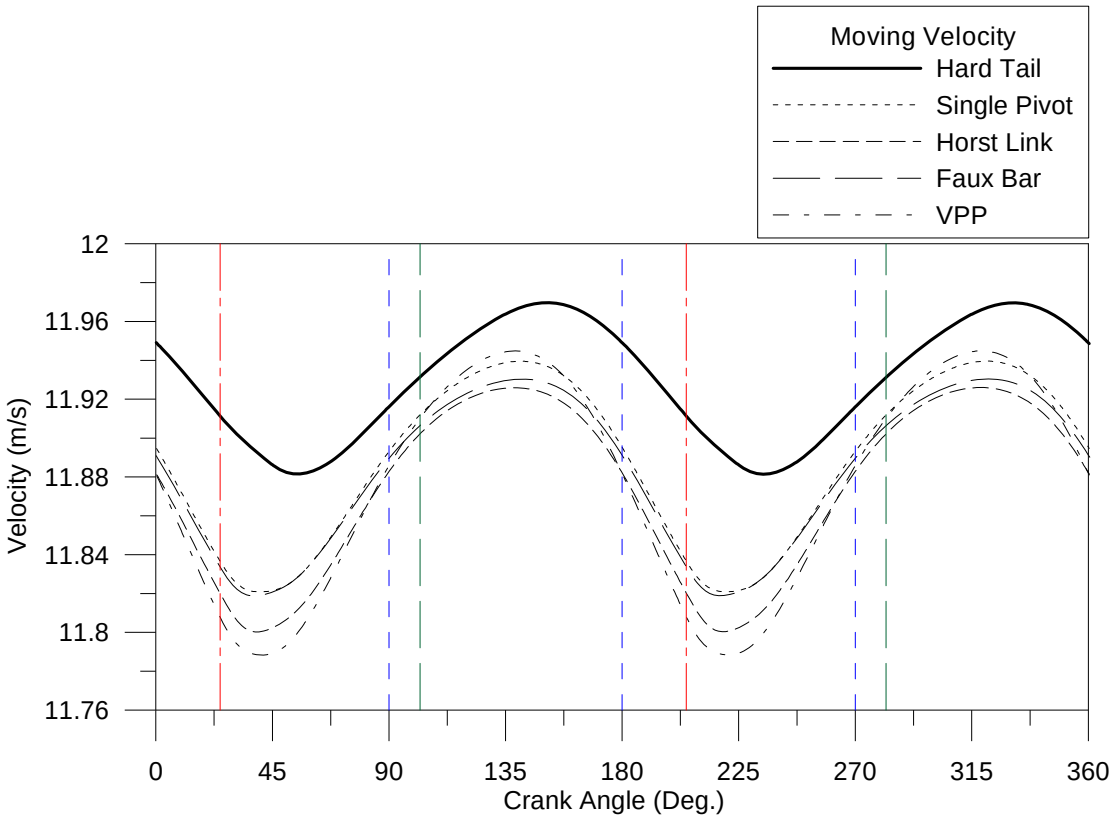

Figure 6.11 The relationship between the moving velocities V_x and the crank angles θ (with θ=0° at top dead centre) for the five rider-bike systems moving on flat road surface and in the steady condition.

Table 6.6 Maximum V_x ($|V_x|_{max}$), minimum V_x ($|V_x|_{min}$), and average V_x ($\overline{V}_x = \frac{1}{2}(|V_x|_{max} + |V_x|_{min})$) of the five bikes and their variations ($\Delta V_x = |V_x|_{max\ or\ min} - \overline{V}_x$)

V_x (m/s)	Hard Tail	Single Pivot	Horst Link	Faux Bar	VPP
$\lvert V_x\rvert_{max}$	11.969	11.939	11.925	11.930	11.944
$\lvert V_x\rvert_{min}$	11.881	11.820	11.800	11.818	11.788
$\overline{V}_x = \frac{1}{2}(\lvert V_x\rvert_{max} + \lvert V_x\rvert_{min})$	11.925	11.8795	11.8625	11.874	11.866
$\Delta V_x = \lvert V_x\rvert_{max\ or\ min} - \overline{V}_x$	±0.044	±0.0595	±0.0625	±0.056	±0.078

6.3.3 Contact Forces on Front and Rear Wheels

In the “stationary” condition, the maximum “quasi-static” contact forces of the front and rear wheels for each bike due to the rider sitting on the bike are shown in Table 6.7. As shown in Figure 5.37 for the hard tail bike, the maximum contact forces of both wheels appear at the start of simulation when the rider sits on each of the bikes. From the table, one can see that the hard tail bike has the biggest “maximum contact force” at front wheel, while the horst link bike has the biggest “maximum contact force” at rear wheel. Besides, the four FS bikes have higher contact forces at their rear wheels than the hard tail bike, this is beneficial for the FS bikes, from the viewpoint of pushing force (opposite to the frictional force), because the maximum traction is proportional to the contact force of “rear” wheel of a bike.

The relationship between the contact forces and crank angles of the front and rear wheels for each of the five rider-bike systems moving on flat road surface in the “steady” condition are shown in Figures 6.12(a) and 6.12(b), respectively, and the maximum, minimum, and average contact forces are summarized in Table 6.8. It is seen that, for the front wheel, the hard tail bike has the biggest “maximum contact force”, and the VPP bike has the smallest “maximum contact force” and the smallest “average contact force”. For the rear wheel, the faux bar bike has the biggest “maximum contact force”, the hard tail bike has the smallest “maximum contact force”, and the VPP bike has the biggest “average contact force”.

Since a bike with bigger contact force between its wheel and ground will have better traction control as shown in Section 5.5.4, the FS bikes will be better than the hard tail bike in this aspect as one may see from Table 6.8.

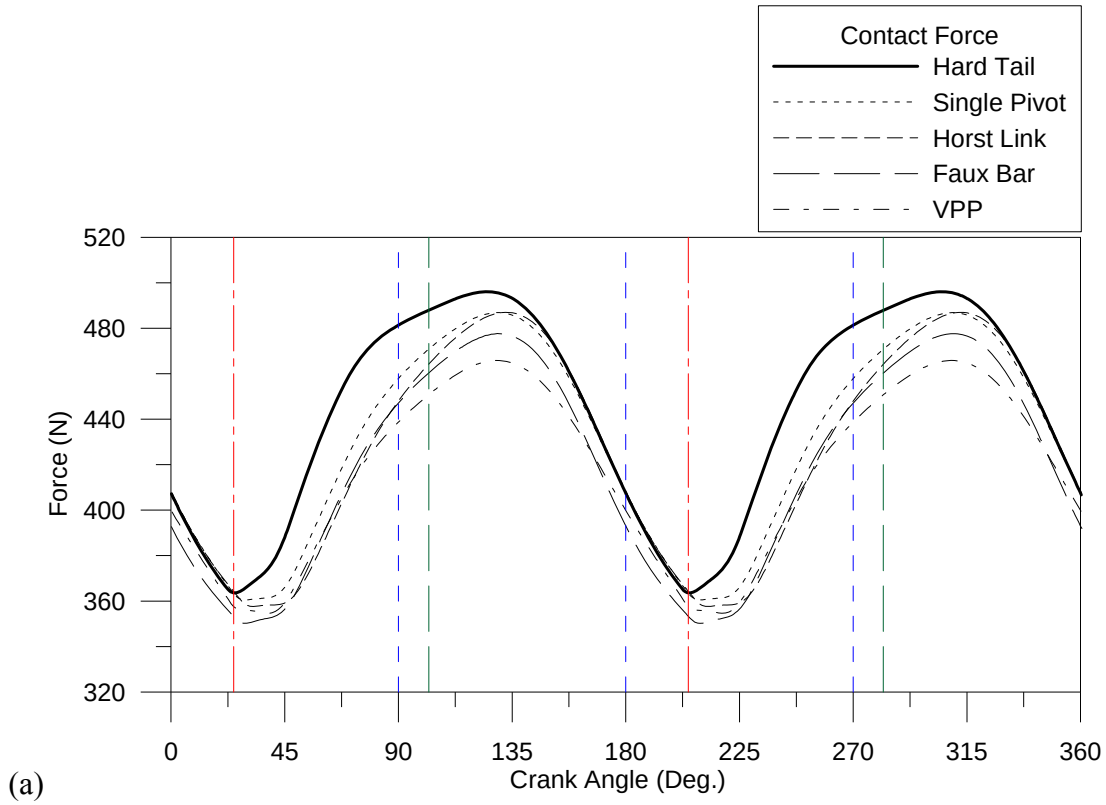

(a)

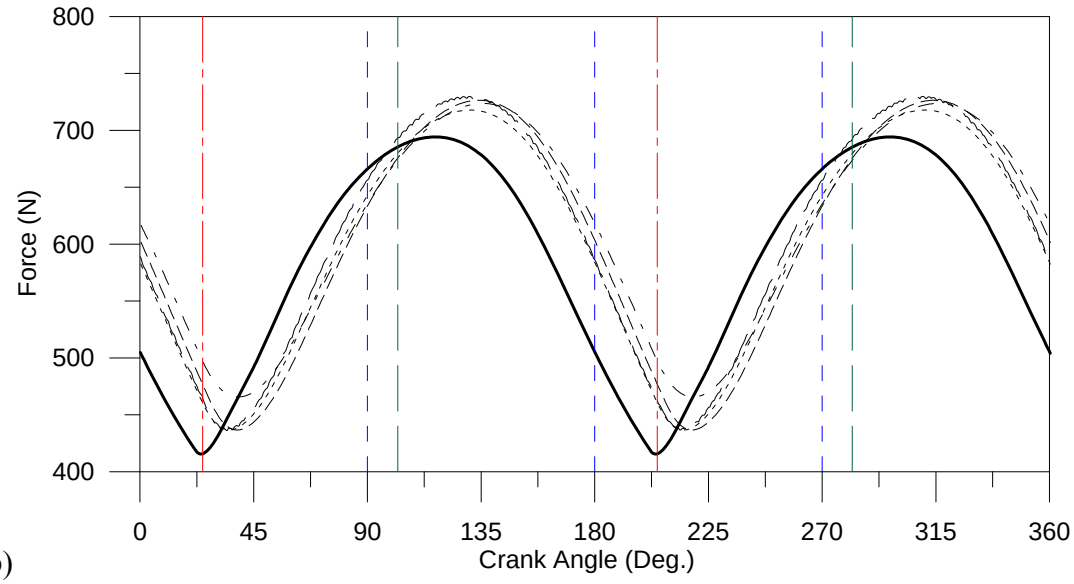

(b)

Figure 6.12 The "dynamic" contact forces of the five rider-bike systems moving on flat road surface as a function of crank angles θ (with θ=0° at top dead centre) in the steady condition for: (a) Front wheel (b) Rear wheel

Table 6.7 Maximum “quasi-static” contact forces on the front and rear wheels for each bike due to the rider sits on the bike in the stationary condition

Max. contact force (N)	Hard Tail	Single Pivot	Horst Link	Faux Bar	VPP
Front wheel	953.34	836.10	803.82	815.98	797.78
Rear wheel	1247.86	1381.74	1467.30	1409.17	1368.67

Table 6.8 Maximum “dynamic” contact forces on the front and rear wheels for each of the rider-bike systems moving on flat road surface in the steady condition

Contact force (N)	Hard Tail	Single Pivot	Horst Link	Faux Bar	VPP
Front Wheel					
Maximum	496.08	486.85	487.02	477.67	465.82
Minimum	363.57	360.51	357.64	350.23	354.63
Average	429.825	423.68	422.33	413.95	410.225
Variation	±66.255	±63.17	±64.49	±63.72	±55.595
Rear Wheel					
Maximum	694.19	717.77	726.35	729.78	723.57
Minimum	415.54	436.68	436.64	436.17	465.71
Average	554.865	577.225	581.495	582.975	594.64
Variation	±139.325	±140.545	±144.855	±146.805	±128.93

6.3.4 Fork Compression and Shock Compression

In the steady condition, the trend for the compressions of each front fork as a function of crank angle shown in Figure 6.13 is similar to that for the contact forces [shown in Figures 6.12(a) and 6.12(b)] or pedalling forces (shown in Figure 6.8), because all of the above-mentioned dynamic responses are dependent on the variations of moving velocity of each rider-bike system. From Figure 6.13 one sees that the maximum fork compression of hard tail bike (5.96mm) is greater than those of the other four FS bikes (5.42mm ~ 5.75mm), this is because some part of the rider-induced load [14] is absorbed by each rear suspension system leading to the front fork of each FS bike to be subjected to smaller load.

In Figure 6.13, the maximum and minimum compressions represent, at certain moments, the front fork being compressed tightly and loosely, respectively, and they are summarized in Table 6.9. It is noted that the “maximum” or “minimum” value of each parameter is based on its “absolute values”.

Among the four FS bikes, the maximum fork compression of the single pivot bike is biggest, that of the VPP bike is smallest, and those of horst link bike and faux bar bike are approximately equal to each other.

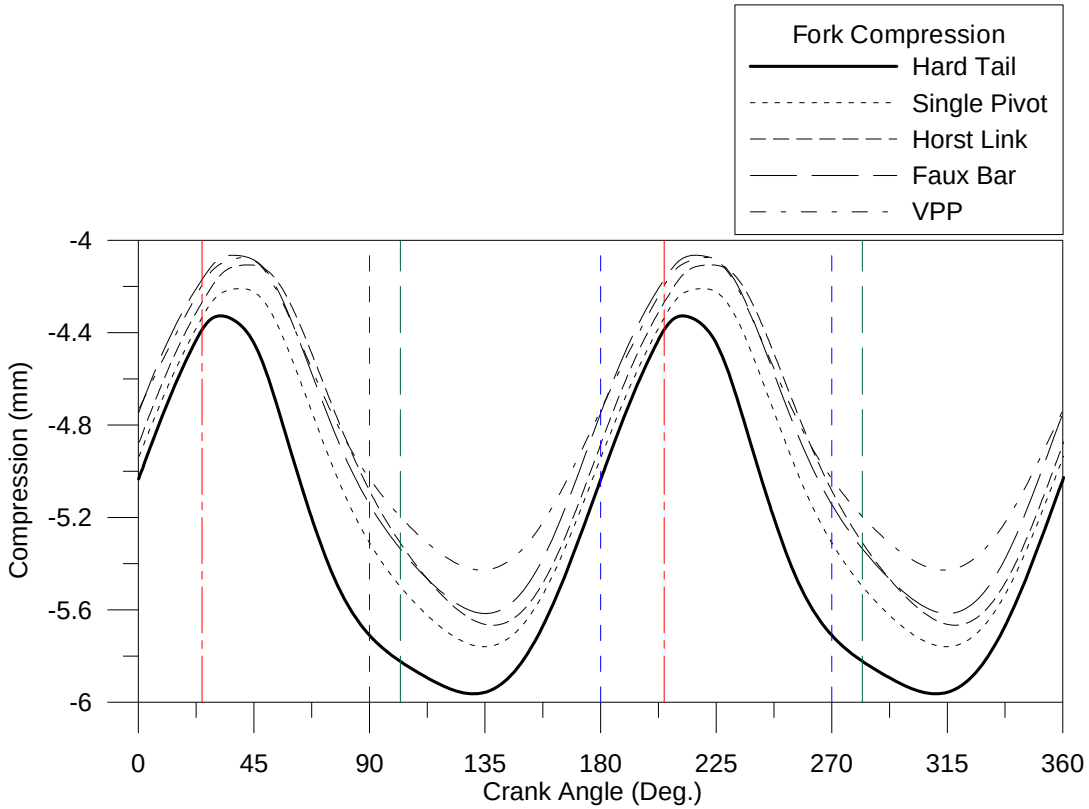

Figure 6.13 The "dynamic" fork compressions as a function of crank angle for each rider-bike system moving on flat road surface and in the steady condition

Table 6.9 Minimum, maximum, and average fork compressions for each rider-bike system moving on flat road surface and in the steady condition

Fork Compression (mm)	Hard Tail	Single Pivot	Horst Link	Faux Bar	VPP
*Minimum	4.32	4.20	4.10	4.06	4.07
*Maximum	5.96	5.75	5.66	5.61	5.42
*Average	5.14	4.975	4.88	4.835	4.745
Variation	±0.82	±0.775	±0.78	±0.775	±0.675

* Based on the "absolute values"

The "dynamic" shock compressions (in rear shock absorbers) as a function of crank angles are shown in Figure 6.14. Since the shock compression is calculated by subtracting the instantaneous distance between the two shock eyes from the initial spring length (i.e. the initial distance between the two shock eyes), the maximum and minimum shock compressions shown in Figure 6.14 are obtained with the shock absorber being compressed tightly and loosely, respectively. For a rider-bike system

moving on the flat road surface, the only load on its rear shock absorber is due to the rider's pedalling motion and is called the rider-induced load [17]. From Figure 6.14 one can find that the rear shock absorber of VPP bike is most sensitive to the rider's pedalling motion.

Based on Figure 6.14, the maximum and minimum shock compressions are summarized in Table 6.10. It is seen that, on the flat road surface and in steady condition, the average shock compression and the variation for each bike are in the same order and their ranks are: VPP (biggest), horst link, single pivot, and faux bar (smallest).

The bobbing effect comes from the activation of rear suspension system due to the rider's pedalling motion. Figure 6.14 indicates that the bobbing effect does exist for each of the four FS bikes. Among the four rear suspension systems, the bobbing effect of VPP bike is biggest and that of the faux bar bike is smallest. Besides, the shock compression of horst link bike and that of single pivot bike are similar, but the latter is slightly smaller than the former.

Comparing Table 6.9 with Table 6.10, one sees that the difference of fork compressions between any two bikes is very small. However, the maximum "dynamic" shock compression of the VPP bike is much greater than those of the other three FS bikes.

In order to confirm the bobbing effect of the VPP bike is biggest among the four FS bikes, the average "dynamic" shock compressions (with the bikes moving forward) shown in Table 6.10 are subtracted from the corresponding "real-static" ones (with the bikes in stationary condition and subjected to "static" force) shown in Table 6.3 (Section 6.2.4), and the results are shown in Table 6.11. It is found that the difference of maximum shock compression of the VPP bike is biggest (4.05mm), that of the faux bar is smallest (2.73mm), while that of single pivot bike (2.975mm) is slightly higher than that of horst link bike (2.915mm).

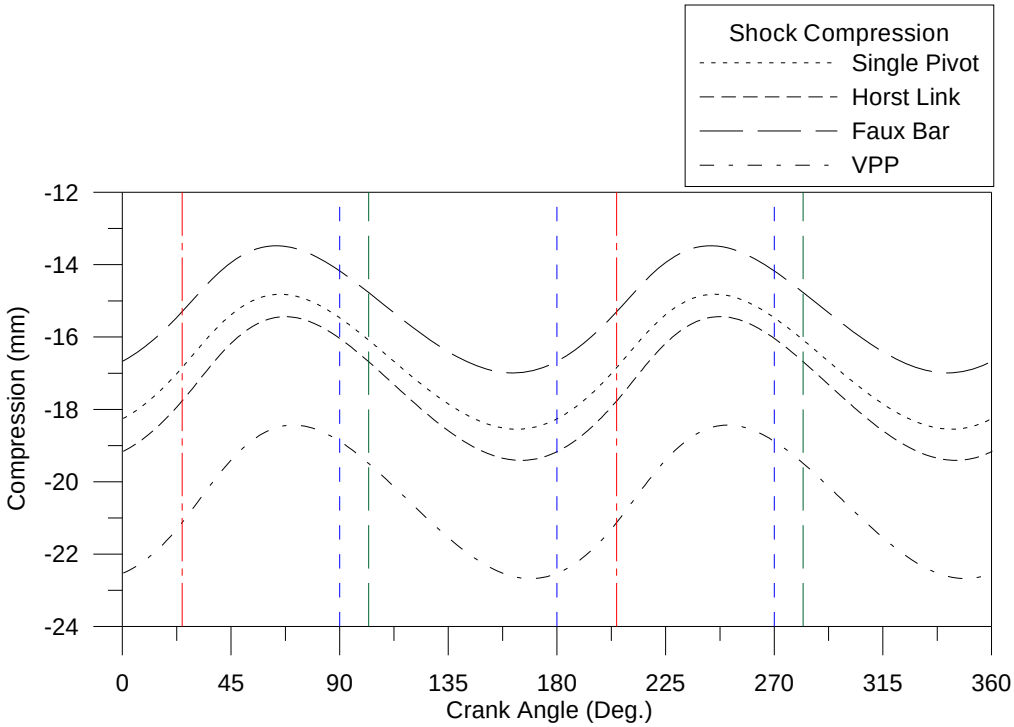

Figure 6.14 The "dynamic" shock compressions as a function of crank angles of the four FS rider-bike systems moving on the flat road surface and in the steady condition

Table 6.10 Minimum, maximum and average shock compressions for each of the rider-bike systems moving on flat road surface and in the steady condition

Shock Compression (mm)	Hard Tail	Single Pivot	Horst Link	Faux Bar	VPP
*Minimum	—	14.81	15.43	13.47	18.43
*Maximum	—	18.54	19.40	16.99	22.67
*Average	—	16.675	17.415	15.23	20.55
Variation	—	±1.865	±1.985	±1.76	±2.12

* Based on the "absolute values"

Table 6.11 Differences between maximum "dynamic" shock compressions (with the bikes in moving condition) and the corresponding "real-static" ones (with the bikes in stationary condition and subjected to "static" force)

Types of bikes	Hard Tail	Single Pivot	Horst Link	Faux Bar	VPP
Difference between compressions (mm)	—	2.975	2.915	2.73	4.05

6.3.5 Sprocket Distance and Chain Tension

In the steady condition, the variations of sprocket distances and chain tension forces as a function of crank angle for each rider-bike system moving on the flat surface are shown in Figures 6.15(a) and 6.15(b), respectively. Since the hard tail bike has no rear suspension, its sprocket distance is almost unchanged and so is its chain tension force. When each rider-bike system has reached the steady condition at the time $t \approx 11\text{sec}$, the sprocket distance of faux bar bike keeps at about -0.7mm and that of horst link bike is about 0.2mm (with corresponding chain tension force about 2.2N). Throughout the full pedalling cycle, the variations of the single pivot bike and VPP bike are greater than those of the other two FS bikes, and the "average" sprocket distances of single pivot bike and VPP bike keep at about 4mm and 5mm, respectively.

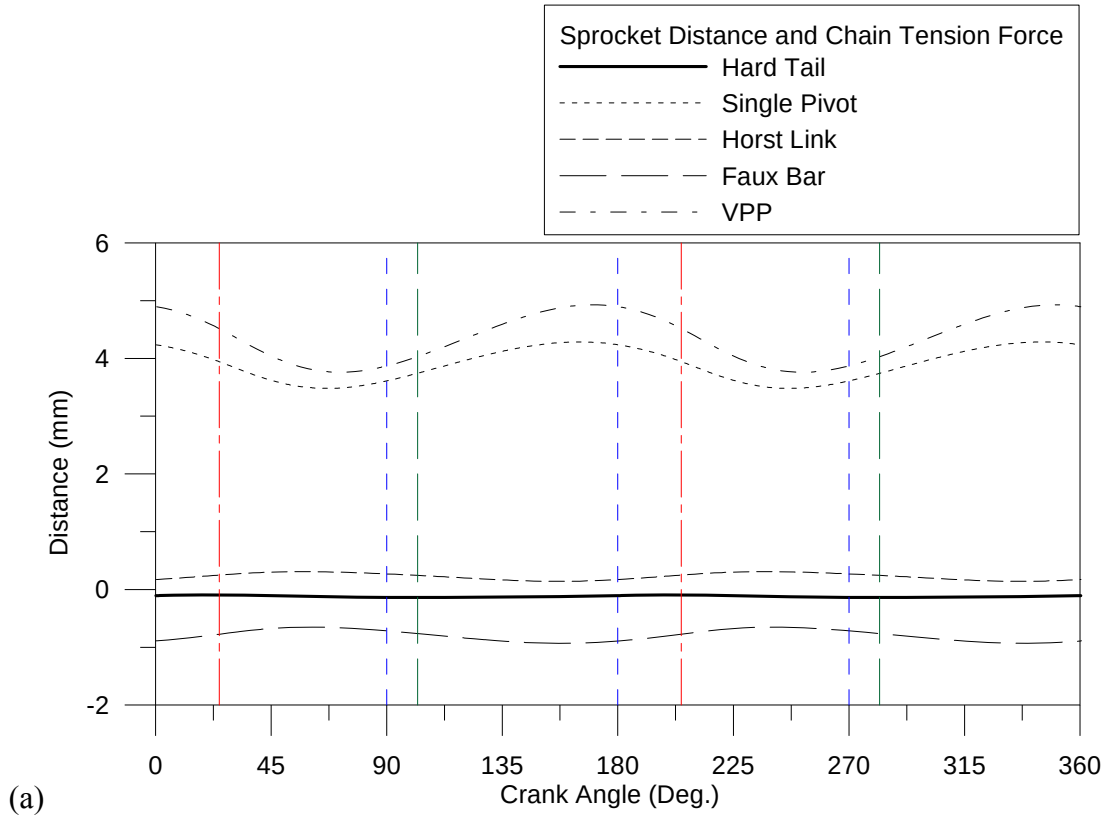

(a)

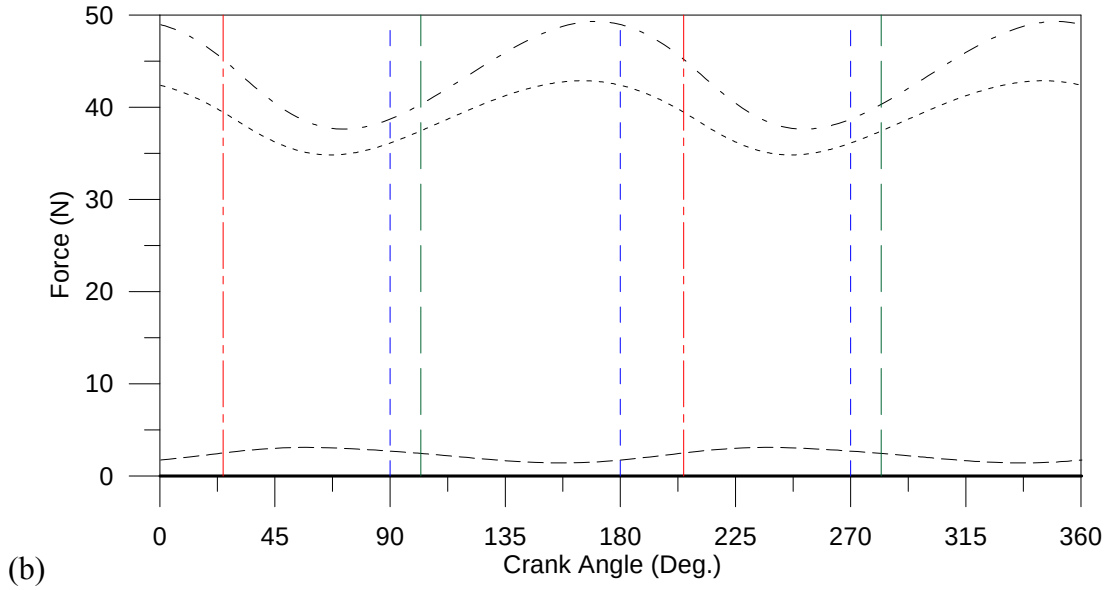

(b)

Figure 6.15 Variations of (a) sprocket distances and (b) chain tension forces as a function of crank angle for each rider-bike system moving on the flat road surface and in the steady condition

6.3.6 Vertical Accelerations of Handlebar and Seat

In the steady condition, the variations of the vertical (y) accelerations at CG of handlebar and seat for each rider-bike system moving on the flat road surface as a function of the crank angle are shown in Figures 6.16 and 6.17, respectively. Since the rider's weight is mainly supported by the handlebar and seat, only the vertical accelerations at CG of handlebar and seat are studied and considered as the parameters for assessing the degree of comfort and bobbing effect. From Figures 6.16 and 6.17 one sees that the trends of the five bikes are very similar and, for comparisons, the “minimum” and “maximum” vertical accelerations are summarized in Table 6.12. It is seen that, for the hard tail bike, its vertical acceleration at seat is smaller than that at handlebar because it has front fork and no rear suspension system. Since all the FS bikes have the front fork, the difference between the maximum vertical accelerations at handlebars is very small. However, that at seats is bigger because of the different rear suspension systems. The order of average vertical accelerations at seats of the four FS bikes is: horst link (biggest), faux bar, single pivot and VPP (smallest). The variation of average vertical acceleration at seat of VPP bike is highest, that of single pivot bike is close to that of horst link bike, and that of faux bar bike is smallest. The biggest amplitude of VPP bike means that its bobbing effect will be the most serious.

Although the vertical accelerations at handlebar and seat of the four FS bikes are greater than those of hard tail bike on the flat road surface as shown in Table 6.12, this situation will be changed on the road surface with bumps as one may see from Chapter 7, because the rear suspension system of each FS bike can absorb some part of the impulsive force when it passes through the bumps.

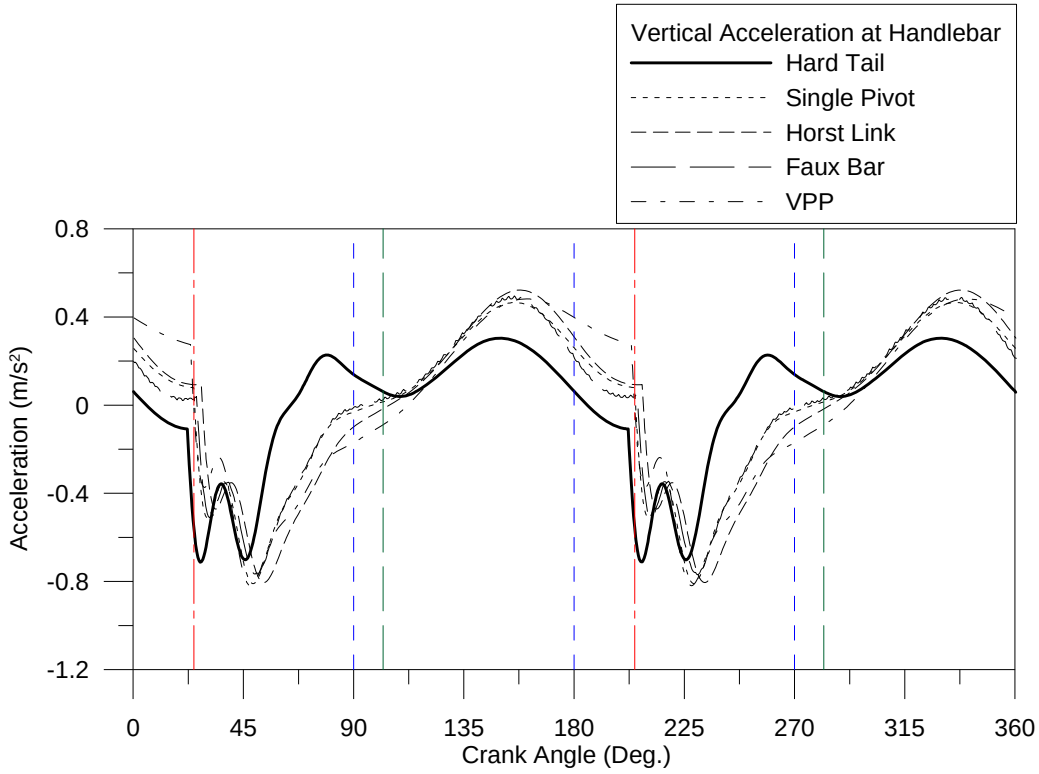

Figure 6.16 Vertical acceleration at CG of handlebar as a function of crank angle for each rider-bike system moving on the flat road surface and in the steady condition

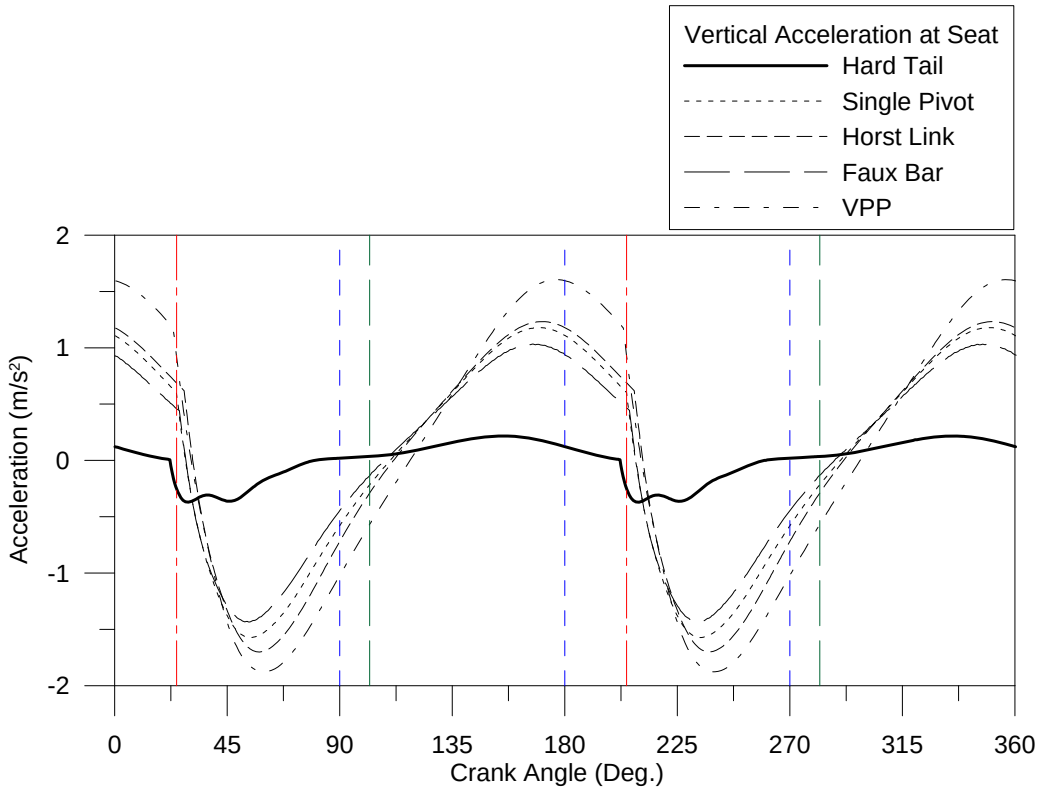

Figure 6.17 Vertical acceleration at seat as a function of crank angle for each rider-bike system moving on the flat road surface and in the steady condition

Table 6.12 The maximum vertical accelerations at handlebar and seat for each rider-bike system moving on the flat road surface and in the steady condition

Accelerations (m/s^2)	Hard Tail	Single Pivot	Horst Link	Faux Bar	VPP
Handlebar					
Maximum	0.303	0.465	0.522	0.493	0.481
Minimum	-0.712	-0.809	-0.805	-0.763	-0.819
Average	-0.2045	-0.172	-0.1415	-0.135	-0.169
Variations	±0.5075	±0.637	±0.6635	±0.628	±0.65
Seat					
Maximum	0.216	1.178	1.232	1.032	1.604
Minimum	-0.371	-1.571	-1.699	-1.431	-1.876
Average	-0.0775	-0.1965	-0.2335	-0.1995	-0.135
Variations	±0.2935	±1.3745	±1.4655	±1.2315	±1.741

6.4 Discussion and Conclusion

In this chapter, the quasi-static analysis of the stationary bare bike is implemented to study the characteristics of the five mountain bikes. Then, the dynamic analyses of each of the five rider-bike systems moving on the flat road surface without bumps are conducted to study the dynamic responses of each rider-bike system due to external excitations. Discussions of the analyses are presented in the following subsections.

6.4.1 Quasi-Static Analysis

In the quasi-static analysis of each stationary bare bike, a vertical downward force F_y=-1000sin$\omega_e t$ N (with exciting frequency ω_e=0.5rad/sec) is applied on either the seat or the handlebar of each of the five bikes to observe the time histories of travel paths of rear axle, contact forces of rear wheel, variations of sprocket distances, chain tension forces, fork compressions, and shock compressions.

For the travel paths of rear axle, the ratios of maximum vertical movement of rear axle to the maximum horizontal one ($|\delta_y|_{max}/|\delta_x|_{max}$) of the five bikes are obtained and the bike with biggest value of $|\delta_y|_{max}$ is determined. Due to no rear suspension system, the ratio $|\delta_y|_{max}/|\delta_x|_{max}$ of the hard tail bike is much bigger than that of the four FS bikes. From highest to lowest, the rank of ratios $|\delta_y|_{max}/|\delta_x|_{max}$ of the four FS bikes is: single pivot, VPP, faux bar, horst link, in which the value of $|\delta_y|_{max}$ of VPP bike is biggest (in spite of its value of $|\delta_y|_{max}/|\delta_x|_{max}$ to be smaller than single pivot). Since the contact force of each rear wheel is proportional to its maximum vertical movement of rear axle, $|\delta_y|_{max}$, the corresponding contact forces of rear wheels of the five bikes show the same trends as their values of $|\delta_y|_{max}$.

For the variations of sprocket distances, due to no rear suspension system, the sprocket distance of the hard tail bike is nearly unchanged, and that of each of the four FS bikes is varied significantly. Since the variations of sprocket distances of faux bar bike are negative, no chain force is applied on the rear axle or bottom bracket. For the

other three FS bikes, the variations of sprocket distances of single pivot bike and VPP bike are similar, but those of the latter are larger, and those of horst link bike are less than 1.0 mm.

For the “fork” compressions, it is found that the greater (steeper) the head angle is, the bigger the fork compression is. On the other hand, for the “shock” compressions, the quasi-static analysis shows that, from highest to lowest, the rank of the four FS bikes is: VPP, single pivot, horst link, faux bar. However, if the dynamic downward force is replaced by a static one, the numerical results show that the real-static shock compression for each of the four FS bikes is only about one half of its quasi-static one, and the trend of ranks is similar except that the ranks of horst link bike and faux bar are exchanged.

In this quasi-static analysis, it is found that the hard tail bike is not significantly affected by the vertical downward force F_y due to no rear suspension system except for its fork compression being slightly less than that of the single pivot bike, because its head angle is very steep (69°) to be 0.5° smaller than that of the single pivot bike. Furthermore, among the four FS bikes, all responses of the VPP bike are the biggest ones except for the fork compression to be smaller than that of the single pivot bike.

6.4.2 Dynamic Analysis of Loaded Bike Moving on Flat Road Surface

In the dynamic analyses of the five rider-bike systems moving on the flat road surfaces, the dynamic responses in the steady conditions including effective pedalling forces, effective pedalling torques and powers, forward velocities V_x in horizontal (x) direction, contact forces of front and rear wheels, fork compressions, shock compressions, variations of sprocket distances, chain tension forces, and vertical accelerations at handlebars and seats are studied, and all the dynamic responses are represented as functions of the crank angles $\overline{\theta}$ with $\overline{\theta} = 0^o$ to $\overline{\theta} = 360^o$ (where $\overline{\theta} = 0^o$ is located at the top dead centre of the right crank).

(a). For the maximum effective pedalling force, that of hard tail bike is biggest due to no rear suspension, and with this value as the benchmark, the decrement of that resulting from the activation of rear suspension system of each FS bike is biggest for the VPP bike and is smallest for the faux bar bike.

(b). For the effective pedalling torques and powers, the maximum pedalling power required by the hard tail bike is biggest. With respect to the hard tail bike, Table 6.5 reveals that the percentage decrement of maximum pedalling power is 2.98% for faux bar bike, is bigger than 3% for each of the other three FS bikes, and is highest (4.13%) for the VPP bike.

(c). For the forward velocities V_x, their averages $\overline{V}_x$ and variations ΔV_x shown in Table 6.6 indicate that the value of $\overline{V}_x$ of the hard tail bike is highest and the corresponding value of ΔV_x is smallest. Among the four FS bikes, the rank of the value of $\overline{V}_x$ from highest to lowest is: single pivot, faux bar, VPP, horst link, while the rank of the value of ΔV_x from highest to lowest is: VPP, horst link, single pivot, faux bar. From the above two ranks, one can find that the bobbing effect of VPP bike will be most serious, because its average moving velocity $\overline{V}_x$ is lowest and the variation ΔV_x is highest. For the other three FS bikes, the $\overline{V}_x$ of horst link bike is lowest and its ΔV_x is highest (only lower than that of the VPP bike), and the performance of single pivot bike and that of faux bar bike are very similar with slight

difference. The lower average moving velocities $\overline{V}_x$ of the four FS bikes reveals that the bobbing effect will be possible to occur on each FS bike.

(d). For the contact forces of front and rear wheels, from Table 6.8, one can see that the rank of average contact force of "front" wheel from biggest to smallest is: hard tail, single pivot, horst link, faux bar, VPP, and that of "rear" wheel is reversed because, for each bike, its average contact force of "rear" wheel is equal to the vertical applied force (F_y) minus that of "front" wheel and the value of F_y is a constant.

(e). For the fork and shock compressions, the average fork compression of hard tail bike is biggest (5.14 mm), while that of VPP bike is smallest (4.745 mm). The rank of average fork compressions from biggest to smallest is the same as that of average contact forces of front wheel, because the latter are proportional to the former. However, the rank of average shock compressions from biggest to lowest is: VPP, horst link, single pivot, faux bar, which is different from that of average contact forces of rear wheels, but the average shock compression and average contact force of rear wheel of the VPP bike are biggest. It is noted that the bigger average contact forces between the wheels and ground can make the rider-bike system more stable during riding, but the bigger variations of average fork or shock compressions can make the rider-bike system more unstable at the same time. From Tables 6.8 to 6.10, one can see that the average contact force of front wheel of hard tail bike and that of rear wheel of VPP bike are biggest, respectively. However, the variation of average fork compression of hard tail is highest, while that of average shock compression of VPP bike is highest.

(f). For the variations of sprocket distances and chain tension forces, from Figure 6.15(a), one can see that the variations of sprocket distances of VPP bike and single pivot bike are similar and much bigger than those of the other three bikes. In addition, the configurations for the rear suspension designs of the VPP and single pivot bikes make the sprocket distances varied more frequently than the four-bar-linkage designs of the horst-link and faux-bar bikes. For the two four-bar-linkage bikes, the variation of sprocket distances of horst link bike is small (about 0.2mm), and that of faux bar bike is about -0.7mm. Due to no rear suspension system, the variation of sprocket

distances of hard tail bike is close to zero.

(g). For the vertical accelerations at handlebar, the differences between the bikes are very small, because the front suspensions of the five bikes are similar to each other. However, from Figure 6.17 one can see that the vertical acceleration at seat of hard tail bike is smallest, and those of the four FS bikes are about two times of that of hard tail bike. Among the four FS bikes, the vertical acceleration at seat of VPP bike is biggest. Therefore, once again, one can confirm that the bobbing effect of VPP bike will be most serious.

From the foregoing discussions, one can see that, for each of the five rider-bike systems moving on the flat road surface and in the steady condition, the performance of hard tail bike will be highest and that of VPP bike will be lowest from the point of view of bobbing effect. The performance difference between the other three FS bikes is small, but that of single pivot bike will be lowest, especially the variations of sprocket distances caused by the activation of its rear shock absorber (and resulting in the bobbing effect). The performances of the two four-bar-linkage bikes are similar, but that of the faux-bar bike will be higher than that of horst-link bike since the moving velocity V_x of the former is higher than that of the latter.

6.4.3 Conclusion

In this chapter, the quasi-static analyses of stationary bare bikes and the dynamic analyses of the five rider-bike systems moving on the flat road surfaces without bumps are studied. It is found that the performance of hard tail bike is best. Due to the rear suspension systems, all four FS bikes have the bobbing effect, which is induced by the activation of each rear suspension due to the rider's pedalling motion, and among the four FS bikes, the bobbing effect of VPP bike is most serious.

Chapter 7 Dynamic Analyses of Loaded Bikes Moving on Flat Road Surface with Bumps

7.1 Introduction

The quasi-static and dynamic responses of bare and loaded bikes in stationary and moving conditions with effect of bumps neglected have been studied in Chapter 6. This chapter is a continuation of the last chapter to study the dynamic responses of various rider-bike systems moving on flat road surface with bumps (bump height h=±0.03m). The pedalling cadence is 86 rpm which will result in the convergence of forward velocity to 11.96 m/s at t=11sec. The related titles include the variations (versus crank angles) of effective pedalling forces, effective pedalling torques and powers, moving velocities V_x in horizontal (x) direction, contact forces of front and rear wheels, fork compressions, shock compressions, sprocket distances, chain tension forces and vertical accelerations at handlebars and seats for each of the five rider-bike systems passing over a hump and through a hollow.

7.2 Effective Pedalling Forces for the Rider-Bike System of a Hard Tail Bike Passing over a Hump and through a Hollow, Respectively

In this subsection, dynamic responses of the rider-bike system of a hard tail bike passing over a long hump and through a long hollow, respectively, are analyzed. The heights of the hump and the hollow are given by h_b=+0.03m and h_b=-0.03m as shown in Figures 7.1(a) and 7.1(b), respectively.

For convenience, either the hump or the hollow is assumed to be located at the position so that the rider-bike system will meet the left end of it at t=11.5sec and leave the right end of it at t=12.5sec, i.e., Δt_b=1.0 second. The time histories of the effective pedalling forces are shown in Figure 7.2 and, for easier observations, the relationship between the effective pedalling forces and the crank angles in the time interval from t=10.94sec to t=13.03sec with corresponding crank angles from $\overline{\theta} = 0^o$ to

$\overline{\theta} = 1080^o$ are shown in Figure 7.3.

When the rider-bike system hits the left side of the hump as shown in Figure 7.1(a) at the moment t=11sec, the instantaneous vertical acceleration due to the hump is upward and "opposite" to the downward gravitational acceleration g = 9.81 m/sec^2, and when it leaves the right end of the hump at the moment t=12.5sec, the instantaneous vertical acceleration due to the hump is downward and "identical" to the downward gravitational acceleration g. In other words, the "gravitational (or inertial) force" of the bike during hitting the left side of the hump is much smaller than that during leaving the right end of the hump, so that the "peak" effective pedalling force of the rider-bike system during hitting the left side of the hump is smaller than that during leaving the right end of the hump as one may see from the solid curves (——) appearing in Figures 7.2 and 7.3.

On the contrary, the situations for the rider-bike system passing through the "hollow" as shown in Figure 7.1(b) are opposite to those passing over the "hump". In other words, when the rider-bike system meets the left end of the hollow as shown in Figure 7.1(b) at the moment t=11.5sec, the instantaneous vertical acceleration due to the hollow is downward and "identical" to the downward gravitational acceleration g and when it hits the right side of the hollow at the moment t=12.5sec, the instantaneous vertical acceleration due to the hollow is upward and "opposite" to the downward gravitational acceleration g. For the last reason, the "gravitational (or inertial) force" of the bike during meeting the left end of the hollow is much greater than that during hitting the right side of the hollow and, in turn, the "peak" effective pedalling force of the rider-bike system during meeting the left end of the hollow is greater than that during hitting the right side of the hollow as one may see from the dashed curves (– – –) appearing in Figures 7.2 and 7.3.

In addition to the foregoing reasonable results, Figures 7.2 and 7.3 reveal that the solid curves (——) and the corresponding dashed curves (– – –) are overlapped each other except at the vicinities of meeting and leaving the bumps, this is also a reasonable one.

For convenience of comparisons, the "peak" effective pedalling forces due to the

rider-bike system of the hard tail bike meeting and leaving a hump and a hollow shown in Figure 7.2 or 7.3 are summarized in Table 7.1. It is seen that, for the rider-bike system passing over the "hump", the minimum (reverse) peak effective pedalling force is 132.91N during hitting the left side of the hump and the maximum peak force is 581.99N during leaving the right end of the hump, while for the rider-bike system passing through the "hollow", the maximum peak effective pedalling force is 582.79N during meeting the left end of the hollow and the minimum (reverse) peak force is 122.87N during hitting the right side of the hollow. Since the effect of the rider-bike system hitting the left side of the hump is the same as that hitting the right side of the hollow to produce the upward accelerations, this is the reason why the minimum (reverse) peak effective pedalling force of the rider-bike system during hitting the left side of the hump (132.91N) is near that during hitting the right side of the hollow (122.87N) with difference ΔF_{up}=132.91-122.87=10.04N (with the subscript of the symbol ΔF_{up} denoting the accelerations due to the bumps is "upward"). Similarly, the effect of the rider-bike system leaving the right end of the hump is the same as that meeting the left end of the hollow to produce the downward accelerations, this is the reason why the maximum peak effective pedalling force of the rider-bike system during leaving the right end of the hump (581.99N) is near that during meeting the left end of the hollow (582.79N) with difference ΔF_{down}=582.79-581.99=0.8N (with the subscript of the symbol ΔF_{down} denoting the accelerations due to the bumps is "downward"). In general, the "phase angle" between the time instant of meeting the left end of the bump and the associated pedalling stroke, $\Delta\theta_{meet} = \omega_e \Delta t_m$ (with Δt_m denoting the phase time interval at meeting the left end of the bump as shown in Figure 7.2), is different from that of leaving the right end of the bump and the associated pedalling stroke, $\Delta\theta_{leave}=\omega_e \Delta t_l$ (with Δt_l denoting the phase time interval at leaving the right end of the bump as shown in Figure 7.2), and this is the reason why the foregoing values of ΔF_{up} and ΔF_{down} are not equal to zero.

If Δt_b (= 1.0 second for the current example) denotes the time duration from the rider-bike system meeting the left end of the bump to that leaving the right end of the bump [see Figures 7.1 and 7.2] and T_p denotes the period of the pedalling forces or strokes (see Figure 7.2), then one of the simplest ways to achieve the condition of

$\theta_{hit} = \theta_{leave}$ so that $\Delta F_{up} = \Delta F_{down} = 0$ is to set the ratio of Δt_b to T_p to be equal to the integers, i.e., $\Delta t_b / T_p = 1,2,3,...$

To confirm the last statement, a simulation is implemented, where the period of the pedalling forces after the rider-bike system of the hard tail bike reaching the steady condition is $T_p \approx 0.694$sec. As shown in Figure 7.3, when the rider-bike system meets the left end of the hump (or hollow) and then moves on the top of the hump (or the bottom of the hollow), it will restore the steady condition in the next pedalling stroke (with crank angle θ=360°~720°). Therefore, if one sets Δt_b to be three times of T_p, i.e., $\Delta t_b = 3T_p = 0.694 \times 3 = 2.082$sec, then the rider-bike system will restore the steady condition before leaving the right end of the hump (or hollow). Since the rider-bike system meets the left end of the hump (or hollow) at t=11.5sec (see Figure 7.1), the phase angle of meeting the left end of the bump (either hump or hollow) will be equal to that of leaving the right end of the bump (i.e., $\theta_{meet} = \theta_{leave}$) if the moment of leaving the right end of the bump is selected at t=11.5+2.082=13.582sec.

Based on the last assumption of $\Delta t_b = 3T_p = 0.694 \times 3 = 2.082$sec, the time histories of pedalling forces for the rider-bike system meeting the left end of the bump and leaving the right end of the bump (including "hump" and "hollow") are shown in Figure 7.4, and for easier observations and explanations, the time histories in the time interval from t=10.94sec to t=13.72sec with corresponding crank angles from $\overline{\theta} = 0^o$ to $\overline{\theta} = 1440^o$ are shown in Figure 7.5, and the maximum and minimum peak forces (based on the "absolute" values) and the corresponding crank angles for the rider-bike system meeting the left end of the bump and leaving the right end of the bump are summarized in Table 7.2. It is seen that, for the rider-bike system passing over the "hump" (denoted by the solid curves, ——), the minimum (reverse) peak effective pedalling force is 132.91N during meeting the left end of the hump at the crank angle $\overline{\theta} = 305.03^o$, and the maximum peak force is 582.27N during leaving the right end of the hump at the crank angle $\overline{\theta} = 1366.37^o$ [=(360°×3)+286.37°], while for the rider-bike system passing through the "hollow" (denoted by the dashed curves, – – –), the maximum peak effective pedalling force is 582.79N during meeting the left end of the hollow at the crank angle $\overline{\theta} = 288.7^o$, and the minimum (reverse) peak force is

132.16N during hitting the right side of the hollow at the crank angle $\overline{\theta} = 1358.35^{o}$ [=(360°×3)+303.47°].

Therefore, the difference between the minimum (reverse) peak effective pedalling force of "hitting the left side of the hump" and that of "hitting the right side of the hollow" is ΔF_{up}=132.91-132.16=0.75N and the difference between the corresponding phase angles is $\Delta\theta_{up}$=305.03°-303.47°=1.56°. Similarly, the difference between the maximum peak effective pedalling force of "leaving the right end of the hump" and that of "meeting the left end of the hollow" is ΔF_{down}=582.79-582.27=0.52N and the difference between the corresponding phase angles is $\Delta\theta_{down}$=288.7°-286.37°=2.33°. The foregoing slight differences of phase angles and pedalling forces may be due to the time duration (Δt_b=3T_p=0.694×3= 2.082sec) for the rider-bike system moving on the top of the hump (or the bottom of the hollow) to be not long enough, so that the rider-bike system cannot completely restore to the steady condition at leaving the right end of the hump (or hollow). However, it is evident that if Δt_b=3T_p, then the phase angle for the rider-bike system meeting the left end of the bump (either "hump" or "hollow") is close to that leaving the right end of the bump (i.e., $\theta_{meet} \approx \theta_{leave}$) so that the minimum (reverse) peak effective force due to hitting the left side of the hump is close to that hitting the right side of the hollow (i.e, $F_{up,hump} \approx F_{up,hollow}$ or $\Delta F_{up} \approx 0$) and the maximum peak effective force due to leaving the right end of the hump is close to that meeting the left end of the hollow (i.e., $F_{down,hump} \approx F_{down,hollow}$ or $\Delta F_{down} \approx 0$).

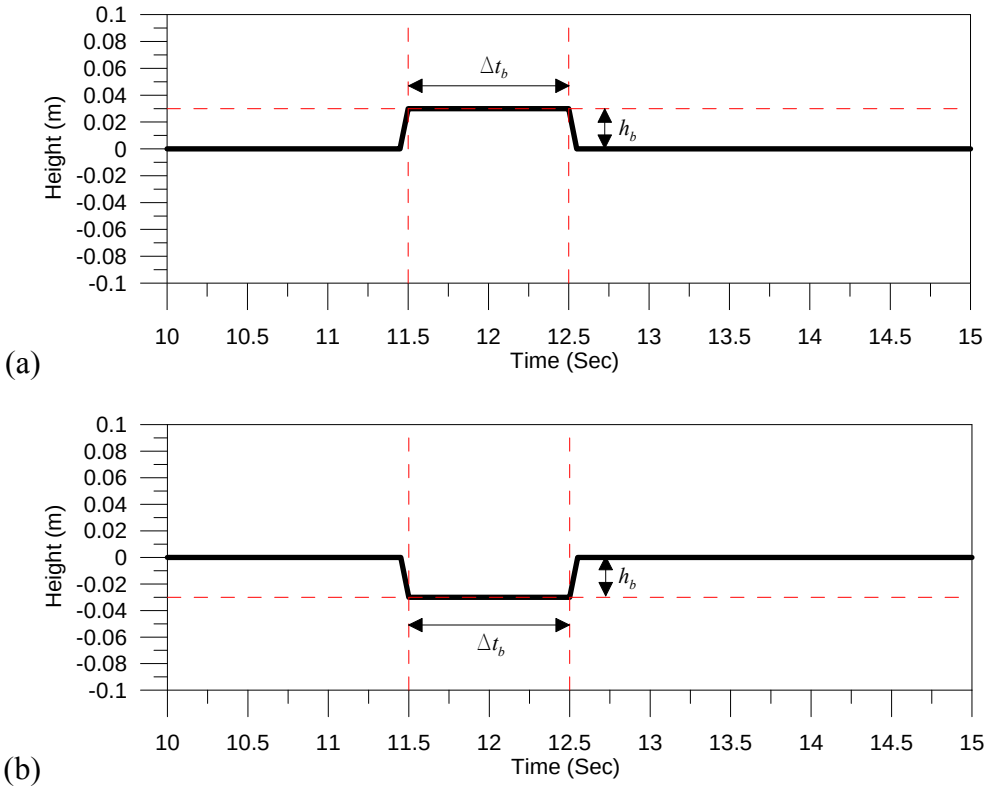

Figure 7.1 Types of the bumps: (a) Hump, (b) Hollow

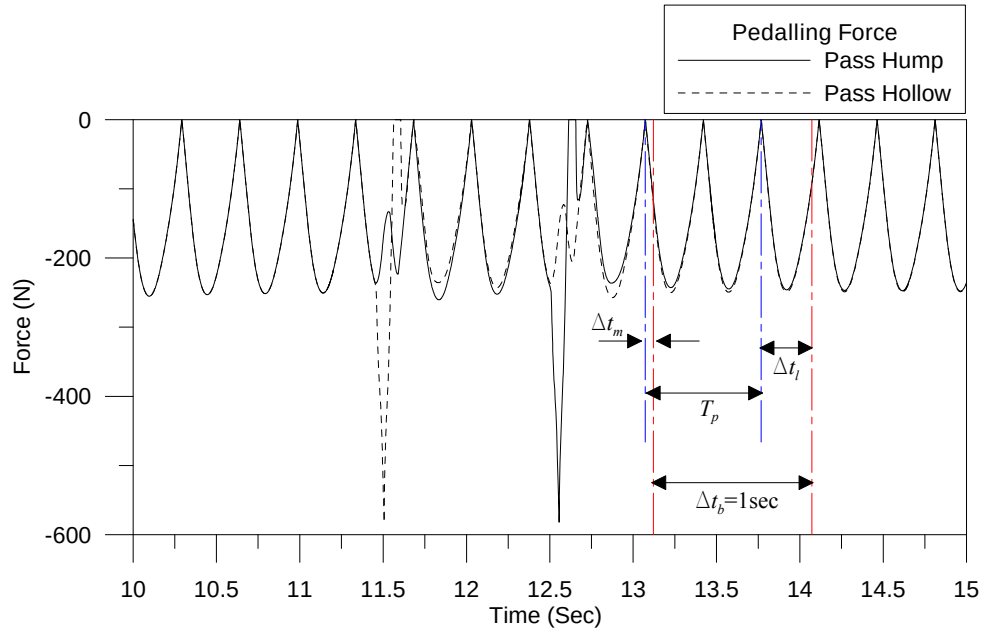

Figure 7.2 Time histories of effective pedalling forces due to the rider-bike system of a hard tail bike passing over a "hump" [Figure 7.1(a)] (denoted by the solid curves, ——) and through a "hollow" [Figure 7.1(b)] (denoted by the dashed curves, – – –), respectively. Where Δt_m and Δt_l denote the phase time intervals associated with the phase angles $\Delta\theta_{meet} = \omega_e \Delta t_m$ and $\Delta\theta_{leave} = \omega_e \Delta t_l$ at meeting and leaving the bumps, respectively, and ω_e is the angular velocity of the rotating crank.

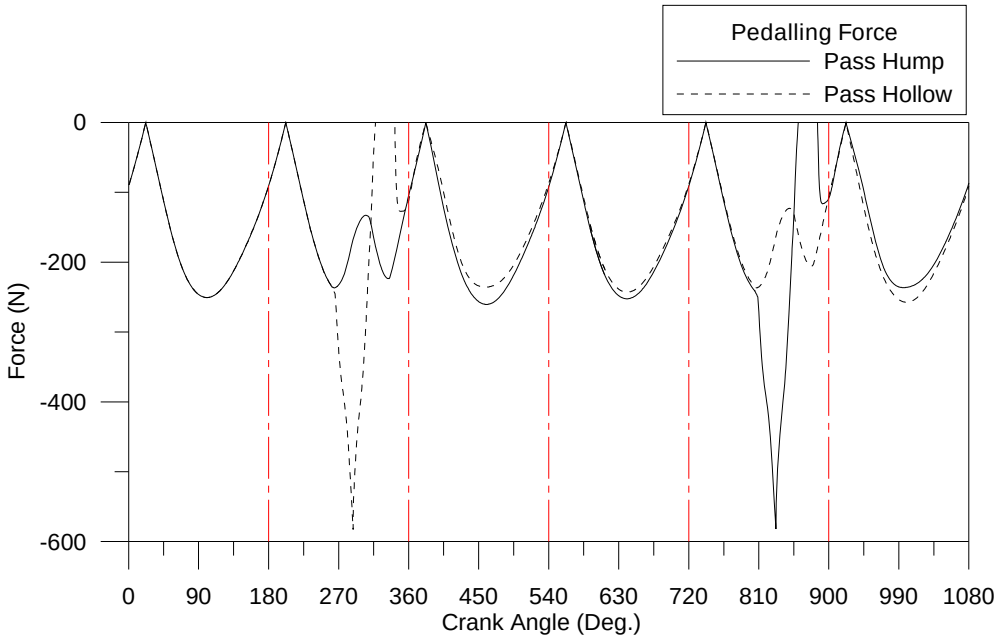

Figure 7.3 The relationship between the effective pedalling forces and the associated crank angles due to the rider-bike system of a hard tail bike passing over a "hump" [Figure 7.1(a)] (denoted by the solid curves, ——) and through a "hollow" [Figure 7.1(b)] (denoted by the dashed curves, – – –), respectively.

Table 7.1 Minimum and maximum peak effective pedalling forces due to the rider-bike system of the hard tail bike meeting and leaving a hump [Figure 7.1(a)] and a hollow [Figure 7.1(b)], respectively

Conditions	Min./max. peak effective pedalling forces (N)	
	Hump	Hollow
Meeting	132.91*	581.99**
Leaving	582.79**	122.87*

* Minimum (reverse) peak force (based on the "absolute" values)

** Maximum peak force (based on the "absolute" values)

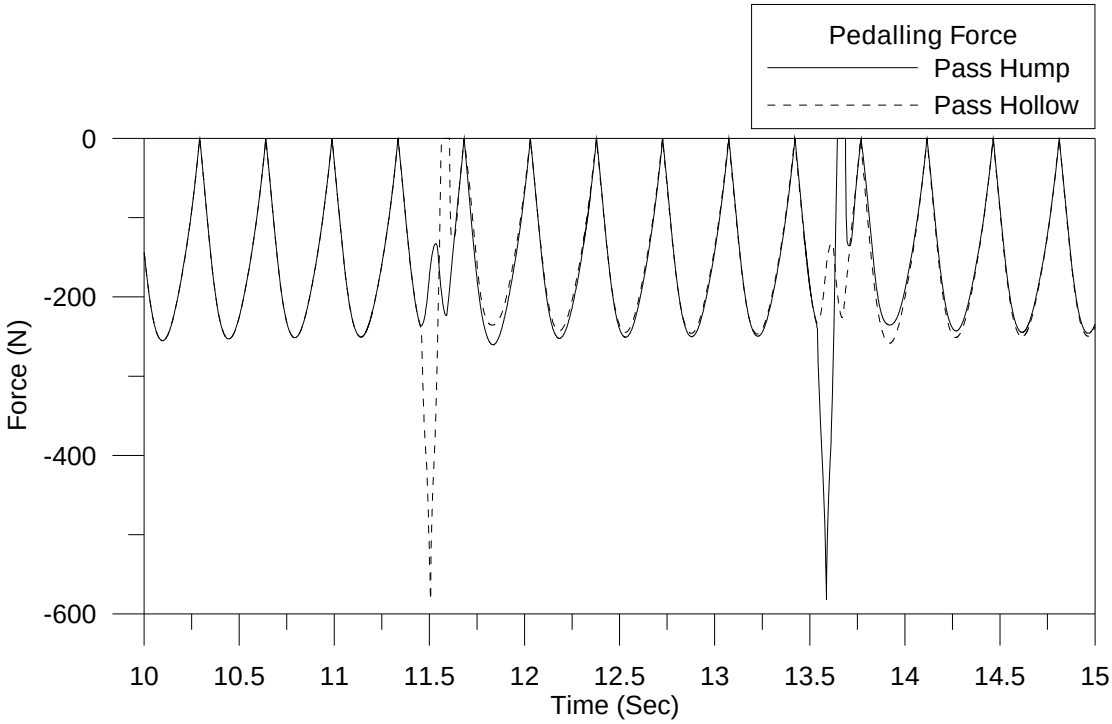

Figure 7.4 Time histories of effective pedalling forces for the rider-bike system meeting the "hollow" (denoted by the dashed curves, - - -) and leaving the "hump" (denoted by the solid curves, ——), respectively, with the same phase angle.

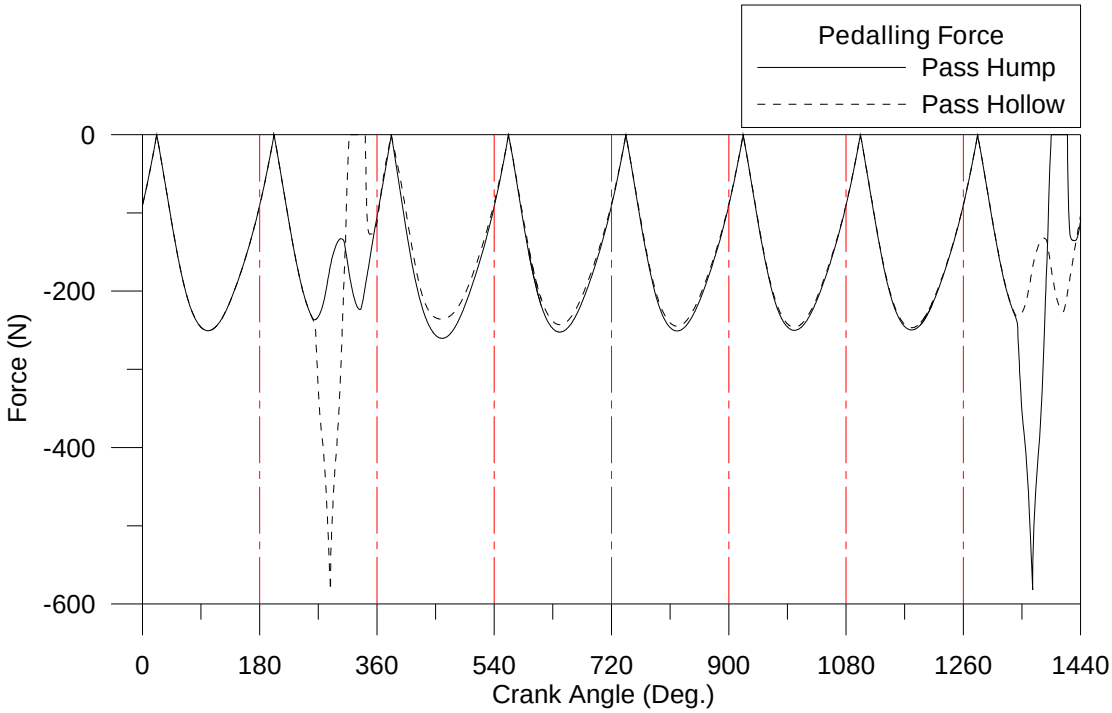

Figure 7.5 The relationship between the effective pedalling forces and crank angles for the rider-bike system meeting the "hollow" (denoted by the dashed curves, - - -) and leaving the "hump" (denoted by the solid curves, ——), respectively, with the same phase angle

Table 7.2 Minimum and maximum peak effective pedalling forces and associated phase angles for the rider-bike system of the hard tail bike meeting and leaving a hump and a hollow with $\Delta t_b = 3T_p$, respectively.

Conditions	—	Hump	Hollow
Hitting	Peak forces (N)	132.91*	582.79**
	Phase angles	305.03°	288.70°
Leaving	Peak forces (N)	582.27**	132.16*
	Phase angles	1366.37° =(360°×3)+286.37°	1383.47° =(360°×3)+303.47°

* Minimum (reverse) peak force (based on the "absolute" values)

** Maximum peak force (based on the "absolute" values)

7.3 Effective Pedalling Forces for each Rider-Bike System of the Five Bikes Passing over a Hump and through a Hollow

After testing the rider-bike system of a hard tail bike passing over a hump and through a hollow, respectively, now the dynamic responses for each of the five rider-bike systems passing through the flat road surface with both a hump and a hollow will be analyzed. For the current simulation, since each rider-bike system will reach the steady condition with constant speed V_x=12m/s at time $t \approx 11$sec, the two bumps (see Figure 7.6) are assumed to be located at the positions so that the bike hits the left side of the hump (first bump) at t=11.5sec (to rapidly lift up a bump height at t=11.45sec), leaves the right end of the hump at t=12.144sec (11.45sec+T_p) and then returns to the ground at t=12.194sec; next, the bike meets the left end of the hollow (second bump) at t=12.888sec [to rapidly lower a bump height at t=12.838sec (=12.144sec+T_p)], hits the right side of the hollow at t=13.532sec (12.838sec+T_p), then returns to the ground at t=13.582sec. Thus, the phase angles of hitting the left side and leaving the right end of the hump (first bump) are approximately equal to the corresponding ones of meeting the left end and hitting the right side of the hollow (second bump), so that $\theta_{meet} \approx \theta_{leave}$ and the time histories in the time interval from t=10sec to t=15sec are studied.

The types of the hump and the hollow are shown in Figure 7.6, in which the heights of both bumps are the same as those shown in Figures 7.1(a) and 7.1(b), i.e., h_b = +0.03m for the hump and h_b = -0.03m for the hollow, respectively.

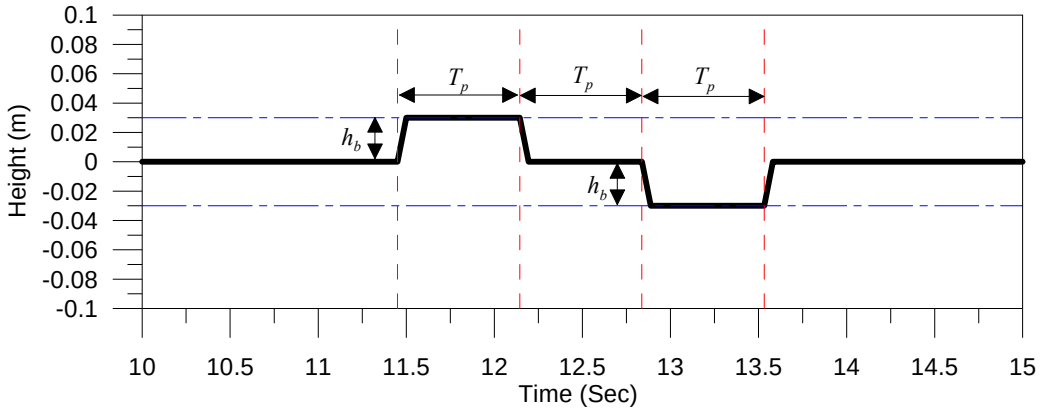

Figure 7.6 The mathematical model for the flat road surface with both "reference" bumps (a hump and a hollow) for each rider-bike system of the five bikes.

The relationship between pedalling forces and crank angles for each of the five rider-bike systems passing through the bumps is shown in Figure 7.7. Since each of the five rider-bike systems pedals 3960° (i.e., 11 pedalling cycles) at time $t \approx 11$sec, for convenience, the crank angle with its "origin" located at time t=0 is denoted by $\theta(t)$ and that at time t=11sec by $\bar{\theta}(t)$ in the foregoing and following discussions. Based on the last statements one has the relationship $\bar{\theta}(t) = \theta(t)$-3960°, thus, $\bar{\theta}(t) = \theta(t)$-3960°=3960°-3960°=0° at time t=11sec. According to Figure 6.7, although the period of pedalling stroke of each rider-bike system may be assumed to be the same (T_p=0.694sec), actually, there exists a slight "time difference" to reach the "steady" condition (to be less than 1.0sec) between the five rider-bike systems. Therefore, the two bumps for each rider-bike system are arranged in such locations that the "time difference" to reach the steady condition for each rider-bike system can be as small as possible and that the associated phase angles of the five rider-bike systems passing through their (two) bumps are close to each other, as shown in Table 7.3. Thus, one may easily find the differences between the responses of the five rider-bike systems passing through their bumps and there is no need to worry out the influences due to different phase angles.

If each rider-bike system is assumed to hit the left side of the hump at the moment with crank angle $\bar{\theta}_1$=299.5° and to meet the left end of the hollow at the moment with $\bar{\theta}_3$=1003.158° (see Table 7.3), then the dynamic responses of the five rider-bike systems are shown in Figure 7.7 and for easier observations, the last dynamic responses are further magnified and shown in Figures 7.8(a) together with 7.8(b).

From Figure 7.8(a) one sees that, when each bike hits the left side of the hump, the pedalling force decreases to some degree because the upward acceleration (induced by the hump) reduces the gravitational effect of the bike frame, so that the pedalling force applied for passing over the hump is smaller than the normal one. At the moment with crank angle $\bar{\theta}_2$=644.792°, each rider-bike system begins to leave the right end of the hump (and return to flat road surface), this leads to the bike rapidly falling h_b=0.03m and producing the downward acceleration. Thus, the corresponding pedalling force becomes greater than the normal one.

From Figure 7.8(b), one can see when each bike begins to meet the left end of the hollow at the moment with the crank angle $\bar{\theta}_3$=1003.158°, it rapidly falls h_b=0.03m and produces the downward acceleration (with direction identical to the gravitational acceleration g), so that the maximum instantaneous pedalling force appears. At the moment with crank angle $\bar{\theta}_4$=1373.436°, the rider-bike system hits the right side of the hollow and returns to flat road surface, now, the bike rapidly raises h_b=0.03m and produces the upward acceleration (with direction opposite to g) so that the pedalling force is smaller than the normal one.

Based on Figures 7.8(a) and 7.8(b), the peak effective pedalling forces and the four corresponding crank angles are summarized in Table 7.3, for convenience, the above-mentioned four crank angles are called "peak" crank angles. For convenience, the minimum (reverse) peak force corresponding to $\bar{\theta}_1 = 299.5^o$ is represented by $|F_p|_{\bar{\theta}_1,j}$ with the subscript "j" referring to the j-th rider-bike system, and the maximum "normal" effective pedalling force for each rider-bike system moving on the flat road surface (without bumps) shown in Table 6.4 is also listed in the 3rd row of Table 7.3 and denoted by $|F_p|_{steady,j}$ with the subscript "steady" denoting the rider-bike system to be in "steady" condition. From the difference between $|F_p|_{steady,j}$ and $|F_p|_{\bar{\theta}_1,j}$, $\Delta|F_p|_{hit\ hump,j}=|F_p|_{steady,j}-|F_p|_{\bar{\theta}_1,j}$ (j=1~5), one can find the variation of the pedalling forces for each of the five bikes hitting the left side of the hump. From Table 7.3, one can see that the value of $\Delta|F_p|_{hit\ hump,j}$ for each of the FS bikes is smaller than that for the hard tail bike due to the effects of rear suspension systems of the FS bikes. Based on the values of $\Delta|F_p|_{hit\ hump,j}$, with the smaller one denoting the higher rank, the ranks of the four FS bikes are: horst link bike, faux bar bike, single pivot bike, VPP bike. It is noted that the value of $\Delta|F_p|_{hit\ hump,j}$ for the VPP bike (with last rank) is slighter greater than that for the single pivot bike.

In Table 7.3, the maximum peak effective pedalling force corresponding to the crank angle $\bar{\theta}_2$=644.792° for each of the five rider-bike systems is represented by $|F_p|_{\bar{\theta}_2,j}$. Therefore, from the difference between $|F_p|_{\bar{\theta}_2,j}$ and $|F_p|_{steady,j}$, $\Delta|F_p|_{leave\ hump,j}=|F_p|_{\bar{\theta}_2,j}-|F_p|_{steady,j}$ (j=1~5), one can find the variation of the pedalling forces for each of the five bikes leaving the right end of the hump. It is seen that the value of $\Delta|F_p|_{leave}$

$_{hump,j}$ for each of the FS bikes is smaller than that for the hard tail bike, and is close to that of meeting the left end of the hollow.

Based on the values of $\Delta|F_p|_{leave\ hump,j}$, with the smaller one denoting the higher rank, the ranks of the four FS bikes are: horst link bike, faux bar bike, single pivot bike, VPP bike. It is noted that the value of $\Delta|F_p|_{leave\ hump,j}$ for the VPP bike (with last rank) is also slighter greater than that for the single pivot bike.

In Table 7.3, if the maximum effective pedalling force corresponding to the crank angle $\bar{\theta}_3$=1003.158° is represented by $|F_p|_{\bar{\theta}_3,j}$, then the variations of pedalling forces due to meeting the left end of the hollow is determined by $\Delta|F_p|_{meet\ hollow,j}$= $|F_p|_{\bar{\theta}_3,j}$ -$|F_p|_{steady,j}$. It is seen that the magnitudes of $\Delta|F_p|_{meet\ hollow,j}$ for the four FS bike do not have much difference, but that $\Delta|F_p|_{meet\ hollow,j}$ for the VPP bike is slightly higher than that for the hard tail bike.

Finally, if the minimum (reverse) effective pedalling force corresponding to the crank angle $\bar{\theta}_4$ =1373.436° is represented by $|F_p|_{\bar{\theta}_4,j}$, then the variations of them due to hitting the right side of the hollow is determined by $\Delta|F_p|_{leave\ hollow,j}=|F_p|_{steady,j}-|F_p|_{\bar{\theta}_4,j}$. From Table 7.3, one sees that the ranks of the four FS bikes based on the values of $\Delta|F_p|_{leave\ hollow,j}$ are the same as that based on those of $\Delta|F_p|_{hit\ hump,j}$, but the values of $\Delta|F_p|_{leave\ hollow,j}$ are slightly higher than the corresponding ones of $\Delta|F_p|_{hit\ hump,j}$, except that of the VPP bike.

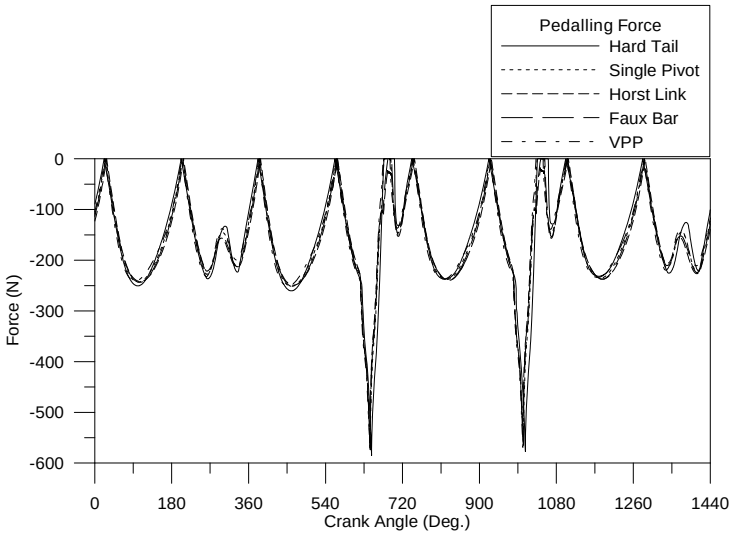

Figure 7.7 The relationship between pedalling forces and crank angles for each of the rider-bike systems passing through its both bumps (a hump and a hollow)

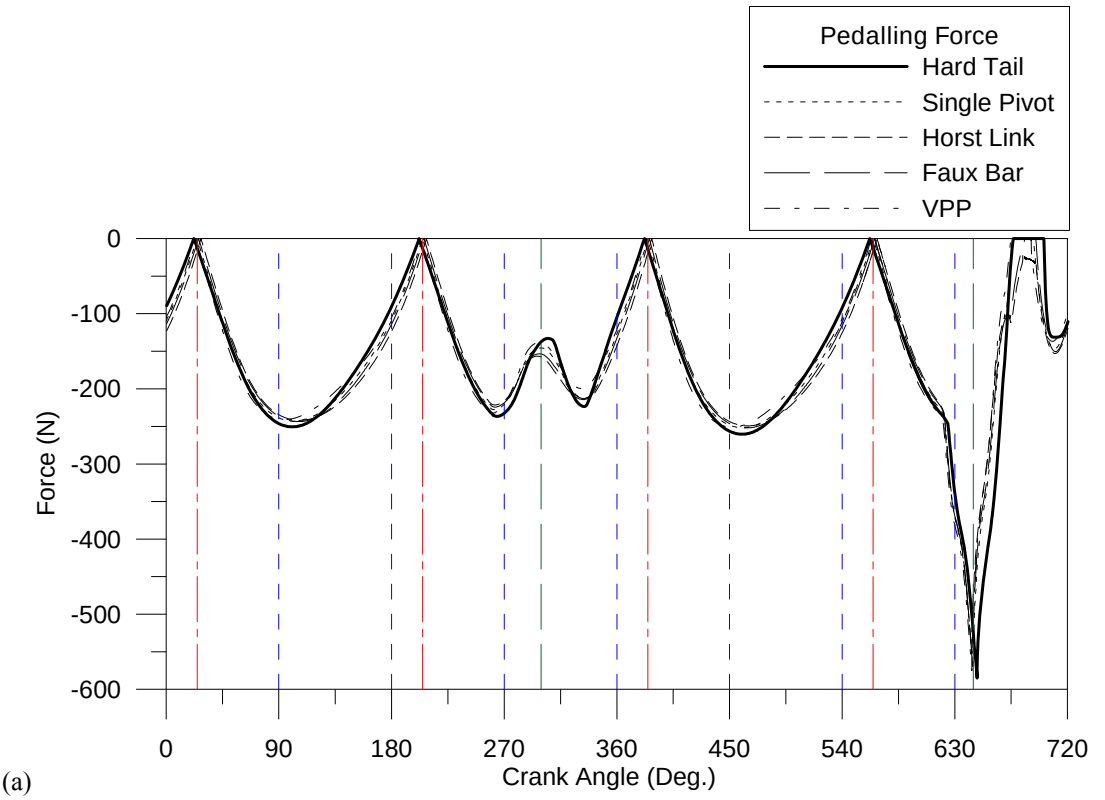

(a)

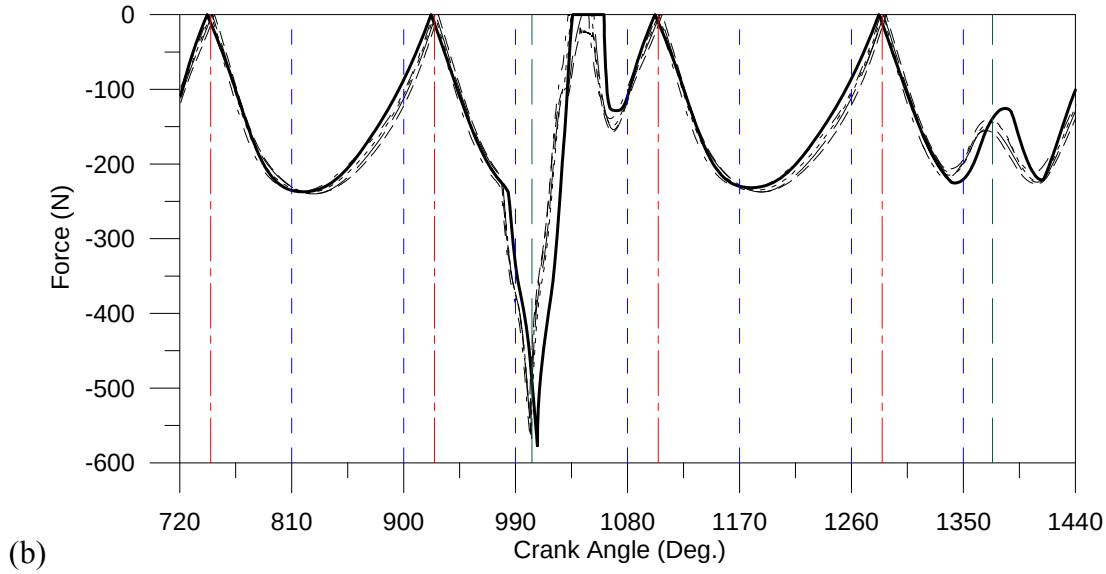

(b)

Figure 7.8 The relationship between effective pedalling forces and crank angles due to each of the rider-bike systems passing (a) over a hump and (b) through a hollow.

Table 7.3 Minimum and maximum peak effective pedalling forces and the corresponding "peak" crank angles for each of the five rider-bike systems passing through its two bumps

Types of bike		Hard Tail (j=1)		Single Pivot (j=2)		Horst Link (j=3)		Faux Bar (j=4)		VPP (j=5)	
Min./max. peak pedalling forces and corresponding peak crank angles		$\lvert F_p \rvert$ (N)	$\overline{\theta}$ (deg.)	$\lvert F_p \rvert$ (N)	$\overline{\theta}$ (deg.)	$\lvert F_p \rvert$ (N)	$\overline{\theta}$ (deg.)	$\lvert F_p \rvert$ (N)	$\overline{\theta}$ (deg.)	$\lvert F_p \rvert$ (N)	$\overline{\theta}$ (deg.)
$\lvert F_p \rvert_{steady,j}$ (on flat road without bumps)		248.65		240.95		239.81		241.63		239.05	
Hump	Min. (reverse) Peak, $\lvert F_p \rvert_{\overline{\theta}_1,j}$ ($\overline{\theta}_1$=299.5°)	132.91	305.03°	145.52	299.49°	156.50	296.63°	153.43	297.97°	137.80	298.38°
	$\Delta\lvert F_p \rvert_{hit\ hump,j}$	115.74		95.43		83.31		88.2		101.25	
	Max. Peak, $\lvert F_p \rvert_{\overline{\theta}_2,j}$ ($\overline{\theta}_2$=644.792°)	587.97	647.80° (287.80°)	573.70	644.55° (284.55°)	554.49	643.61° (283.61°)	569.59	644.32° (284.32°)	574.94	643.68° (283.68°)
	$\Delta\lvert F_p \rvert_{leave\ hump,j}$	339.32		332.75		314.68		327.96		335.89	
Hollow	Max. Peak, $\lvert F_p \rvert_{\overline{\theta}_3,j}$ ($\overline{\theta}_3$=1003.158°)	575.66	1007.47° (287.47°)	566.92	1002.83° (282.83°)	543.97	1001.45° (281.45°)	562.48	1002.45° (282.45°)	568.78	1001.59° (281.59°)
	$\Delta\lvert F_p \rvert_{meet\ hollow,j}$	327.01		325.97		304.16		320.85		329.73	
	Min. (reverse) Peak, $\lvert F_p \rvert_{\overline{\theta}_4,j}$ ($\overline{\theta}_4$=1373.436°)	125.57	1383.28° (303.28)	144.51	1373.03° (293.03°)	155.48	1368.72° (288.72°)	152.28	1371.03° (291.03°)	139.49	1371.12° (291.12°)
	$\Delta\lvert F_p \rvert_{leave\ hollow,j}$	123.08		96.44		84.33		89.35		99.56	

$\overline{\theta}_i$ (i=1~4): Average peak crank angle: Summation of five corresponding peak crank angles divided by five

$\Delta \lvert F_p \rvert_{hit\ hump,j} = \lvert F_p \rvert_{steady,j} - \lvert F_p \rvert_{\overline{\theta}_1,j}$; $\Delta \lvert F_p \rvert_{leave\ hump,j} = \lvert F_p \rvert_{\overline{\theta}_2,j} - \lvert F_p \rvert_{steady,j}$;

$\Delta \lvert F_p \rvert_{meet\ hollow,j} = \lvert F_p \rvert_{\overline{\theta}_3,j} - \lvert F_p \rvert_{steady,j}$; $\Delta \lvert F_p \rvert_{leave\ hollow,j} = \lvert F_p \rvert_{steady,j} - \lvert F_p \rvert_{\overline{\theta}_4,j}$ (j=1~5 , numberings of bikes)

7.4 Pedalling Power Developed by the Rider Riding Each of the Five Bikes Passing over a Hump and through a Hollow

The relationship between pedalling powers and crank angles from $\overline{\theta} = 0^o$ to $\overline{\theta} = 1440^o$ are shown in Figures 7.9(a) and 7.9(b). The trend is similar to that of Figures 7.8(a) and 7.8(b) for the effective pedalling forces. The pedalling powers developed by the rider to ride each of the five bikes at four moments corresponding to the four "peak" crank angles ($\overline{\theta}_1$ to $\overline{\theta}_4$) are summarized in Table 7.4, in which, the maximum pedalling powers for the five rider-bike systems moving on flat road surface (without bumps) shown in Table 6.5 are also listed in the 2nd row of the table and denoted by $W_{steady,\,j}$.

In the Section 6.3.1, Table 6.5 shows that the power developed by the rider of a hard tail bike ($W_{steady,\,1}$) is biggest so that the hard tail bike has the highest pedalling efficiency. From Table 7.4, one can see that, either hitting the left side of the hump or hitting the right side of the hollow, the power required by the hard tail bike ($W_{\overline{\theta}_1,1}$ or $W_{\overline{\theta}_4,1}$) is lowest while that of leaving the right end of the hump or meeting the left end of the hollow ($W_{\overline{\theta}_2,1}$ or $W_{\overline{\theta}_3,1}$) is highest. On the contrary, the power required by the horst link bike during hitting the left side of the hump or hitting the right side of the hollow ($W_{\overline{\theta}_1,3}$ or $W_{\overline{\theta}_4,3}$) is highest, and that of leaving the right end of the hump or meeting the left end of the hollow ($W_{\overline{\theta}_2,3}$ or $W_{\overline{\theta}_3,3}$) is lowest.

From the difference between $W_{steady,j}$ and $W_{\overline{\theta}_i,j}$ (i=1~4, j=1~5), one can see that which bike is more suitable for riding on the off-road terrains. Basically, the lower value of the variation (ΔW_j) is, the less variable the bike is. From Table 7.4, one can see that the ranks of the four variations ($\Delta W_{hit\ hump,j}$, $\Delta W_{leave\ hump,j}$, $\Delta W_{meet\ hollow,j}$, $\Delta W_{leave\ hollow,j}$) from lowest to highest are: horst link, faux bar, single pivot, VPP, hard tail (except that the value of $\Delta W_{meet\ hollow,j}$ for the VPP bike is slightly higher than that for the hard tail bike). This rank reveals that both four-bar-linkage bikes are more suitable for the rider to ride on the off-road terrains, because the powers developed by the rider are not decreased too much comparing with that developed by the rider of the hard tail bike. It is noted that, for all cases of Table 7.4, the pedalling powers of single pivot bike are the third rank among the five bikes, which means that the performance of

single pivot bike is the least variable.

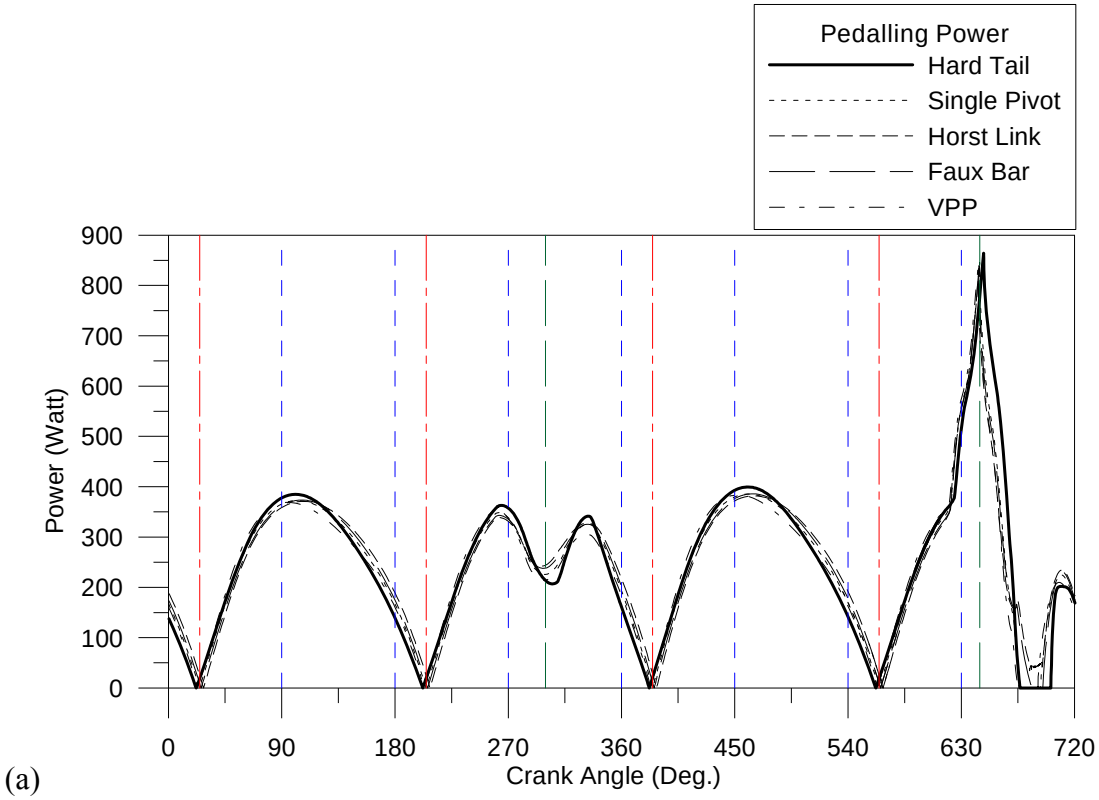

(a)

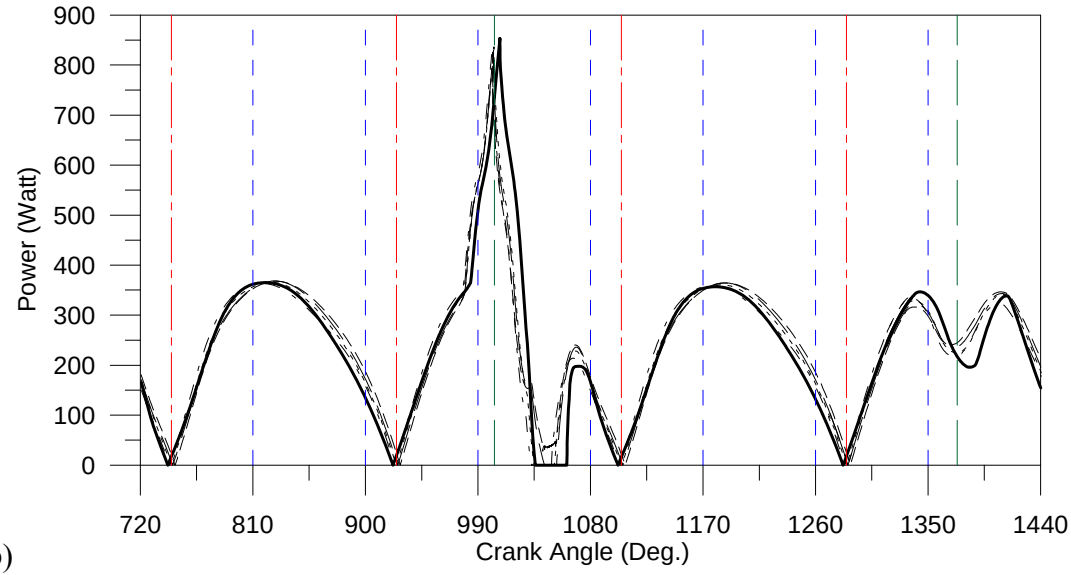

(b)

Figure 7.9 The relationship between pedalling power and crank angles for each rider-bike system passing (a) over a hump and (b) through a hollow.

Table 7.4 Minimum and maximum pedalling powers developed by the rider riding each of the five bikes passing through the bumps at the moments corresponding to the four "peak" crank angles ($\overline{\theta}_1$ to $\overline{\theta}_4$)

—		Pedalling Power (Watts)	Hard Tail (j=1)	Single Pivot (j=2)	Horst Link (j=3)	Faux Bar (j=4)	VPP (j=5)
Maximum pedalling power in steady condition on flat road (without bumps)		$W_{steady,\,j}$	382.05	369.65	367.79	370.66	366.24
Hump	Minimum ($\overline{\theta}_1$=299.5°)	$W_{\overline{\theta}_1,j}$	206.99	225.86	242.46	237.86	213.92
	$\Delta W_{hit\ hump,j} = W_{steady,j} - W_{\overline{\theta}_1,j}$		175.06	143.79	125.33	132.80	152.32
	Maximum ($\overline{\theta}_2$=644.792°)	$W_{\overline{\theta}_2,j}$	864.16	845.83	813.91	839.67	846.98
	$\Delta W_{leave\ hump,j} = W_{\overline{\theta}_2,j} - W_{steady,j}$		482.11	476.18	446.12	469.01	480.74
Hollow	Maximum ($\overline{\theta}_3$=1003.158°)	$W_{\overline{\theta}_3,j}$	853.24	836.19	803.01	829.50	838.13
	$\Delta W_{meet\ hollow,j} = W_{\overline{\theta}_3,j} - W_{steady,j}$		471.19	466.54	435.22	458.84	471.89
	Minimum ($\overline{\theta}_4$=1373.436°)	$W_{\overline{\theta}_4,j}$	196.04	224.33	240.85	236.10	216.50
	$\Delta W_{leave\ hollow,j} = W_{steady,j} - W_{\overline{\theta}_4,j}$		186.01	145.32	126.94	134.56	149.74

7.5 Forward Velocities for each of the Rider-Bike Systems of the Five Bikes Passing over a Hump and through a Hollow

The relationship between forward velocities (V_x) and crank angles of front wheel are shown in Figures 7.10(a) and 7.10(b), and that of rear wheel are shown in Figures 7.11(a) and 7.11(b). The moving velocities at the moments corresponding to the four "peak" crank angles ($\overline{\theta}_1$ to $\overline{\theta}_4$) due to each of the rider-bike systems passing through the bumps (a hump and a hollow) are summarized in Table 7.5, in which the symbol $|\overline{V}_x|_{steady,j}$ given in the 3rd row of the table denotes the average speed of each bike shown in Table 6.6. Since there exists a small time difference between the front and rear wheels hitting the bump, as discussed in Section 5.5.3, the dynamic responses between front and rear wheels are also slightly different. The moving velocity of either front or rear wheel increases slightly when each bike hits the left side of the hump (at $\overline{\theta}_1$=299.5°) or hits the right side of the hollow (at $\overline{\theta}_4$=1373.436°), as shown in Figures 7.10 and 7.11. The peak values are summarized in Table 7.5 and denoted by $|V_x|_{hit\ hump,j}$ and $|V_x|_{leave\ hollow,j}$, respectively. It is seen that the average speed of VPP bike is only slightly higher than horst link bike. However, when the VPP bike hits the left side of the hump or hits the right side of the hollow, its moving velocities ($|V_x|_{hit\ hump,j}$ and $|V_x|_{leave\ hollow,j}$) are only slightly smaller than the corresponding ones of hard tail bike (for both front and rear wheels).

When the value of V_x reaches the minimum due to each bike has left the right end of the hump (at $\overline{\theta}_2$=644.792°) or met the left end of the hollow (at $\overline{\theta}_3$=1003.158°) and the front wheel touches the ground, the value of V_x rises to the maximum rapidly, as shown in Figures 7.10 and 7.11. The two minimum values of V_x ($|V_x|_{min,1,j}$ and $|V_x|_{min,2,j}$) and the two maximum ones ($|V_x|_{max,1,j}$ and $|V_x|_{max,2,j}$) are summarized in Table 7.5.

In the road bike competitions, a good road bike should be able to help the rider keeping the forward velocity as high as possible. This is also the requirement for the mountain bike competitions. However, when the mountain bikes move in the off-road conditions full of obstacles and different terrains, those external factors will result in a decreases of their forward velocities V_x, especially during meeting hollows (or bumps). Therefore, one another performance index for a bike is its variation of V_x, and the

smaller the latter, the better the stability of the bike.

To observe the variation of V_x for each rider-bike system moving on the uneven road surface, the two "minimum values" of V_x ($|V_x|_{min,1,j}$ and $|V_x|_{min,2,j}$) are subtracted from the two "maximum values" of V_x ($|V_x|_{max,1,j}$ and $|V_x|_{max,2,j}$), respectively, and denoted by $\Delta|V_x|_1$ and $\Delta|V_x|_2$, respectively, as shown in Table 7.5, in which the variation of V_x (denoted by ΔV_x) shown in the final row is obtained from $\Delta|V_x|_1$ plus $\Delta|V_x|_2$, i.e., $\Delta V_x = \Delta|V_x|_1 + \Delta|V_x|_2$.

With the "Variation of V_x" as the performance index, one can find that the variation of V_x for the hard tail bike is maximum, while those for all the FS bikes are smaller. Among the four FS bikes, the variation of V_x of single pivot bike is highest, and that of faux bar bike is slightly higher than that of VPP bike. The horst link bike has the smallest variation of V_x.

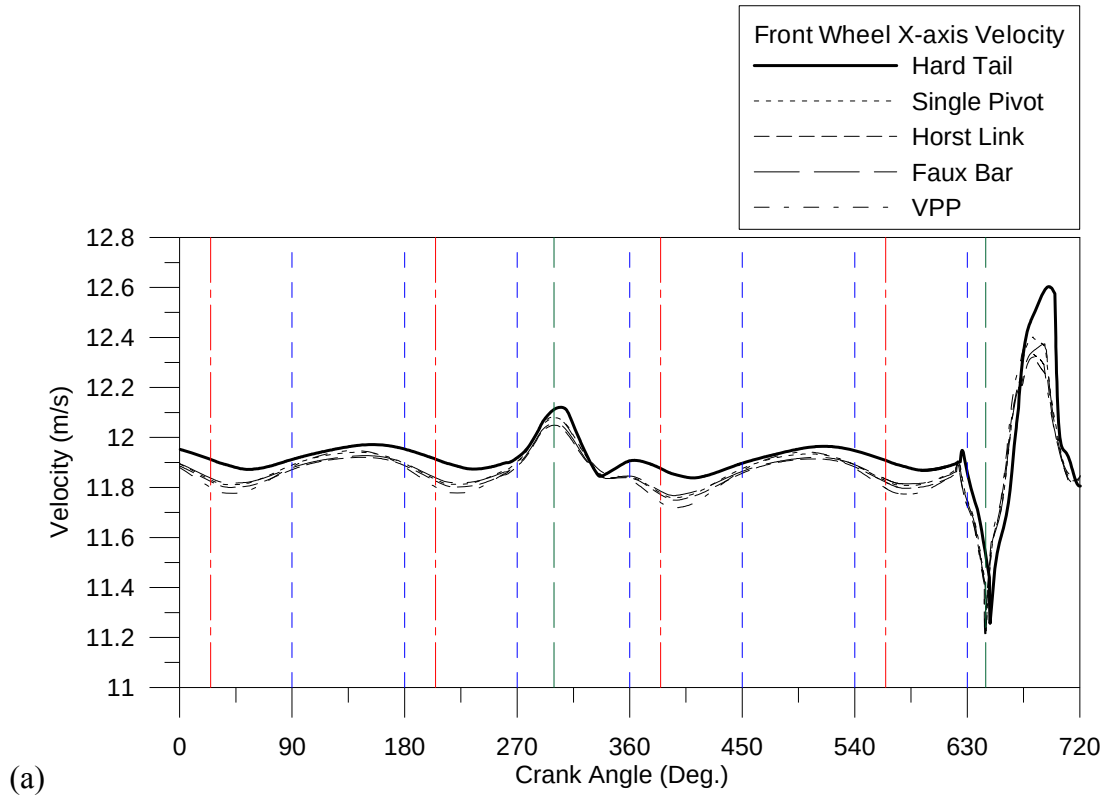

(a)

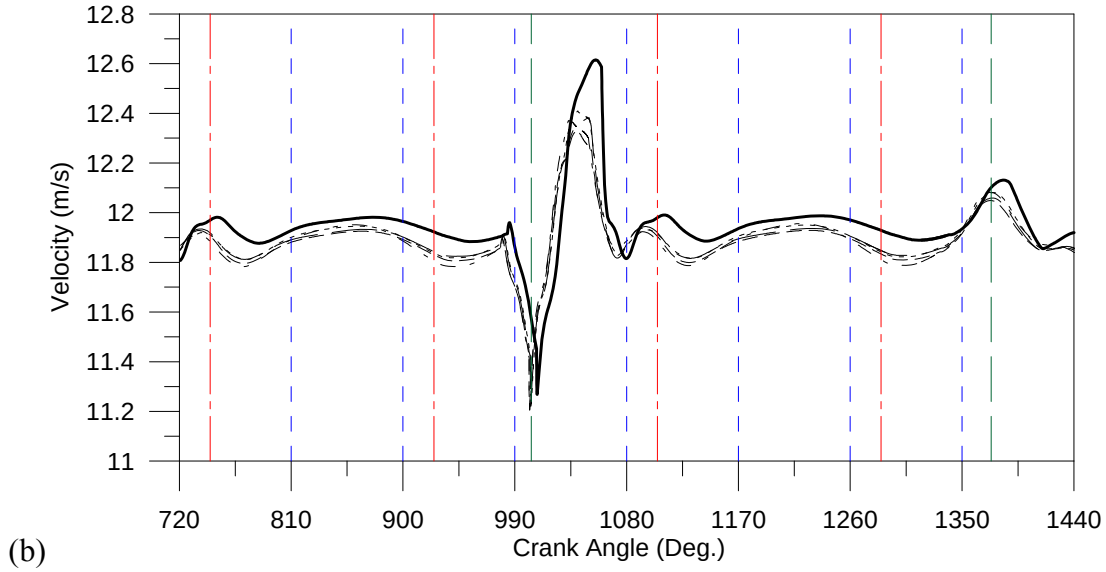

(b)

Figure 7.10 The relationship between forward velocities (V_x) and crank angles for front wheel due to each rider-bike system passing (a) over a hump and (b) through a hollow

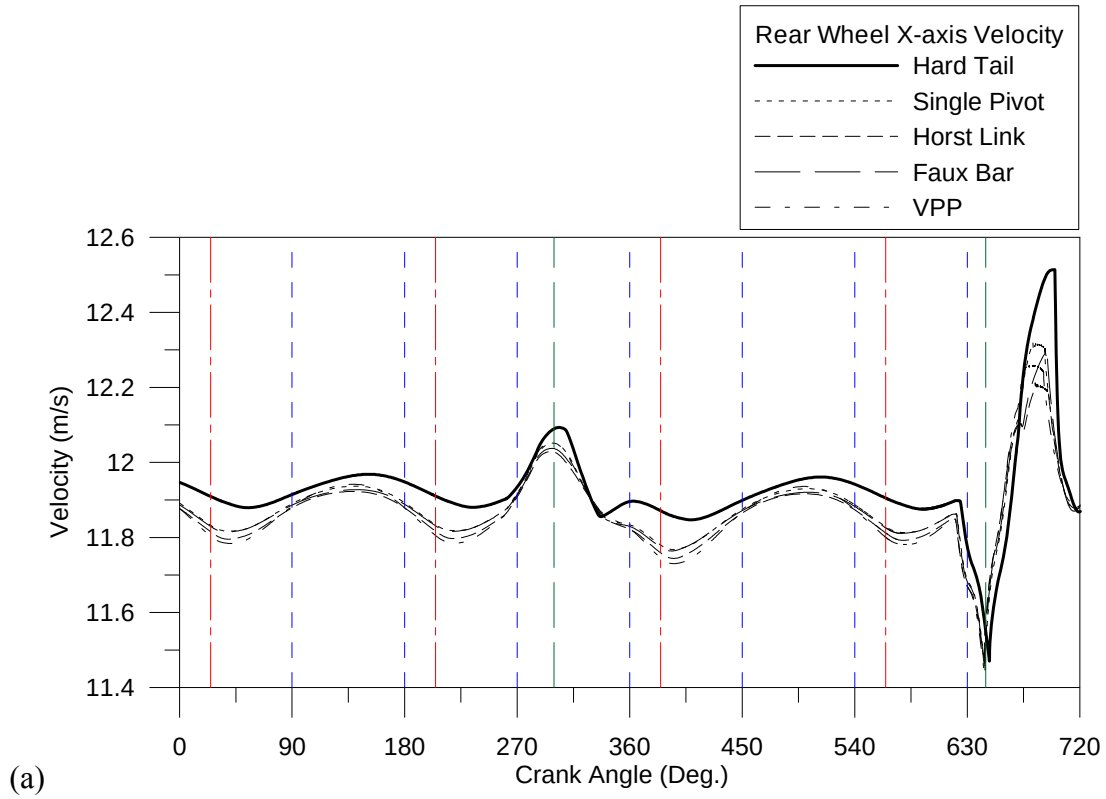

(a)

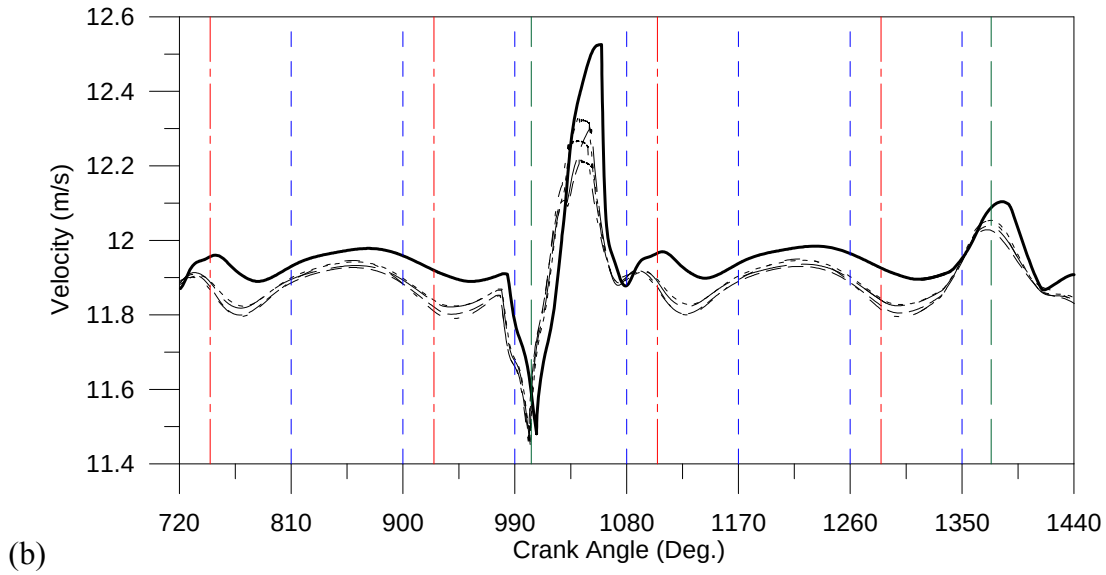

(b)

Figure 7.11 The relationship between forward velocities (V_x) and crank angles for rear wheel due to each rider-bike system passing (a) over a hump and (b) through a hollow

Table 7.5 Forward velocities (V_x) of front and rear wheels at the moments corresponding to the four "peak" crank angles ($\overline{\theta}_1$ to $\overline{\theta}_4$) due to each rider-bike system passing the two bumps (over a hump and through a hollow)

Conditions	Velocities (m/s)	Hard Tail (j=1)		Single Pivot (j=2)		Horst Link (j=3)		Faux Bar (j=4)		VPP (j=5)	
		Front	Rear	Front	Rear	Front	Rear	Front	Rear	Front	Rear
Average speed on flat road (no bumps) and in steady condition	$\left\|\overline{V}_x\right\|_{steady,j}$	11.925		11.8795		11.8625		11.874		11.866	
Meet hump	$\|V_x\|_{meet\ hump,j}$	12.121	12.093	12.078	12.051	12.049	12.029	12.058	12.037	12.083	12.053
Leave hump	$\|V_x\|_{min,1,j}$	11.258	11.470	11.226	11.447	11.216	11.459	11.215	11.446	11.202	11.438
	$\|V_x\|_{max,1,j}$	12.603	12.514	12.402	12.319	12.323	12.211	12.374	12.303	12.363	12.258
$\Delta\|V_x\|_1=\|V_x\|_{max,1,,j}$ -$\|\ V_x\ \|_{min,1,j}$		1.345	1.044	1.176	0.872	1.107	0.752	1.159	0.857	1.161	0.820
Meet hollow	$\|V_x\|_{min,2,j}$	11.267	11.480	11.230	11.452	11.219	11.462	11.220	11.450	11.205	11.441
	$\|V_x\|_{max,2,j}$	12.614	12.525	12.409	12.327	12.330	12.218	12.382	12.311	12.371	12.266
$\Delta\|V_x\|_2=\|V_x\|_{max,2,,j}$ -$\|\ V_x\ \|_{min,2,j}$		1.347	1.045	1.179	0.875	1.111	0.756	1.162	0.861	1.166	0.825
Leave hollow	$\|V_x\|_{leave\ hollow,j}$	12.131	12.103	12.080	12.053	12.048	12.028	12.059	12.038	12.081	12.051
$\Delta V_x=\Delta\|V_x\|_1+\Delta\|V_x\|_2$		2.692	2.089	2.355	1.747	2.218	1.508	2.321	1.718	2.327	1.645

7.6 Contact Forces of Front and Rear Wheels for Each of the Rider-Bike Systems of the Five Bikes Passing over a Hump and through a Hollow

The relationship between contact forces of front and rear wheels and crank angles is shown in Figures 7.12(a) and 7.12(b), respectively. Figure 7.12(a) shows that the five bikes have the similar responses, and the maximum contact force occurs when the bike leaves the right end of the hump and touches the ground at $\overline{\theta}_2$=644.792°, or meets the left end of the hollow and touches the bottom of the hollow at $\overline{\theta}_3$=1003.158°. However, it is very difficult to observe the contact force of rear wheel shown in Figure 7.12(b). Due to the rear suspension systems, the three FS bikes, including single pivot bike, horst link bike, and VPP bikes have dense excitations when each of their rear wheels hits the right side of the hollow and returns to the ground, but this is not true for the faux bar bike and hard tail bike. The maximum contact forces of front and rear wheels appearing in Figures 7.12(a) and 7.12(b) are summarized in Table 7.6, it is seen that the contact forces of the four FS bikes are bigger that those of hard tail bike.

Since the single pivot bike, horst link bike, and VPP bike can induce dense excitations (of contact forces) on the rear wheels when each of them hits the left side of the hollow and returns to the ground, this will activate rear shock absorber to absorb the vibration and lead to the bouncing of rear wheel. The dense excitation is most predominant on VPP bike, as shown in Figure 7.13. At the crank angle $\overline{\theta} = 1032^o$ (corresponding to the moment t =12.632sec), the VPP bike has met the left end of the hollow and touched the bottom of the hollow, which causes the biggest contact force 8081.23N as shown in Table 7.6. The shock absorber is activated and the contact force of the rear wheel becomes zero during the interval from t=12.632sec to t=12.635sec, and then returns to the ground again, which caused the second maximum contact force. The last responses will be attenuated when the rider-bike system restores to the steady condition gradually and ended at about t=12.660 sec.

From Figure 7.12(b) one sees that the response curves in the narrow bands of crank angles, $\overline{\theta} = 675^0 \sim 697^o$ and $\overline{\theta} = 1035^0 \sim 1057^o$, are overlapped. This is due to the high-frequency oscillations (or vibrations) of the rear suspension system and the effect

of dampers on the high-frequency responses is significant so that the oscillations (or vibrations) induced by the rider-bike system passing through the bumps are damped out rapidly. On the contrary, for the phenomenon of dense excitation of contact forces on the rear wheel of VPP bike shown in Figure 7.13, since the effect of damper is small on the lower-frequency oscillations, the dynamic responses due to the rider-bike system passing through the bumps cannot be damped out in a short time. Therefore, the oscillations spread throughout the wide band of the crank angles after passing through the bumps. Furthermore, the spacing between any two adjacent responses (or signals) becomes smaller gradually because the old responses are overlapped with the new ones when the rider-bike system passes through more bumps. It is noted that the structure connected with the front fork is much simpler than that of the bike frame attached to the rear suspension system, and this should be the reason why the response curves appearing in Figure 7.12(a) are much simpler that those shown in Figure 7.12(b).

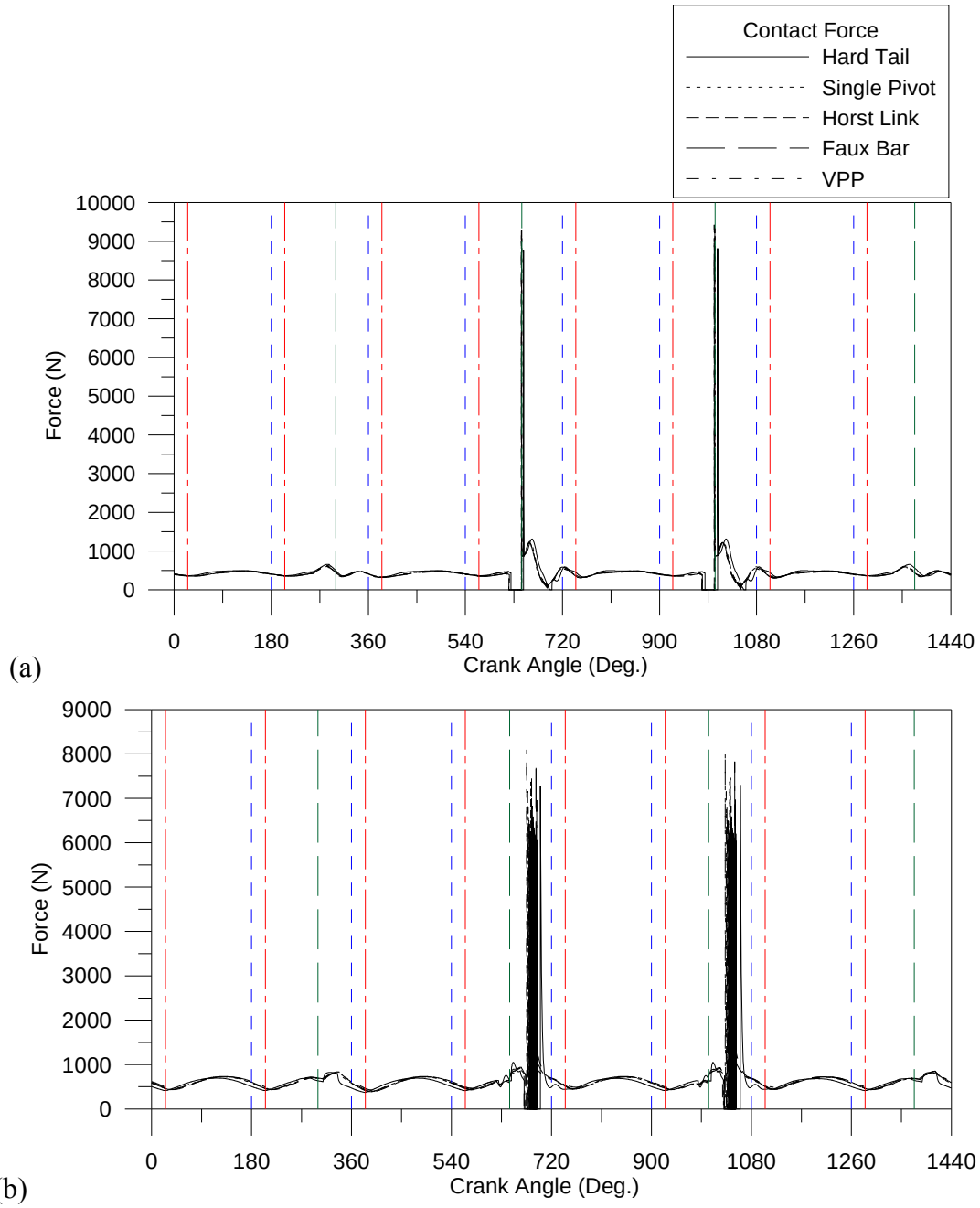

Figure 7.12 Contact forces of (a) front wheels and (b) rear wheels due to each rider-bike system passing both bumps (over a hump and through a hollow)

Table 7.6 Maximum peak contact forces of front and rear wheels of the five bikes due to each rider-bike system passing over a hump and through a hollow

Conditions	Maximum peak contact forces (N)				
	Hard Tail	Single Pivot	Horst Link	Faux Bar	VPP
Front Wheel					
Leave hump	8776.04	9162.66	9012.19	9287.59	9377.30
Meet hollow	8816.39	9212.81	9079.30	9338.97	9423.49
Rear Wheel					
Leave hump	7276.57	7373.40	7465.14	7822.68	8099.64
Meet hollow	7305.11	7377.37	7463.82	7826.62	8081.23

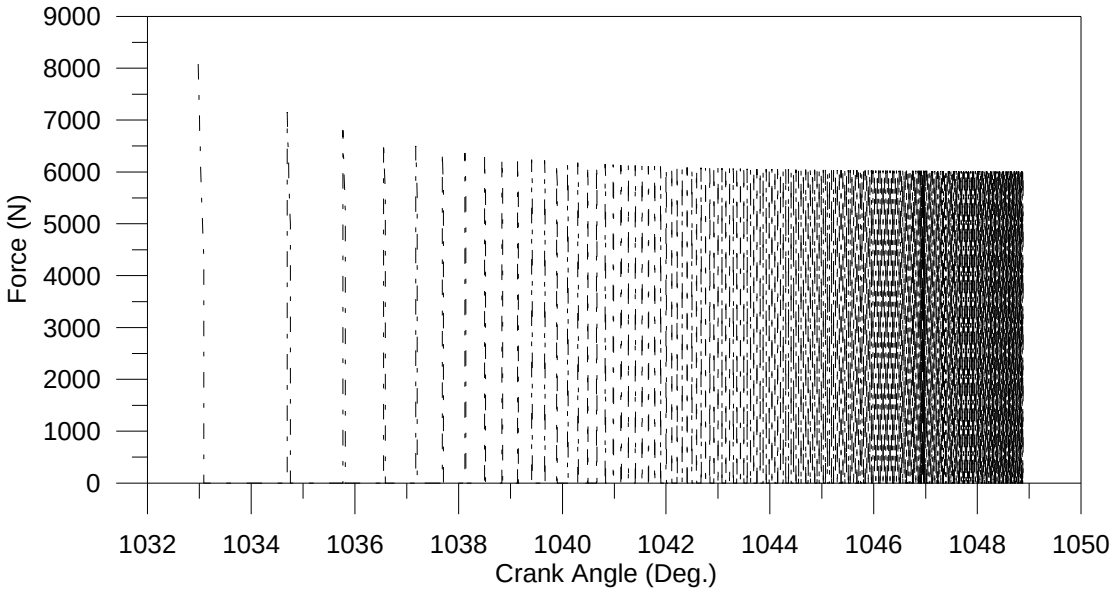

Figure 7.13 Bouncing of rear wheel of the VPP bike due to its rider-bike system hitting the left side of the hollow

7.7 Fork Compressions for each of the Rider-Bike Systems of the Five Bikes Passing over a Hump and through a Hollow

The relationship between fork compressions and crank angles due to each rider-bike system leaving the right end of the hump (at $\overline{\theta}_2$) and meeting the left end of the hollow (at $\overline{\theta}_3$) is shown in Figure 7.14. The forks of all five bikes have the similar responses during leaving the right end of the hump and meeting the left end of the hollow, and the two minimum and maximum fork compressions at the two moments corresponding to the "peak" crank angles $\overline{\theta}_2$ and $\overline{\theta}_3$ are summarized in Table 7.7. When each bike leaves the right end of the hump, the fork is loosen, and the fork will extend slightly due to gravity, so the minimum fork compressions in Table 7.7 are positive, but all fork compressions with positive values are very small (less than 0.1mm) and can be neglected. Next, the fork has the maximum compression when the front wheel leaves the right end of the hump and touches the ground. The situation is the same as that each bike meets the left end of the hollow and touches the bottom of the hollow.

The minimum and maximum fork compressions for each rider-bike system leaving the right end of the hump (at $\overline{\theta}_2$) and meeting the left end of the hollow (at $\overline{\theta}_3$) are summarized in Table 7.7, it is similar to Table 7.8 that the fork compression of hard tail bike is greater than those of the four FS bikes. Among the four FS bikes, the fork compression of single pivot bike is biggest, while that of horst link bike and that of faux bar bike are similar. The fork compression of VPP bike is smallest, which is slightly lower than that of horst link bike.

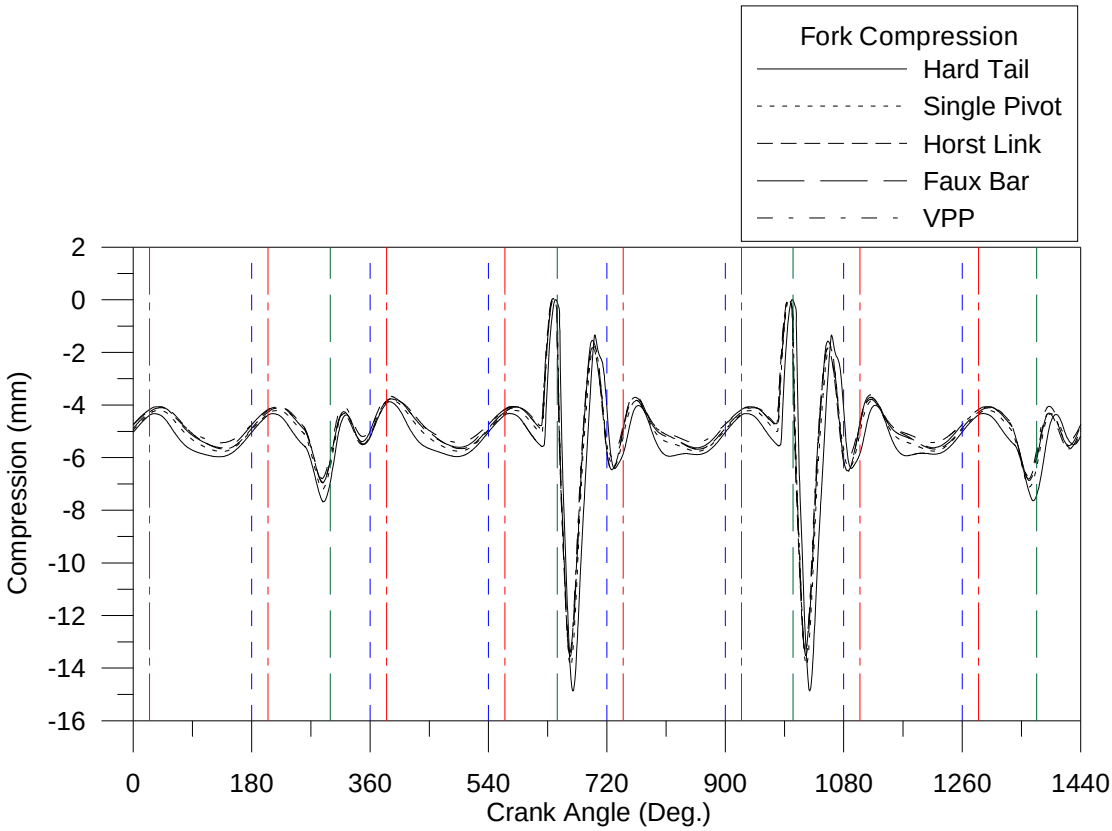

Figure 7.14 The relationship between the fork compressions and crank angles due to each rider-bike system passing over a hump and through a hollow

Table 7.7 Minimum and maximum fork compressions for each rider-bike system leaving a hump (at $\overline{\theta}_2$) and meeting a hollow (at $\overline{\theta}_3$)

Conditions		Fork Compressions (mm)				
		Hard Tail	Single Pivot	Horst Link	Faux Bar	VPP
Leave hump	Minimum	+0.002	+0.011	+0.047	+0.017	+0.023
	*Maximum	-14.866	-13.928	-13.408	-13.551	-13.386
Meet hollow	Minimum	+0.001	+0.014	+0.050	+0.020	+0.026
	*Maximum	-14.856	-13.902	-13.358	-13.521	-13.357

* Based on the "absolute" values.

7.8 Shock Compressions for each Rider-Bike System Passing over a Hump and through a Hollow

The relationship between shock compressions and crank angles is shown in Figure 7.15. From the figure, one can find the response of rear shock absorber is not too much when each rider-bike system hits the left side of the hump or the right side of the hollow. It is similar to front fork, the minimum and maximum shock compressions happen at the moments the rear wheel hitting the left side of the hump and the right side of the hollow, respectively. The two pairs of minimum and maximum compressions of four FS bikes are shown in Table 7.8.

Referring to the discussion of shock compression shown in Section 6.3.4, each average shock compression is obtained by the summation of the corresponding minimum and maximum compressions dividing by two in Table 7.8. It is seen that the trend of the two sets of average shock compressions are the same, and the rank from highest to lowest is: VPP, horst link, single pivot, and faux bar. Although the average shock compression for VPP bike is highest, its variation is lowest, which means that the VPP bike can effectively reduce the vibration when it passes through the obstacles and will be more comfortable for its rider. It is noted that, for the VPP bike, its variation of shock compression on off-road terrains is opposite to that on flat road without bumps (with the highest variation of shock compression).

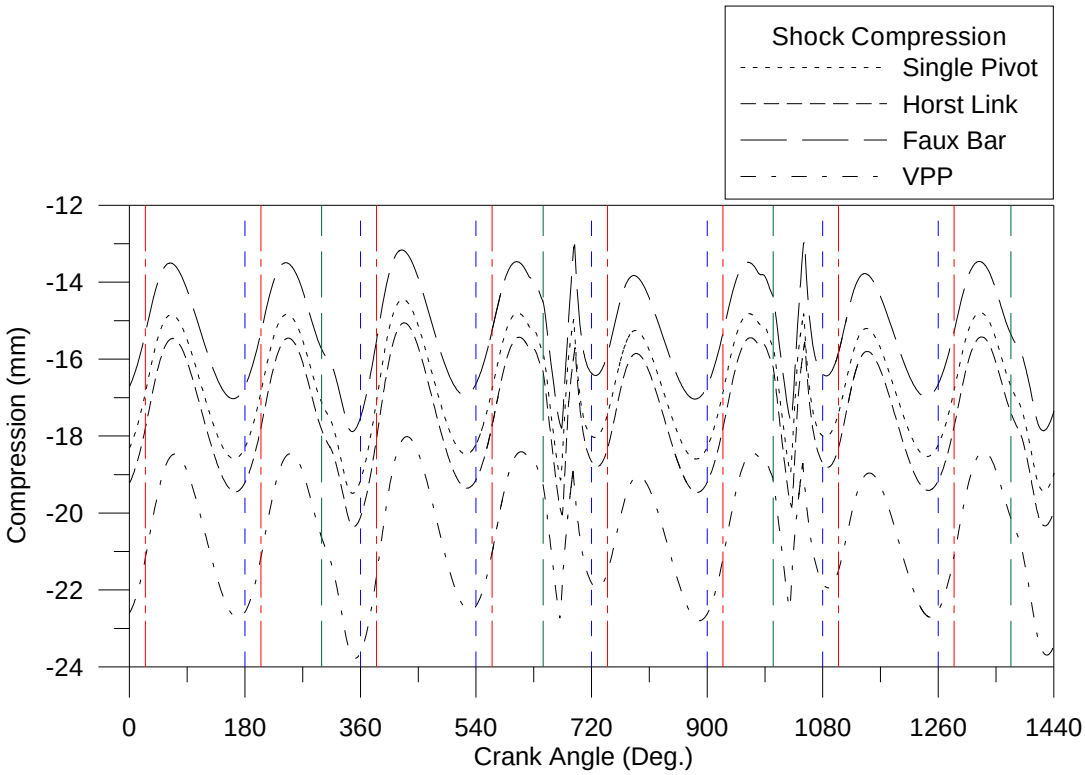

Figure 7.15 The relationship between the shock compressions and crank angles due to each rider-bike system passing over a hump and through a hollow

Table 7.8 Minimum and maximum shock compressions due to each rider-bike system leaving a hump and meeting a hollow

Conditions		Shock Compressions (mm)				
		Hard Tail	Single Pivot	Horst Link	Faux Bar	VPP
Leave hump	*Minimum	—	14.96	15.69	13.02	18.91
	*Maximum		19.13	20.04	17.79	22.72
	Average		17.045	17.865	15.405	20.815
	Variation		±2.085	±2.175	±2.385	±1.905
Meet hollow	Minimum	—	14.82	15.54	12.91	18.70
	Maximum		18.96	19.84	17.63	22.48
	Average		16.89	17.69	15.27	20.59
	Variation		±2.07	±2.15	±2.36	±1.89

*Based on the absolute values.

7.9 Variations of Sprocket Distances and Chain Tension Forces due to each Rider-Bike System Passing over a Hump and through a Hollow

The relationship between variations of sprocket distances and crank angles, and that between chain tension forces and crank angles are shown in Figures 7.16(a) and 7.16(b), respectively. Although the hard tail bike has no rear suspension, its sprocket distance increases 0.42mm when its front wheel hits the left side of the hump or the right side of the hollow, and decreases 1.72mm when its front wheel leaves the right end of the hump or meets the left end of the hollow. The trends of the horst link bike and faux bar bike are similar to that of the hard tail bike. Since the variations of sprocket distances for both single pivot bike and VPP bike are bigger, so are their chain tension forces. It is noted that the chain tension forces of hard tail bike and horst link bike are quite small (less than 10N). From Figures 7.16(a) and 7.16(b), one can see that the variations of sprocket distances on faux bar bike are negative, so there exist no chain tension forces.

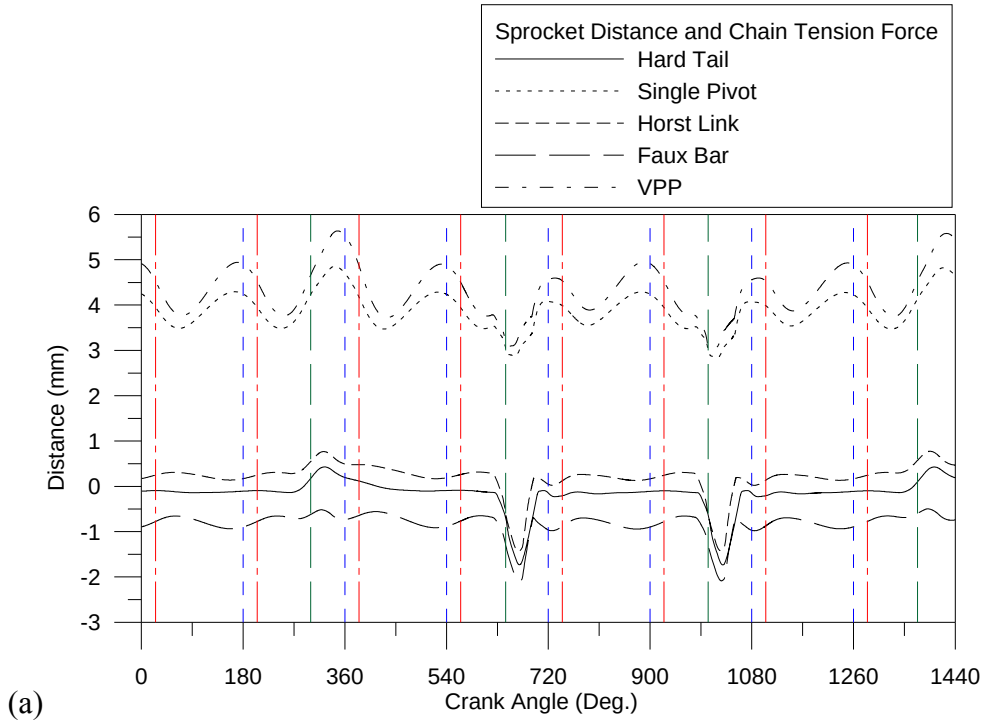

(a)

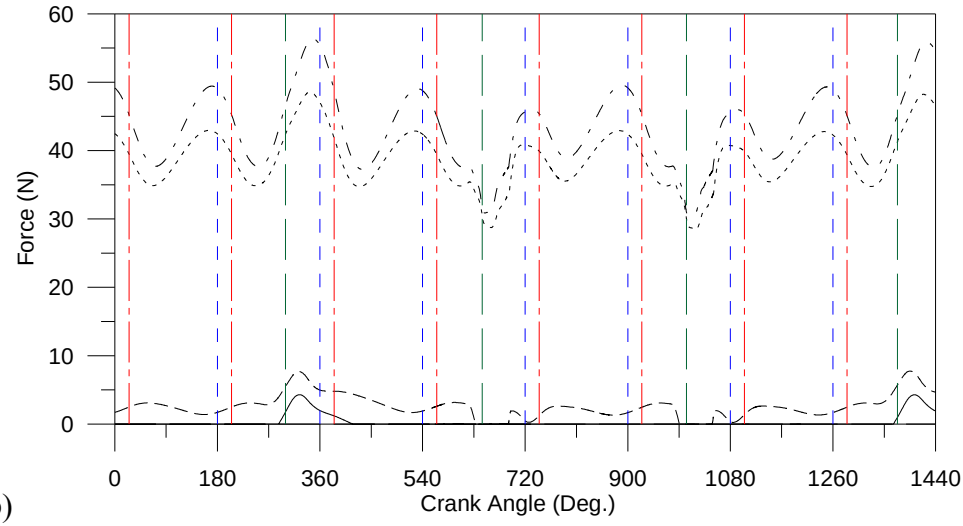

(b)

Figure 7.16 The relationship between (a) sprocket distances and (b) chain tension forces and the crank angles due to each rider-bike system passing over a hump and through a hollow

7.10 Vertical Accelerations at Handlebar and at Seat due to each Rider-Bike System Passing over a Hump and through a Hollow

The relationship between vertical accelerations at handlebar and at seat and the crank angles are shown in Figures 7.17(a) and 7.17(b), respectively. It is seen that the 1st maximum acceleration at handlebar happens at the moment of the front wheel leaving the right end of the hump (1st bump) and the 2nd one occurs at that meeting the left end of the hollow (2nd bump), while the 1st maximum acceleration at seat happens at the moment of the rear wheel leaving the right end of the hump (1st bump) and the 2nd one occurs at that hitting the right side of the hollow (2nd bump). Based on Figures 7.17(a) and 7.17(b), the maximum accelerations at handlebar and seat are summarized in Table 7.9, in which the negative minimum accelerations represent their directions to be downward. It is seen that, the average vertical accelerations at handle bar for the hard tail bike is smallest, while those of the four FS bikes are much bigger. Furthermore, the maximum vertical acceleration at seat of FS bikes are much smaller than that of hard tail bike, because the rear suspension systems of the FS bikes can significantly reduce the vibrations when each rider-bike system passes through the obstacles. Among the four FS bikes, the "instantaneous" vertical acceleration at seat of VPP bike is smallest, which indicates that its rear suspension system is efficient for reducing the vibrations. The average vertical acceleration at seat is one of the important factors to assess the degree of comfort of the riders. Among the four FS bikes, the "average" acceleration at seat of the VPP bike is smallest and that of faux bar bike is biggest. Although the bobbing effect of the VPP bike is most serious, as shown in Section 6.3.6, it is an attractive bike from the point of view of comfort.

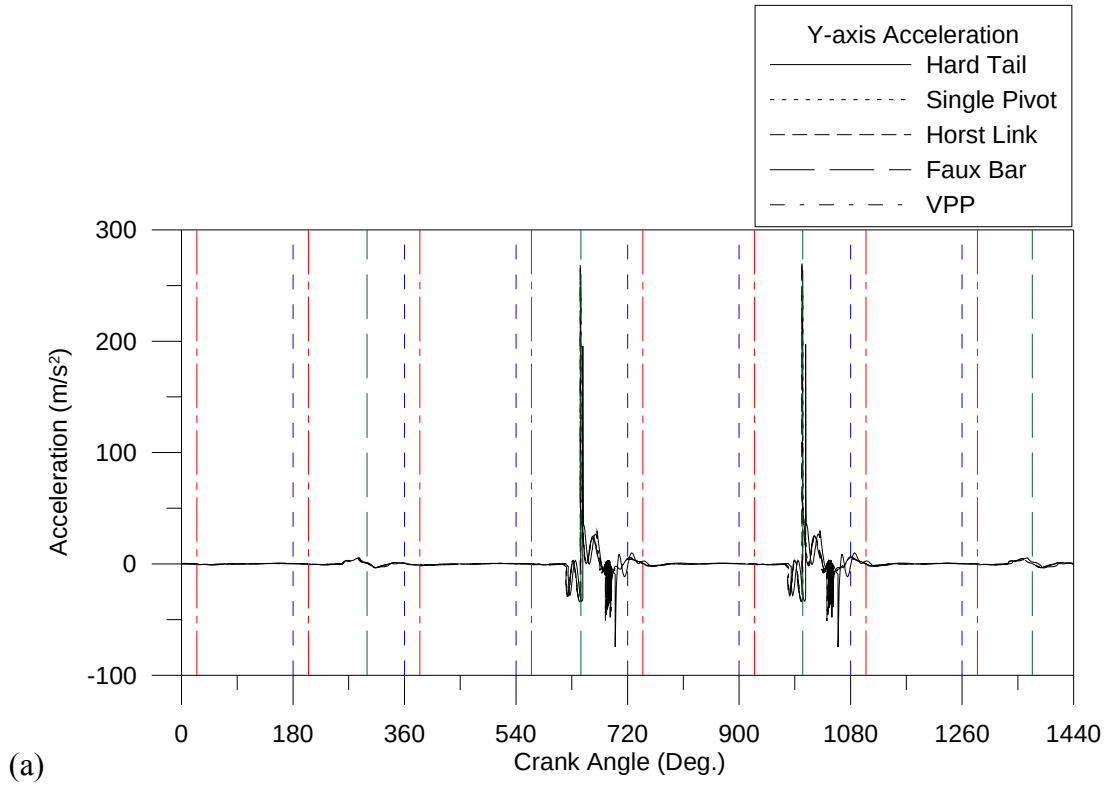

(a)

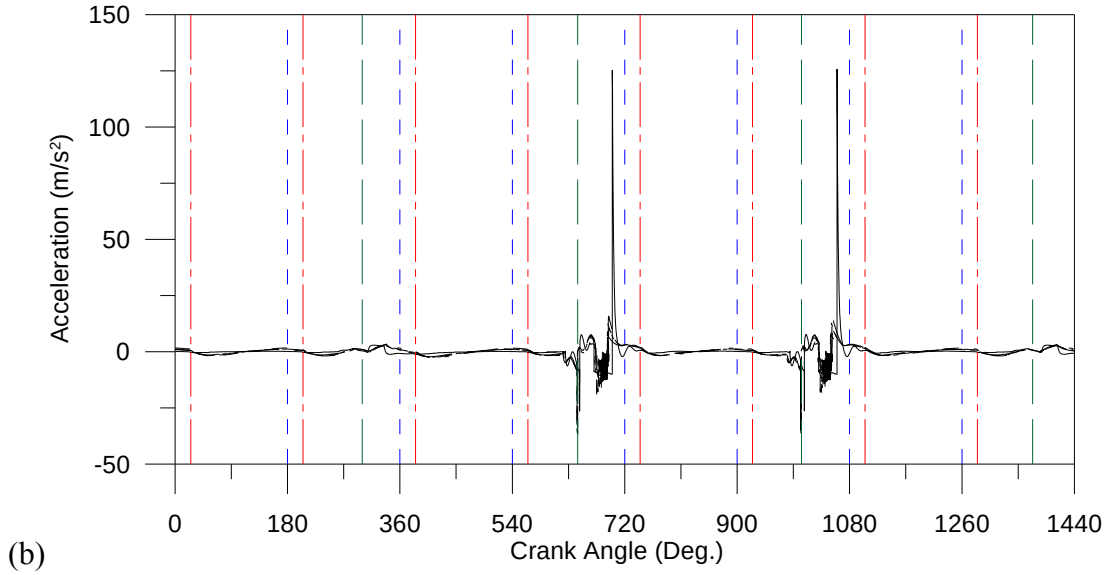

(b)

Figure 7.17 The relationship between the vertical accelerations (a) at handlebar and (b) at seat and the crank angles due to each rider-bike system passing over a hump and through a hollow

Table 7.9 Minimum and maximum vertical (*y*-) accelerations at handlebar and at seat due to each rider-bike system passing over a hump and through a hollow

Conditions		Accelerations (m/s^2)									
		Hard Tail		Single Pivot		Horst Link		Faux Bar		VPP	
		Handlebar	Seat	Handlebar	Seat	Handlebar	Seat	Handlebar	Seat	Handlebar	Seat
Leave hump	Minimum	-74.46	-20.65	-33.99	-36.88	-51.35	-32.99	-47.97	-36.30	-33.41	-37.67
	Maximum	195.71	125.28	238.40	12.46	269.34	10.47	260.42	15.94	266.87	7.57
	Average	60.625	52.315	102.205	-12.21	108.995	-11.26	106.225	-10.18	116.73	-17.96
	Variation	±135.085	±72.965	±136.195	±24.67	±160.345	±21.73	±154.195	±26.12	±150.14	±19.71
Meet/leave hollow	Minimum	-74.72	-26.49	-33.78	-36.90	-51.32	-33.05	-48.01	-36.30	-33.21	-37.63
	Maximum	197.14	125.78	240.89	12.50	272.89	10.44	263.27	15.90	269.54	7.57
	Average	61.21	49.645	103.555	-12.2	110.785	-11.305	107.63	-10.2	118.165	-15.03
	Variation	±135.93	±76.135	±137.335	±24.7	±162.105	±21.745	±155.64	±26.1	±151.375	±22.6

7.11 Discussion and Conclusion

In this chapter, the dynamic analyses for each of the five rider-bike systems passing over a hump and through a hollow are conducted. Discussion and conclusion of the analyses are presented in the following.

7.11.1 Dynamic Analysis of Loaded Bike Moving on Flat Road Surface with Bumps

In the dynamic analyses of the five rider-bike systems moving on the flat roads with bumps in the steady conditions, the dynamic responses of the rider-bike system of the hard tail bike passing through a hump and a hollow, respectively, are studied first. From the effective pedalling forces shown in Figures 7.2 and 7.3, one can see that the two maximum pedalling forces are to happen at the moment of leaving the right end of the hump and that of meeting the left end of the hollow, because the instantaneous vertical accelerations of the bike at the last two moments are downward and identical to the downward gravitational acceleration g. On the contrary, the two minimum pedalling forces occur at the moment of hitting the left side of the hump and that of hitting the right side of the hollow, because the instantaneous vertical accelerations of the bike at the latter two moments are upward and opposite to the downward gravitational acceleration g. From the two pairs of maximum and minimum effective pedalling forces summarized in Table 7.1, one can see that the maximum and minimum effective pedalling forces of passing the hump are not equal to those of passing the hollow, because the phase angle of hitting the bump θ_{meet} is different from that of leaving the bump θ_{leave}. By arranging the time instant for the rider-bike system of hard tail bike hitting the left side of the hump to be very close to that leaving the right end of the hollow so that $\theta_{meet} \approx \theta_{leave}$, the numerical results (see Figures 7.4 and 7.5 and Table 7.2) show that the difference between the maximum pedalling force of leaving the right end of the hump and that of meeting the left end of the hollow is only ΔF_{down}=0.52N with slight difference of phase angles $\Delta\theta_{down}$=2.33°. Similarly, the difference between the minimum pedalling force of hitting the left side of the hump and that of hitting the right side of the hollow is only ΔF_{up}=0.75N with slight

difference of phase angles $\Delta\theta_{up}$=1.56°. From above discussion, one can see that the instantaneous crank angle corresponding to the instant for the rider-bike system passing through a bump is an important factor significantly influencing the dynamic responses of the rider-bike system.

After testing the rider-bike system of a hard tail bike passing over a hump and through a hollow, respectively, the dynamic responses for each of the five rider-bike systems (the same as those mentioned in the Section 6.4.2) passing through the flat road surface with both a hump and a hollow in the steady conditions are analyzed, in which the two bumps for each rider-bike system are arranged in such locations that the "time differences" for reaching the steady conditions between the five rider-bike systems are as small as possible so that the associated phase angles are close to each other.

(a) For the effective pedalling forces, when each bike hits the left side of the hump at $\overline{\theta}_1$=299.5° or hits the right side of the hollow at $\overline{\theta}_4$=1373.436°, the corresponding pedalling forces decrease to some degree due to the upward vertical acceleration. On the contrary, when each bike leaves the right end of the hump at $\overline{\theta}_2$=644.792° or meets the left end of the hollow at $\overline{\theta}_3$=1003.158°, the corresponding pedalling forces are greater than normal ones due to the downward vertical acceleration. Among the five rider-bike systems, the differences between the minimum (reverse) peak pedalling forces or those between maximum ones are small, but one may assess the performance of each bike based on the difference between the maximum (or minimum) pedalling forces for the bike passing over bumps and the corresponding ones for the bike moving on the flat road surface (without bumps) in the steady condition (see $\Delta|F_p|_{meet\ hump,j}$, $\Delta|F_p|_{leave\ hump,j}$, $\Delta|F_p|_{meet\ hollow,j}$, and $\Delta|F_p|_{leave\ hollow,j}$ summarized in Table 7.3). It is found that the values of the four variations $\Delta|F_p|$ of the hard tail are biggest due to no rear suspension system [except that the value of $\Delta|F_p|_{meet\ hollow,j}$ of VPP bike (329.73N) is slightly bigger than that of hard tail bike (327.01N)]. For the four FS bikes, the values of $\Delta|F_p|_{X,j}$ at the four peak crank angles ($\overline{\theta}_1$ to $\overline{\theta}_4$) of VPP bike are biggest, while those of single pivot bike are second, and those of the two four-bar-linkage bikes are lowest.

(b) For the effective pedalling powers, based on the variations of $\Delta W_{meet\ hump,j}$,

$\Delta W_{leave\_hump,j}$, $\Delta W_{meet\ hollow,j}$ and $\Delta W_{leave\ hollow,j}$ summarized in Table 7.4, the ranks of the five bikes from lowest to highest are: horst link, faux bar, single pivot, VPP, hard tail (except that the value of $\Delta W_{meet\ hollow,j}$ for the VPP bike is slightly higher than that for the hard tail bike). Since the higher values of $\Delta|F_p|_{X,j}$ and $\Delta W_{X,j}$ indicate that the rider-bike system will be more unstable during passing through the bumps, the four FS bikes are better than the hard tail bike during riding on the off-road terrains. From Table 7.4, one sees that the two four-bar-linkage bikes are most stable and the horst link bike is slightly better than the faux bar bike.

(c) For the forward velocities V_x, the variations of V_x (see $\Delta|V_x|_1$, $\Delta|V_x|_2$, and ΔV_x in Table 7.5) are used to assess the performance of each bike. Since the lower the variations of $\Delta|V_x|_1$, $\Delta|V_x|_2$, and ΔV_x, the better the traction control of the rider-bike system during passing through the bumps, the ranks of the five bikes from highest to lowest are: hard tail, single pivot, VPP, faux bar, horst link. Therefore, the horst link bike is most stable for riding on the off-road terrains. From Table 7.5, one can see that the values of $\Delta|V_x|_1$ and $\Delta|V_x|_2$ of front wheel of faux bar bike are slightly smaller than those of VPP bike ($\approx$0.004m/s), and the values of $\Delta|V_x|_1$ and $\Delta|V_x|_2$ of rear wheel of faux bar bike are larger than those of VPP bike ($\approx$0.037m/s). Thus, based on the last two small differences, the performance of VPP bike is slightly better than that of faux bar bike.

(d) For the contact forces of front and rear wheels, the rank of maximum contact forces of "front" wheels from highest to lowest is: VPP, faux bar, single pivot, horst link, hard tail, and that of "rear" wheels from highest to lowest is similar (due to the effects of the rear suspension systems), only the ranks of horst link and single pivot are exchanged. Based on the last two ranks, one can see that the contact force of front wheel of hard tail bike is smallest, which is different from that of riding on the flat road surface. In addition, due to the structure of front fork is simpler than that of rear suspension systems, the responses of front wheels are simpler than those of rear wheels, as shown in Figures 7.12(a) and 7.12(b). Since the configurations of the rear suspension systems of single pivot bike, horst link bike, and VPP bike can lead to the dense excitation of contact forces on the rear wheel when each bike passes through the bumps, and among the three bikes, the dense excitation is most predominant on

VPP bike, as shown in Figure 7.13.

It is noted that the rear wheels of full suspension bikes can follow the rough terrains (keep in contact with the ground) better so that the traction control will be increased and the loss of velocity will be decreased as shown in [7,8,10,12,19,20,22,30,34].

(e) For the fork compressions, the two ranks of maximum fork compressions for each of the five rider-bike systems leaving the right end of the hump and meeting the left end of the hollow from highest to lowest are: hard tail, single pivot, faux bar, horst link, VPP. The differences between maximum fork compressions of the five bikes are quite small (with the biggest one to be 1.49 mm). The numerical results show that the front fork of each bike can also absorb the vibration during passing through the bumps.

(f) For the shock compressions, the two ranks of average shock compressions for each of the four FS rider-bike systems leaving the right end of the hump and meeting the left end of the hollow from highest to lowest are: VPP, horst link, single pivot, faux bar. Based on the variations of average shock compressions, the rank from highest to lowest is: faux bar, horst link, single pivot, VPP. From the last ranks, one can see that the average shock compression of VPP bike is highest and its variation is smallest, which means that the rear suspension system of VPP bike can absorb the vibration when it passes through bumps and will be more comfortable for its rider. In addition, the variation of average shock compressions for the VPP bike passing through bumps is opposite to that (riding) on flat road surface (with the highest variation of average shock compression).

(g) For the variations of sprocket distances and chain tension forces, the variations of sprocket distances of hard tail bike, horst link bike, and faux bar bike are similar and very small with the biggest one being about -2.5mm (for faux bar bike), while those of single pivot bike and VPP bike are much bigger. Therefore, the chain tension forces of single pivot bike and VPP bikes are much bigger than those of hard tail bike and horst link bike. It is found that the chain tension forces of faux bar bike are equal to zero due to the negative variations of sprocket distances.

(h) For the vertical accelerations at handlebar and seat, the average vertical

acceleration at handlebar of hard tail bike is smallest, while that of the four FS bikes are much bigger. However, the average vertical acceleration at seat of the four FS bikes are much smaller than that of hard tail bike. This is because the rear suspension systems can absorb the vibration when the FS bikes pass through bumps. Among the four FS bikes, the average acceleration at seat of VPP bike is smallest, and the variation is only slightly bigger than that of horst link bike. Therefore, although the rear suspension system of VPP bike can lead to the most serious bobbing effect, it has the performance of reducing vibrations during passing through bumps and can provide the better comfortable condition for its rider.

Based on the foregoing discussions, one can see that the four FS bikes can provide a more comfortable riding experience than a hard tail bike when they are ridden on the off-road terrains. For the purpose of moving fast without significantly decreasing velocity, the selection of the four-bar-linkage bikes (either horst link or faux bar) may be one of the better choices. However, for the purpose of comfort in the riding condition, the VPP bike may be beneficial in this aspect. The performance of single pivot bike may be in the middle rank among the four FS bikes.

7.11.2 Conclusion

When each of the five rider-bike systems moves on the flat road surface with bumps, stable riding conditions of the four FS bikes are better than that of the hard tail bike. The two four-bar-linkage bikes can move at higher average velocities with smaller variations. The average vertical accelerations at seats of the four FS bikes are much smaller than that of hard tail, which confirms that the four FS bikes can provide more comfortable condition for the rider riding on the off-road terrains. Among the four FS bikes, the VPP bike can provide the most comfortable riding condition for its rider and the performance of single pivot bike is in the middle rank.

Chapter 8 Conclusion and Future Work

After the extensive studies on static and dynamic characteristics of five types of mountain bikes and their riders in the foregoing chapters, this chapter will draw some pertinent conclusions and give some viewpoints to the future works.

8.1 Conclusions

From the foregoing analyses and discussions one obtains the following conclusions:

1. In general, the appropriate match between a rider and his bike is an important factor affecting the pedalling efficiency of the bike rider. However, one cannot find any information concerning evaluation of appropriate match between a rider and his bike in the existing literature, thus, the technique for evaluating the pedalling efficiency of a bike rider presented in Chapter 4 should be novel and significant.
2. In the existing reports, the pedalling stroke is assumed to be from top dead centre (TDC) to bottom dead centre (BDC) of the crank and the pedalling force is assumed to be sinusoidal. However, if the angle between the crank and the rider's lower leg is denoted by α, then, for each half pedalling cycle, its "beginning" is located at the instantaneous position with α=180° and its "end" is located at that with α=0° as one may see from Chapter 4. In other words, if the crank angle θ between TDC of the crank and the last "beginning" of each half pedalling cycle is denoted by $\theta=\theta_{1,U}$, then the "end" of each half pedalling cycle is given by $\theta \approx 180° + \theta_{1,U}$. Therefore, the formulations of Chapters 5 and 6 in this thesis based on the pedalling stroke with crank angles to be from $\theta_{1,U}$ to $180° + \theta_{1,U}$ and pedalling force to be "F_y=constant" should be closer to the realistic conditions and can produce the more accurate results.
3. The dynamic behaviour for a rider-bike system passing over the bumps are complicated. It has been found that, for a rider-bike system, the "phase angle" between the beginning (or end) of each pedalling stroke and the position

corresponding to the instant of time for it to meet (or leave) a bump is one of the important factors affecting its dynamic responses. Therefore, one must carefully arrange the position of each bump for each rider-bike system so that the corresponding "phase angles" between different rider-bike systems may be as small as possible, then one can easily compare the dynamic behaviours between the rider-bike systems passing through the bumps.

4. Since the oscillations (or vibrations) of the front or the rear suspension system are high-frequency and the effect of dampers on the high-frequency responses is significant, the oscillations (or vibrations) induced by each rider-bike system passing through the bumps are damped out rapidly as one may see from Figure 6.29. On the contrary, for the low-frequency excitations (of contact forces) on the rear wheel of a full suspension bike (such as that shown in Figure 6.30), since the effect of damper on the lower-frequency responses is low, the bouncing responses due to the rider-bike system passing through the bumps cannot be damped out in a short time. Therefore, the oscillations spread throughout the wide band of the crank angles after passing through the first bump. Furthermore, the spacing between any two adjacent responses (or signals) becomes smaller gradually because the old responses are overlapped with the new ones when the rider-bike system passes through more bumps.

5. In this thesis, the numerical models of all rider-bike systems are developed in SimMechanics and Matlab, in which, the full suspension bikes are drawn with Linkage and AutoCAD so as to obtain the precise dimension of bike frames and the dimension of the rider model is measured and obtained from BikeCAD.

6. For either a road bike or a mountain bike, its mass is much smaller than the mass of its rider. Thus, for practical applications, either numerical simulations or field experiments should be conducted by using the rider-bike model with the total mass of the rider considered. In addition, the influence due to different mass of different rider should also be taken into account.

7. Comparing with its responses on the flat roads, a full-suspension bike (FS bike) has the smaller the variations of pedalling powers ΔW and moving velocities $\Delta|V_x|$,

bigger contact forces of both front and rear wheels, and smaller vertical accelerations at seat on the rough terrains, thus, it can provide more stable and comfortable riding conditions than the hard tail bike (HT bike) when it is ridden on the off-road terrains. In other words, the advantages of the FS bike are greater than those of the HT bike on the rough roads.

8. Comparing with a FS bike on the flat roads, the HT bike has the higher pedalling efficiency and negligible bobbing effect, thus, the hard tail bike may be the good choice for the rider riding on the flat terrains.

9. The rider model, front wheel model, rear wheel model, front fork model, pedalling controller, transmission system, and chain tension model of the rider-bike system developed in this thesis can be easily modified to simulate other bike models for investigating the characteristics of the new bikes.

10. Comparing with the HT bike, the major drawback of the FS bike is the higher bobbing motion and the lower pedalling efficiency due to its rear suspension system. Therefore, a better FS bike should have a rear suspension system with a versatile mechanism so that one can adjust the effect of its rear suspension system to satisfy various requirements. Since, for some riders, they require a bike with various bobbing motions and pedalling efficiencies for some special purposes (such as health or training), the models of the rider-bike systems developed and the approaches presented in this thesis should be significant to provide the relevant information for designing a versatile FS bike.

11. In engineering, besides the “quantitative” analysis, one also requires the information regarding the results of the “qualitative” analysis. Thus, the reasonable results presented in this thesis will be also useful from the viewpoint of “qualitative” analysis.

8.2 Future Works

Referring to the mathematical models of the five rider-bike systems developed in this thesis, the following works can be continued in the future:

(a) Study the behaviours of the five rider-bike systems moving uphill and downhill. Since the theories and equations for pedalling motions developed in this thesis are based on the bike moving on the horizontal surface, one requires to modify the formulations concerned for accommodating the above-mentioned study on the bike in uphill or downhill conditions. It is found that the results of References [9,11,17] may be helpful for the validation of this future work.

(b) Study the quasi-static and dynamic responses of the five rider-bike systems by using their 3-dimensional (3D) models. Since the 3D model of a rider-bike system is closer to its real configuration, the numerical results should be more accurate. It is obvious that one will encounter many challenges, because more degrees of freedoms for each rider-bike system must be considered and more problems associated with balancing controls must be solved. The study of Cangley et al. [39] and those of Schwab et al. [79~84] may be relevant to this future work.

(c) Study the dynamic responses of the five rider-bike systems by using the finite element method (FEM). The FEM is one of the powerful tools for solving the static and dynamic problems of various complicated structures. However, for the mountain bikes, the information regarding use of the FEM to perform their static and dynamic analyses is rare, thus, the author has devoted himself to this aspect for some time [85]. t is believed this will be also a good work worthy of future study. The experimental results concerning the structural vibrations of the mountain bikes presented by Levy and Smith [28] and Champoux et al. [30] may be useful for the validations of the last study.

(d) In the existing researches, only one study investigated the rider-bike system with standing posture [77]. Therefore, modelling standing riding with and without pedalling motion would be worth studying.

(e) For the mathematical model and dynamic analyses investigated in this thesis, it

would be worth doing a study to analyze a simple bike model with different riders to see how much different riders affect the results obtained.

References

1. P. Rosen. The Social Construction of Mountain Bikes: Technology and Postmodernity in the Cycle Industry. Social Studies of Science, Vol.23, No.3, pp.479-513, August, 1993.
2. I. Iturrioz. Simulation of Mountain Bike Dynamics. Final Year Project Thesis, Department of Mechanical Engineering, University of Glasgow, UK, 2008.
3. J.K. Titlestad. Mountain Bicycle Rear Suspension Dynamics and Their Effects on Cyclists. MSc Thesis, Department of Mechanical Engineering, University of Glasgow, UK, 2001.
4. M. Davie. The Mechanical, Physiological and Psychological Responses to Riding a Fully Suspended Compared to a Hardtail Mountain Bike. PhD Thesis, Department of Mechanical Engineering, University of Glasgow, UK, 2010.
5. F. Impellizzeri, A. Sassi, M. Rodriguez-Alonso, P. Mognoni, and S. Marcora. Exercise Intensity During Off-Road Cycling Competitions. Medicine & Science in Sports & Exercise, 34 (11), pp, 1808-1813, 2002.
6. B. Stapelfeldt, A. Schwirtz, Y. Schumacher, and M. Hillebrecht. Workload Demands in Mountain Bike Racing. International Journal of Sports Medicine, 24 (4), 294-300, 2004.
7. An IMBA-UK Estimate, UK Mountain Usage. International Mountain Biking Association UK. http://imba.org.uk/research-reports/uk-mountainbike-usage/. September, 2005.
8. W. Kenfield. Bicycle. United States Patents. Patent Number: 448750. March, 1891, USA.
9. C. Good and J. McPhee. Dynamics of Mountain Bicycles with Rear Suspensions: Modelling and Simulation. Sports Engineering, 2, pp. 129-143, 1999.
10. J. Olsen. Bicycle Suspension Systems and Mountain Bike Technology. In: Burke, E.R., *High-Tech Cycling*, Second Edition, pp. 49-68, Human Kinetics, USA,

2003.

11. M. González, J. Cuadrado, F. González, and D. Dopico. Optimization of an Off-Road Bicycle with Four-Bar Linkage Rear Suspension. Proceedings of MUSME 2008, the International Symposium on Multibody Systems and Mechatronics, San Juan (Argentina), 8-12 April, 2008.
12. S. Needle and M. Hull. An Off-Road Bicycle with Adjustable Suspension Kinematics. Journal of Mechanical Design, Vol. 199, Issue 3, pp. 370-375, September, 1997.
13. E. Wang and M. Hull. Minimization of Pedalling Induced Energy Losses in Off-Road Bicycle Rear Suspension Systems. Vehicle System Dynamics, 28:4, pp.291-306, 1997.
14. H. Nielens and T. Lejeune. Bicycle Shock Absorption Systems and Energy Expended by the Cyclist. Sports Medicine, Vol.34, No.2, pp. 71-80, 2004.
15. H. Nielens and T. Lejeune. Energy Cost of Riding Bicycles with Shock Absorption Systems on a Flat Surface. International Journal of Sports Medicine, 22(6): pp. 400-404, 2001.
16. T. Ishii, Y. Umemura, and K. Kitagawa. Influences of Mountain Bike Suspension Systems on Energy Supply and Performance. Japanese Journal of Biomechanics in Sports & Exercise, Vol. 7(1), pp. 2-9, 2003.
17. E. Wang and M. Hull. A Model for Determining Rider Induced Energy Losses in Bicycle Suspension Systems. Vehicle System Dynamics, Vol. 25, Issue 3, pp. 223-246, 1996.
18. J. Titlestad, A. Fairlie-Clarke, A. Whittaker, M. Davie, I. Watt, and S. Grant. Effect of Suspension Systems on the Physiological and Psychological Responses to Sub-Maximal Biking on Simulated Smooth and Bumpy Tracks. Journal of Sports Science, 24(2), pp. 125-135, 2006.
19. J. Titlestad, A. Whittaker, A. Fairlie-Clarke, M. Davie, S. Grant. Numerical and Experimental Simulation of Mountain Bike Suspension Systems Subject to Regular Impact Excitation. Materials Science Forum, Vol. 440-441, pp. 111-118,

2003.

20. J. Titlestad, A. Fairlie-Clarke, M. Davie, A. Whittaker. Experimental Evaluation of Mountain Bike Suspension Systems. Acta Polytechnica, 43 (5), pp. 15-20, 2003.

21. F. Impellizzeri and S. Marcora. The Physiology of Mountain Biking (Review Article). Sports Medicine, Vol.37, No.1, pp. 59-71, 2007.

22. M. Berry, T. Koves, and J. Benedetto. The Influence of Speed, Grade and Mass during Simulated Off Road Cycling. Applied Ergonomics, 31 (5), pp. 531-536, 2000.

23. J. Seifert, M. Luetkemeier, M. Spencer, D. Miller, and E. R. Burke. The Effects of Mountain Bike Suspension Systems on Energy Expenditure, Physical Exertion, and Time Trial Performance during Mountain Bicycling. International Journal of Sports Medicine, 18 (3), pp. 197-200, 1997.

24. H.S. Macrae, K.J. Hise, and P.J. Allen. Effects of Front and Dual Suspension Mountain Bike Systems on Uphill Cycling Performance. Medicine and Science in Sports and Exercise, Vol. 32, No. 7, pp. 1276-1280, 2000.

25. M. Padilla and J. Brennan. Bicycle Rear Suspension Study. Human Power Lab, Cornell University, USA, 1996.

26. C. Good and J. McPhee. Dynamics of Mountain Bicycles with Rear Suspensions: Design Optimization. Sports Engineering, 3, pp. 49 – 55, 2000.

27. A. Karchin and M.L. Hull. Experimental Optimization of Pivot Point Height for Swing-Arm Type Rear Suspensions in Off-Road Bicycles. Journal of Biomechanical Engineering, 124, 101-106, February, 2002.

28. M. Levy and G.A. Smith. Effectiveness of Vibration Damping with Bicycle Suspension Systems. Sports Engineering, Vol., 8, No. 2, pp. 99-106, 2005.

29. Y. Champoux, P. Vittecog, P. Maltais, E. Auger, and B. Gauthier. Measuring the Dynamic Structural Load of an Off-Road Bicycle Frame. Experimental Techniques, Vol. 28, Issue 3, pp. 33-36, May, 2004.

30. Y. Champoux, S. Richard, and J.-M. Drouet. Bicycle Structural Dynamics. Sound and Vibration, 16-22, July, 2007.

31. R. Redfield. Large Motion Mountain Biking Dynamics. Vehicle System Dynamics, Vol. 43, Issue 12, pp. 845-864, December, 2005.

32. R. Redfield and C. Sutela. A Bond Graph Model of a Full-Suspension Mountain Bicycle Rear Shock. The Engineering of Sport, 6, 3, pp. 109-114, 2006.

33. C. Stone and M. Hull. The Effect of Rider Weight on Rider-Induced Loads during Common Cycling Situations. Journal of Biomechanics, Vol.28, No.4, pp.365-375, 1994.

34. LMS Web Page. http://www.lmsintl.com

35. H. Wilczynski and M. Hull. A Dynamic System Model for Estimating Surface-Induced Frame Loads during Off-Road Cycling. Journal of Mechanical Design, Vol. 116, Issue 3, pp.816-822, 1994.

36. D. Palmer. Modelling and Control of Suspensions as Used in Interferometric Gravitational Wave Detectors. PhD Thesis, Department of Mechanical Engineering, University of Glasgow, UK, 2001.

37. J. Enright. Simulation of Mountain Bike Dynamics. Industrial Project Report, Department of Mechanical Engineering, University of Glasgow, UK, 2007.

38. SimMechanics. SimMechanics Users Guide. The MathWorks, Inc., 2008.

39. P. Cangley, L. Passfield, H. Carter, and M. Bailey. Modelling Mechanical Enhancements in Competitive Cycling. Bicycle and Motorcycle Dynamics, Netherlands, October, 2010.

    http://bicycle.tudelft.nl/bmd2010/CDProceedingsBMD2010/papers/cangley2010modelling.pdf

40. J. Broker. Chapter 5: Cycling Biomechanics: Road and Mountain. In: Burke, E.R., *High-Tech Cycling*, Second Edition, pp. 119-146, Human Kinetics, USA, 2003.

41. R. Neptune and M. Hull. Accuracy Assessment of Methods for Determining Hip

Movement in Seated Cycling. Journal of Biomechanics 28 (4), pp. 423-437, 1995.

42. R. Neptune and M. Hull. Evaluation of Performance Criteria for Simulation of Submaximal Steady-State Cycling Using a Forward Dynamic Model. Journal of Biomechanical Engineering 120, pp. 334-341, 1998.

43. R. Neptune and A. Bogert. Standard Mechanical Energy Analyses Do Not Correlate with Muscle Work in Cycling. Journal of Biomechanics 31, pp. 239-245, 1998.

44. E. Hansen, L. Jørgensen, K. Jensen, B. Fregly, G. Sjøgaard. Crank Inertial Load Affects Freely Chosen Pedal Rate during Cycling. Journal of Biomechanics 35, pp. 277-285, 2002.

45. D. Sanderson and A. Black. The Effect of Prolonged Cycling on Pedal Forces. Journal of Sports Science 21, pp. 191-199, 2003.

46. S. Duc, W. Bertucci, J. Pernin, F. Grappe. Muscular Activity during Uphill Cycling: Effect of Slope, Posture, Hand Grip Position and Constrained Bicycle Lateral Sways. Journal of Electromyography and Kinesiology 18, pp. 116-127, 2008.

47. E. Vries and J. Brok. Assessing Slip of a Rolling Disc and the Implementation of a Tyre Model in the Benchmark Bicycle. Bicycle and Motorcycle Dynamics, Netherlands, October, 2010.

48. J. Ghidella, T. Denery, P. Mosterman, and R. Shenoy. Creating Flight Simulator Landing Gear Models Using Multidomain Modelling Tools. AIAA Modelling and Simulation Technologies Conference and Exhibit, Keystone, Colorado, August, 2006.

49. M. Dede and S. Tosunoglu. Development of a Real-Time Force-Reflecting Teleoperation System Based on Matlab Simulations. Proceedings of the 19th Florida Conference on Recent Advances in Robotics, Florida International University, Miami, Florida, 2006.

50. J. Peralta, T. Ylikorpi, K. Gulzar, P. Jakubik, and A. Halme. Novel Design of

Biped Robot Based on Linear Induction Motors. International Conference on Humanoid Robots, Paris, France, 2009.

51. S. Winder and J. Esposito. Modelling and Control of an Upper-Body Exoskeleton. 40th Southeastern Symposium on System Theory, pp. 263-268, University of New Orleans, USA, 2008.

52. A. Christopher, D. Caldecott, A. Edwards, M. Jerbic, R. Madigan, M. Haynes, B. Seth, and Z. David. Modelling, Simulation and Control of an Electric Unicycle. Proceedings of the Australasian Conference on Robotics and Automation, ACRA 2010, Brisbane, Australia, December, 2010.

53. F. Braghin, F. Cheli, M. Donzelli, S. Melzi, and E. Sabbioni. Multi-Body Model of a Bobsleigh: Comparison with Experimental Data. Multibody System Dynamics, Vol. 25, No. 2, pp. 185-201, 2011.

54. F. Puccio, E. Franchi, and F. Mattei. Simulating Human Movement in SimMechanics. Abstract, Journal of Biomechanics, Vol. 41, Issue 1, pp. S426, 2008.

55. G. Wood and D. Kennedy. Simulating Mechanical Systems in Simulink with SimMechanics. Technical Report, The MathWorks, Inc., www.mathworks.com, 2003.

56. S. Stan, M. Manic, V. Măties, and R. Bălan. Kinematics Analysis, Design, and Control of an Isoglide3 Parallel Robot. 34th Annual Conference of the IEEE Industrial Electronics Society, Orlando, USA, November, 2008.

57. W. Kailai, Y. Tagawa, and N. Shiba. Simulation of Human Body Motion Under the Conditions of Weightlessness. ICROS-SICE International Joint Conference, pp. 3835-3839, Japan, 2009.

58. I. Besselink. Vehicle Dynamics Analysis Using SimMechanics and TNO Delft-Tyre. IAC 2006 The MathWorks International Automotive Conference, Stuttgart, Germany, 2006.

59. C. Payton and R. Bartlett. Biomechanical Evaluation of Movement in Sport and Exercise, pp.177 and pp.191. BASES (British Association of Sport and Exercise

Science). Routledge, 14th November, 2008.

60. Linkage: Bike Suspension Simulation Software. http://www.bikechecker.com/
61. BikeCAD: Bike Design Software. http://www.bikecad.ca/
62. SlideAway Bicycle. Wade Leisure Business Incorporation. http://www.slideaway.com.tw. Taiwan.
63. Mountain Biker Rider Magazine (MBR), Vol. March 2010, pp.106, UK.
64. E. Burke and A. Pruitt. Chapter 3: Body Positioning for Cycling. In: Burke, E.R., *High-Tech Cycling*, Second Edition, pp. 69-92, Human Kinetics, USA, 2003.
65. Marin Mountain Bikes. http://www.marin.co.uk/2012/
66. Orbea Mountain Bikes. http://www.orbea.com/
67. Specialized Mountain Bikes. http://www.specialized.com/
68. Kona Mountain Bikes. http://www.konaworld.com/
69. Santa Cruz Mountain Bikes. http://www.santacruzbicycles.com/home/
70. H. Leitner. Rear Suspension for Bicycles. United States Patents. Patent Number: 5509679. April, 1996. USA.
71. Dwight, H.B., *Tables of Integrals and Other Mathematical Data*, 3rd Ed., Dept. of Electrical Machinery, Massachusetts Institute of Technology, 1957.
72. Faires, F.D. and Burden, R.L., *Numerical Methods*, Boston: PWS, 1993.
73. V. Swami, D. Einon, and A. Furnham. The Leg-to-Body Ratio as a Human Aesthetic Criterion. Body Image, Vol. 3, pp. 317-323, 2006.
74. A. Howatson, P. Lund, and J. Todd. *Engineering Tables and Data*, Second Edition, Chapman & Hall, UK, 1992.
75. G. Housner and D. Hudson. *Applied Mechanics Dynamics*, Second Edition. Division of Engineering, California Institute of Technology, USA, 1959.
76. R. Dorf and R. Bishop. *Modern Control Systems*, Ninth Edition. Prentice Hall. New Jersey, USA. 2001.

77. P. Soden and B. Adeyefa. Forces Applied to a Bicycle During Normal Cycling. Journal of Biomechanics, Vol. 12, pp. 527 – 541, 1979.

78. J. Koning and K. Soest. Chapter 11: Biomechanics. In: A. E. Jeukendrup, *High-Performance Cycling*, pp. 129-138, Human Kinetics, USA, 2002.

79. A. Schwab, J. Meijaard, and J. Papadopoulos. Benchmark Results on the Linearized Equations of Motion of an Uncontrolled Bicycle. Journal of Mechanical Science and Technology, 19(1), pp.292-304, 2005.

80. J. Meijaard and A. Schwab. Linearized Equations for an Extended Bicycle Model. III European Conference on Computational Mechanics, Solids, Structures and Coupled Problems in Engineering, 18 pages, June, 2006.

81. J. Kooijman, A. Schwab, and J. Meijaard. Experimental Validation of a Model of an Uncontrolled Bicycle. Multibody System Dynamics, Vol. 19, No. 1-2, pp. 115-132, 2008.

82. J. Kooijman, A. Schwab, and J. Moore. Some Observations on Human Control of a Bicycle. Proceedings of the ASME 2009 International Design Engineering Technical Conference & Computers and Information in Engineering Conference, 8 pages, San Diego, California, 2009.

83. A. Schwab and J. Kooijman. Controllability of a Bicycle. 5th Asian Conference on Multibody Dynamics, 6 pages, Kyoto, Japan, 2010.

84. J. Moore, J. Kooijman, A. Schwab, and M. Hubbard. Rider Motion Identification during Normal Bicycling by Means of Principal Component Analysis. Multibody System Dynamics, Vol. 25, No. 2, pp. 225-244, 2011.

85. C.C. Wu. Static and Free Vibration Analyses of a Bike Using Finite Element Method. Technique Report, Department of Mechanical Engineering, University of Glasgow, UK, 2009.

Appendix A

Derivations of Equations for Chapter 4

A.1 Determination of Critical Positions of Rod1, Rod2 and Rod3

This section determines the critical angles of Rod1, Rod2 and Rod3 for the following critical positions of Rod3 and those of Rod 1: (i) The upper leg (Rod3) is in its uppermost position; (ii) The upper leg (Rod3) is in its lowermost position; (iii) The crank (Rod1) is in its rightward position (with $\theta_1=\theta_{1,B}=90°$); (iv) The crank (Rod1) is in its downward position (with $\theta_1=\theta_{1,C}=180°$).

A.1.1 Critical Angles when Upper Leg (Rod3) in its Uppermost Position

From Figure 4.2 one sees that Rod3 (upper leg) is in its uppermost position when the angle between Rod1 (crank) and Rod2 (lower leg) are equal to $\pi(=180°)$ (i.e., on a straight line). Thus, from the figure one sees that

$$(L_1 + L_2)\cos\theta_{1,U} + L_3 \sin\theta_{3,U} = y_c \qquad \text{(A.1)}$$

$$L_3 \cos\theta_{3,U} - (L_1 + L_2)\sin\theta_{1,U} = x_c \qquad \text{(A.2)}$$

or

$$L_{12} \cos\theta_{1,U} + L_3 \sin\theta_{3,U} = y_c \qquad \text{(A.1)'}$$

$$L_3 \cos\theta_{3,U} - L_{12} \sin\theta_{1,U} = x_c \qquad \text{(A.2)'}$$

where

$$L_{12} = L_1 + L_2 \qquad \text{(A.3)}$$

It is noted that the subscripts "U" of θ_1 and θ_3 refer to the "uppermost" position of Rod3.

Eliminating $\theta_{1,U}$ from Equations (A.1)' and (A.2)' and then re-arranging the equations, one obtains

$$(x_c^2 + y_c^2)\sin^2\theta_{3,U} - 2C_1 y_c \sin\theta_{3,U} + (C_1^2 - x_c^2) = 0 \qquad \text{(A.4)}$$

where

$$C_1 = (x_c^2 + y_c^2 + L_3^2 - L_{12}^2)/(2L_3) \tag{A.5}$$

The solution of Equation (A.4) is given by

$$\sin\theta_{3,U} = \frac{C_1 y_c \pm \sqrt{(C_1 y_c)^2 - (x_c^2 + y_c^2)(C_1^2 - x_c^2)}}{x_c^2 + y_c^2} = s_{1_2} \tag{A.6}$$

Thus,

$$\theta_{3,U} = \sin^{-1} s_1 \quad \text{or} \quad \theta_{3,U} = \sin^{-1} s_2 \tag{A.7a,b}$$

From Figure 4.2 one sees that the value of $\theta_{3,U}$ is approximately equal to 7.5° for the initial configuration and the computer output reveals that the selection of negative sign (-) in Equation (A.6) will lead to $\theta_{3,U} \approx 7.5°$, thus, Equation (A.7b) must be used to determine the value of $\theta_{3,U}$. [The selection of positive sign (+) in Equation (A.6) will lead to $\theta_{3,U} \approx 34.35°$, which is not consistent with Figure 4.2.]

From Equation (A.1)', one obtains

$$\cos\theta_{1,U} = (y_c - L_3 \sin\theta_{3,U})/L_{12} \tag{A.8}$$

Thus, the (critical) angle between Rod1 and the upward *y*-axis is given by

$$\theta_{1,U} = \cos^{-1}[(y_c - L_3 \sin\theta_{3,U})/L_{12}] \tag{A.9}$$

From Figure 4.2 one sees that the (critical) angle between Rod2 and *x*-axis is given by

$$\theta_{2,U} = \tfrac{1}{2}\pi - \theta_{1,U} \tag{A.10}$$

From Figure 4.1 one sees that the angle between Rod1 and Rod2 is given by

$$\alpha = 360^\circ - 90^\circ - \theta_1 - \theta_2 = 270^\circ - \theta_1 - \theta_2 \tag{A.11}$$

For the special case studied in this subsection, from Figure 4.2 and Equation (A.10) one sees that

$$\theta_{2,U} + \theta_{1,U} = \tfrac{1}{2}\pi = 90^o \tag{A.12}$$

Substitution of the last equation into Equation (A.11) leads to

$$\alpha = 270^o - (\theta_{1,U} + \theta_{2,U}) = 270^o - 90^o = 180^o \tag{A.13}$$

This agrees with the actual situation, because Rod1 and Rod 2 are on a straight line

when the rider's right (or left) upper leg is in its uppermost position as shown in Figure 4.2.

A.1.2 Critical Angles when Upper Leg (Rod3) in its Lowermost Position

From Figure 4.3 one sees that upper leg (Rod3) is in its *lowermost* position when the path of Joint 1 of Rod1 is tangential to the path of Joint 1 of Rod2 with centre L' on path of Joint 2 and radius to be L_2. If the tangential point between the above-mentioned two paths (arcs) is denoted by L, then $\overline{L'L}$ must pass through the centre "O" of the circle of crank pin (i.e., bottom bracket) because the radius of the circle must be perpendicular to the tangential line at point L. Where the symbol $\overline{L'L}$ denotes the line connecting points L' and L.

From Figure 4.3 one sees that

$$\overline{SP} + \overline{PN} = \overline{SM} + \overline{MN} \tag{A.14}$$

$$\overline{QR} = \overline{PR} - \overline{PQ} = \overline{PR} - (\overline{PL'} - \overline{QL'}) \tag{A.15}$$

Thus,

$$L_3 \sin\theta_{3,L} + L_2 \sin\theta_2 = y_c + L_1 \sin\theta_2 \tag{A.16a}$$

$$L_1 \cos\theta_2 = x_c - (L_3 \cos\theta_{3,L} - L_2 \cos\theta_2) \tag{A.16b}$$

It is similar to Equations (A.1)' and (A.2)' that eliminating θ_2 from Equations (A.16a) and (A.16b) and then performing some mathematical manipulations, one obtains

$$(x_c^2 + y_c^2)\sin^2\theta_{3,L} - 2y_c E_2 \sin\theta_{3,L} + (E_2^2 - x_c^2) = 0 \tag{A.17}$$

where

$$E_2 = [x_c^2 + y_c^2 + L_3^2 - (L_2 - L_1)^2] / (2L_3) \tag{A.18}$$

The solution of Equation (A.17) is given by

$$\sin\theta_{3,L} = \frac{y_c E_2 \pm \sqrt{(y_c E_2)^2 - (x_c^2 + y_c^2)(E_2^2 - x_c^2)}}{x_c^2 + y_c^2} = s_{1_2} \tag{A.19}$$

Thus, the critical angle of Rod3 when it is in its "lowermost" position is given by

$$\theta_{3,L} = \sin^{-1} s_1 \quad \text{or} \quad \theta_{3,L} = \sin^{-1} s_2 \tag{A.20a,b}$$

From Figure 4.3 one sees that the value of $\theta_{3,L}$ is approximately equal to $\pi/3 (\approx 60°)$ for the current configuration and the computer output indicates that the selection of

negative sign (-) in Equation (A.19) leads to $\theta_{3,L} \approx \pi/3 (\approx 60°)$. Thus, Equation (A.20b) must be used to calculate the value of $\theta_{3,L}$. [The selection of positive sign (+) in Equation (A.19) leads to $\theta_{3,L} \approx 85.18°$, which is not consistent with Figure 4.3.]

From Equation. (A.16a) one obtains

$$\sin\theta_2 = (y_c - L_3 \sin\theta_{3,L}) / (L_2 - L_1) \tag{A.21}$$

Thus, the angle of Rod2 corresponding to the lowermost position of Rod3 is given by

$$\theta_2 = \theta_{2,L} = \sin^{-1}[(y_c - L_3 \sin\theta_{3,L}) / (L_2 - L_1)] \tag{A.22}$$

From Figure 4.3, one sees that the angle between Rod1 and upward y-axis is given by

$$\theta_{1,L} = \pi + \theta'_{1,L} = \pi + (0.5\pi - \theta_2) = 1.5\pi - \theta_2 \tag{A.23}$$

Substituting Equation (A.23) into Equation (A.11) leads to

$$\alpha = 270^o - \theta_1 - \theta_2 = 270^o - (270^o - \theta_2) - \theta_2 = 0 \tag{A.24}$$

It is obvious that the last result agrees with the actual situation appearing in Figure 4.3 where Rod1 and Rod2 overlap each other.

A.1.3 Critical Angles when Crank (Rod1) in Rightward Position ($\theta_1=\theta_{1,B}=90°$)

When Rod1 is in its horizontal position with Joint 1 at point B and $\theta_1=\theta_{1,B}=90°$ as shown in Figure 4.4, one has

$$\overline{SM} = \overline{SP} + \overline{PM}\ ,\quad \overline{PB'} = \overline{PQ} + \overline{QR} + \overline{RB'} \qquad \text{(A.25a,b)}$$

Thus,

$$y_c = L_3 \sin\theta_{3,B} + L_2 \sin\theta_2\ ,\quad L_3 \cos\theta_{3,B} = x_c + L_1 + L_2 \cos\theta_2 \qquad \text{(A.26a,b)}$$

Eliminating θ_2 from Equations (A.26a) and (A.26b), and then manipulating the resulting expression mathematically, one obtains

$$(C_3^2 + y_c^2)\sin^2\theta_{3,B} - 2D_3 y_c \sin\theta_{3,B} + (D_3^2 - C_3^2) = 0 \qquad \text{(A.27)}$$

where

$$C_3 = x_c + L_1\ ,\quad D_3 = (C_3^2 + y_c^2 + L_3^2 - L_2^2)/(2L_3) \qquad \text{(A.28a,b)}$$

The solution of Equation (A.27) is given by

$$\sin\theta_{3,B} = \frac{D_3 y_c \pm \sqrt{(D_3 y_c)^2 - (C_3^2 + y_c^2)(D_3^2 - C_3^2)}}{(C_3^2 + y_c^2)} = s_{1\atop 2} \qquad \text{(A.29)}$$

Thus,

$$\theta_{3,B} = \sin^{-1} s_1 \quad \text{or} \quad \theta_{3,B} = \sin^{-1} s_2 \qquad \text{(A.30a,b)}$$

From Figure 4.4 one sees that the value of $\theta_{3,B}$ is approximately equal to 25° for the current configuration and the computer output indicates that the selection of negative sign (-) in Equation (A.29) will lead to $\theta_{3,B} \approx 25°$. Thus, Equation (A.30b) must be used to determine the critical value of $\theta_{3,B}$ corresponding to the horizontal position of Rod1. [The selection of positive sign (+) in Equation (A.29) will lead to $\theta_{3,B} \approx 81.13°$, which is not consistent with Figure 4.4.]

From Equation (A.26a), one obtains

$$\sin\theta_2 = (y_c - L_3 \sin\theta_{3,B})/L_2 \qquad \text{(A.31)}$$

Thus, when the crank (Rod1) is in the horizontal position with Joint 1 at point B and $\theta_1=\theta_{1,B}=90°$, the angle between Rod2 and x-axis is given by

$$\theta_2 = \theta_{2,B} = \sin^{-1}[(y_c - L_3 \sin\theta_{3,B})/L_2] \qquad \text{(A.32)}$$

From Figure 4.4 one sees that the angle between Rod1 and Rod 2 is given by

$$\alpha = 270^o - \theta_1 - \theta_2$$

which agrees with Equation (A.11).

A.1.4 Critical Angles when Crank (Rod1) in Downward Position ($\theta_1=\theta_{1,C}=180°$)

When Rod1 is in vertical position with Joint 1 at point C and $\theta_1=\theta_{1,C}=180°$ as shown in Figure 4.5, one has

$$\overline{SM} = \overline{SP} + \overline{PN} - \overline{NM}\ ,\ \ \overline{PC'} = \overline{PQ} + \overline{QC'} \qquad \text{(A.33a,b)}$$

Thus,

$$y_c = L_3 \sin\theta_{3,C} + L_2 \sin\theta_2 - L_1\ ,\ \ L_3 \cos\theta_{3,B} = x_c + L_2 \cos\theta_2 \qquad \text{(A.34a,b)}$$

Eliminating θ_2 from Equations (A.34a) and (A.34b), and conducting some mathematical operations of the resulting expression produce

$$(x_c^2 + C_4^2)\sin^2\theta_{3,C} - 2C_4D_4 \sin\theta_{3,C} + (D_4^2 - x_c^2) = 0 \qquad \text{(A.35)}$$

where

$$C_4 = y_c + L_1\ ,\ \ D_4 = (x_c^2 + C_4^2 + L_3^2 - L_2^2)/(2L_3) \qquad \text{(A.36a,b)}$$

The solution of Equation (A.35) is given by

$$\sin\theta_{3,C} = \frac{C_4D_4 \pm \sqrt{(C_4D_4)^2 - (x_c^2 + C_4^2)(D_4^2 - x_c^2)}}{(x_c^2 + C_4^2)} = s_{1_2} \qquad \text{(A.37)}$$

Thus,

$$\theta_{3,C} = \sin^{-1} s_1 \ \text{ or } \ \theta_{3,C} = \sin^{-1} s_2 \qquad \text{(A.38a,b)}$$

Since Figure 4.5 reveals that the value of $\theta_{3,C}$ is approximately equal to 60° and the selection of negative sign (-) in Equation (A.37) will lead to $\theta_{3,C} \approx 60°$ as one may see from the computer output, Equation (A.38b) must be used to determine the critical value of $\theta_{3,C}$. [The selection of positive sign (+) in Equation (A.37) will lead to $\theta_{3,C} \approx 77.74°$, which is not consistent with Figure 4.5.]

From Equations (A.34a) and (A.36a), one obtains

$$\sin\theta_2 = (C_4 - L_3 \sin\theta_{3,C})/L_2 \qquad \text{(A.39)}$$

Thus,

$$\theta_2 = \theta_{2,C} = \sin^{-1}[(C_4 - L_3 \sin\theta_{3,C})/L_2] \qquad \text{(A.40)}$$

From Figure 4.5 one sees that the angle between Rod1 and Rod 2 is given by

$$\alpha = 90^o - \theta_2 \tag{A.41}$$

which agrees with the following result obtained from Equation (A.11) by substituting the value of $\theta_1=\theta_{1,C}=180°$ (see Figure 4.5)

$$\alpha = 270^o - \theta_1 - \theta_2 = 270^o - 180^0 - \theta_2 = 90^o - \theta_2 \tag{A.42}$$

A.2 Positions of Rod1 and Rod2 Associated with any Specified Positions of Rod3

This section determines the instantaneous positions of Rod1 and Rod2 corresponding to the positions of Rod3, $\theta_3(t)$, in the following three intervals: (i) $\theta_{3,U} \le \theta_3(t) < \theta_{3,B}$, (ii) $\theta_{3,B} \le \theta_3(t) < \theta_{3,C}$ and (iii) $\theta_{3,C} \le \theta_3(t) < \theta_{3,L}$.

A.2.1 Positions of Rod1 and Rod2 Associated with $\theta_{3,U} \le \theta_3(t) < \theta_{3,B}$

When upper leg (Rod3) is in the arbitrary position within the interval $\theta_{3,U} \le \theta_3(t) < \theta_{3,B}$, the position of crank (Rod1) must be in the interval $\theta_{1,U} \le \theta_1(t) < 0.5\pi$ as shown in Figure 4.6.

From Figure 4.6 one obtains

$$\overline{SN} = \overline{SP} + \overline{PM} + \overline{MN} \tag{A.43a}$$

$$\overline{PT} = \overline{PQ} + \overline{QR} + \overline{RT} \tag{A.43b}$$

Thus,

$$y_c = L_3 \sin\theta_3 + L_2 \sin\theta_2 + L_1 \cos\theta_1 \tag{A.44a}$$

$$L_3 \cos\theta_3 = x_c + L_1 \sin\theta_1 + L_2 \cos\theta_2 \tag{A.44b}$$

Therefore, if the position of Rod3 (with angle θ_3) is given, then the corresponding positions of Rod1 and Rod2 (with angles θ_1 and θ_2) can be determined as follows:

Eliminating θ_2 from Equations (A.44a) and (A.44b) and then performing some mathematical operations, one obtains

$$(C_5^2 + D_5^2)\sin^2\theta_1 - 2E_5 D_5 \sin\theta_1 + (E_5^2 - C_5^2) = 0 \tag{A.45}$$

where

$$C_5 = y_c - L_3 \sin\theta_3, \quad D_5 = -x_c + L_3 \cos\theta_3, \quad E_5 = (C_5^2 + D_5^2 + L_1^2 - L_2^2)/(2L_1) \tag{A.46a,b,c}$$

The solution of Equation (A.45) is given by

$$\sin\theta_1 = \frac{E_5 D_5 \pm \sqrt{(E_5 D_5)^2 - (C_5^2 + D_5^2)(E_5^2 - C_5^2)}}{(C_5^2 + D_5^2)} = s_{1_2} \qquad \text{(A.47)}$$

Thus,

$$\theta_1 = \sin^{-1} s_1 \quad \text{or} \quad \theta_1 = \sin^{-1} s_2 \qquad \text{(A.48a,b)}$$

Since the value of θ_1 must be in the interval $\theta_{1,U} \le \theta_1(t) < 0.5\pi$ and the selection of positive sign (+) in Equation (A.47) will lead to the desired value of θ_1, Equation (A.48a) is correct for the present case. [Numerical example indicates that selection of negative sign (-) in Equation (A.47) will lead the value $\theta_1(t)$ outside the interval $\theta_{1,U} \le \theta_1(t) < 0.5\pi$.]

From Equations (A.44a) and (A.46a), one obtains

$$\sin\theta_2 = (C_5 - L_1 \cos\theta_1)/L_2 \qquad \text{(A.49)}$$

Thus,

$$\theta_2 = \sin^{-1}[(C_5 - L_1 \cos\theta_1)/L_2] \qquad \text{(A.50)}$$

From Figure 4.6 one sees that the angle between Rod1 and Rod 2 is given by

$$\alpha = \angle OVT = 270^o - \theta_1 - \theta_2$$

The last result agrees with that obtained from Equation (A.11).

A.2.2 Positions of Rod1 and Rod2 Associated with $\theta_{3,B} \le \theta_3(t) < \theta_{3,C}$

When upper leg (Rod3) is in the arbitrary position within the interval $\theta_{3,B} \le \theta_3(t) < \theta_{3,C}$, the position of crank (Rod1) must be in the interval $0.5\pi \le \theta_1(t) < \pi$ as shown in Figure 4.7. In such a case, from the figure one sees that

$$\overline{SM} = \overline{SP} + \overline{PN} - \overline{MN} \tag{A.51a}$$

$$\overline{PT} = \overline{PQ} + \overline{QR} + \overline{RT} \tag{A.51b}$$

Thus,

$$y_c = L_3 \sin\theta_3 + L_2 \sin\theta_2 - L_1 \sin\theta_1' \tag{A.52a}$$

$$L_3 \cos\theta_3 = x_c + L_1 \cos\theta_1' + L_2 \cos\theta_2 \tag{A.52b}$$

Therefore, if the value of θ_3 is given, then the corresponding values of θ_1 and θ_2 can be determined as follows:

Eliminating θ_2 from Equations (A.52a) and (A.52b), and then conducting some mathematical operations will lead to

$$(C_5^2 + D_5^2)\cos^2\theta_1' - 2E_5 D_5 \cos\theta_1' + (E_5^2 - C_5^2) = 0 \tag{A.53}$$

Where C_5, D_5 and E_5 take the same forms as those given by Equations (A.46a,b,c), i.e.,

$$C_5 = y_c - L_3 \sin\theta_3, \quad D_5 = -x_c + L_3 \cos\theta_3 \tag{A.54a,b}$$

$$E_5 = (C_5^2 + D_5^2 + L_1^2 - L_2^2)/(2L_1) \tag{A.54c}$$

The solution of Equation (A.53) is given by

$$\cos\theta_1' = \frac{E_5 D_5 \pm \sqrt{(E_5 D_5)^2 - (C_5^2 + D_5^2)(E_5^2 - C_5^2)}}{(C_5^2 + D_5^2)} = s_{1_2} \tag{A.55}$$

Thus,

$$\theta_1' = \cos^{-1} s_1 \quad \text{or} \quad \theta_1' = \cos^{-1} s_2 \tag{A.56a,b}$$

Since the correct position of Rod1 must be in the interval $0.5\pi \le \theta_1(t) < \pi$ and $\theta_1 = 0.5\pi + \theta_1'$ as one may see from Figure 4.7, the value of θ_1' must be $0 \le \theta_1'(t) \le 0.5\pi$. From the computer output one finds that the selection of positive sign (+) in Equation

(A.55) will lead to the desired result and numerical example indicates that selection of negative sign (-) in Equation (A.55) will lead the value $\theta_1(t)$ outside the interval $0.5\pi \le \theta_1(t) < \pi$, thus, Equation (A.56a) must be used to calculate the value of θ_1' and the corresponding position of Rod1 is given by

$$\theta_1 = 0.5\pi + \theta_1' \tag{A.57}$$

Now, from Equations (A.52a) and (A.54a), one obtains

$$\sin\theta_2 = (C_5 + L_1 \sin\theta_1')/L_2 \tag{A.58}$$

Thus,

$$\theta_2 = \sin^{-1}[(C_5 + L_1 \sin\theta_1')/L_2] \tag{A.59}$$

From Figure 4.7 one sees that the angle between Rod1 and Rod 2 is given by

$$\alpha = \angle OVT = 270^o - \theta_1 - \theta_2$$

The above equation is identical to Equation (A.11).

A.2.3 Positions of Rod1 and Rod2 Associated with $\theta_{3,C} \le \theta_3(t) < \theta_{3,L}$

When the upper leg (Rod3) is in the arbitrary position $\overline{SG'}$ within the interval $\theta_{3,C} \le \theta_3(t) < \theta_{3,L}$, the position of crank (Rod1) must be in the interval $\pi \le \theta_1(t) < \theta_{1,L}$ as shown in Figure 4.8 denoted by $\overline{OG}$. In such a case, from the figure one sees that

$$\overline{SM} = \overline{SP} + \overline{PN} - \overline{MN}, \quad \overline{PG'} = (\overline{PR} - \overline{QR}) + \overline{QG'} \qquad \text{(A.60a,b)}$$

Thus,

$$y_c = L_3 \sin\theta_3 + L_2 \sin\theta_2 - L_1 \cos\theta_1' \qquad \text{(A.61a)}$$

$$L_3 \cos\theta_3 = (x_c - L_1 \sin\theta_1') + L_2 \cos\theta_2 \qquad \text{(A.61b)}$$

Eliminating θ_2 from the above two equations and manipulating the resulting expression mathematically, one obtains

$$(C_6^2 + D_6^2)\sin^2\theta_1' - 2D_6E_6 \sin\theta_1' + (E_6^2 - C_6^2) = 0 \qquad \text{(A.62)}$$

where

$$C_6 = -y_c + L_3 \sin\theta_3, \quad D_6 = x_c - L_3 \cos\theta_3, \qquad \text{(A.63a,b)}$$

$$E_6 = (C_6^2 + D_6^2 + L_1^2 - L_2^2)/(2L_1) \qquad \text{(A.63c)}$$

The solution of Equation (A.62) is given by

$$\sin\theta_1' = \frac{D_6E_6 \pm \sqrt{(D_6E_6)^2 - (C_6^2 + D_6^2)(E_6^2 - C_6^2)}}{(C_6^2 + D_6^2)} = s_{1_2} \qquad \text{(A.64)}$$

Thus,

$$\theta_1' = \sin^{-1} s_1 \quad \text{or} \quad \theta_1' = \sin^{-1} s_2 \qquad \text{(A.65a,b)}$$

Since the correct position of Rod1 must be in the interval $\pi \le \theta_1(t) < \theta_{1,L}$ and $\theta_{1,L} = \pi + \theta_{1,L}'$ as one may see from Figure 4.3, the value of θ_1' must be $0 \le \theta_1'(t) < \theta_{1,L}'$. From the computer output one finds that the selection of positive sign (+) in Equation (A.64) will lead to the desired result and Numerical example indicates that selection of negative sign (-) in Equation (A.64) will lead the value $\theta_1(t)$ outside the interval $\pi \le \theta_1(t) \le \theta_{1,L}$, thus, Equation (A.65a) must be used to calculate the value of θ_1' and the corresponding position of Rod1 is given by

$$\theta_1 = \pi + \theta_1' \tag{A.66}$$

Furthermore, from Equations (A.61a) and (A.63a), one obtains

$$\sin\theta_2 = (L_1 \cos\theta_1' - C_6)/L_2 \tag{A.67}$$

Thus,

$$\theta_2 = \sin^{-1}[(L_1 \cos\theta_1' - C_6)/L_2] \tag{A.68}$$

If the angle between +*y*-axis and Rod2 is denoted by β, then Figure 4.8 indicates that the angle between Rod2 and *x*-axis is given by

$$\theta_2 = 0.5\pi - \beta \tag{A.69}$$

Introducing the values of θ_1 and θ_2 given by Equations (A.66) and (A.69) into Equation (A.11) produces

$$\alpha = 270^o - \theta_1 - \theta_2 = 1.5\pi - (\pi + \theta_1') - (0.5\pi - \beta) = \beta - \theta_1' \tag{A.70}$$

The above value of α agrees with the actual situation as shown in Figure 4.8.

A.3 Positions of Rod2 and Rod3 Associated with any Specified Positions of Rod1

This section determines the angles of Rod2 and Rod3 corresponding to the (given) prescribed angle of Rod1 at any instant of time t, $\theta_1(t)$, within the following three intervals: (i) $\theta_{1,U} \le \theta_1(t) < 0.5\pi$, (ii) $0.5\pi \le \theta_1(t) < \pi$ and (iii) $\pi \le \theta_1(t) < \theta_{1,L}$.

A.3.1 Positions of Rod2 and Rod3 Associated with $\theta_{1,U} \le \theta_1(t) < 0.5\pi$

For the current case, the configuration of the crank (Rod1), the rider's right (or left) lower leg (Rod2) and his upper leg (Rod3) is the same as that shown in Figure 4.6. From that figure, one obtains

$$y_c = L_3 \sin\theta_3 + L_2 \sin\theta_2 + L_1 \cos\theta_1 \qquad \text{(A.71a)}$$

$$L_3 \cos\theta_3 = x_c + L_1 \sin\theta_1 + L_2 \cos\theta_2 \qquad \text{(A.71b)}$$

The above two equations are identical to Equations (A.44a) and (A.44b), but the given angle is θ_1 (of Rod1) instead of θ_3 (of Rod3).

Eliminating θ_2 from Equations (A.71a,b) and considering θ_1 as the given parameter, one obtains an equation for the unknown angle θ_3

$$(C_5'^2 + D_5'^2)\sin^2\theta_3 - 2C_5'E_5' \sin\theta_3 + (E_5'^2 - D_5'^2) = 0 \qquad \text{(A.72)}$$

where

$$C_5' = y_c - L_1 \cos\theta_1, \quad D_5' = -x_c - L_1 \sin\theta_1 \qquad \text{(A.73a,b)}$$

$$E_5' = (C_5'^2 + D_5'^2 + L_3^2 - L_2^2)/(2L_3) \qquad \text{(A.73c)}$$

The solution of Equation (A.72) is given by

$$\sin\theta_3 = \frac{C_5'E_5' \pm \sqrt{(C_5'E_5')^2 - (C_5'^2 + D_5'^2)(E_5'^2 - D_5'^2)}}{(C_5'^2 + D_5'^2)} = s_{1_2} \qquad \text{(A.74)}$$

Thus,

$$\theta_3 = \sin^{-1} s_1 \quad \text{or} \quad \theta_3 = \sin^{-1} s_2 \qquad \text{(A.75a,b)}$$

From the previous sections one sees that the value of θ_3 must be in the interval of $\theta_{3,U} \le \theta_3(t) < \theta_{3,B}$ for the case with $\theta_{1,U} \le \theta_1(t) < 0.5\pi$. Since the selection of negative sign (-) in Equation (A.74) will lead to the desired result, Equation (A.75b) is correct for the present case.

Now, from Equations (A.71a) and (A.73a), one obtains

$$\sin\theta_2 = (C_5' - L_3 \sin\theta_3)/L_2 \tag{A.76}$$

Thus,

$$\theta_2 = \sin^{-1}[(C_5' - L_3 \sin\theta_3)/L_2] \tag{A.77}$$

and the angle between Rod1 and Rod 2 is given by Equation (A.11), i.e.,

$$\alpha = \angle OVT = 270^o - \theta_1 - \theta_2$$

A.3.2 Positions of Rod2 and Rod3 Associated with $0.5\pi \le \theta_1(t) < \pi$

For the current case, the configuration of the crank (Rod1), the rider's right (or left) lower leg (Rod2) and his upper leg (Rod3) is the same as that shown in Figure 4.7. It is obvious that the relevant equations are the same as Equations (A.52a) and (A.52b), i.e.,

$$y_c = L_3 \sin\theta_3 + L_2 \sin\theta_2 - L_1 \sin\theta_1' \tag{A.78a}$$

$$L_3 \cos\theta_3 = x_c + L_1 \cos\theta_1' + L_2 \cos\theta_2 \tag{A.78b}$$

Eliminating θ_2 from Equations(A.78a,b) and considering θ_1' as the given parameter, one has

$$(C_5''^2 + D_5''^2)\cos^2\theta_3 - 2D_5''E_5''\cos\theta_3 + (E_5''^2 - C_5''^2) = 0 \tag{A.79}$$

where

$$C_5'' = y_c + L_1 \sin\theta_1', \quad D_5'' = x_c + L_1 \cos\theta_1' \tag{A.80a,b}$$

$$E_5'' = (C_5''^2 + D_5''^2 + L_3^2 - L_2^2)/(2L_3) \tag{A.80c}$$

The solution of Equation (A.79) is given by

$$\cos\theta_3 = \frac{D_5''E_5'' \pm \sqrt{(D_5''E_5'')^2 - (C_5''^2 + D_5''^2)(E_5''^2 - C_5''^2)}}{(C_5''^2 + D_5''^2)} = s_{1_2} \tag{A.81}$$

Thus,

$$\theta_3 = \cos^{-1} s_1 \quad \text{or} \quad \theta_3 = \cos^{-1} s_2 \tag{A.82a,b}$$

From the previous sections one sees that the value of θ_3 must be in the interval of $\theta_{3,B} \le \theta_3(t) < \theta_{3,C}$ when $0.5\pi \le \theta_1(t) < \pi$. Since the selection of positive sign (+) in Equation (A.81) will lead to the desired result, Equation (A.82a) is correct for the present case.

From Equations (A.78a) and (A.80a), one obtains

$$\sin\theta_2 = (C_5'' - L_3 \sin\theta_3)/L_2 \tag{A.83}$$

Thus,

$$\theta_2 = \sin^{-1}[(C_5'' - L_3 \sin\theta_3)/L_2] \tag{A.84}$$

As one may see from Figure 4.7, the angle between Rod1 and positive *y*-axis is given by

$$\theta_1 = 0.5\pi + \theta_1' \tag{A.85}$$

and the angle between Rod1 and Rod2 is given by

$$\alpha = 270^o - \theta_1 - \theta_2$$

A.3.3 Positions of Rod2 and Rod3 Associated with $\pi \le \theta_1(t) < \theta_{1,L}$

For the current case, the configuration of the crank (Rod1), the rider's right (or left) lower leg (Rod2) and his upper leg (Rod3) is the same as that shown in Figure 4.8, thus, the relevant equations are the same as Equations (A.61a) and (A.61b), i.e.,

$$y_c = L_3 \sin\theta_3 + L_2 \sin\theta_2 - L_1 \cos\theta_1' \tag{A.86a}$$

$$L_3 \cos\theta_3 = (x_c - L_1 \sin\theta_1') + L_2 \cos\theta_2 \tag{A.86b}$$

Eliminating θ_2 from Equations (A.86a,b) and considering θ_1' as the given parameter, one has

$$(C_6'^2 + D_6'^2)\cos^2\theta_3 + 2D_6'E_6'\cos\theta_3 + (E_6'^2 - C_6'^2) = 0 \tag{A.87}$$

where

$$C_6' = y_c + L_1 \cos\theta_1' \ , \quad D_6' = -x_c + L_1 \sin\theta_1' \tag{A.88a,b}$$

$$E_6' = (C_6'^2 + D_6'^2 + L_3^2 - L_2^2)/(2L_3) \tag{A.88c}$$

The solution of Equation (A.87) is given by

$$\cos\theta_3 = \frac{-D_6'E_6' \pm \sqrt{(D_6'E_6')^2 - (C_6'^2 + D_6'^2)(E_6'^2 - C_6'^2)}}{(C_6'^2 + D_6'^2)} = s_{1_2} \tag{A.89}$$

Thus,

$$\theta_3 = \cos^{-1} s_1 \ \text{ or } \ \theta_3 = \cos^{-1} s_2 \tag{A.90a,b}$$

From the previous sections one sees that the value of θ_3 must be in the interval of $\theta_{3,C} \le \theta_3(t) < \theta_{3,L}$ when $\pi \le \theta_1(t) < \theta_{1,L}$. Since the selection of positive sign (+) in Equation (A.89) will lead to the desired result, Equation (A.90a) is correct for the present case.

From Equations (A.86a) and (A.88a), one obtains

$$\sin\theta_2 = (C_6' - L_3 \sin\theta_3)/L_2 \tag{A.91}$$

Thus,

$$\theta_2 = \sin^{-1}[(C_6' - L_3 \sin\theta_3)/L_2] \tag{A.92}$$

From Figure 4.8 one sees that the angle between Rod1 and *positive y*-axis is given by

$$\theta_1 = \pi + \theta_1' \tag{A.93}$$

Furthermore, if the angle between Rod2 and *positive y*-axis is represented by β, then the angle between Rod2 and *x*-axis is given by

$$\theta_2 = 0.5\pi - \beta \tag{A.94}$$

Introducing the values of θ_1 and θ_2 given by Equations (A.93) and (A.94) into Equation (A.11), one has

$$\alpha = 1.5\pi - \theta_1 - \theta_2 = 1.5\pi - (\pi + \theta_1') - (0.5\pi - \beta) = \beta - \theta_1' \tag{A.95}$$

The last result agrees with that appearing in Figure 4.8.

Appendix B

Theory of Simpson Rule

In order to find the area under the curve $f(x)$ vs. x as shown in Figure B.1, the "3-point" curve segment passing through the three points $i-1$, i and $i+1$ is represented by the "quadratic" equation

$$f(x) = a + bx + cx^2 \tag{B.1}$$

or

$$\bar{f}(\bar{x}) = \bar{a} + \bar{b}\bar{x} + \bar{c}\bar{x}^2 \tag{B.2}$$

with

$$\bar{x} = x - x_{i-1} \tag{B.3}$$

Furthermore, if the ordinates of the three points, $i-1$, i and $i+1$, are represented by $\bar{f}_{i-1}$, $\bar{f}_i$ and $\bar{f}_{i+1}$, respectively, then from Figure B.1 one sees that

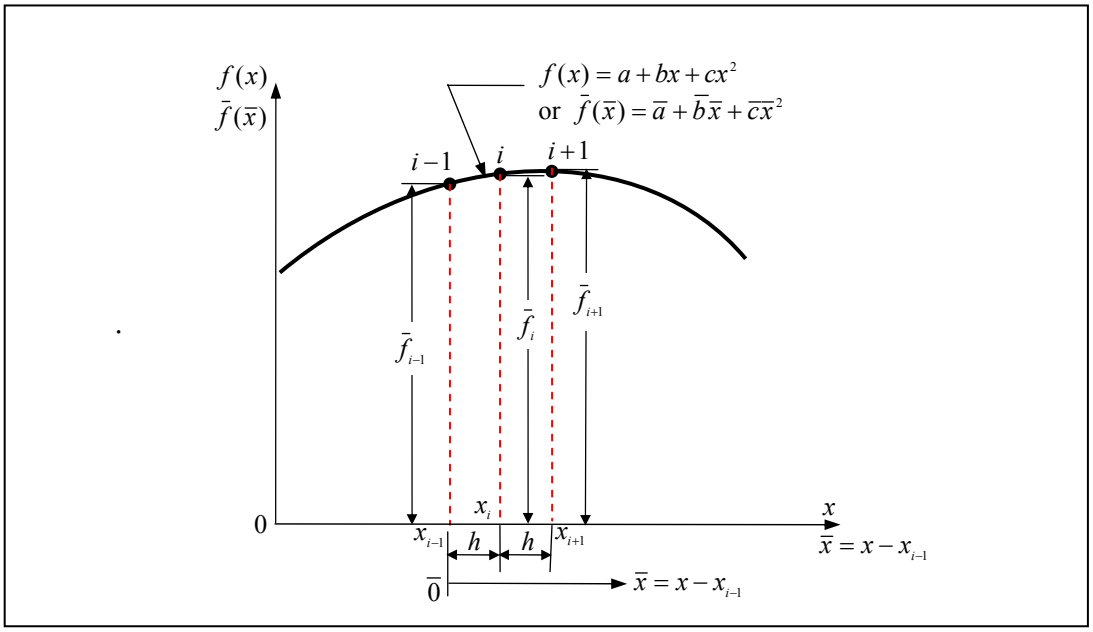

Figure B. 1 The "3-point" curve segment passing through the three points, $i-1$, i and $i+1$, is represented by the "quadratic" equation $f(x) = a + bx + cx^2$ or $\bar{f}(\bar{x}) = \bar{a} + \bar{b}\bar{x} + \bar{c}\bar{x}^2$ with $\bar{x} = x - x_{i-1}$.

$$\bar{f}_{i-1} = \bar{f}(0) = \bar{a} \qquad (\text{at } \bar{x} = 0) \tag{B.4a}$$

$$\bar{f}_i = \bar{f}(h) = \bar{a} + h\bar{b} + h^2\bar{c} \qquad (\text{at } \bar{x} = h) \tag{B.4b}$$

$$\bar{f}_{i+1} = \bar{f}(2h) = \bar{a} + 2h\bar{b} + 4h^2\bar{c} \qquad (\text{at } \bar{x} = 2h) \tag{B.4c}$$

where h is the spacing (in x-direction) between points $i-1$ and i, which is equal to that between points i and $i+1$, as one may see from Figure B.1.

From Equation (B.4a) one obtains

$$\bar{a} = \bar{f}_{i-1} \tag{B.5a}$$

From Equations (B.4b) and (B.4c) one has

$$2\bar{f}_i - \bar{f}_{i+1} = \bar{a} - 2h^2\bar{c}$$

or

$$\bar{c} = \frac{-(2\bar{f}_i - \bar{f}_{i+1} - \bar{a})}{2h^2} = \frac{-(2\bar{f}_i - \bar{f}_{i+1} - \bar{f}_{i-1})}{2h^2} \tag{B.5b}$$

Substituting the values of $\bar{a}$ and $\bar{c}$ given by Equations (B.5a,b) into Equation (B.4b) produces

$$\bar{b} = \frac{\bar{f}_i - \bar{a} - h^2\bar{c}}{h} = \frac{1}{h}\left[\bar{f}_i - \bar{f}_{i-1} + \frac{1}{2}(2\bar{f}_i - \bar{f}_{i+1} - \bar{f}_{i-1})\right] = \frac{1}{2h}(4\bar{f}_i - \bar{f}_{i+1} - 3\bar{f}_{i-1}) \tag{B.5c}$$

From Figure B.1 one sees that the area under the "3-point" curve segment passing through the three points, $i-1$, i and $i+1$, is given by

$$\begin{aligned} A_i &= \int_0^{2h} \bar{f}(\bar{x})d\bar{x} = \int_0^{2h} (\bar{a} + \bar{b}\bar{x} + \bar{c}\bar{x}^2)d\bar{x} = \left[\bar{a}\bar{x} + \frac{1}{2}\bar{b}\bar{x}^2 + \frac{1}{3}\bar{c}\bar{x}^3\right]_0^{2h} \\ &= 2\bar{a}h + 2\bar{b}h^2 + \frac{8}{3}\bar{c}h^3 \end{aligned} \tag{B.6}$$

Substituting the values of $\bar{a}$, $\bar{b}$ and $\bar{c}$ by Equations (B.5a,b,c) into Equation (B.6) gives

$$\begin{aligned} A_i &= 2\bar{a}h + 2\bar{b}h^2 + \frac{8}{3}\bar{c}h^3 = 2h\bar{f}_{i-1} + h(4\bar{f}_i - f_{i+1} - 3f_{i-1}) - \frac{4h}{3}(2\bar{f}_i - \bar{f}_{i+1} - \bar{f}_{i-1}) \\ &= \frac{h}{3}(\bar{f}_{i-1} + 4\bar{f}_i + f_{i+1}) \end{aligned} \tag{B.7}$$

Which is the formula for obtaining the area under the "3-point" curve segment passing

through the three points, $i-1$, i and $i+1$, and consisting of two adjacent "identical" spacings as shown in Figure B.1 and is the basic theory for Simpson rule. It is noted that the spacing (in the *x*-direction) *h* between points $i-1$ and i must be equal to that between points i and $i+1$.

Appendix C

Matrices for Mass Moments of Inertias (Inertia Tensors)

In order to develop the mathematical models in SimMechanics, the masses and inertia tensors of every rigid body must be defined. Inertia tensor here means the matrix for mass moment of inertia with unit $\mathrm{kg}\cdot\mathrm{m}^2$. Generally, it takes the form

$$I = \begin{bmatrix} I_{xx} & I_{xy} & I_{xz} \\ I_{yx} & I_{yy} & I_{yz} \\ I_{zx} & I_{zy} & I_{zz} \end{bmatrix} \tag{C.1}$$

Where x, y and z are the coordinate axes passing through the centroid of the rigid body, and the non-diagonal elements in Equation (C.1) are equal to 0 if the three axes are the principal axes. Since the values of the diagonal elements, I_{xx}, I_{yy}, and I_{zz}, have something to do with the configuration (or shape) of the rigid body, they must be determined carefully.

Several kinds of inertia tensors are required for developing various rider-bike system models in SimMechanics. For the bike models, most of the main frame tubes are the thick-walled cylindrical tubes and some of them are the solid rods. The front and rear wheels are modelled as the knife-edged circular disc (Euler disc) [39,47]. For the rider model, the head is modelled as a circular disc, and other muscular parts are modelled as the solid rods.

From [74] and [75], one can obtain the mass moments of inertias for all the above-mentioned rigid bodies. For simplicity, in this study, it is assumed that the centre of gravity (CG) of each rigid body is identical with its centroid.

For a thin solid rod with length l (m) and mass m (kg) as shown in Figure C.1, the matrix for its mass moments of inertias about the centroid coordinate axes xyz is given by

$$I_{\text{solid rod}} = \begin{bmatrix} 0 & 0 & 0 \\ 0 & \frac{1}{12}ml^2 & 0 \\ 0 & 0 & \frac{1}{12}ml^2 \end{bmatrix} \tag{C.2}$$

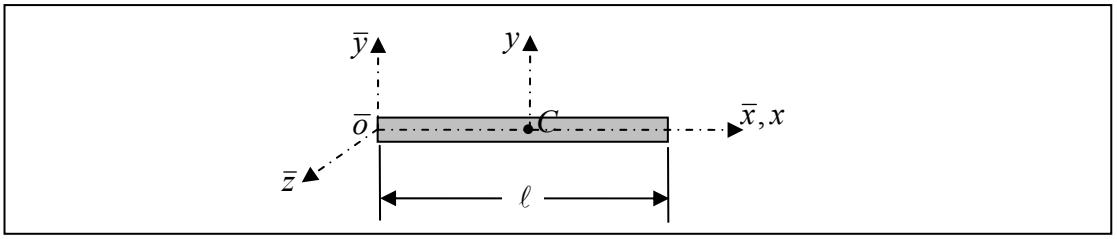

Figure C. 1 The reference coordinate axes $\bar{x}\bar{y}\bar{z}$ and the centroid ones *xyz* for a thin solid rod with length *l*, mass *m* and centroid C.

For a hollow circular cylinder with length *l*, mass *m*, inner radius r_i and outer radius r_o as shown in Figure C.2, the matrix for its mass moments of inertias about the centroid coordinate axes *xyz* is given by

$$I_{\text{hollow circular cylinder}} = \begin{bmatrix} \frac{1}{12}m\left[3\left(r_i^2 + r_o^2\right) + l^2\right] & 0 & 0 \\ 0 & \frac{1}{2}m\left(r_i^2 + r_o^2\right) & 0 \\ 0 & 0 & \frac{1}{12}m\left[3\left(r_i^2 + r_o^2\right) + l^2\right] \end{bmatrix} \tag{C.3}$$

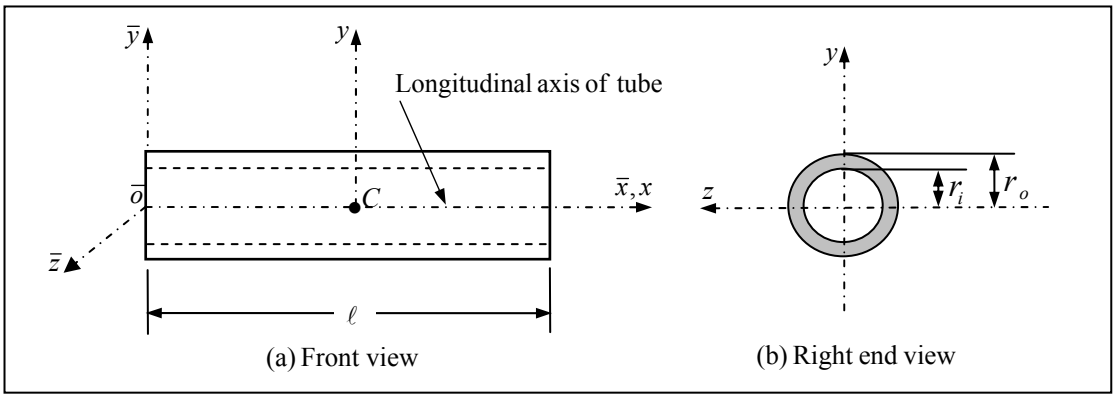

Figure C. 2 The reference coordinate axes $\bar{x}\bar{y}\bar{z}$ and the centroid ones *xyz* for a hollow circular cylinder with length *l*, inner radius r_i , outer radius r_o and centroid C.

For a solid disc with radius *r* and mass *m* as shown in Figure C.3, the matrix for its mass moments of inertias about the centroid coordinate axes *xyz* is given by

$$I_{\text{solid disc}} = \begin{bmatrix} \frac{1}{4}mr^2 & 0 & 0 \\ 0 & \frac{1}{4}mr^2 & 0 \\ 0 & 0 & \frac{1}{2}mr^2 \end{bmatrix} \tag{C.4}$$

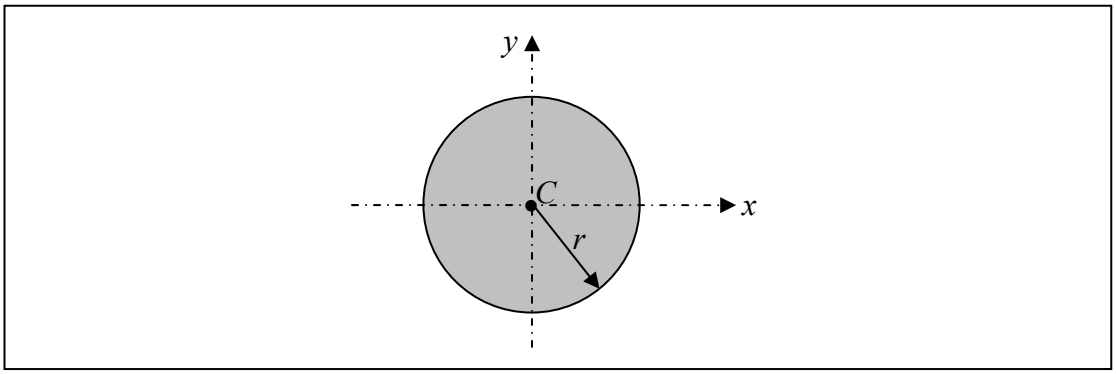

Figure C. 3 A solid disc with radius r, mass m and centroid C

For the muscular parts of a rider model, including shanks, thighs, torso, upper and lower arms, the inertia tensor is modified from Equation (C.2) and takes the form

$$I_{\text{muscular part}} = \begin{bmatrix} \frac{1}{12\times 8} ml^2 & 0 & 0 \\ 0 & \frac{1}{12} ml^2 & 0 \\ 0 & 0 & \frac{1}{12} ml^2 \end{bmatrix} \tag{C.5}$$

By adding the mass moment of inertia about x-axis, $I_{xx}=ml^2/(8\times 12)$, given in Equation (C.5), the shape of a solid rod shown in Figure C.1 will be similar to an ellipsoid and can represent the muscular part better. In other words, the only difference between Equations (C.2) and (C.5) is the value of I_{xx}.

Based on Equations (C.1)-(C.5), various bike models and the rider models can be developed in SimMechanics as one may see from Chapter 5.

Appendix D

Theoretical Analysis for Parameter Transmission between Sprockets

If the radii of the front and rear sprockets are denoted by r_f and r_r, respectively, and the corresponding angular velocities by ω_f and ω_r, respectively, then, the tangential velocity of the chain is given by (see Figure D.1)

$$V_t = r_f \omega_f = r_r \omega_r \tag{D.1}$$

Thus,

$$\omega_r = \left(\frac{r_f}{r_r} \right) \omega_f \tag{D.2}$$

If the torque applied on the front sprocket is $T_f(t)$, then the force in the chain is determined by

$$F_f(t) = \frac{T_f(t)}{r_f} \tag{D.3}$$

The force equilibrium in the chain requires that $F_r(t) = F_f(t)$, thus,

$$F_r(t) = F_f(t) = T_f(t) / r_f \tag{D.4}$$

Therefore, the torque applied on the rear sprocket is given by

$$T_r(t) = F_r(t) \cdot r_r = \left(\frac{r_r}{r_f} \right) T_f(t) \tag{D.5}$$

Since the power of a rotating shaft is given by $P = T\omega$, the power developed by the rear sprocket shaft is determined by

$$P_r = T_r \omega_r = \left(\frac{r_r}{r_f} \right) T_f \cdot \left(\frac{r_f}{r_r} \right) \omega_f = T_f \omega_f = P_f \tag{D.6}$$

In Equation (D.6), T_r and ω_r are given by Equations. (D.5) and (D.2), respectively.

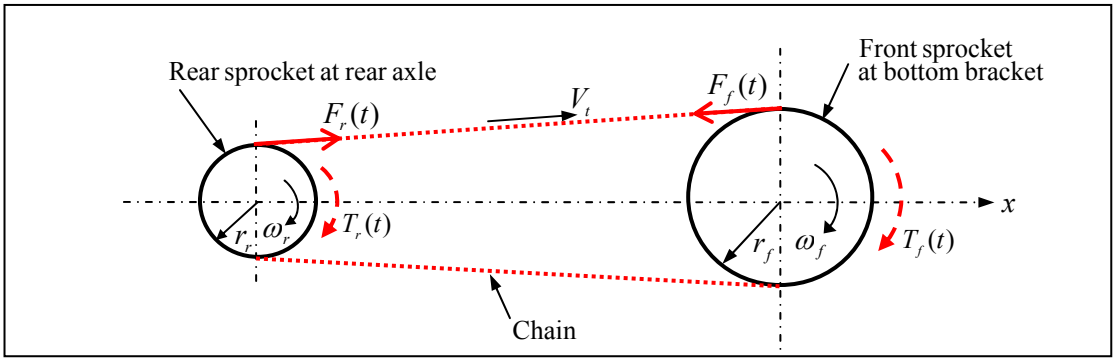

Figure D. 1 Determination of torque transmitted from the front sprocket to the rear sprocket

From Equation (D.6) one sees that $P_r \equiv P_f$, this is correct if the energy loss is neglected.

If the radius of front sprocket, r_f, is 4 times of the radius of the rear sprocket, r_r, that is to say r_r/r_f=1/4=0.25, then from Equation (D.5) one obtains

$$T_r(t) = F_r(t) \cdot r_r = (r_r / r_f) T_f(t) = 0.25 T_f(t) \tag{D.7}$$

In other words, at any time the torque of the rear sprocket is only 0.25 of that of the front sprocket. However, because the angular velocity of the rear sprocket, ω_r, is 4 times of that of the front sprocket, ω_f, as one may see from Equation (D.2), the power of the rear sprocket is equal to that of the front sprocket.

For the case of r_r/r_f=1/4=0.25, Figure D.2 shows the relationship between the external torque on the front sprocket $T_f(t)$ (denoted by the solid line, ——) and that on the rear sprocket $T_r(t)$ (denoted by the dotted line, ·····). It is seen that at the same time t, one has

$$T_r(t) = T_f(t) / 4 = 0.25 T_f(t) \tag{D.5}'$$

$$\theta_r(t) = 4\theta_f(t) \tag{D.8}$$

From Equation (D.2) one has

$$\theta_r = \omega_r t = \left(\frac{r_f}{r_r} \right) \omega_f t = \left(\frac{r_f}{r_r} \right) \theta_f \tag{D.9}$$

Therefore, for the case of r_f/r_r=4, Equation (D.9) reduces to Equation (D.8).

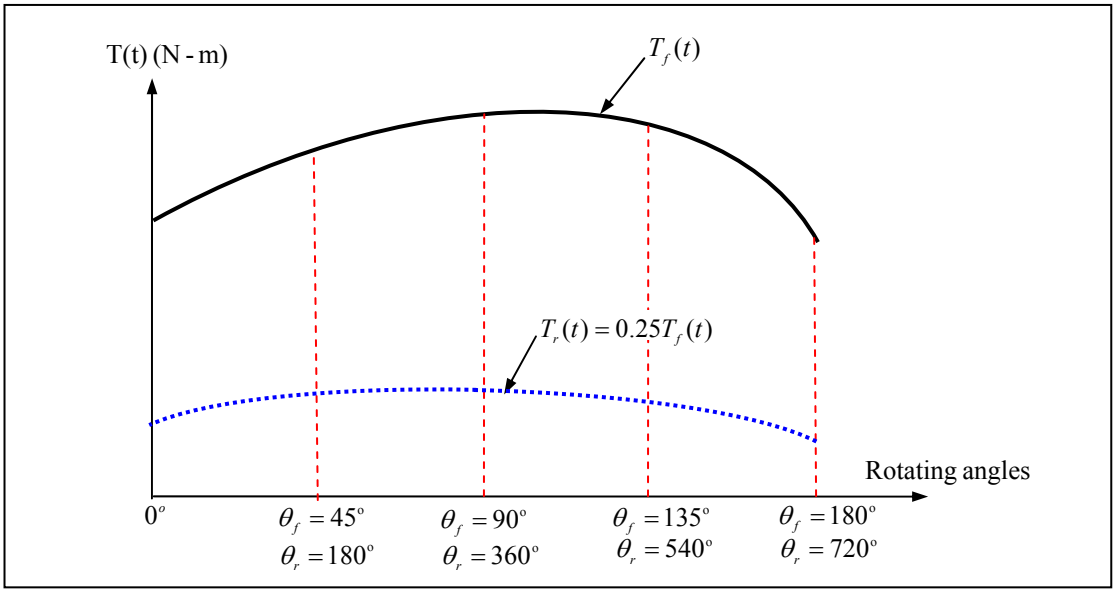

Figure D. 2 Time histories of external torques: if r_f/r_r=4, then at the same time t, the torque on the rear sprocket is given by $T_r(t)=T_f(t)/4=0.25T_f(t)$ with rotating angle $\theta_r(t)=4\theta_f(t)$.

If the external torque $T_r(t)$ on the rear sprocket given by Equation (D.5) can be transformed into external force $F_x(t)$ on the rear wheel (or on the rear axle) by using the next equation

$$F_x(t) = T_r(t)/R_w \tag{D.10}$$

then, from Figure D.3 one sees that the average moving speed $V_x(t)$ of the entire bike is given by

$$V_x(t) \approx R_w \omega_r \tag{D.11}$$

Where R_w is the radius of rear wheel and the subscript x of $F_x(t)$ denotes the force to be in the horizontal (x) direction. The actual value of $V_x(t)$ may be smaller than that given by Equation (D.11) due to inertia forces of the entire bike, frictions or sliding on the road surface, etc.

Substituting Equation (D.5) into Equation (D.10), one obtains

$$F_x(t) = T_r(t)/R_w = \left(\frac{r_r}{r_f R_w}\right) \cdot T_f(t) \tag{D.12a}$$

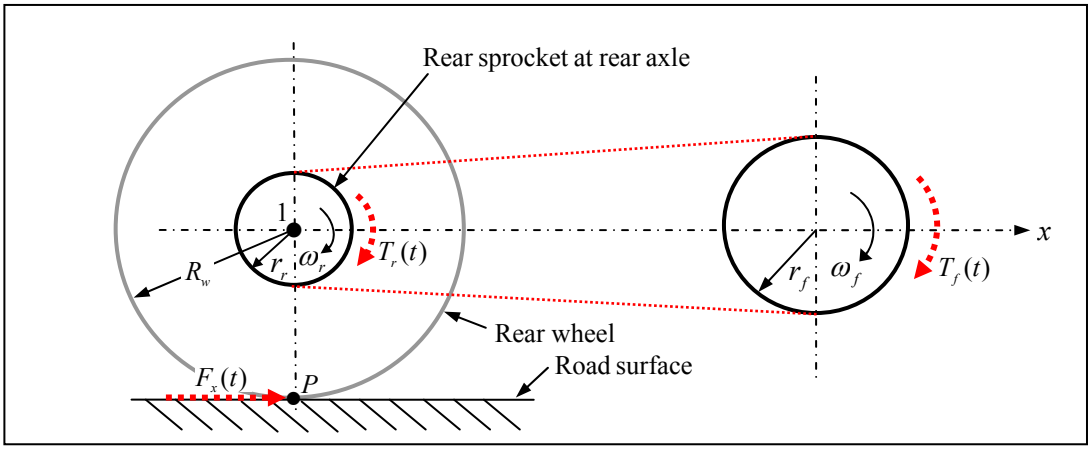

Figure D. 3 External torque $T_r(t)$ on rear sprocket is transformed into external force $F_x(t)=T_r(t)/R_w$

Therefore, if the external torque $T_f(t)$ obtained from rider-bike system is given, then one may obtain the corresponding external force $F_x(t)$ from Equation (D.12a). Applying the external force $F_x(t)$ at point P as shown in Figure D.3 will determinate the responses of the bike.

Another method for obtaining the responses of the bike is to apply the external force $F_x(t)$ together with a counterclockwise torque at point 1 (see Figure D.3)

$$T_z(t) = F_x(t) \cdot R_w \qquad \text{(D.12b)}$$

This is due to the fact that the influence on the rigid body W of the force $F_x(t)$ applying at point P (see Figure D.4) is the same as that of the parallel force $F'_x(t)$ together with a moment $T_z(t)=F_x(t) \cdot R_w$ applying at point 1, where $F'_x(t)= F_x(t)$ and R_w is the distance between the two parallel forces $F_x(t)$ and $F'_x(t)$. The above statement is called "theory for parallel shift of a force" and may be proved as follows (see Figure D.4):

For convenience, one applies two forces $F'_x(t)$ and $-F'_x(t)$ at point 1 with $|F'_x(t)|=|-F'_x(t)|=|F_x(t)|$. Because the two forces have the same magnitudes and opposite directions, their influence on the equilibrium of the rigid body W is nil. However, the force $F_x(t)$ (applying at point P) and the force $-F'_x(t)$ (applying at point 1) constitute a counterclockwise moment or couple given by Equation (D.12b), and the force $F_x(t)$ (applying at point P) is now replaced by the parallel force $F'_x(t)$ (applying at point 1).

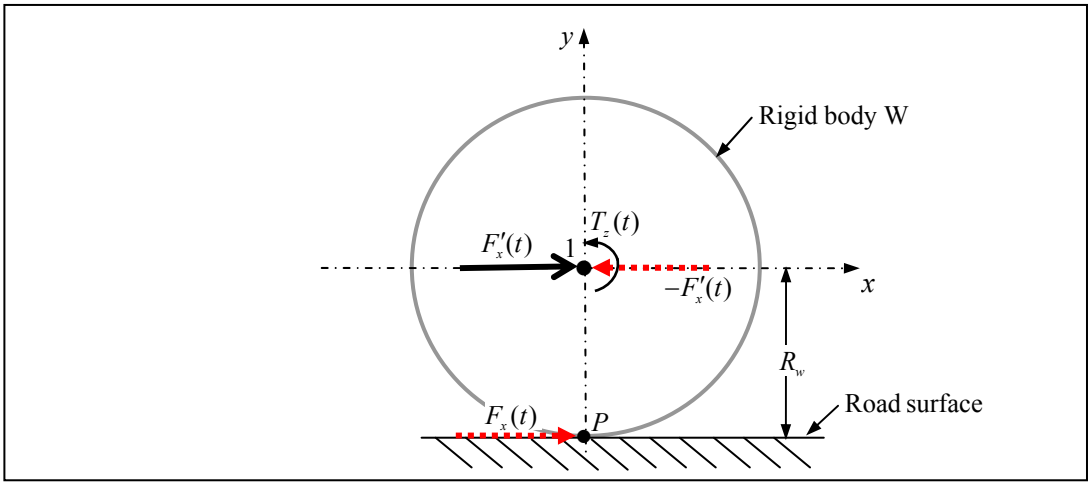

Figure D. 4 Theory for parallel shift of a force: The influence on the rigid body W of the force $F_x(t)$ applying at point P is the same as that of the parallel force $F'_x(t)$ together with a moment $T_z(t)=F_x(t) \cdot R_w$ applying at point 1, where $F'_x(t)= F_x(t)$ and R_w is the distance between the two parallel forces $F_x(t)$ and $F'_x(t)$.

Appendix E

Resistance and Contact Forces

E.1 Overall Resistance

If the entire bike is considered as a "rigid body" and moving in *x*-direction, then its equation of motion is given by

$$m\ddot{x}(t) + c_{equi}\dot{x}(t) + kx(t) = F_x(t) \tag{E.1}$$

where m, c_{equi} and k are mass, *equivalent viscous* damping coefficient and spring constant, respectively, and $F_x(t)$ is the effective applied force in *x*-direction.

Since the spring must be fixed to the ground, for a moving rigid body, one may set k=0, in such a situation, Equation (E.1) reduces to

$$m\ddot{x}(t) + c_{equi}\dot{x}(t) = F_x(t) \tag{E.2}$$

A conventional damper (with damping coefficient c) must also be fixed to the ground, however, since a "damping force" is also one kind of "resistant force", for convenience, one may replace all resistances such as "air resistance" and "frictional resistance" by an "overall resistance" and evaluated by the next formula

$$F_R(t) = c_{equi}\dot{x}(t) \tag{E.3}$$

Since "air resistance" and "frictional resistance" are not linearly proportional *to* the moving velocity $\dot{x}(t)$, for the theoretical analysis, the coefficient c_{equi} in Equation (E.3) is called the *equivalent* viscous damping coefficient**,** for convenience. It is noted that the coefficient c of a conventional damper is called the *viscous* damping coefficient because its damping force is *linear* proportional to the moving velocity $\dot{x}(t)$, i.e., $F_d(t) = c\dot{x}(t)$. For the theoretical analysis, the value of c_{equi} may be obtained from assumptions.

E.2 Contact Force between Wheels and Ground

In Equations (E.1) and (E.2), the effective mass m may be evaluated by

$$m = m_{bike} + m_{rider} \tag{E.4a}$$

with m_{bike} and m_{rider} denoting the bike mass and rider mass, respectively. The contact forces between the two wheels and ground are mainly due to the vertical gravitational force given by

$$F_{contact} = mg = m_{bike}g + m_{rider}g \tag{E.4b}$$

If the total mass of the rider m_{rider} is shared by the handlebar and saddle according to reasonable proportion, then, the contact force on the rear wheel $F_{c,r}$ and that on the front wheel $F_{c,f}$ are determined by

$$F_{c,r} = \frac{\ell_f}{\ell} mg \quad \text{(for rear wheel)} \tag{E.5a}$$

$$F_{c,f} = \frac{\ell_r}{\ell} mg \quad \text{(for front wheel)} \tag{E.5b}$$

where ℓ is the horizontal distance between the rear axle and front axle, ℓ_r and ℓ_f are the horizontal distances between CG of the "entire bike and the rider" and rear axle and front axle, respectively. Of course, if the applied force has the "downward" component $F_{y,c}$ in vertical (y) direction, then Equations (E.5a,b) should be replaced by

$$F_{c,r} = \frac{\ell_f}{\ell} mg + \frac{\tilde{\ell}_f}{\ell} F_{y,c} \quad \text{(for rear wheel)} \tag{E.6a}$$

$$F_{c,f} = \frac{\ell_r}{\ell} mg + \frac{\tilde{\ell}_r}{\ell} F_{y,c} \quad \text{(for front wheel)} \tag{E.6b}$$

where $\tilde{\ell}_{\mathrm{r}}$ and $\tilde{\ell}_{\mathrm{f}}$ are the horizontal distances between the acting point of the force component $F_{y,c}$ and real axle and front axle, respectively.